

Alisa Selimovic

Wadham College

Supervisors

Dr. Paul Watton
Prof. Yiannis Ventikos

PATIENT-SPECIFIC MODELS OF CEREBRAL ANEURYSM EVOLUTION

A thesis submitted for the degree of Doctor of Philosophy

Hilary 2013

A thesis submitted for the degree of Doctor of Philosophy.

Patient-specific models of cerebral aneurysm evolution

By Alisa Selimovic, Wadham College.

Submitted Hilary 2013.

Societal Impact Summary

A cerebral aneurysm (CA) is an abnormal distension of the wall of an artery in the brain, which results from arterial wall weakening. CAs are poorly understood, but are believed to be the result of a combination of biological and life-style factors. The low incidence of rupture coupled with risks of interventional treatments provide motivation for identifying and treating only those aneurysms at risk of rupture. Computational models of aneurysm evolution may provide great insight into CA disease mechanisms, and guide clinical decision-making.

It is well known that vascular cells sense mechanical forces exerted by blood-flow (i.e. haemodynamic forces), which are translated into a myriad of intra- and inter-cellular responses. In this thesis, hypotheses on the role of the patient-specific haemodynamic environment on the evolution of CAs is examined. Arterial geometries are obtained from images of patient-specific vasculature, and the physiological aneurysm is virtually removed and replaced by a novel, fluid-solid-growth (FSG) model. The model incorporates a constitutive model for the artery, growth and remodelling (G&R) hypotheses for arterial wall constituents, and links between G&R and the haemodynamic environment, which is simulated utilising computational fluid dynamics.

It is observed that coupling G&R to the patient-specific haemodynamic environment profoundly impacts the shape and size of the evolving aneurysm geometry; in some cases, the model aneurysm is qualitatively similar to the corresponding physiological aneurysm. This provides tentative support for the hypotheses on haemodynamics-induced G&R investigated here, and motivates the need for improved understanding of arterial adaptation to physiological conditions. This will facilitate the improvement and validation of the model, and may ultimately lead to predictive models with clinical application on a patient-specific basis.

Statement of Originality

I hereby declare that this submission is my own work and to the best of my knowledge it contains no materials previously published or written by another person, or substantial proportions of material which have been accepted for the award of any other degree or diploma at the University of Oxford or any other educational institution, except where due acknowledgement is made in the thesis.

Any contribution made to the research by others, with whom I have worked at the University of Oxford or elsewhere, is explicitly acknowledged in the thesis.

I also declare that the intellectual content of this thesis is the product of my own work, except to the extent that assistance from others in the project's design and conception or in style, presentation and linguistic expression is acknowledged.

Alisa Selimovic
4th February 2013

Acknowledgements

First and foremost, I thank my primary supervisor, Dr. Paul Watton, whose guidance and friendship have made the DPhil an excellent experience. I also thank Professor Yiannis Ventikos, who has been a great support and always a source of good advice throughout my time at Oxford.

Finally, a huge thanks goes to my family, and friends in and outside of the FBG lab, who have made me laugh every day and helped to keep me sane through the most difficult parts.

I gratefully acknowledge the support of The Sir Robert Menzies Memorial Trust, who have funded my time at Oxford.

This thesis template was created by Brett Tully (2010) *'Allostasis of Cerebral Water: Modelling the Transport of Cerebrospinal Fluid'*, PhD Thesis, University of Oxford.

Dissemination

Peer-Reviewed Journal Papers and Conference proceedings

1. Watton P.N., Chen H., Selimovic A., Thompson H., Ventikos Y., 2013, *Intracranial Aneurysms: Modeling Inception and Enlargement*, In: GA. Holzapfel (ed.), Proceedings of IUTAM Symposium on Computer models in Biomechanics: from nano to macro, Springer-Verlag, Heidelberg, pp 161-173.

2. Selimovic A., Ventikos Y., Watton P.N., 2013, *Modelling the Evolution of Cerebral Aneurysms: Biomechanics, Mechanobiology and Multiscale Modelling*, The 23rd International Congress of Theoretical and Applied Mechanics (submitted)

3. Chen H., Selimovic A., Thompson H., Chiarini A., Penrose J., Ventikos Y., Watton P.N., 2013, *Investigating the Influence of Haemodynamic Stimuli on Aneurysm Inception*, Annals of Biomedical Engineering (submitted)

4. Watton PN, Selimovic A et al., 2010. *Modelling evolution and the evolving mechanical environment of saccular cerebral aneurysms*, Biomechanics and modeling in mechanobiology, 10:1, 109-132

5. Selimovic A., Brawanski A., Ventikos Y., Watton P.N., 2013, *Growth, CFD and Structural Analysis of unruptured aneurysms: A follow up study*, American Journal of Neuroradiology (in preparation).

6. Selimovic A., Ventikos Y., Watton P.N., 2013, *Computational framework for patient-specific models of cerebral aneurysm evolution*, ASME Journal of Biomechanical Engineering (in preparation).

Peer-Reviewed Conference Proceedings

1. Selimovic A., Ventikos Y., Watton P.N., *Investigating growth and remodelling hypotheses for patient-specific models of cerebral aneurysm evolution*, 8th European Solid Mechanics Conference, Graz, Austria, July 9th-13th, 2012.

2. Selimovic A., Chen H., Penrose J., Ventikos Y., Watton P.N., 2011, *Low wall shear stress: a driving mechanism for cerebral aneurysm evolution? Modelling development on patient-specific vasculature geometries*, ANSYS UK User Conference, The Heritage Motor Centre, Gaydon, November 9th-10th, 2011.

3. Chen H., Thompson H., Selimovic A., Penrose J., Ventikos Y., Watton P.N., *Investigating blood vessel haemodynamic environment prior to cerebral aneurysm formation: Novel methodology and study of 20 clinical cases*, ANSYS UK User Conference, The Heritage Motor Centre, Gaydon, November 9th-10th, 2011.

4.Watton P.N., Selimovic A., Chen H., Thompson H., Ventikos Y., *Patient-Specific Modelling of Cerebral Aneurysm Evolution*, 2nd International Conference on Mathematical and Computational Biomedical Engineering, Washington DC, USA, March 30th-April 1st, 2011.

5. Selimovic A., Watton P.N., Ventikos Y., *The role of pulsatility on the development of cerebral aneurysms; a computational modelling approach*, Bioengineering 2010 conference, Nottingham, UK, September 15th-16th, 2010.

6. Selimovic A., Penrose J., Bogunovic H., Villa-Uriol M-C, Holzapfel G.A., Ventikos Y., Watton P.N., *A Computational Framework to Explore the Role of Pulsatile Haemodynamics on Cerebral Aneurysm Development for Patient-Specific Arterial Geometries*, 6th World Congress of biomechanics, August 1st-6th, 2010.

Invited lectures

1. Watton P.N., Selimovic A., Chen H., Holzapfel G.A., Ventikos Y., *Modelling Evolution of Cerebral Aneurysms: Biomechanics, Mechanobiology and Multi-scale Modelling*, Mini-symposia on Fluid-Structure Interactions in Biological Systems, International Congress on Theoretical and Applied Mechanics (ICTAM 2012), Beijing, China, 19th-24th August 2012.

2. Watton PN, Selimovic A, Chen H, Thompson H, Ventikos Y., *Modelling aneurysm evolution*, IUTAM Symposium on Computer Models in Biomechanics: From Nano to Macro, Stanford University, California, USA, August 29th-Sept 2nd, 2011.

CONTENTS

Contents vii

List of Figures ix

List of Tables xiv

Acronyms xvi

1 Introduction 1
- 1.1 Healthy arterial structure . . . 3
- 1.2 Mechanical response of the artery . . . 6
- 1.3 Haemodynamics and Mechanobiology . . . 7
- 1.4 Haemodynamics . . . 10
- 1.5 Research aims . . . 25

2 Methods for Quantifying Growth 28
- 2.1 3D geometry alignment . . . 30
- 2.2 The Displacement Index (DI) . . . 33
- 2.3 The Area Stretch Ratio (ASR) . . . 45
- 2.4 Computational Fluid Dynamics Methods . . . 53

3 Haemodynamics and Growth: A Correlation? 61
- 3.1 Haemodynamic and growth index distributions . . . 63
- 3.2 Statistical analysis of correlations . . . 76
- 3.3 Discussion: Visual vs. statistically-assessed correlations . . . 88

4 Models of Cerebral Aneurysm Evolution: A Review 97
- 4.1 Modelling the healthy artery . . . 98
- 4.2 Structural models of aneurysm evolution . . . 100
- 4.3 General computational framework . . . 105

4.4 A Fluid-Solid-Growth framework 110

5 PS FSG Methods 121
5.1 Model integration into PS geometries: ICEM-based method 122
5.2 Model integration into PS geometries: algorithmic method 131

6 PS FSG Results 156
6.1 Pulsatile-flow haemodynamics and aneurysm inception 157
6.2 Effect of WSS and cyclic stretch on aneurysm evolution 167

7 Summary and recommendations 203
7.1 Recommendations for model refinement: modelling ECs 213
7.2 Concluding comments 217

References 219

A Statistical methods for assessing correlations 227
A.1 Correlation vs. regression 227
A.2 Choosing the correct correlation test 228
A.3 Statistical significance of correlations 229

LIST OF FIGURES

1.1 The arteries surrounding the Circle of Willis, with common locations of saccular cerebral aneurysms 2
1.2 Structure of a healthy artery, showing the intima, media and adventitia. Note that cerebral arteries do not have an external elastic lamina 4
1.3 Scanning electron microscope image showing the crimped nature of collagen fibres 5
1.4 Elastin and collagen contributions to the tension-length response of human iliac arteries. 7
1.5 Forces acting on endothelial cells and the activation of cellular signalling pathways in response to mechanical stimuli 8
1.6 Blood-flow patterns in bifurcation and sidewall aneurysms 13
1.7 Simple vs. complex intra-aneurysmal flow 14

2.1 Skeletons and spatial locations of the ICA and BT t_1 and t_2 geometries . . 32
2.2 Overlays and labelling of the t_1 and t_2 ICA and BT geometries 33
2.3 Quantifying displacement between two triangles in 3D space 35
2.4 Determining if line-plane intersect lies within a triangle 36
2.5 DI analytical example 1: sphere within sphere; centrepoints and normals 37
2.6 $SS\,E_i$ normal and corresponding $LS\,E_j$ intersects, and the DI 39
2.7 Plot of the Displacement Index for the sphere-within-sphere example . . 40
2.8 DI analytical example 2: inwardly-directed intersect 41
2.9 Plot of the Displacement Index for the intersecting-spheres example . . . 42
2.10 Overlay of t_1 and t_2 ICA geometries showing an incorrect intersect 43
2.11 The DI plotted as a surface map for the (a) ICA and (b) BT cases 44
2.12 Overview of the ASR algorithm 46
2.13 Differences in numbers and angular displacement of adjacent element normals between coarse and fine meshes 48
2.14 Differences in location of intersects on the t_2 surface for a change in t_1 mesh resolution and radius 49

2.15 Effect of non-uniform displacement between t_1 and t_2 surfaces on t_2 surface intersects . . . 50
2.16 Plot of the ASR for the sphere-within-sphere example . . . 50
2.17 Plot of the ASR for the sphere-within-sphere example with large displacement . . . 51
2.18 The ASR plotted as a surface map for the (a) ICA and (b) BT cases . . . 52
2.19 Control volume, with cell centre P and cell surface normal, $\mathbf{n}$ . . . 54
2.20 A fine mesh, with three prism layers at the vessel boundaries . . . 54
2.21 Application of inlet velocity and outlet pressure boundary conditions in `@neufuse` . . . 57
2.22 Inlet velocity and outlet pressure profiles for the ICA t_1 geometry . . . 58

3.1 Average WSS and WSSG distributions for the ICA case . . . 64
3.2 Plots of average WSS and WSSG against the DI on the ICA t_1 geometry . . . 65
3.3 Plots of average WSS and WSSG against the ASR on the ICA t_1 geometry . . . 66
3.4 WSS and WSSG distributions for the BT case . . . 67
3.5 Plots of WSS and WSSG against the DI and ASR for the BT t_1 geometry . . . 68
3.6 OSI distributions for the ICA case . . . 69
3.7 Comparison of OSI, and DI and ASR distributions for the ICA geometry . . . 70
3.8 OSI distributions for the BT case . . . 71
3.9 AFI(min) and ASR distributions for the ICA case . . . 72
3.10 Comparison of AFI(min), and DI and ASR distributions on the t_1 ICA geometry . . . 73
3.11 AFI(min) distributions for the BT case . . . 73
3.12 GON distributions for the ICA case . . . 74
3.13 Comparison of GON, and DI and ASR distributions for the ICA geometry 75
3.14 GON distributions for the BT case . . . 75
3.15 Linear/LOWESS curve fittings for displacement vs. WSS^{-1} from Boussel et al. (2008) . . . 77
3.16 Scatterplots of the raw ICA and BT DI and haemodynamic index data . . . 79
3.17 Linear, LOWESS, and non-linear fittings to the ICA DI vs WSS^{-1} data . . . 82
3.18 Linear, LOWESS, and non-linear fittings to the BT DI vs WSS^{-1} data . . . 82
3.19 Scatter plots of the ICA and BT raw ASR and haemodynamic index data . . . 85
3.20 Linear, LOWESS, and other fittings to the ICA ASR vs WSS^{-1} data . . . 87
3.21 Linear, LOWESS, and other fittings to the BT ASR vs WSS^{-1} data . . . 87
3.22 Pulsatile-flow blood-flow patterns for the ICA and BT geometries . . . 90

4.1 Unloaded and initially-loaded configurations of the model artery . . . 106

4.2 A body-fitted Lagrangian coordinate system to describe the arterial membrane . . . 107
4.3 Mappings between different cylinder membrane configurations . . . 110
4.4 Computational framework for fluid-solid modelling of cerebral aneurysm growth . . . 111
4.5 Prescribed degradation of elastinous constituents within a small circular patch . . . 115

5.1 Segmentation of geometry and centreline extraction using `@neufuse` segmentation software . . . 122
5.2 Determining cylinder length and radius . . . 123
5.3 Translation of imported geometry to the global axis, and positioning of the cylindrical geometry in ICEM . . . 125
5.4 Creation of smooth connecting surfaces between the up/downstream geometries and the cylinder in ICEM . . . 126
5.5 Labelling, and boundary conditions applied to the physiological geometry 127
5.6 Evolution of WSS following the initial perturbation to the system, and the corresponding evolution of the elastin concentration . . . 129
5.7 Evolution of the medial Green-Lagrange elastin strains and the medial Green-Lagrange collagen strain . . . 130
5.8 Comparison of the original aneurysmal geometry and the connecting surfaces created in ICEM . . . 131
5.9 Limited length of aneurysmal segment to be removed and reconstructed for an aneurysm developing near a bifurcation . . . 133
5.10 The problem of overlapping cross-sections in Chen's (2012) surface-reconstruction method . . . 134
5.11 Definition of the upstream and downstream segments . . . 136
5.12 Plot of cylinder generated in `MATLAB`, and cylinder STL . . . 137
5.13 Reinterpolation of the physiological geometry boundaries . . . 138
5.14 Effect of varying cubic spline tangent magnitudes at the knots . . . 140
5.15 Definition of the straight-line segment between boundary centrepoints, and segments $\mathbf{r_1}$ and $\mathbf{r_2}$ linking boundary centrepoints and intersects . . . 142
5.16 Sigmoid function, defined over the interval $t \in [-1,1]$ . . . 143
5.17 Definition of splines $\mathbf{r_{c_1}}$ and $\mathbf{r_{c_2}}$, with tangents continuous at the upstream and downstream boundaries respectively . . . 143
5.18 Definition of a spline $\mathbf{r_c}$, with tangents continuous at both the upstream and downstream boundaries . . . 145
5.19 Reconstructed surfaces in terms of the sigmoid-weighted splines and STLs 146

5.20 Translation and rotation of a geometry between local and global coordinate systems . . . 148
5.21 Evolution of the WSS and elastin concentration for the algorithmically-reconstructed geometry . . . 150
5.22 Comparison of the final geometries corresponding to the **ICEM**-based, and algorithmic methods . . . 151
5.23 The evolving WSS shown for the full **ICEM** and algorithmic geometries . . . 151
5.24 The cylindrical model embedded within 16 patient-specific, physiological geometries . . . 153
5.25 Comparison of spatial distributions of haemodynamic indices at inception for Chen et al. (2013) pre-aneurysmal geometries vs. the cylindrical model . . . 155

6.1 Definition of the region of interest within which correlations are assessed 158
6.2 WSS distributions for the 12 cases at inception . . . 160
6.3 WSSG distributions for the 12 cases at inception . . . 160
6.4 OSI distributions for the 12 cases at inception . . . 161
6.5 AFI(min) distributions for the 12 cases at inception . . . 161
6.6 GON distributions for the 12 cases at inception . . . 162
6.7 Visually-observed correlation between low WSS, high OSI and minimum AFI . . . 163
6.8 WSS distribution across the full geometry for the 12 cases . . . 164
6.9 Patches of locally elevated *and* reduced WSS within the ROI . . . 164
6.10 Locally reduced WSS, and high WSSG within ROIs of cases 3 and 5 . . . 165
6.11 Effect of second-order discontinuity of cylinder-connecting surface boundaries on the distributions of haemodynamic indices . . . 166
6.12 The evolving WSS environment of 6 cases . . . 169
6.13 Qualitatively similar evolution of model aneurysmal geometries to the corresponding original aneurysmal segments . . . 171
6.14 Evolving WSS and WSSG distributions on the case 3 and 5 model aneurysmal geometries . . . 172
6.15 Evolving systolic and diastolic geometries, A_c^{CS}, E_{M+}^{C} and m_{M+}^{C} for the test physiological case without the CAF . . . 179
6.16 Evolving systolic and diastolic geometries, A_c^{CS}, E_{M+}^{C} and m_{M+}^{C} for the test physiological case with the CAF . . . 180
6.17 Comparison of the final test physiological geometries with/without CAF to the original aneurysmal geometry . . . 181
6.18 Overlays of the evolving aneurysmal geometry, with and without the CAF, for 6 cases . . . 182

6.19 Evolving WSS and elastin concentration distributions for cases 2 and 4 with CAF . . . 183
6.20 Evolution of the WSS distributions for case 4 with and without the CAF . . 185
6.21 Overlay of the case 4 cylindrical geometries with (blue) and without (grey) CAF at $t = 5$ years . . . 185
6.22 Evolving CAF and medial collagen concentration for case 2 . . . 185
6.23 Evolving CAF and medial collagen concentration for case 4 . . . 186
6.24 Comparison of five functional forms for the CAF . . . 188
6.25 Comparison of size of geometries for which the CAF is implemented as a multiplicative vs. additive function . . . 189
6.26 Evolution of the areal cyclic stretch and the medial collagen concentration for the exponential CAF implemented as a multiplicative vs. additive function for years 1-5 . . . 190
6.27 Evolution of the areal cyclic stretch and the medial collagen concentration for the exponential CAF implemented as a multiplicative vs. additive function for years 1-5 . . . 191
6.28 Comparison of the five functional forms of the CAF over the extended interval 0-0.59 . . . 194
6.29 The evolving systolic and diastolic geometries, and corresponding systolic areal cyclic stretch and medial collagen concentration for the test physiological case with a sigmoid multiplicative CAF . . . 197
6.30 The evolution of the CAF when implemented as a combination of a multiplicative sigmoid and additive exponential . . . 198
6.31 The evolving systolic and diastolic geometries, and corresponding areal cyclic stretch and medial collagen concentration for the test physiological case with a sigmoid multiplicative, and exponential additive CAF . . . 199
6.32 The evolving WSS and elastin concentration for the test physiological case with a sigmoid multiplicative, and exponential additive CAF . . . 199
6.33 Comparison of the trajectory of the CAF function for varying values of β^{CS} 202

7.1 Layers of the artery, showing ECs, the internal elastic lamina, vSMCs and vSMC-produced elastin, and collagen . . . 214
7.2 The preferentially axial alignment of ECs, influenced by WSS and cyclic stretching . . . 215

LIST OF TABLES

2.1 Meshing parameters applied to the ICA and BT t_1 and t_2 geometries . . . 54

3.1 Summary of visually-assessed correlations between the haemodynamic indices and the DI (a) and ASR (b) . . . 76
3.2 Kolmogorov-Smirnov normality tests for raw (a) and transformed (b) ICA and BT DI and WSS data . . . 80
3.3 Spearman's Rank bivariate correlation for raw ICA and BT DI and haemodynamic index data . . . 81
3.4 Table of transformations applied to raw growth index and WSS data . . . 81
3.5 Linear, logarithmic, inverse, quadratic and exponential model summaries for ICA DI vs. WSS^{-1} data . . . 83
3.6 Linear, logarithmic, inverse, quadratic and exponential model summaries for BT DI vs. WSS^{-1} data . . . 83
3.7 Kolmogorov-Smirnov normality tests for raw (a) and transformed (b) ICA and BT ASR and WSS data . . . 84
3.8 Spearman's Rank bivariate correlation for raw ICA and BT ASR and haemodynamic index data . . . 84
3.9 Linear, logarithmic, inverse, quadratic and exponential model summaries for ICA ASR vs. WSS^{-1} data . . . 87
3.10 Linear, logarithmic, inverse, quadratic and exponential model summaries for BT ASR vs. WSS^{-1} data . . . 88
3.11 Correlations between haemodynamic indices for both the ICA and BT cases . . . 92

4.1 Material, geometry and physiological parameters for modelling the human internal carotid artery (Watton et al., 2011) . . . 113

5.1 Summary of modelling parameters applied to the steady-flow simulation on the test physiological case . . . 128
5.2 Summary of patient information corresponding to the selected 12 cases . 153

5.3 Summary of the main growth and remodelling parameters applied to FSG simulations on 12 physiological cases 154

6.1 Summary of positive correlations in this study, and compared to that found in the study by Chen et al. (2013) for the same 12 cases 159
6.2 Critical WSS thresholds for onset and maximum elastin degradation . . . 168
6.3 Critical WSS thresholds for onset and maximum elastin degradation . . . 168
6.4 Multiplicative vs additive medial collagen concentrations, strains, cyclic stretches, and the CAF 192
6.5 Comparison of maximum cyclic areal stretch and the corresponding maximum deviation of the cyclic areal stretch from the homestatic stretch 193

ACRONYMS

AFI	Aneurysm formation indicator
ASR	Area stretch ratio
BA	Basilar artery
BT	Basilar terminus
CA	Cerebral aneurysm
CAF	Cyclic area function
CFD	Computational fluid dynamics
DI	Displacement index
EC	endothelial cell
ECM	Extracellular matrix
GON	Gradient oscillatory number
G&R	Growth and remodelling
ICA	Internal carotid artery
IEL	Internal elastic lamina
LPCA	Left posterior cerebral artery
LSCA	Left superior cerebellar artery
MCA	Middle cerebral artery
OSI	Oscillatory shear index
PS	Patient-specific
RPCA	Right posterior cerebral artery
RSCA	Right superior cerebellar artery
TPC	Test physiological case
VSMC	Vascular smooth muscle cell
WSS	Wall shear stress
WSSG	Wall shear stress gradient



CHAPTER 1

ARTERIAL STRUCTURE AND CEREBRAL ANEURYSMS

A cerebral aneurysm is best described as an abnormal distension of the wall of a cerebral artery, resulting from arterial wall weakening. Once formed, it is believed that haemodynamic forces resulting from blood-flow coupled with a degradation of the arterial wall may cause aneurysm enlargement, which, in turn, may lead to rupture due to the corresponding decline in wall strength (Humphrey and Canham, 2000). While the incidence of cerebral aneurysms is relatively high (occurring in between 2-5% of the adult population (Humphrey, 2008b)), the risk of rupture is very low, with less than 1% of detected aneurysms rupturing per year (Ingall et al. (2000); Juvela (2004)). However, rupture usually results in subarachnoid haemorrhage with high mortality, with 45% of ruptured aneurysms resulting in death in the first 30 days (Brisman et al., 2006). The outlook for survivors is also grave, with 30% facing moderate to severe morbidity (Brisman et al., 2006).

Cerebral aneurysms most commonly occur on the arteries surrounding the Circle of Willis (particularly at regions of high curvature, and bifurcations), and have either a fusiform (spindle), or, more commonly (>90%), a saccular ("berry-like") shape (Humphrey and Canham, 2000). As such, general discussion of cerebral aneurysms in this section is with respect to saccular cerebral aneurysms. Figure 1.1 shows the vessels of and surrounding the Circle of Willis, and the common locations of saccular cerebral aneurysms.

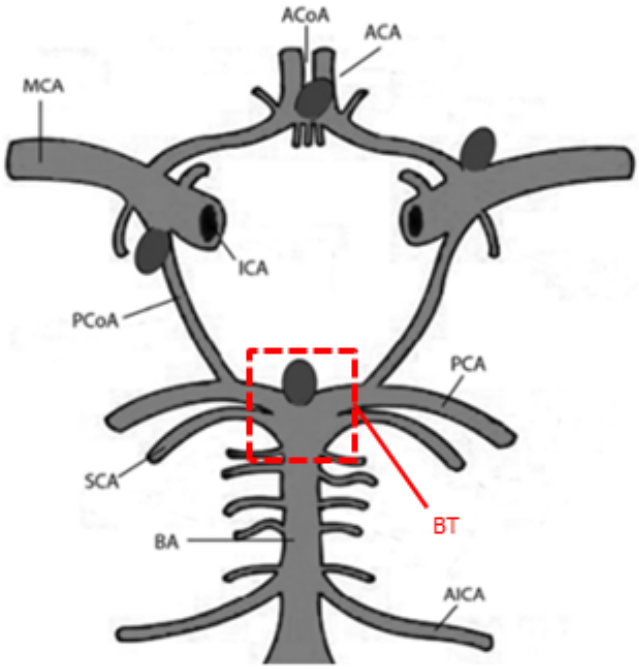


Figure 1.1: Diagram showing the arteries surrounding the Circle of Willis, with common locations of saccular cerebral aneurysms (adapted from Nixon et al. (2010)). Artery names are abbreviated; some that feature frequently in discussion in this thesis are the internal carotid artery (ICA), middle cerebral artery (MCA), basilar artery (BA), and posterior/anterior communicating artery (PCA/ACA). The region highlighted in red comprises the basilar terminus (BT)

The exact cause of cerebral aneurysms is not yet known, but it is well accepted that they are a result of a complex interplay between multiple factors, including blood-flow, arterial wall composition, cell populations, genetics and signalling pathways (Ventikos et al., 2009). The interactions of these factors are poorly understood, and as such, there is currently no accurate means of determining the outcome for a detected aneurysm. In addition, cerebral aneurysms are predominantly asymptomatic prior to rupture, and consequently, they are often detected in an in-

cidental exam, or when symptoms present due to a great increase in size (Sforza et al., 2009).

Improvement of imaging techniques has resulted in increased detection of unruptured aneurysms, but, given that prognosis of aneurysm rupture is still poor, it has also resulted in increased clinical intervention (Sforza et al., 2009). The current measure of the risk of rupture (on which the need for clinical intervention is assessed) is based predominantly on aneurysm size or aspect ratio, which do not account for patient-specific variabilities including family history and life-style, as well as haemodynamic variabilities (Ventikos et al., 2009). Furthermore, while it may seem intuitive that larger aneurysms are at greater risk of rupture, as Lasheras (2007) points out some small aneurysms have been found to rupture, while others have been found to grow to very large sizes without rupture. Additionally, the current interventional procedures for treatment of an unruptured aneurysm are not without risk to the patient, with associated morbidity and mortality rates of <6% and <2.5% respectively (Peters et al., 2001). Therefore, it is clear that there is great merit in developing a rigorous method for identifying those aneurysms that are likely to rupture, and thus, require interventional treatment. Ultimately, such models aim to assist clinicians in determining the need for intervention, as well as the appropriate interventional treatment on a patient-specific basis.

1.1 HEALTHY ARTERIAL STRUCTURE AND HOMEOSTASIS

In order to understand aneurysm evolution, we must first have an understanding of the structure and physiology of the healthy artery. In general, human arteries consist of three layers: the tunica intima, the tunica media, and the tunica adventitia (Figure 1.2).

The tunica intima consists of a monolayer of endothelial cells (ECs) attached to a basement membrane (Lee, 1995). It is the thinnest layer, and is considered to have little contribution to the solid mechanical properties of the arterial wall (Holzapfel et al., 2000). However, the EC layer acts to regulate the effect of haemodynamic forces on arterial wall remodelling, and as an effective barrier and non-thrombogenic surface for blood and its constituents.

The media is separated from the intima by the internal elastic lamina and con-

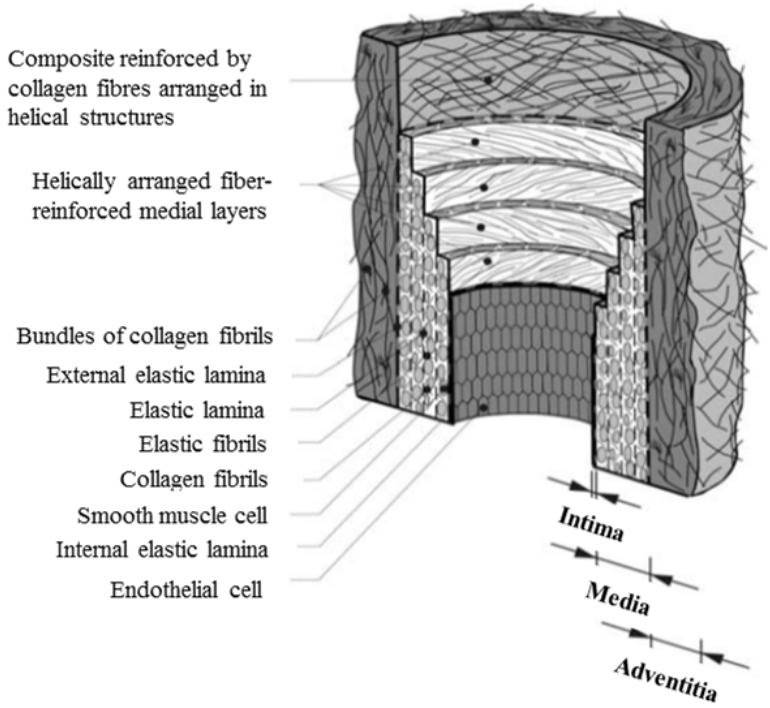


Figure 1.2: Diagram of the structure of a healthy artery, showing the intima, media and adventitia. Note that cerebral arteries do not have an external elastic lamina (adapted from Holzapfel et al. (2000))

tains a three-dimensional network of vascular smooth muscle cells (vSMCs), elastin fragments and collagen fibers (Lee (1995); Holzapfel et al. (2000)). The elastin and collagen fibrils, elastic laminae and vSMCs are interconnected and oriented in such a way as to form a fibrous helix with a small pitch, such that the fibrils are in near-circumferential orientation (Holzapfel et al., 2000). This arrangement accounts for the high strength, resilience and resistance to loads in both longitudinal and circumferential directions of the media (Holzapfel et al., 2000), which make it, structurally, the most significant layer. Elastin, a rubber-like, highly extensible protein, gives elasticity to arterial tissue, while vSMCs act to control the diameter of the artery via vasoconstriction and vasodilation (Wang and Thampatty, 2006).

The adventitia is separated from the media by the external elastic lamina, and composed predominantly of crimped collagen fibres, and fibroblasts (Lee, 1995) (see Figure 1.3). While medial collagen is arranged in two helically distributed families, all with near circumferential orientation, adventitial collagen orientation spans all angles to the azimuthal axis (Gasser et al., 2006). In contrast to elastin fibres, col-



Figure 1.3: Scanning electron microscope image showing the crimped nature of collagen fibres (from:
http://education.vetmed.vt.edu/Curriculum/VM8054/Labs/Lab5/Lab5.htm)

lagen fibres act as a stiff, protective sheath to prevent overdistension of the artery (Shadwick, 1999). Fibroblasts perform many vital functions during development and after maturity, including organizing and maintaining connective tissues, and synthesising collagen types I and III, and other constituents of the extra-cellular matrix (ECM) to which they are attached (Wang and Thampatty, 2006). The ECM acts as a scaffold for cells, and plays a pivotal role in signalling events that mediate cellular proliferation, migration and apoptosis (Cummins et al., 2007). The ECM is maintained by fibroblasts, which produce various growth factors, and matrix metalloproteinases (MMPs), which are involved in connective tissue maintenance, repair, and remodelling (Wang and Thampatty, 2006).

The continual maintenance of the ECM by fibroblasts necessitates a continuous turnover of collagen fibres, which are rapidly synthesised and secreted (in minutes) and turned over, with a reported half-life of between 60-70 days in the normotensive rat aorta and 17 days in hypertensive conditions (Nissen et al., 1978). This rapid turn-over allows a rapid adjustment of the arterial wall to altered mechanical conditions, such as altered flow, or increased pressure (Gleason and Humphrey (2004); Gleason et al. (2004)). According to Alberts et al. (2002), the collagen fibres are attached and configured by fibroblasts in a state of stretch, hereon referred to as the "attachment stretch". As will be seen in the coming chapters, continuous collagen synthesis and degradation, and the deposition of new collagen in the same state of stretch have been pivotal concepts in the proposal of fundamental hypotheses for arterial growth and remodelling. This has in turn been pivotal to the formulation and sophistication of computational models of arterial tissue.

Finally, it must be noted that cerebral arteries exhibit some structural differences compared with systemic arteries, i.e. a well-developed internal elastic lamina, a lesser amount of elastic fibres in the media, little adventitial tissue, absence of vasa vasorum and no external elastic lamina (Lee, 1995). As a result, cerebral arteries exhibit differences in elasticity compared with systemic arteries, though their mechanical responses are qualitatively similar (Holzapfel et al., 2000). Humphrey (2008b), also note that compared with systemic arteries, cerebral arteries lack supporting perivascular tissue, and, particularly at bifurcations, exhibit structural irregularities.

1.2 THE MECHANICAL RESPONSE OF THE ARTERY

The major structural constituents of the artery give rise to its mechanical response in homeostatic maintenance, as well as during disease progression. In a review on the continuum mechanics of soft biological tissues, Humphrey (2003) points to early in vitro experiments in which it was observed that arteries exhibit an anisotropic response, creep (which signifies a viscoelastic character), and a thermoelastic behaviour similar to rubber. Additionally, the experiments showed that in terms of material properties, arteries exhibit both local and regional heterogeneity (i.e. material properties differ at various locations of the same artery, and between different arteries), that they change with exercise, age and disease, and that they exhibit differences between genders. Thus, as Humphrey summarises, arteries exhibit a nonlinear, inelastic, heterogeneous, anisotropic character that varies from point to point, from time to time and from individual to individual. Additionally, within the physiological environment, arteries are subject to an axial in situ stretch (or "pre-stretch"), which can be observed in the form of shortening of the artery upon its removal from the body, as well as residual stress in the wall, such that the load-free configuration is not stress-free (Holzapfel et al., 2000). The non-linear mechanical response of the artery is thought to be predominantly attributed to the combination of elastin and collagen constituents, where the initial compliance of the artery at low pressures is attributed to elastin, while the exponential stiffening effect at higher pressures is attributed to the gradual recruitment and straightening of the wavy collagen fibres (Shadwick (1999); Holzapfel et al. (2000)). The broad distribution of medial and adventitial collagen fibres with respect to the azimuthal axis, along with the structural arrangement of medial vascular smooth muscle cells

gives rise to arterial tissue anisotropy. Figure 1.4 below shows the largely linear response of elastinous constituents, the highly non-linear response of collagenous constituents, and the overall non-linear response of elastin and collagen combined:

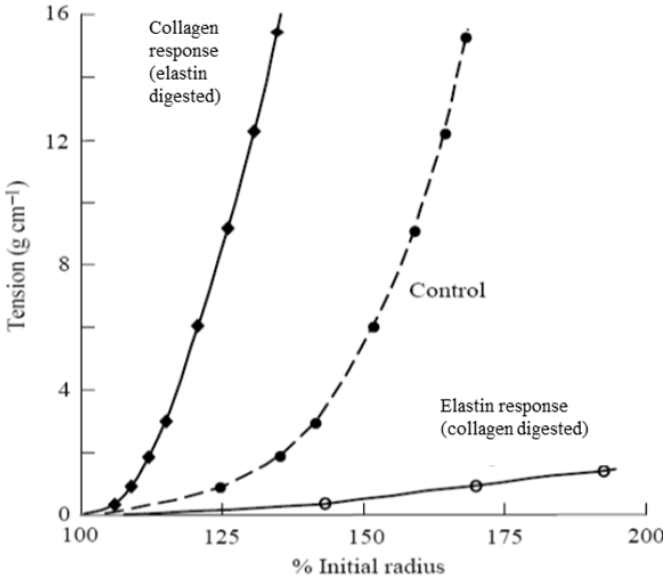


Figure 1.4: Elastin and collagen contributions to the tension-length response of human iliac arteries. The elastin-only response is shown as the line with unfilled circles. The collagen-only response is shown as the curve with diamonds. The "control" curve shows the combined collagen-elastin response (adapted from Shadwick (1999))

1.3 HAEMODYNAMICS AND MECHANOBIOLOGY

Steinman et al. (2003) state that, among other diseases such as atherosclerosis, mechanobiology certainly has a key role in the development, enlargement and rupture of cerebral aneurysms. Mechanobiology is an interdisciplinary field, the focus of which is to improve our understanding of the process by which mechanical stimuli are converted by cells into biological signals. This process is commonly referred to as "mechanotransduction", whereby mechanical stimuli activate cellular mechanosensors, signaling pathways, and gene and protein expressions (see Figure 1.5(b)) (Chien, 2007). A key component of the transduction process is the cellular cytoskeleton. In an extensive review, Kolahi and Mofrad (2010) describe the cytoskeleton as a stress-bearing structure, which not only governs cell shape, but also provides a mechanical link between the external and internal cell environments. It can,

for example, bind directly, or indirectly, to all endothelial cell shear stress receptors, and itself undergoes rapid changes in response to flow (Resnick et al., 2003), cellular movement and shape change (Kolahi and Mofrad, 2010). Salameh and Dhein (2012) note that the deformation of the ECM by mechanical forces can also be transduced by stretch-activated ion channels and by surface receptors, such as integrins, which bind to the ECM. Integrins mediate cellular attachment to the ECM, and their interactions lead to transmission of mechanical stresses into the cell, resulting in both intra- and extra-cellular responses (Okada et al., 1998).

While the cerebral artery wall cannot directly detect the rate of blood-flow, it has been shown to respond to the frictional force of blood (*shear stress*) and pressure (Meng et al., 2011). These are discussed in detail in §1.4. Intimal ECs in cerebral arteries have been shown to respond to many forces (see Figure 1.5(a)), such as axial and circumferential stresses, pressure, the cyclical strain due to distension of the artery, and wall shear stress (WSS) (Wang and Thampatty, 2006).

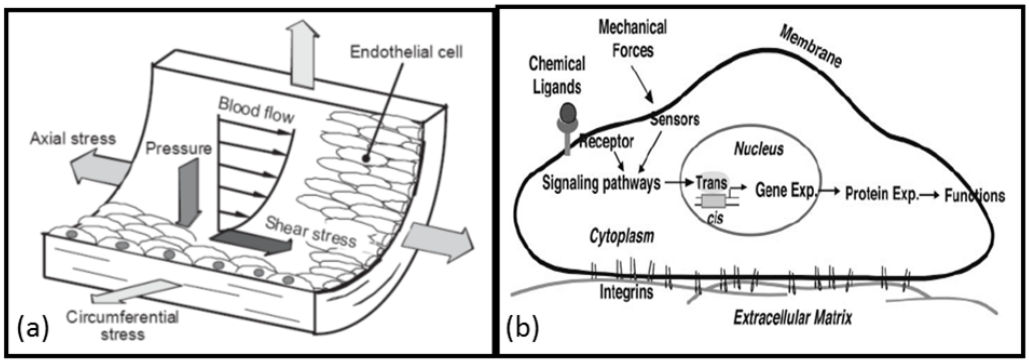


Figure 1.5: (a) Forces acting on endothelial cells: axial and circumferential stresses, pressure, and shear stresses due to blood flow (Ohashi and Sato, 2005) (b) Activation of a complex chain of cellular signalling pathways in response to mechanical stimuli (Chien, 2007)

As Chien (2007) discusses, directed mechanical forces acting on ECs influence the regulation of inflammatory and proliferative pathways. Mechanical forces with a clear direction (e.g., the pulsatile shear stress resulting from strong forward, laminar flow in straight regions of arteries) cause a transient activation of pro-inflammatory and proliferative signalling pathways, which become down-regulated when such forces are sustained. In contrast, mechanical forces without a definitive direction (e.g. disturbed flow observed at regions of complex arterial geometry, such as branching regions) result in a sustained activation of pro-inflammatory and pro-

liferative pathways. Chien (2007) goes on to explain that EC responses to directed mechanical stimuli involve the remodelling of the cellular structure to minimise the change in intracellular stress/strain from homeostatic levels, and induce adaptive changes in EC signalling in response to sustained stimuli. This constitutes an important feedback control system, which protects the artery from the onset of diseases such as atherosclerosis. However, this protective mechanism is less effective in regions of complex geometry, where blood-flow is strongly vortical, and the mechanical stimuli are not coherently directed (Chien, 2007).

The feedback control system discussed by Chien (2007) is part of the process of "normal", or non-pathophysiological arterial wall remodelling. Kolega et al. (2011) discuss normal remodelling as a constructive process. For example, in response to an increase in blood-flow, and thereby, WSS, arterial remodelling is such as to include a slight, transient degradation of the ECM (Kolega et al., 2011) and the IEL due to the early expression of matrix metalloproteinases (MMP-2 and -9) (Hashimoto et al., 2006). The degradation of the IEL then allows the expansion of the arterial wall scaffold, which acts to return WSS to a baseline level (Hashimoto et al., 2006). Meanwhile, synthesis of additional ECM, and proliferation of ECs and vSMCs occurs to cover the newly enlarged surface (Hashimoto et al. (2006); Kolega et al. (2011)). Humphrey (1999) also notes that in the case of a prolonged increase in flow, the arterial wall constituents may remodel to achieve an entirely new state of homeostasis.

However, it must be noted that during this process, ECs are not the only cells in the arterial wall that respond to mechanical forces. Shyu (2011) note that, while ECs are primarily affected by WSS, vSMCs are primarily subjected to cyclic stretch arising due to the pulsatile changes in blood pressure. While it seems the effect of WSS on vascular cells, particularly in pathological conditions, has been extensively researched, cyclic stretch is only recently receiving more attention. However, it has been shown to affect both EC and vSMC orientation and signalling, as well as phenotype (Iba and Sumpio (1991); Cummins et al. (2007); Shyu (2011)).

Furthermore, Kolega et al. (2011) discuss the change in vSMCs from a "normal" *contractile* phenotype, to a *proliferative* phenotype, which has been observed in diseased arterial states. As Humphrey (1999) notes, an acute increase in blood-flow results in up-regulation of the production of nitric oxide (NO), and down-regulation of endothelin-1, which act on vSMCs to cause vasodilation and vasoconstriction respectively. This mechanism allows the arterial lumen cross-section to increase to

restore WSS to a homeostatic level (Humphrey, 1999). Additionally, NO acts to inhibit vSMCs proliferation, and some pro-inflammatory factors (Nixon et al., 2010). Similarly, the rate of synthesis and degradation of ECM material by fibroblast cells is affected by the strains they experience during the cardiac cycle, where an increase in strain results in an increase in the production of collagen fibres, and decrease in the production of matrix-degrading enzymes, while a decrease in strain produces a converse result (Wang and Thampatty, 2006). Therefore, while cells such as ECs, vSMCs and fibroblasts are not considered to contribute highly to the bulk mechanical response of the artery, it is clear that their representation within arterial models is important in providing insight into the mechanisms behind arterial disease.

1.4 Haemodynamics and Aneurysm Evolution: A review

In the previous section, the notion of "normal" arterial wall remodelling was introduced, which includes destruction of the ECM and IEL to allow arterial wall expansion, and the subsequent proliferation of ECs and vSMCs to cover the enlarged arterial wall surface. Pathophysiological, or *destructive*, remodelling, as occurs during aneurysm development, appears to be an exacerbated form of normal remodelling. A common feature of aneurysmal walls, particularly during the early stages of aneurysm development, is a disrupted IEL and disrupted EC layers, a thinned media with a scarcity of vSMCs (due to a combination of apoptosis and inhibition of proliferation), and the presence of inflammatory cells (Hashimoto et al., 2006). While much of the focus of examined literature is on the role of haemodynamic forces in aneurysm inception and growth, it is clear that the blood-flow pattern at the site of aneurysm formation is itself dependent on two main factors:

- arterial geometry -i.e. highly curved segments and arterial bifurcations exhibit disturbed flow compared to relatively straight arterial segments, and
- pre-existing conditions, such as smoking and hypertension, which influence blood viscosity and pressure respectively

However, while certain geometric features (e.g. arterial bifurcations) exhibit what are believed to be more "dangerous" haemodynamic conditions, these features are

common across the population, and it remains to be understood why only some people develop aneurysms in these regions, while others do not. In fact, only about 40% of the population has a "textbook" Circle of Willis (Nixon et al., 2010), so it is clear that geometry alone cannot account for aneurysm development. Given the inter-person variability in arterial geometry and the incidence of aneurysms on both highly curved and straight arterial segments, it seems more likely that, with perhaps the exception of genetic factors, aneurysm development is an unfortunate coincidence of multiple factors.

1.4.1 A note on hypertension

While the exact combination of factors that lead to aneurysm development is unknown, hypertension (or sustained high blood pressure) appears to be a strongly-linked, and pre-requisite condition for aneurysm initiation. It is often associated with a high WSS, resulting from a sustained increase in flow (discussed in detail in §1.4.3). Humphrey (2008b) points to the fact that, given factors like the lack of external elastic lamina, and irregularities at bifurcations of cerebral arteries, the haemodynamic loads, particularly under hypertension, may be enough to cause local arterial wall weakening. In a follow-up study of a patient with a history of severe obesity and hypertension, Kulcsár et al. (2011) found that the WSS at the basilar apex was nearly six times the average value. Chronic hypertension can cause endothelial dysfunction (Penn et al., 2011), which can result in a downregulation in eNOS (the synthesising agent for NO) and, thereby, inhibition of vessel dilation (Metaxa et al., 2008) and amplification of WSS (Penn et al., 2011). Hypertension also results in increased circumferential stretch of the vessel, which in turn leads to a release of growth and migration factors resulting in the thickening of the vSMC layer and a loss of vessel elasticity (Hahn and Schwartz, 2008). Circumferential stretch also upregulates the secretion of the potent vasoconstrictor, endothelin-1, which has been shown to promote vSMC apoptosis (Penn et al. (2011); Hashimoto et al. (2006)) resulting in weakening of the arterial wall. Indeed, many *in-vivo* studies of aneurysm development using animal models impose hypertensive and/or high-flow conditions by, for example, maintaining the animals on a high-salt diet, and by performing arterial ligation (e.g. Gao et al. (2008); Meng et al. (2011); Kolega et al. (2011)), following which an aneurysm is observed to form.

1.4.2 The effect of arterial and aneurysmal geometry on blood-flow characteristics

Penn *et al.* (2011) discuss that compared to systemic arteries, the small radii and high flow of cerebral arteries means that they are in general exposed to higher WSS. Additionally, as discussed earlier in the chapter, cerebral aneurysms can occur at or near arterial bifurcations, less commonly on the lateral walls of curved vessels, and, occasionally, on the walls of relatively straight arterial segments, which all exhibit different haemodynamic patterns. In straight regions of vasculature, pulsatile flow is steady and laminar, while at curvatures and bifurcations, flow is disturbed and features large oscillations (Shyu, 2011). Resnick et al. (2003) explain that at bifurcations and regions of high curvature, steady laminar flow is disrupted, forming regions of separated flow and recirculation sites. In previous sections, the protective effects of strongly-directed forward flow were discussed, along with the fact that these effects are reduced in regions where flow is disturbed. While laminar shear stress stimulates EC proliferation and inhibits apoptosis, ECs exposed to disturbed flow experience oxidative stress, increased expression of markers of inflammation and monocyte recruitment (Shyu, 2011). Disturbed flow also promotes vSMC migration and proliferation, which are found to occur more frequently at bifurcations and regions of high curvature compared to regions of steady laminar flow (Shyu, 2011). Additionally, regions of high curvature and the apices of bifurcations are often sites of blood-flow impingement, where, as Tateshima et al. (2007) explain, a dynamic pressure resulting from this impingement is superimposed onto the hydrostatic pressure, thereby exposing these regions to a overall higher pressure.

The aneurysmal geometry itself influences blood-flow patterns. For example, in their *in-vivo* measurements of intra-aneurysmal pressure and flow pattern, Moftakhar et al. (2007) identified three types of flow for sidewall vs. bifurcation aneurysms. The former featured a recirculating pattern with entry through one channel at the distal neck, and exit at the proximal neck, while the latter featured either a jet, or re-circulation pattern (Figure 1.6).

In their CFD study on 210 patient-specific geometries, Cebral and Meng (2012) examined the intra-aneurysmal flow and defined three distinct categories based on flow characteristics:

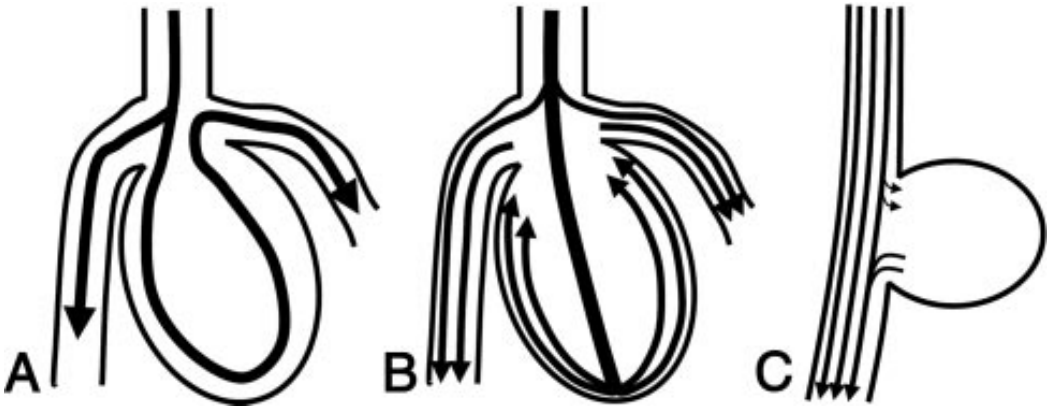


Figure 1.6: Flow patterns in bifurcation and sidewall aneurysms. (A) and (B) Recirculating and jetting flow in a bifurcation aneurysm. (B) shows flow-impingement, whereby the blood impinges on the dome of the aneurysm, and separates into two streams; (C) low velocity flow into and out of a sidewall aneurysm (adapted from Moftakhar et al. (2007))

- simple flow, featuring a single recirculation zone within the aneurysm. An example of a single recirculating zone is shown in Figure 1.7(a), where the flow is observed to both enter and exit the aneurysm dome at the distal neck, and circulate in an anti-clockwise direction within the dome.
- complex flow, featuring flow separations within the aneurysm, and containing more than one recirculation zone. This can be observed in Figure 1.7(b), where flow inside the aneurysm features two recirculation zones (at the proximal neck and dome) and a separation zone in the central region. This pattern is different at a different point of the cardiac cycle.
- stable flow, featuring any persisting flow pattern across a number of cardiac cycles.

The effect of aneurysmal geometry on flow has been investigated utilising CFD on both analytically-defined, and patient-specific geometries obtained from scanning procedures. For example, Hoi et al. (2004) used an idealised mathematical model of a saccular cerebral aneurysm on the lateral wall of a parent artery, and experimented with increasing aneurysm neck width and parent artery curvature. They found that flow impingement intensified with increasing parent artery curvature, while the *area* of impingement increased with increasing curvature and neck size. Tateshima et al. (2010) used CFD to investigate the effect of aneurysm

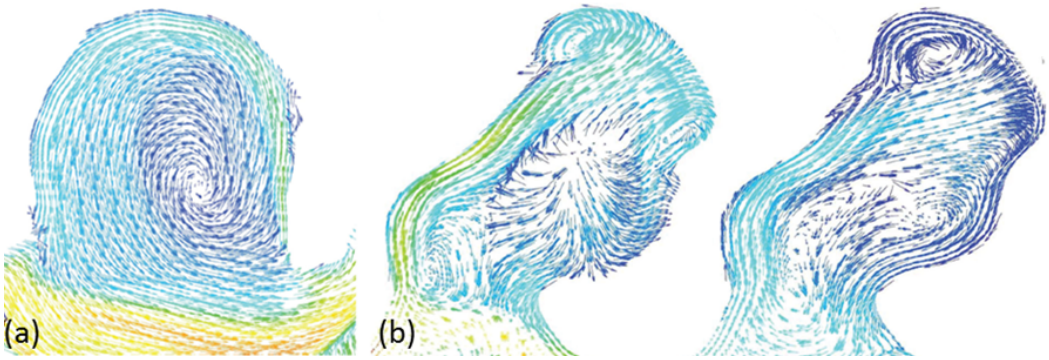


Figure 1.7: Velocity vectors fields within two aneurysms (a) a simple, single-recirculating intra-aneurysmal flow pattern; (b) complex intra-aneurysmal flow pattern at two different time-points during the cardiac cycle (adapted from Kulcsár et al. (2011))

neck and dome sizes on the intra-aneurysmal flow in eight cases of patient-specific opthalmic artery aneurysms. They found that as the aneurysm size increases, the intra-aneurysmal flow velocity and WSS decerase.

1.4.3 The role of haemodynamics in cerebral aneurysm inception

Hashimoto et al. (2006) hypothesise that aneurysm inception is a result of normal outward remodelling, which may become asymmetric or focalised due to particular geometric features; this focus then results in a small, initial bulge. The loss of the IEL appears to be the first prominent change in the wall (Meng et al. (2011); Frösen et al. (2012)), followed by death of vSMCs, which, according to Frösen et al. (2012), is the key difference between normal and destructive arterial wall remodelling. At this point, the artery wall does not protrude out beyond the parent artery (Meng et al., 2011); however, with the loss of the IEL and vSMCs, the weakened arterial wall bulges outward under the force of blood, and an infiltration of inflammatory cells follows (Frösen et al., 2012). Interestingly (and as will be discussed throughout this chapter), the role of inflammatory cells in aneurysm development appears contested in the literature, with some studies hypothesising that inflammatory cells contribute to the initial destructive process, and others that they become important only at later stages of development and rupture.

Both *in-vivo* and computational studies have been employed in an attempt to elucidate the role of haemodynamics in cerebral aneurysm inception. Several

haemodynamic indices relating to aneurysm formation have been defined in addition to WSS and WSSG (the Oscillatory Shear Index (Ku et al., 1985), the Aneurysm Formation Index (Mantha et al., 2006) and the Gradient Oscillatory Number (Shimogonya et al., 2009b)). With perhaps the exception of the oscillatory shear index, very few large-scale investigations of the aneurysm formation index and gradient oscillatory number have been reported, which merits their further investigation. These indices are discussed in more detail in §1.4.3.2. However, as will be discussed in detail in the following sections, the most consistently emerging hypotheses relate to a combination of WSS and WSSG as the main haemodynamic instigators of inception.

Meng et al. (2007) created artificial bifurcations in six dogs. Following euthanisation at two weeks or two months, they performed a histological examination on the newly-created region, as well as CFD studies to examine the flow characteristics. At the impingement region (in this case, the apex of the bifurcation), both WSS and WSSG were found to be high, and it appeared that normal remodelling was occurring here, with an increase in vSMCs, and the formation of intimal collagen padding, which is also observed in natural bifurcations. Adjacent to this region, they found an *acceleration* region, where WSS increased further still, but more gradually, such that the WSSG remained high, but was reduced compared to the impingement region. In this region, Meng et al. (2007) found destructive remodelling, with a decreased wall thickness, a loss of IEL, endothelium, collagen matrix and vSMCs. Adjacent to the acceleration region, they found a recovery region, where the wall was unchanged, and the WSS returned to baseline levels. The authors conclude that a combination of high WSS and high WSSG form a dangerous haemodynamic environment, which may induce aneurysmal remodelling. However, it remains to be understood if (a) a *high* WSS and WSSG can indeed be clearly defined; and (b) if this kind of haemodynamic insult needs to be continuously applied for an aneurysm to form.

As ECs are the main cells of the arterial wall affected by WSS, many *in-vitro* studies using ECs embedded in a fluid chamber have been performed in order to investigate the effect of WSS magnitude on EC shape and alignment. As discussed in §1.3, in a healthy artery, ECs are elongated, and aligned with the direction of flow. However, although 1.5Pa appears to be a commonly-reported “physiological” level of WSS (Nixon et al., 2010), this seems in fact to vary depending on the nature of the flow. For instance, the experiments of Metaxa et al. (2008) on bovine ECs in a flow-

chamber showed that an increased production of eNOS (a response to a change from homeostatic levels of WSS) already occurs at WSS > 3Pa. However, the same experiments also showed that so long as flow is laminar, the integrity of the EC layer was maintained even for very high values of WSS.

In fact, it seems that a supraphysiological threshold of WSS may only be defined in the presence of a high WSSG. DePaola et al. (1992) also performed flow-chamber studies on confluent ECs, with an artificially-created region of separated flow, to mimic a bifurcation. The cells were subjected to laminar WSS for 48 hours, and the spatial distributions of WSS and WSSG were examined. For WSS above 0.8Pa, they found that ECs were both elongated, and aligned with direction of flow. Interestingly, after 48 hours, they found adjacent regions of differing cell density, with lower density in regions of high WSS and high WSSG (near the "bifurcation") compared to that at regions further downstream of the bifurcation, where WSS is high, but WSSG is low. However, they found that cell division occurred near the bifurcation, and not in the downstream regions where cell density was higher, which suggests that WSSG induces cell division and cell migration *away* from the region of high WSSG. In their flow-chamber studies, LaMack and Friedman (2007) found that expression of eNOS transcriptional factors increased with WSS magnitude, but was independent of WSSG. In contrast, they found that expression of Monocyte-Chemoattractant-Protein-1 (MCP-1, a key molecule facilitating the binding of monocytes to the arterial wall) is dependent on the interaction of WSS and WSSG, with highest expression occurring when both WSS and WSSG are high. Finally, they found that the expression of Intercellular Adhesion Molecule-1 (a molecule involved in the maintaining of tight junctions between adjacent ECs) also depended on an interaction of WSS and WSSG, but showed a strong inverse relationship when WSSG is introduced (i.e. highest expression at high WSS/low WSSG).

The question then arises: what is a *high* WSSG? According to Sakamoto et al. (2010), WSSG greater than 3Pa/mm is considered to be high WSSG at arterial bifurcations. In an *in-vitro* investigation, Sakamoto et al. (2010) exposed confluent ECs to WSS between 2-10Pa, and a WSSG of up to 24Pa/mm for periods of 24 and 72 hours. They found that without a WSSG, ECs eventually aligned themselves in the direction of flow regardless of the WSS magnitude. In contrast, when exposed to WSS with a WSSG, ECs remained polygonal with no preferred alignment. The authors discuss that the effect of WSSG on endothelial cells is not clear, but that the difference in

shear force experienced by adjacent cells under high WSSG conditions may create a tensile force between the cells, which inhibits the production of stress fibres. Hence, while it appears that ECs may adapt to high WSS over time, this ability to adapt may be impaired with the introduction of WSS gradients. However, it is unclear at what magnitudes the interaction of WSS and WSSG begins to be significant.

Given this ability of ECs to adapt to conditions over time, Meng et al. (2011) went on to address the question of just how long a "destructive" haemodynamic stimulus needs to be applied for an aneurysm to form. They performed an *in-vivo* study on rabbits, examining the basilar terminus, which is a region of disturbed and separating flow. Carotid artery ligation was performed to increase flow, and the rabbits were euthanised at 5 days, 3 weeks, 12 weeks and 27 weeks. They found that IEL loss and initial bulge formation were already present at 5 days; at 3 weeks, the shape of the apex changed with more bulging observed; at 12 weeks, sustained IEL loss and fewer medial cells were observed; at 27 weeks, a large bulge was observed, with extensive wall degradation to a thin, collagenous layer with few vSMCs. They found that changes occurred most rapidly in the first 5 days, while, despite a sustained stimulus, further changes occurred more slowly after 5 days, suggesting that an initial insult of high WSS and high WSSG triggers early destructive remodelling, which leads to aneurysm development. A follow-up study on induced aneurysms at the rabbit basilar terminus by the same group (Kolega et al., 2011) found that when flow was increased, ECM degradation, upregulation of MMPs 2 and 9, and increased cellular apoptosis were found in the region adjacent to the apex as early as 2 days, *prior* to inflammatory-cell infiltration. In this region, they found a combination of high WSS and high WSSG, and suggest that this stimulus triggers the early release of MMPs from vSMCs, *instead* of inflammatory cells. They also found that IEL damage often occurred without loss of the EC layer, indicating that the few macrophage found within the wall not migrate into the wall. Hence, it is possible that the inflammatory cell infiltration occurs over a longer period of time, and hence, its role in destructive remodelling may become significant at more advanced stages of growth.

Several CFD studies also support the hypothesis that a combination of high WSS and high WSSG is the most likely haemodynamic instigator of aneurysm formation. Singh et al. (2010) investigated the effect of smoking and hypertension on 2 patient-specific cases using CFD, where the original aneurysm was virtually removed, and a healthy, "pre-aneurysmal" artery was analytically reconstructed. They performed

CFD simulations on the reconstructed arteries with normal flow, and with increased blood-viscosity corresponding to smoking and hypertensive patients. They found that with normal flow, the WSS was above the physiological range in the region of aneurysm formation (although they arbitrarily chose WSS=15Pa as the upper physiological threshold). With higher blood viscosity, they found a non-linear increase in the size of the region exposed to high WSS, with approximately 5 times higher WSS at the site of aneurysm initiation, compared to normal flow. In a study on 22 clinical cases, Chen et al. (2013) also utilised analytical reconstruction of the artery to achieve a pre-aneurysmal state, and investigated the existence of correlations between several indices of aneurysm formation proposed in the literature (discussed in detail §2.4.1). They found that high WSS showed the highest positive correlation with the site of aneurysm formation (16/22 cases), followed by high WSSG (7/22 cases).

1.4.3.1 Possible mechanisms for high WSS/high WSSG-induced destructive remodelling

The *in-vitro* studies discussed in the previous section already introduced the notion that, while ECs may adapt to high levels of WSS over time, this adaptive response appears to be modulated by the presence of WSSG. ECs exposed to elevated WSS release vasodilation factors to remodel the wall so that WSS is brought down to baseline (Hoi et al., 2004). NO is known to be involved in the activation of MMPs (Metaxa et al., 2008), which act to degrade the ECM and dilate the arterial wall by relaxing vSMCs at the site of flow impingement (Hoi et al., 2004). Hoi et al. (2004) suggest that in sustained high WSS conditions, the degradation of the ECM is sustained, and the absence of ECM components, particularly collagen and elastin, decreases the mechanical strength of the wall. Interestingly, however, under high WSSG conditions, ECs have been found to fail to trigger relaxation of vSMCs in response to high flow (Hahn and Schwartz, 2008). Nixon et al. (2010) discuss that high WSSG in the presence of high WSS promotes the loss of intercellular adhesion, which can result in EC dysfunction leading to a loss of eNOS activity. In turn, this leads to a reduction in NO production, and hence, inhibited vasodilation. In addition to its role as a vasodilator, NO appears to mediate cell proliferation in high WSS conditions (Metaxa et al., 2008), while high WSSG increases EC migration, resulting in a decrease in MMP inhibitors (Tanoue et al. (2011); Meng et al. (2007)). Hence, it seems that in high WSS/high WSSG conditions, it is a combination of normal and

abnormal remodelling (vasodilation in response to high flow together with MMP inhibition, and EC migration in response to high WSSG) that facilitates the destruction of the IEL. The lack of EC proliferation may mean that the junctional gaps between ECs will become wider as the arterial wall expands, making it susceptible to inflammatory cell infiltration, or even damage due to a direct haemodynamic insult. Tanoue et al. (2011) propose that following high WSSG-induced destruction of the IEL via MMPs, the resulting initial bulging leads to formation of a region of reduced WSS. In turn, low WSS encourages the adhesion of inflammatory cells, which may easily penetrate the wall, particularly in regions where the intimal layer of ECs is absent. Aoki and Nishimura (2010) note that vSMC apoptosis is another mechanism of media thinning, which is linked to (in addition to other factors), inflammatory cell infiltration (Tanoue et al., 2011).

It must be noted, however, that the majority of studies on inception discussed in this section focused on the complex haemodynamic environment of arterial bifurcations. Reports on studies of side-wall aneurysm initiation, particularly aneurysms occurring on relatively straight arterial segments, where flow is steady and laminar, have not been found in the literature search. However, given the lesser occurrence of side-wall aneurysms, and the steady, laminar-flow conditions through straight arterial segments, it is reasonable to deduce that mechanisms other than complex haemodynamics must play a more pivotal role in aneurysm initiation in these cases.

1.4.3.2 Oscillatory shear and aneurysm inception

Several studies performed CFD simulations similar to those of Chen et al. (2013) and Singh et al. (2010), whereby pulsatile-flow haemodynamic patterns were examined on a virtually-reconstructed, hypothetically “healthy” pre-aneurysmal artery in an attempt to predict the likely region of aneurysm formation. These studies focused on investigating oscillatory shear (OS) (i.e.,temporal changes in WSS distribution due to pulsatile flow) which, in addition to WSS and WSSG, may be pivotal in the development of aneurysms. OS affects mechanotransduction in ECs, and it has been well-established that OS can result in gene expression patterns that fuel the pathological processes underlying other arterial diseases, such as atherosclerosis. For example, the in-vitro study on mouse aortic ECs by Platt et al. (2007) revealed that the expression of cathepsin K, a potent, elastin-degrading enzyme, increased upon application of a proatherogenic level ($\pm$0.5Pa) of WSS. The same study also showed a positive correlation between cathepsin K expression, and the disruption

of the internal elastic laminae (IEL) in atherosclerotic arteries. In his in-vitro studies on ECs in a step-flow chamber, Chien (2007) found that OS resulting from disturbed flow acts to upregulate the Ras-MAPK pathway, which results in increased monocyte attraction into the arterial wall. Ogunrinade et al. (2002) found that this results in an accumulation of macrophage, and Tozer and Carew (1997) explain further that such an accumulation can give rise to a protrusion of clusters of ECs, which are then exposed to a different WSS environment. Furthermore, Tozer and Carew (1997) explain that there is a subsequent accumulation of macrophage-derived cholesterol, which results to atherosclerotic lesions. Given that both elastin degradation and the presence of inflammatory cells are also associated with aneurysm aetiology, Watton et al. (2011) conclude that OS may have a similarly pathogenic effect on cerebral arteries, leading to aneurysm formation.

Several indices were developed to investigate the effect of oscillatory shear (OS), which is a feature of pulsatile flow, and is particularly prominent in regions of disturbed flow. An already well-established indicator of atherosclerosis (Giddens et al. (1993); Buchanan et al. (2003); Blanco et al. (2006)), the Oscillatory Shear Index (OSI) has also been found to be elevated in regions where aneurysm formation is common, e.g. apices of bifurcations (Meng et al., 2007). It was originally defined by Ku et al. (1985), and represents the degree of deviation of the direction of the WSS vector from its average direction. More recently, the Aneurysm Formation Indicator (AFI) (Mantha et al., 2006) and the Gradient Oscillatory Number (GON) (Shimogonya et al., 2009b), have been proposed. Both groups performed computational studies involving the virtual removal of the aneurysmal section, and a reconstruction of the cerebral artery. Based on a haemodynamic analysis on the reconstructed artery, Mantha et al. (2006) proposed the AFI, which is given by the cosine of the angle between the instantaneous WSS vector, and the time-averaged WSS vector. They found a correlation between a low, but rotating OS, and the site of aneurysm formation. Shimogonya et al. (2009b) proposed the Gradient Oscillatory Number (GON) as an alternative time-averaged index to the OSI, whereby the WSSG, rather than the WSS vectors, are considered in their calculations and, capture the degree of oscillation of the WSSG vector. They compared the GON to WSS, WSSG, OSI and AFI, and found that only the GON showed a positive correlation with the region of aneurysm formation. These findings were supported by the study by Ford et al. (2009), in which GON was also found to be the most-correlated index (in 4/5 cases). However, the authors note that, as with the original study by Shimogonya et al. (2009b) and

the study by Chen et al. (2013), the GON was also observed to be high in healthy regions of the artery. Furthermore, the conclusions of studies by Mantha et al. (2006), Ford et al. (2009) and Shimogonya et al. (2009b) are limited by the small number of cases examined (in the latter-most case, only a single geometry).

Additionally, a major limitation of all studies involving the virtual reconstruction of a pre-aneurysmal artery is the lack of available data for the healthy cerebral artery, such that results of these studies are likely to be affected by the method of reconstruction of the artery after virtual removal of the aneurysm. While this limitation also applies to the study by Chen et al. (2013), they examined 22 clinical cases (the largest such study to date) and found that, compared to high WSS and high WSSG, the OSI, AFI and GON were positively correlated with the site of aneurysm formation for a very small number of cases (3/22, or less). However, the fact that this appears to be the only such examination across a large number of cases merits further investigation of these indices, alongside WSS and WSSG.

1.4.4 The role of haemodynamics in cerebral aneurysm growth

Much of the recent literature suggests that similar, if not the same, processes involved in aneurysm inception are also responsible for aneurysm enlargement. In this case, the majority of studies found in the literature involve taking follow-up images of patients' aneurysms and performing CFD simulations, although some studies also utilise patient-specific silicon models of arteries and either simulate flow *in-vitro*, or apply CFD on the models. Here, hypotheses for the main haemodynamic instigator of growth appear divided into high-flow (high WSS/high WSSG) and low-flow (low WSS) theories, some of which also focus on the role of high WSSG. Tateshima et al. (2007) studied an MCA aneurysm featuring a bleb that grew after a 1-year follow-up. They found high WSS at both the neck region, and at the margin of the bleb. They also observed flow separation with elevated WSSG in this region, and low WSS within the dome of the bleb following growth. Similarly, in their CFD studies on 20 middle cerebral artery (MCA) aneurysms Shojima et al. (2004)) observed that the aneurysm neck was exposed to a higher WSS than the healthy artery, while a low WSS was observed at the aneurysm dome. In a yearly follow-up CFD study over 4 years, Sforza et al. (2012) investigated the effect of the perianeurysmal environment on a growing aneurysm. They found that it was difficult to determine if some regions of growth were in fact growth, or a *displacement* of the dome im-

posed by the surrounding bony structures, where the growth is actually occurring. However, they observed one region where growth was unaffected by the presence of bony structures, and in this region, they found that WSS changed over time: before growth, WSS was elevated, but reduced after growth. These studies suggest that the combination of high WSS and high WSSG is the main haemodynamic driver of growth.

However, other studies hypothesise that it is low WSS, or low WSS in combination with high WSSG (arising due to unstable flow within the growing aneurysm) that drives growth. For example, Tanoue et al. (2011) created patient-specific silicone models of 2 cases (one growing, one non-growing) of anterior communicating artery aneurysms followed up at 4 stages over 2 years. They performed CFD simulations on the models, and compared the haemodynamic patterns over the 4 stages by matching up the parent arteries. In the case of the growing aneurysm, they found a elevated WSS away from the region of growth, high WSSG in the region *adjacent* to growth (similar to the *in-vivo* findings of Meng et al. (2007)), and low WSS in the region of growth, where they also observed recirculating flow. In contrast, they did not find low WSS in the dome of the non-growing aneurysm, and hence postulate that a combination of low WSS and high WSSG are responsible for growth. In a similar study, Jou et al. (2005) investigated two cases of patient-specific, basilar fusiform aneurysms at 1-year intervals over a 2-year period, with only one of the aneurysms growing over the 2-year period. They found a positive correlation between very low WSS (<0.1Pa) and the region of highest growth (>3mm), and that for similarly sized aneurysms, the growing aneurysm is exposed to a larger area of low WSS. Furthermore, during aneurysmal growth, a larger area of low WSS was observed.

Boussel et al. (2008) performed patient-specific CFD studies on 7 aneurysms, with images taken at two time-points. Like Jou et al. (2005), they found an inverse relationship between regions of high displacement and low WSS. Sugiyama et al. (2011) also performed patient-specific, 6-monthly follow-ups on a single patient with 6 unruptured aneurysms on the posterior ICA. They found that 2 of the aneurysms grew after 1 year, and interestingly, they found different haemodynamic conditions at each site. One aneurysm grew near the inflow zone where WSS was elevated (0.45Pa-1.2Pa) due to a higher blood velocity; following growth, the WSS reduced. In contrast, the second aneurysm grew in a region of very low WSS (0.02-0.45Pa). Doenitz et al. (2010) captured the formation of a de novo aneurysm on the

posterior side of the basilar tip, and its subsequent rupture after 44 days. In contrast to the majority of studies discussed in §1.4.3, they found a permanently low WSS at the site of aneurysm inception, which remained low following growth. They hypothesise that a combination of pre-existing conditions at a particular site (i.e. pre-existing low WSS due to geometry, increased flow due to hypertension, and an inherent weakness of the arterial wall) fuels the abnormal dilation of this region. As the vessel wall dilates, a region of low WSS evolves, which causes endothelial damage. Meanwhile, the sustained increase in pressure continues to dilate the region, leading to rapid growth of the aneurysm, and potentially rupture, due to insufficient time for the aneurysmal wall constituents to reorganise.

1.4.4.1 Mechanisms for low WSS-induced growth

While the studies examined in §1.4.4 reveal a divide between high flow or low flow theories, it appears that *disturbed* flow, and perhaps more specifically, disturbed flow featuring high WSSG, is an integral player in both events. For example, in their numerical studies, Tremmel et al. (2009) virtually varied the aneurysm-to-parent-artery size ratio, and showed that aneurysm enlargement is followed by a decreased WSS, and often, an increased flow instability, including high shear gradients. The possible mechanisms by which high WSS and high WSSG could instigate destructive remodelling characteristic of aneurysm formation were discussed in §1.4.3.1; this section aims to discuss the effects of the combination of low WSS and high WSSG, which may arise in conditions of low, *disturbed* flow.

It seems that a common thread of low-flow theories of growth is the hypothesis that low WSS results in inflammatory cell infiltration. Cebral and Meng (2012) hypothesise that low WSS induces an inflammatory response from the endothelium, which involves the release of MMPs by macrophage (Aoki and Nishimura (2010); Kanematsu et al. (2011)), resulting in structural degradation of the arterial wall. Aoki and Nishimura (2010) recently characterised the shear-stress sensitive transcriptional factor NF-κB as a mediator of chronic inflammation in aneurysmal walls by induction of the MCP-1 pathway. In previous studies on mice, they showed that the suppression of the MCP-1 pathway significantly reduced the incidence of aneurysms. Kanematsu et al. (2011) induced aneurysms on adult mice utilising a combination of a hypertensive diet to increase flow, and an injection of elastase to initiate the destruction of the arterial wall. They found that mice with MCP-1 knockout have a reduced monocyte/macrophage count and impaired macrophage func-

tion, and that these mice showed a lower incidence of aneurysm fromation. Boussel et al. (2008) note that low WSS (<0.4Pa) induces a high EC turnover through both proliferation and apoptosis, which may also render the wall susceptible to inflammatory cell infiltration.

However, although low WSS has been shown to cause endothelial dysfunction (including reduced NO production resulting in inhibition of vessel dilation (LaMack and Friedman, 2007)), several studies hypothesise that it is mainly the presence of a high *WSSG* that triggers the cascade of events which results in destructive remodelling and inflammation. In §1.3, the experiments of Chien (2007,2008) were discussed, in which it was shown that in disturbed flow conditions, ECs show no preferential alignment and exhibit a polygonal shape. This may affect transendothelial permeability to monocytes, due to the widening of junctional gaps between adjacent endothelial cells. The study by LaMack et al. (2005) on porcine iliac arteries suggests that transendothelial permeability is more likely to be elevated in low WSS conditions, and particularly so in the presence of large WSSG. Hashimoto et al. (2006) note that disturbed flow increases the residence time of inflammatory cells near the arterial wall, and that high WSSG in particular has been found to increases monocyte adhesion to ECs. As discussed in §1.4.3.1, high WSSG also induces EC migration away from the region of high WSSG, which could allow unimpeded infiltration of inflammatory cells into the wall.

1.4.4.2 Low flow and aneurysm rupture

Although aneurysm rupture is not studied in this work, it is worth noting that some studies hypothesise that in addition to facilitating growth, low, disturbed flow may also be the haemodynamic trigger of rupture. For example, Takao et al. (2012) found a statistically significant correlation between low WSS and aneurysm rupture for ICA aneurysms. Tateshima et al. (2007) hypothesise that, given that unruptured cerebral aneurysms often have an intact endothelium, the rupture of some small aneurysms occurs due to a non-uniform distribution of WSS (i.e. due to high WSS gradients between adjacent cells). In contrast, Frösen et al. (2012) discuss the case of aneurysms where a depletion of ECs has occurred over time and note that this loss of ECs can lead to thrombus formation (believed to be facilitated by low, disturbed flow) on the exposed collagen surface. In turn, this leads to a release of factors that act to further increase EC permeability, and may negatively modulate vSMC proliferation and survival.

1.5 AIMS OF THIS RESEARCH

The primary focus of this research is an investigation into the role of patient-specific haemodynamics in aneurysm evolution utilising computational fluid dynamics (CFD). The main aims of the project are to

- gain insight into the current hypotheses on haemodynamics as a driver of aneurysm evolution;
- determine if a relationship exists between established haemodynamic indices and measures of aneurysm growth;
- determine the effect of a complex, physiological haemodynamic environment on the evolution of a state-of-the-art model of cerebral aneurysm evolution; and
- implement and examine the effect of new hypotheses for linking haemodynamics to G&R on the evolving model cerebral aneurysm.

To elucidate the nature of the relationship between haemodynamics and aneurysm enlargement, correlations between haemodynamic indices reported in the literature and aneurysm inception and growth are examined in two types of investigation:

1. CFD studies on aneurysmal geometries extracted from images of real patient vasculature (which are the most commonly performed studies in the field), and
2. CFD studies on a novel, Fluid-Solid-Growth computational model of aneurysm evolution, embedded within real patient vasculature (which, to date, has not been previously reported)

In both cases, the extensive review on the hypotheses for the role of haemodynamics in aneurysm evolution presented here informs the choice of indices to study. The review reveals the existence of two theories of flow-mediated aneurysm development in the literature: a *high*-flow theory, where high WSS coupled with high WSS gradient are thought to be the main instigators of destructive remodelling, and a *low*-flow theory, focusing on the potential destructive effects of a combination of

low WSS and high WSSG. In the first investigation, two automated methods of quantifying the amount of enlargement that has occurred between aneurysmal geometries observed at two time-points are defined and compared. Surface maps of the haemodynamic and growth indices are compared. The commonly-applied method of visually determining the existence of correlations based on surface maps of indices is compared to a rigorous statistical assessment of the correlations. The second part of this research concerns the coupling of a recently developed Fluid-Solid-Growth framework for aneurysm evolution to the patient-specific haemodynamic environment. An examination into the current state of such models is covered in an extensive review, and the framework used in this research is described in detail (Chapter 4). This framework incorporates a realistic model of the mechanical response of the main structural constituents of the artery (elastin and collagen), and G&R hypotheses for these constituents, which are linked to the evolving flow environment. Two methods for implementing the model within patient-specific geometries (one manual, the other automatic) are described and compared Chapter 5. In both cases, the original aneurysmal region is removed virtually from the patient-specific vasculature, and replaced by the model geometry, which is linked to the physiological geometry by analytically-defined surfaces. The automated method is utilised to embed the framework within 12 patient-specific geometries. This enables the examination of spatial distributions of haemodynamic indices in the region where the original aneurysm developed, with the aim of determining if any or a combination of indices could be linked to aneurysm inception to further refine the modelling of inception. Similarly, embedding the model within physiological geometries also enables an investigation of hypotheses on how the local haemodynamic environment is linked to G&R of tissue during aneurysm enlargement. In this work, the hypothesis that low flow is linked to aneurysm enlargement is investigated by coupling elastin degradation to locally low WSS. The effect on the model aneurysm geometry of linking the deposition of collagen to cyclic stretch is also investigated (Chapter 6). Comparison of the evolved model geometries with their physiological counterparts reveals that the local haemodynamic environment can have a profound impact on the size and shape of the model geometry. In some cases, the shape of the model aneurysmal geometry is shown to be very similar to the original, physiological aneurysmal geometry, which suggests some tentative support for the hypothesis linking low WSS to elastin degradation. The investigation also shows that linking cyclic stretch to the evolution of collagen mass provides

a mechanism for constraining the deformation of the aneurysmal geometry, which may be much like the physiological event of aneurysm stabilisation.

As such, this research offers new insights into how we can begin to progress from studying the mechanisms underlying aneurysm growth using CFD studies on static geometries, to modelling these events such that we can observe the changes in response to the haemodynamic environment. However, as only elastin and collagen are presently modelled, refinement of the model is needed in the form of a more explicit representation of vascular cells in the arterial wall, i.e. ECs, vSMCs and fibroblasts. A possible method of incorporating a more explicit representation of ECs is outlined in Chapter 7. Importantly, the present framework is easily adaptable, and as such allows the implementation of new physiological data and new G&R hypotheses. To inform these, a better understanding of the mechanobiology is needed, which will allow for a better coupling of haemodynamic and G&R events.



CHAPTER 2

QUANTIFYING ANEURYSM GROWTH: METHODOLOGY

In the previous chapter, the mechanisms by which haemodynamics, in particular WSS and WSSG, may facilitate aneurysm inception and growth were discussed. However, the great majority of studies discuss aneurysm growth qualitatively -i.e. they define broad regions of growth, without quantifying *how much* growth has occurred. Although follow-up imaging studies on growing aneurysms provide us with a visualisation of aneurysm growth, currently, no methods exist which reliably determine which regions of the aneurysm have grown, how much they have grown, and in which direction any individual point, or patch on a surface has grown. Furthermore, it appears that the existence of correlations between haemodynamic patterns and aneurysm growth in CFD studies is deduced largely based on visual inspection -i.e. by observing the contour map of, say, WSS on the aneurysmal surface prior to growth, and comparing the location of elevated or reduced WSS to regions of growth. While many studies have employed statistical analysis to investigate correlations between haemodynamics and risk-of-rupture measures (e.g. Shojima et al. (2004); Cebral and Meng (2012); Valencia et al. (2008)), the lack of quantitative methods has meant that such an examination has not been possible in the case of aneurysm growth.

Three CFD studies mentioned in the previous chapter (Jou et al. (2005); Boussel et al. (2008); Sforza et al. (2012)) have described growth quantitatively, in an attempt to determine if any correlations exist between specific haemodynamic patterns and regions of "high growth". All three studies utilised aligned images obtained at a minimum of two time-points. However, only Boussel et al. (2008) have reported their methods for capturing growth between them. In their study, growth was defined as the displacement between the centre of each surface element of the aneurysmal surface at time-point one, to the intersect of the element normal on the aneurysmal surface surface at time-point two. Jou et al. (2005) did not define a threshold of *significant* growth; Boussel et al. (2008) defined significant growth as any displacement beyond $\pm 0.3mm$ (half a pixel width), while Sforza et al. (2012) appear to have arbitrarily chosen a minimum threshold of $\pm 0.5mm$. Both Jou et al. (2005) and Boussel et al. (2008) found an inverse correlation between WSS and growth. In contrast, Sforza et al. (2012) found only one region where growth was certain to be unimpeded by the perianeurysmal environment, and where WSS was found to be elevated.

In this section, the method of quantifying growth described in the study by Boussel et al. (2008) and described above is applied to two sets of patient-specific geometries: a basilar terminus (BT) aneurysm (the same case examined in the study by Doenitz et al. (2010)), and an ICA aneurysm, supplied by the same group. In both cases, growth is examined between two geometries, hereon referred to as the t_1 and t_2, geometry. The t_2 geometry represents a point in time *after* the aneurysm has grown. For the BT aneurysm, the time-difference between the t_1 and t_2 geometries is 44 days, and two years for the ICA aneurysm. The existence of correlations between pulsatile-flow haemodynamic indices and growth is examined both visually and statistically. The aims are two-fold:

- to compare the correlations determined visually (the common method applied in the field of aneurysm research) to correlations determined statistically, which has, to date, not been previously done, and
- to determine if statistical examination indeed reveals positive correlations between specific haemodynamic indices and growth, which would provide motivation for linking those indices to G&R hypotheses in the model of CA evolution.

To examine the effect on correlations of specific methods of quantification of aneurysm growth, a second method of quantifying growth is described, and the results compared.

2.1 ALIGNMENT OF GEOMETRIES IN 3D SPACE

In both the ICA and BT cases, the t_1 and t_2 geometries were positioned at different locations in space, which is likely to be the result of different positioning of the patients within the scanner. An optimal alignment of the two geometries is required for accurate comparison of the aneurysm dome sizes. In the study by Sforza et al. (2012), a distance-minimisation technique was utilised to align portions of the parent artery, while Jou et al. (2005) and Boussel et al. (2008) achieved co-registration manually, by using vessel junctions to guide alignment.

In this work, the inbuilt *procrustes* function in `MATLAB` (The MathWorks, Inc., Natick, Massachusetts) was an effective, automated tool to achieve alignment, which is executed as below:

$$[d, Z, \text{transform}] = \text{procrustes}(X, Y),$$

The function determines the optimal linear transformation (translation, reflection, orthogonal rotation, and scaling) that will conform the points of matrix Y to that of matrix X. The optimal fit is determined utilising distance minimisation, where d is the minimised value of the sum of the squared errors between the matrices, *transform* is an array composed of translation, rotation and scale components c, T, and b respectively, and Z is the mapped matrix Y, i.e.

$$Z = b \times Y \times T + c$$

A requirement of the function is that matrices X and Y are the same size. In the case of complex geometries, however, and particularly in the case where the geometry changes over time, we can expect that the matrices which hold the t_1 and t_2 geometry coordinates will be different in size. As such, the geometry skeletons (i.e. the medial axis of each geometry) were utilised for this purpose. The skeletons were extracted from the t_1 and t_2 geometries utilising a skeletonisation algorithm (Esteban et al., 2007) embedded within `@neufuse` segmentation software (Figure 2.1). The software was developed for the European project @neurIST (*www.aneurist.org*:

Integrated Biomedical Informatics for the Management of Cerebral Aneurysms, see Villa-Uriol et al. (2011)). The aim of the project was stated as below:

> *@neurIST will transform the management of cerebral aneurysms by providing new insights, personalized risk assessment, and methods for the design of improved medical devices and treatment protocols.*(Villa-Uriol et al., 2011)

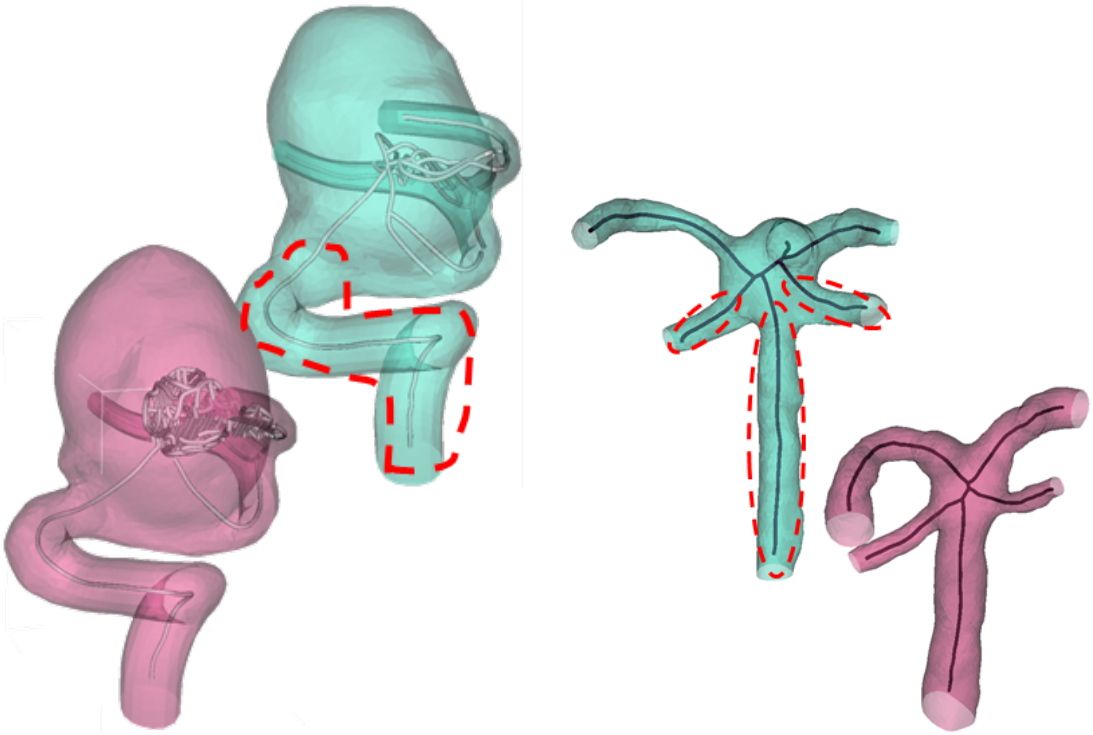
`@neufuse` forms just one part of a suite of software intended for this purpose, and specifically deals with the fusion of patient data from different modalities (e.g. MRI scans and patient records), and extraction of biomechanical indices of interest (i.e. it is coupled to ANSYS fluid dynamics software (ANSYS Inc., Canonsburg, Pensylvania), allowing for the coupling of segmented geometries to fluid-flow within the one software) (Villa-Uriol et al., 2011). In this research, the software is used for image segmentation, skeleton extraction, and application of boundary conditions for individual cases (see Figure 2.21 in §2.4).

The extracted skeletons were exported to `MATLAB` as sets of data-points, where they were re-interpolated, and used to obtain the transform matrix T and the translation component c (geometries did not require scaling -i.e. $b = 1$).

The skeletons of the t_1 and t_2 geometries were clipped, such that the aneurysmal region was excluded, and the coordinates of the portions running through the parent artery were arranged in single matrices. The new t_1 and t_2 skeletons were re-interpolated using `MATLAB`'s inbuilt interpolation function, *interp1*, to achieve two matrices of equal size. The *procrustes* function was applied to the re-interpolated skeletons, and in turn, the resulting transform matrix T and the scaling component c were used to translate and rotate the t_2 geometry to match the t_1 geometry.

Figure 2.2 shows the t_2 ICA and BT geometries (transparent blue) over their corresponding t_1 geometries (grey), and the labelling of different regions of the geometries used throughout this section.

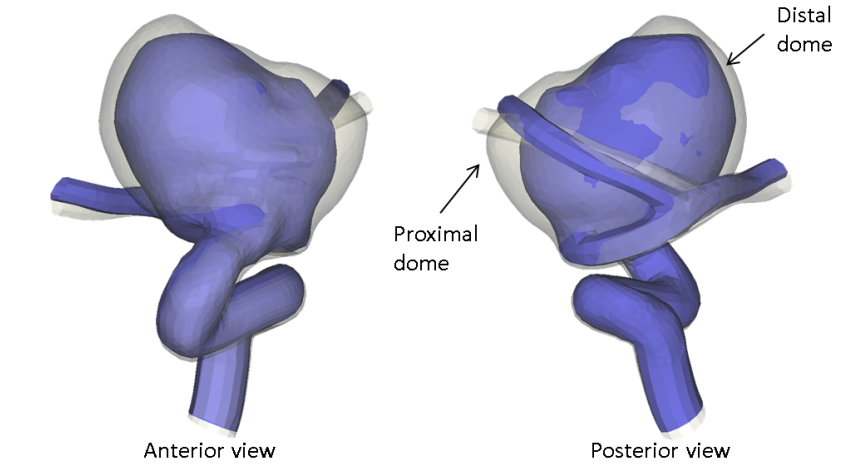
In the BT case, the direction of growth is strictly towards the posterior, and strictly outward. In contrast, it appears that the main regions of growth for the ICA case are the distal and proximal parts of the aneurysm dome, and that growth is directed towards the anterior. However, it can also be seen that in both cases, the t_1 and t_2 geometries are not perfectly aligned, which may exaggerate the amount of



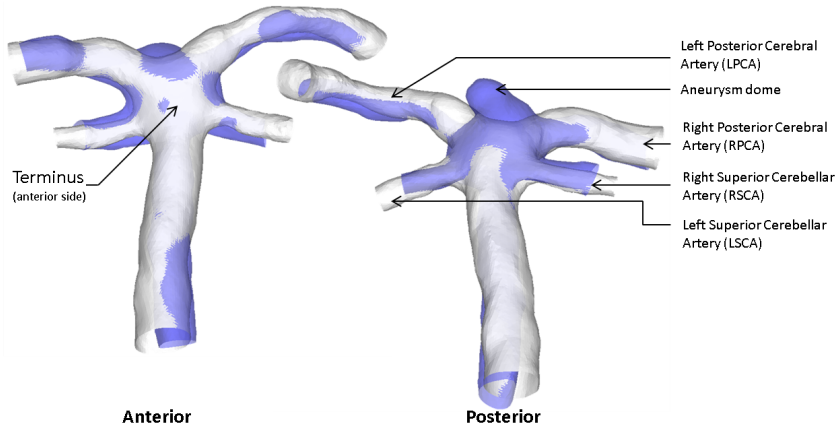
(a) (b)

Figure 2.1: The original locations of the (a) ICA and (b) BT t_1 (pink) and t_2 (green) geometries. Due to the large size of the ICA aneurysm, the skeleton inside the aneurysm appears as a bundle of skeleton segments. However, these segments are not utilised in the positioning of the geometries; the skeleton segments used as inputs to the Procrustes function in `MATLAB` are highlighted in red on the t_1 geometries.

growth observed. Furthermore, it is unclear whether the shift between the geometries accounts for the observation that some posterior regions of the ICA t_1 dome appear to have imploded, or "grown inwards", or if this may be the result of tissue degradation and remodelling.



(a)



(b)

Figure 2.2: Overlays and labelling of the t_1 and t_2 ICA (a) and BT (b) geometries

2.2 Quantifying growth: The Displacement Index

To quantify growth, the aligned aneurysm domes were isolated through segmentation in `@neufuse`, and the coordinates and connectivity matrices were exported to `MATLAB`. In `MATLAB`, an algorithm was constructed and applied, which

- determines the centrepoint and normal of each triangular surface element of the t_1 dome,
- determines the point of intersection (if it exists) of the normal of each t_1 element with the t_2 surface,

- for each t_1 element, stores the nearest intersection point which lies within a triangle of the t_2 dome,
- computes the scalar distance between each centrepoint on the t_1 dome and the corresponding intersection point on the t_2 dome,
- interpolates onto each node of the t_1 mesh a scalar distance (the final displacement value) which is computed as the average of the scalar distances corresponding to all elements connected to that node.

Given the complexity of the geometries, and in particular, given the fact that the growth of the ICA dome is not strictly in the outward direction, the algorithm was constructed through well-defined, analytical examples.

2.2.1 Displacement Index algorithm: Analytical examples

The *Displacement Index* relies on determining whether a normal to an element on the t_1 dome

1. intersects the plane of an element on the t_2 dome, and
2. lies within this element.

This comprises a simple, well-documented "ray-triangle intersection" problem (see, e.g. Möller and Trumbore (1997)). Consider two triangles, P and Q in 3D space, specified by points with position vectors $\mathbf{p_1}$, $\mathbf{p_2}$, and $\mathbf{p_3}$, and $\mathbf{q_1}$, $\mathbf{q_2}$, and $\mathbf{q_3}$ respectively. We wish to determine if the normal of triangle P,$\mathbf{n_p}$, projected from triangle P centrepoint, $\mathbf{c_p}$, intersects triangle Q.

We can determine the normals of both triangles, $\mathbf{n_p}$ and $\mathbf{n_q}$, by taking the cross product of the triangle vertices, i.e.

$$\mathbf{n_p} = (\mathbf{p_2} - \mathbf{p_1}) \times (\mathbf{p_3} - \mathbf{p_1})$$

and

$$\mathbf{n_q} = (\mathbf{q_2} - \mathbf{q_1}) \times (\mathbf{q_3} - \mathbf{q_1})$$

It is important that the vertices are ordered counter-clockwise, in order to generate two outward normals. Any two vertices of triangle P can be used to specify the plane

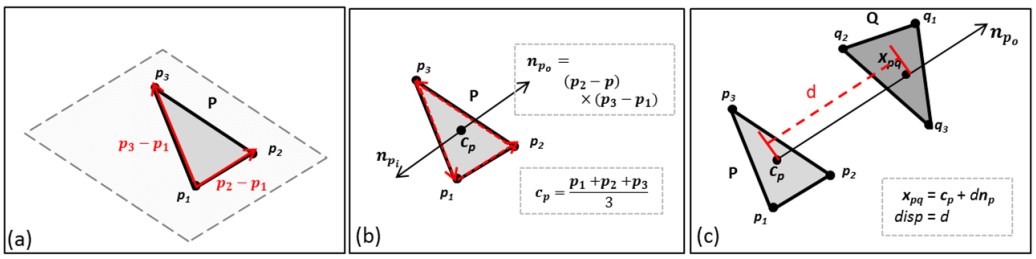


Figure 2.3: Quantifying the displacement between two triangles P& Q. (a) Triangle P, lying in a plane defined by vertices $\mathbf{p_2} - \mathbf{p_1}$ and $\mathbf{p_3} - \mathbf{p_1}$; (b) Anti-clockwise ordering of triangle vertices ensures that the cross product,$(\mathbf{p_2} - \mathbf{p_1}) \times (\mathbf{p_2} - \mathbf{p_1})$, produces an outward normal $\mathbf{n_{p_o}}$; (c) The displacement, d, defined as the distance between the centrepoint, $\mathbf{c_p}$, of triangle P, to the intersect point, $\mathbf{x_{pq}}$.

in which Q lies (Figure 2.3). Hence, we take any point on the triangle, say $\mathbf{p_1}$ to be a point on this plane.

The centrepoint of triangle P, $\mathbf{c_p}$, is computed as the mean of $\mathbf{p_1}$,$\mathbf{p_2}$, and $\mathbf{p_3}$. The position vector of a point of intersection, $\mathbf{x_{pq}}$, is given by

$$\mathbf{x_{pq}} = \mathbf{c_p} + d\mathbf{n_p} \tag{2.1}$$

Hence, we must determine the value of d, which is given by

$$d = \frac{(\mathbf{q_1} - \mathbf{c_p}) \cdot \mathbf{n_q}}{\mathbf{n_p} \cdot \mathbf{n_q}} \tag{2.2}$$

If triangle Q is on the outward side of triangle P -i.e. if $\mathbf{n_p} \cdot \mathbf{n_q} \geq 0$ -d will be a positive value; if triangle Q is on the inward side of triangle P ($\mathbf{n_p} \cdot \mathbf{n_q} \geq 0$), d will be a negative value. The sign of d therefore determines the direction of growth. Now that the existence of an intersection point on the plane of triangle Q is confirmed, we must determine whether this point lies *inside* the triangle (Figure 2.4).

Again, for points $\mathbf{q_1}$, $\mathbf{q_2}$, and $\mathbf{q_3}$ ordered counter-clockwise, we can see that an intersect point that lies inside the triangle must be located counter-clockwise with respect to each of the vertices $\mathbf{q_2} - \mathbf{q_1}$, $\mathbf{q_3} - \mathbf{q_2}$, and $\mathbf{q_1} - \mathbf{q_3}$. We can check whether $\mathbf{x_{pq}}$ is counter-clockwise from $\mathbf{q_2} - \mathbf{q_1}$, by checking the position of the vector $\mathbf{x_{pq}} - \mathbf{q_1}$ with respect to $\mathbf{q_2} - \mathbf{q_1}$.

If $\mathbf{x_{qp}}$ is inside the triangle, then the cross-product of vectors $\mathbf{q_2} - \mathbf{q_1}$ and $\mathbf{x_{pq}} - \mathbf{q_1}$ should yield an outwardly-directed vector, such that

$$(\mathbf{q_2} - \mathbf{q_1} \times \mathbf{x_{pq}} - \mathbf{q_1}) \cdot \mathbf{n_q} \geq 0$$

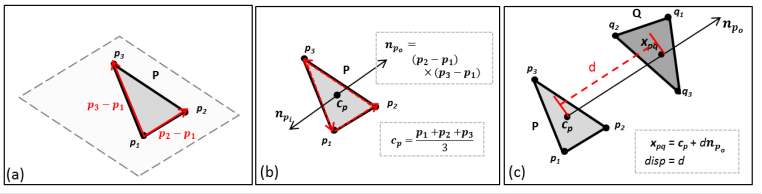


Figure 2.4: Determining if intersect, x_{pq}, lies within triangle Q. If $\mathbf{x_{pq}}$ is located anti-clockwise with respect to each vertex on triangle, then, as $\mathbf{x_{pq}}$ lies in the plane of Q, the cross product of a vertex at any point, $\mathbf{q_i}$, with a vector $(\mathbf{x_{pq}} - \mathbf{q_i})$ will produce a vector identical in direction to the outward triangle normal, $\mathbf{n_{q_o}}$. Hence, the dot product of the two will be 0.

The same check can then be applied to the other two vertices of triangle Q -i.e. if $\mathbf{x_{qp}}$ is inside the triangle, then the following three conditions must all be satisfied:

$$\left(\mathbf{q_2} - \mathbf{q_1} \times \mathbf{x_{pq}} - \mathbf{q_1}\right) \cdot \mathbf{n_q} \geq 0, \tag{2.3}$$

$$\left(\mathbf{q_3} - \mathbf{q_2} \times \mathbf{x_{pq}} - \mathbf{q_2}\right) \cdot \mathbf{n_q} \geq 0, \text{and} \tag{2.4}$$

$$\left(\mathbf{q_1} - \mathbf{q_3} \times \mathbf{x_{pq}} - \mathbf{q_3}\right) \cdot \mathbf{n_q} \geq 0 \tag{2.5}$$

This method was implemented in MATLAB, and examined for two different analytical cases. The first case is a smaller sphere inside a larger sphere, such that "growth" of the smaller sphere is directed purely outwards. The second is a smaller sphere intersecting a larger sphere, which mimics the real, physiological case, where it appears that some growth is directed inwards.

2.2.2 Sphere within a sphere

Two spheres, both centred about the origin and with equal numbers of points, were defined using MATLAB's inbuilt function *sphere(n)*, which computes a sphere of $n+1$-by-$n+1$ size. The radius of the larger sphere (*LS*) was set to twice the radius of the smaller, unit sphere (*SS*). Connectivity matrices were specified such that the sphere surfaces are represented by triangular elements, and such that the points specifying each triangle are ordered counter-clockwise. Two *for*-loops were employed: the first to compute and store the centrepoint and unit normal of each element on the *SS* in two matrices, say $\mathbf{C_S}$ and $\mathbf{N_1}$, respectively; the second to compute and store the unit

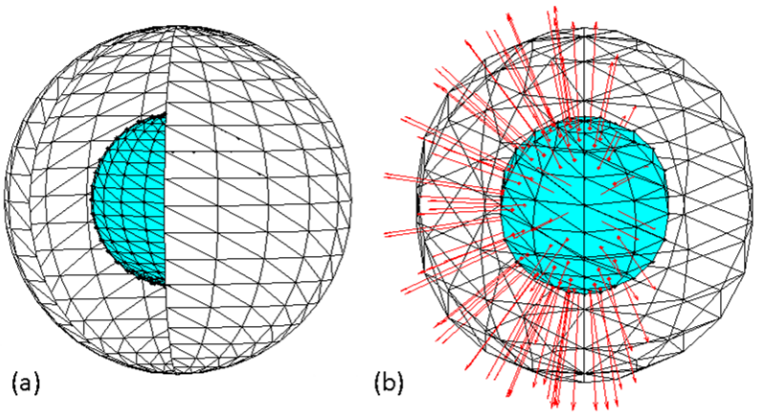


Figure 2.5: (a) the unit *SS* (blue) within *LS* ($r_{LS} = 2$) and (b) the *SS* element normals shown for half the *SS* (in red), emanating from the centre of each element

normal of each element on the *LS* in matrix $\mathbf{N_2}$, such that

$$\mathbf{C_S} = \begin{bmatrix} c_{s_{x1}} & c_{s_{y1}} & c_{s_{z1}} \\ c_{s_{x2}} & c_{s_{y2}} & c_{s_{z2}} \\ c_{s_{x3}} & c_{s_{y3}} & c_{s_{z3}} \\ \vdots & \vdots & \vdots \\ c_{s_{xn}} & c_{s_{yn}} & c_{s_{zn}} \end{bmatrix}, \mathbf{N_1} = \begin{bmatrix} n_{1_{x1}} & n_{1_{y1}} & n_{1_{z1}} \\ n_{1_{x2}} & n_{1_{y2}} & n_{1_{z2}} \\ n_{1_{x3}} & n_{1_{y3}} & n_{1_{z3}} \\ \vdots & \vdots & \vdots \\ n_{1_{xn}} & n_{1_{yn}} & n_{1_{zn}} \end{bmatrix}, \text{ and } \mathbf{N_2} = \begin{bmatrix} n_{2_{x1}} & n_{2_{y1}} & n_{2_{z1}} \\ n_{2_{x2}} & n_{2_{y2}} & n_{2_{z2}} \\ n_{2_{x3}} & n_{2_{y3}} & n_{2_{z3}} \\ \vdots & \vdots & \vdots \\ n_{2_{xm}} & n_{2_{ym}} & n_{2_{zm}} \end{bmatrix}$$

where n and m are the sizes of the smaller and larger sphere coordinate matrices respectively (in this case $n = m$). Figure 2.5(b) shows the outwardly-directed normals of the *SS*, emanating from the centre of each element.

A nested *for*-loop was then defined, and comprises:

- an outer loop of size n, which extracts the centre-point, $\mathbf{c_{s_i}}$,from $\mathbf{C_S}$, and normal, $\mathbf{n_{1_i}}$, from $\mathbf{N_1}$ associated with the i^{th} element of the *SS* surface, and
- an inner-loop, of size m, which takes the current $\mathbf{c_{s_i}}$, and $\mathbf{n_{1_i}}$, and for each j^{th} element on the *LS* surface

  1. determines the value of d and the intersect point (if it exists),$\mathbf{x_{ij}}$ as specified by equations Equation (2.1) and Equation (2.2),
  2. checks the position of $\mathbf{x_{ij}}$ with respect to each vertex corresponding to the j^{th} element on the *LS* surface and stores the result of each in a variable,
  3. if all three checks are satisfied -i.e. if the intersect point $\mathbf{x_{ij}}$ lies inside the j^{th} triangle

4. stores the coordinates of the intersect point, the corresponding value of d, the current element on the *SS*, i, and the corresponding element on the *LS*, j in a single matrix, say **INTSCT**, i.e.

$$\mathbf{INTSCT_{n\times 6}} = \begin{bmatrix} x_{x_1} & x_{y1} & x_{z_1} & t_1 & i_1 & j_1 \\ x_{x_2} & x_{y2} & x_{z_2} & t_2 & i_2 & j_2 \\ x_{x_3} & x_{y_3} & x_{z_3} & t_3 & i_3 & j_3 \\ \vdots & \vdots & \vdots & \vdots & \vdots & \\ x_{x_n} & x_{y_n} & x_{z_n} & t_n & i_n & j_n \end{bmatrix}$$

Now, it can be seen that every element of the *SS* will have two intersect points on the *LS* surface (Figure 2.6(b)): one in the outward direction, and another in the inward direction. Both are stored in the **INTSCT** matrix.

Clearly, the intersect which lies in the outward direction is the correct choice (because growth in this case occurs only in the outward direction), while the intersect in the inward direction is incorrect and must be eliminated. In this case, where the *SS* is *entirely* within the *LS*, the d value corresponding to each intersect point can, alone, be used to eliminate the incorrect point. A positive d value indicates an *outward* intersect point, while a negative d value indicates an *inward* intersect point; hence, each intersect point with a negative d value is removed to form the final matrix as specified above.

Finally, each point on the *SS* is assigned a displacement index, or DI, value. The magnitude of d represents the scalar distance between centrepoint c_{s_i} and the corresponding intersect point x_{ij}. Hence, for each *SS* point, the DI is computed as the average of the d values of all elements connected to that point (Figure 2.6(c)). Figure 2.7 shows the plot of the displacement index for the sphere-within-sphere example. The effect of mesh resolution of the *SS* and displacement between the spheres was examined. The radius and mesh resolution of the *LS* were held constant ($n = 10$ giving $11 \times 11 = 121$ points, 180 elements; $r_{LS} = 2$), while the radius and mesh resolution of the *SS* were varied in the following combinations:

- **Case 1: Coarse mesh and large displacement**, with $n_{SS} = 10$ (121 points, 180 elements) and $r_{SS} = 1$;
- **Case 2: Coarse mesh and small displacement**, with $n_{SS} = 1.7 \times n_{SS_1} = 17$ (324 points, 544 elements) and $r_{SS_2} = 1.7 \times r_{SS_1}$;

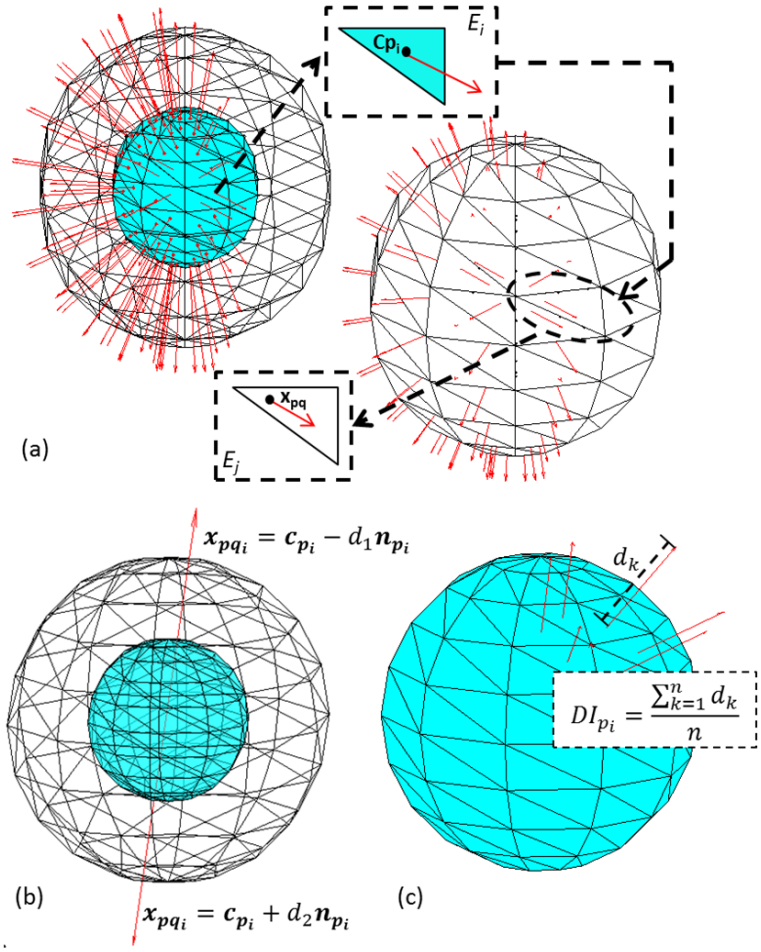


Figure 2.6: (a) and (b) *SS* E_i normal and corresponding *LS* E_j intersects, x_{pq_i}; (c) the DI at point p_i, calculated as the average of d values corresponding to the elements surrounding p_i

- **Case 3: Fine mesh and large displacement**, with $n_{SS} = 20$ (441 points, 760 elements) and $r_{SS} = 1$; and
- **Case 4: Fine mesh and small displacement**, with $n_{SS} = 1.7 \times n_{SS_3} = 34$ (1225 points, 2244 elements) and $r_{SS} = 1.7 \times r_{SS}$.

As expected, the DI is larger for $R_{SS} = 1$. For the same displacement, different mesh resolutions of the *SS* result in a similar range of magnitudes of the DI (e.g. for $r_{SS} = 1$, $DI = 0.94 - 0.942$ and $0.926 - 0.934$ for $E_{SS} = 180$ and $E_{SS} = 760$ respectively). Hence, although a fine mesh might result in a smaller angular displacement between adjacent *SS* surface normals, this translates into only a small change in displacement

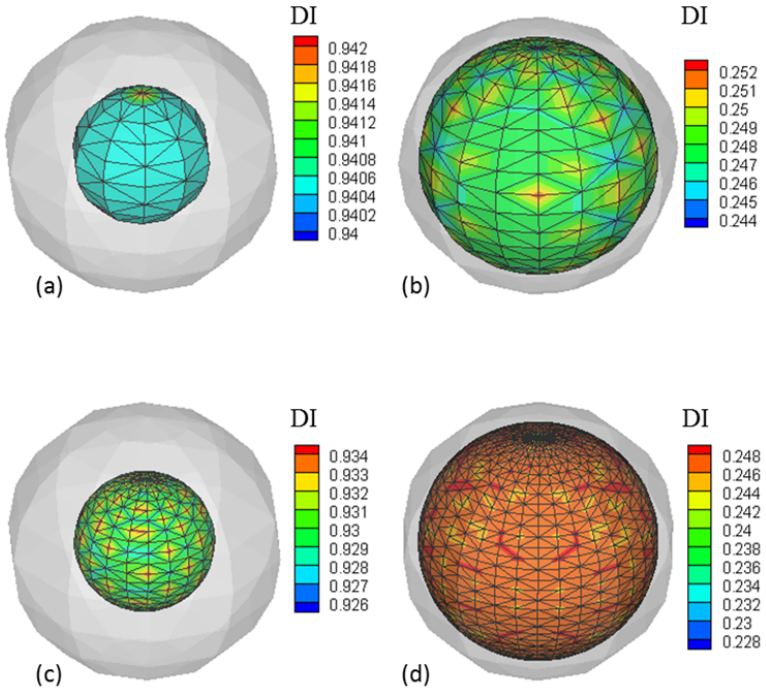


Figure 2.7: Plot of the DI for different *SS* mesh resolution, E, and radius, R. (a) $R_{SS} = 1$, $E_{SS} = 180$; (b) $R_{SS} = 1.7$, $E_{SS} = 544$; (c) $R_{SS} = 1$, $E_{SS} = 760$; (d) $R_{SS} = 1.7$, $E_{SS} = 2224$.

between each element centrepoint and the corresponding point of intersection of the normals on the *LS* surface.

In the next section, a second analytical case was considered where the smaller sphere intersects the larger sphere. This reflects the real physiological ICA case where some regions of the dome appear to have shifted inwards.

2.2.3 Intersecting spheres

As before, two spheres were generated using the inbuilt `MATLAB` function: the smaller with a unit radius, the larger with a radius of 2. This time, however, the *SS* was defined to have half the number of points of the *LS*, and the centre of the *SS* was set to $(0,0,2)$, such that the *SS* intersected the *LS* (see Figure 2.8(a)). As before, the centrepoint and normal of each element of the *SS* was determined, as well as each normal of the *LS*. The same nested *for*-loop developed for the sphere-within-sphere example was utilised to compute the intersect points, and to determine whether each intersect point lies within a triangle of the *LS*. However, this time, the selection criteria for the correct intersect point are different, as there are some regions of

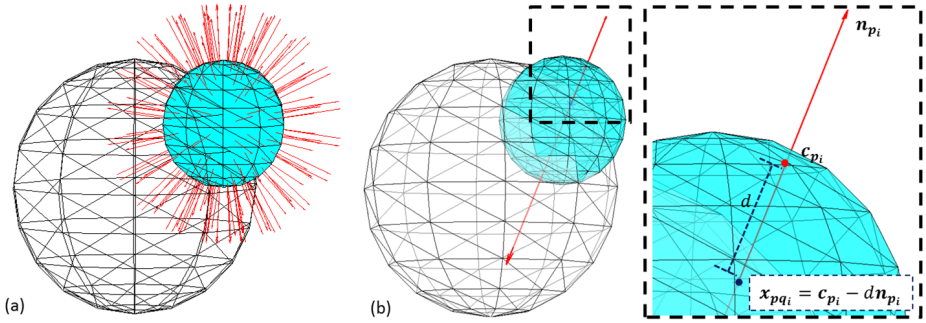


Figure 2.8: *SS* of radius 1 intersecting the *LS* ($r_{LS} = 2$). (a) *SS* element normals (red); (b) an instance where no outwardly-directed intersect exists, and the inwardly-directed intersect is the correct choice

the *SS* which lie outside of the *LS*. For these sections, an intersect point located in the outward direction does not exist (Figure 2.8(b)) -hence, the intersect point located in the *inward* direction is the correct, and only choice. Furthermore, it must be noted that although intersection of the two spheres provides a line of intersect points, in fact, the intersect point corresponding to each element on the *SS* is still determined by the intersection of its normal and the *LS* surface.

This time, the selection of correct intersect points must be based on both the direction of the scalar value d, *and* its size. For sections of the *SS* located inside the *LS*, the selection is made as before: the point located outwards of the *SS* surface is selected, while the point located inwards is discarded. For sections of the *SS* that lie outside the *LS*, there may be one or two intersect points, both located inward of the *SS* surface (Figure 2.8). In this case, the correct intersect point is selected based on $|d|$, where the smaller d-value yields the correct intersect point. Hence, to automate this process, the algorithm was modified to check for the existence of multiple negative d-values for each element of the *SS*:

- if only one negative, or only one positive d-value exists (i.e. only one intersect point exists in the inward or outward direction), then this is clearly the correct value;
- if two negative values exist, then the intersect point with the smaller d value is correct;
- if one negative and one positive value exist, the intersect point with the positive d-value is correct.

Figure 2.9 shows the plot of the displacement index for the intersecting spheres example. As in the previous section, the effect of mesh resolution and displacement between the spheres was examined (the same radii and element numbers were applied to the *SS*). This time the positive DI is smaller for $r_{SS} = 1.7$ compared to $r_{SS} = 1$,

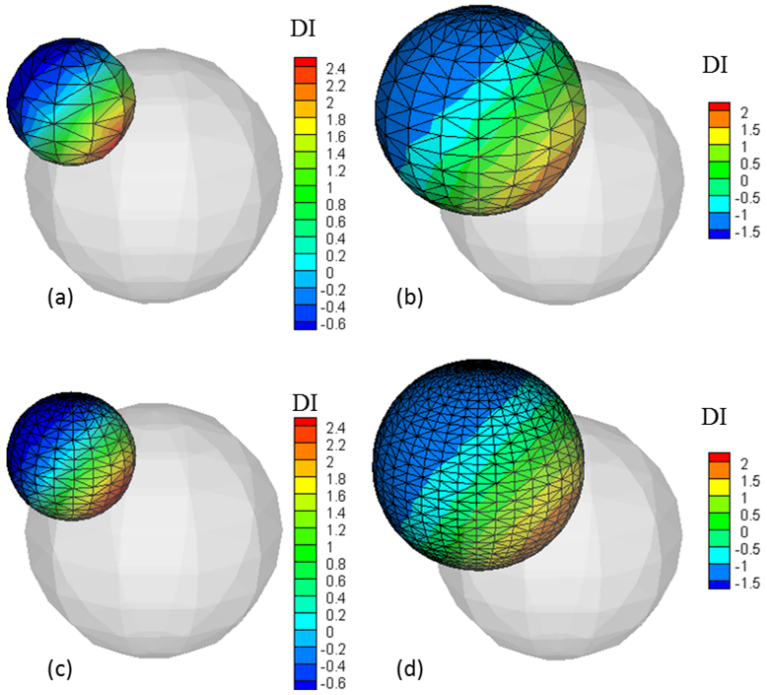


Figure 2.9: Plot of the DI for different *SS* mesh resolution, E_{SS}, and radius, r_{SS}. (a) $r_{SS} = 1$, $E_{SS} = 180$; (b) $r_{SS} = 1.7$, $E_{SS} = 544$; (c) $r_{SS} = 1$, $E_{SS} = 760$; (d) $r_{SS} = 1.7$, $E_{SS} = 2224$.

as a larger portion of the *SS* surface is inside the *LS*, and hence the distance to the *LS* surface in the direction of the outward normal is smaller. In contrast, the negative DI is larger for $r_{SS} = 1.7$, as a greater portion of the *SS* surface is outside of the *LS*. Again, for the same radius, mesh resolution appears to make no difference to the magnitude of the DI.

2.2.4 Displacement Index algorithm applied to real, physiological geometries

The algorithm developed through the two analytical cases discussed in §2.2.2 and §2.2.3 was then applied to the real, physiological geometries (the segmented aneurysm domes of the t_1 and t_2 ICA, and BT geometries).

However, the criteria for selecting a *correct* intersect point are again different to that employed in the analytical examples. Firstly, due to the spatial shift between the geometries, it is impossible to determine a set of exactly corresponding points on the two geometries, which could be used as a guide to segment the geometry. In particular, segmenting the regions around the neck of the aneurysm is difficult, as it is unclear where exactly the parent artery ends, and the aneurysm dome begins. Therefore, segmentation of the geometries to isolate the domes was a subjective, visually-guided process, which yielded the dome geometries in Figure 2.10.

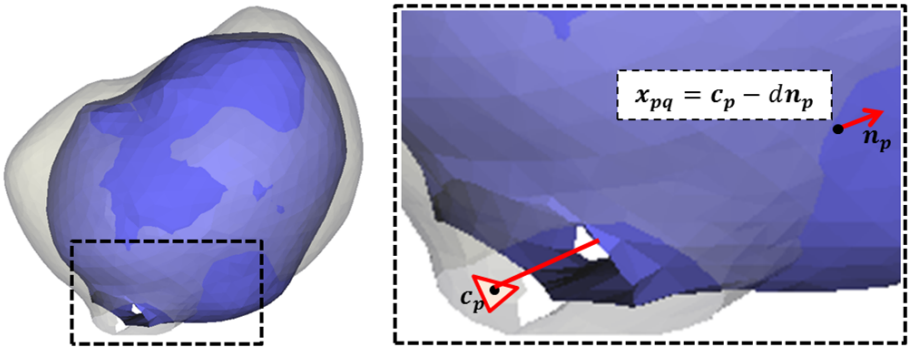


Figure 2.10: Overlay of the t_1 (blue) and t_2 (grey) ICA domes. Boundary elements on the t_1 geometry may only have a single, inwardly-directed intersect, which is incorrect and must be eliminiated. In this case, no correct intersect exists

From close visual inspection, it can be seen that there are elements of the t_1 dome at the boundary, for which only one point of intersection exists between the t_1 element normal and the t_2 geometry, in the inward direction (Figure 2.10). However, unlike the analytical example discussed in §2.2.3 where a single intersect point in the inward direction is the only and correct choice, here, this intersect point is obviously incorrect. In fact, in this case, it is clear that there exists no *correct* intersect point.

In the case of the real, physiological geometry, each element (for which a intersect point exists) will have one of the following:

- a single outward intersect point, which is the correct and only choice;
- two outward intersects, of which the correct point has the smaller d-value;
- two inward intersects, of which the correct point has the smaller d-value, and

- two or more outward, and one inward intersect, of which the correct point has the smallest, *positive* d-value;
- a single, *inward* intersect, with a small d-value (special case)

In the special case where only a single inward intersect exists, the corresponding t_1 and t_2 triangles are located at the geometry boundaries, with the t_1 triangle on the outer side of the t_2 triangle. Therefore, visual inspecton is necessary in this case to determine if such a point is correct. While this method was utilised in this study, it may in fact be more appropriate to exclude triangles at the geometry boundaries, as it is less clear if these regions are part of the aneurysm dome.

Once the correct intersect points are determined for each point on the t_1 dome, a corresponding DI value was computed as the average of d-values of all elements connected to that point. Figure 2.11 shows the DI distributions on the anterior side of the ICA, and the posterior side of the BT.

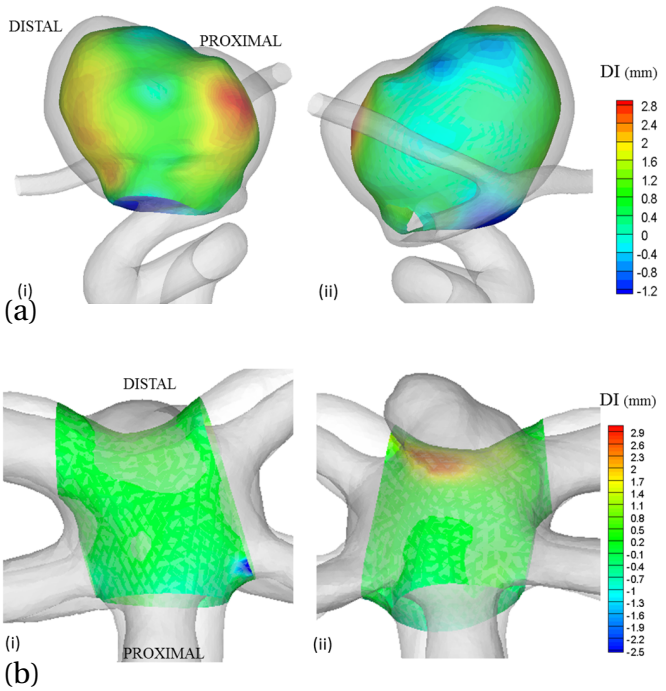


Figure 2.11: The DI plotted as a surface map on the t_1 geometries of (a) the ICA and (b) the BT. In both cases (i) shows the anterior side of the geometry, while (ii) shows the posterior side.

The main regions of high DI for the ICA are the distal and proximal parts of the aneurysm dome. Figure 2.11(a) shows that the region of largest DI (>2.8mm) occurs at the proximal-anterior part of the dome. For the BT case (Figure 2.11(b)), a high DI is more localised compared to the ICA case, and is highest at the distal part of the proximal terminus (>2.9mm).

2.3 QUANTIFYING GROWTH: THE AREA STRETCH RATIO

To examine the effect of the method of growth quantification on correlation, a second, novel index, the *Area Stretch Ratio* (ASR), was devised for this purpose. As with the *Displacement Index*, growth is determined by comparing the aligned t_1 and t_2 geometries. However, this time, growth is considered as the *stretching* of the t_1 surface over time, which is a function of the displacement between the t_1 and t_2 surfaces. The rationale for this comes from examples of tissue growth and remodelling such as the growing abdomen during pregnancy, where, as the baby grows, the skin grows and remodels outward. A simple measure of this stretching of tissue is the ratio of the t_2 surface area to that at t_1, which provides a more sophisticated descriptor of growth compared to the simple, Eulerian distance between two points captured by the Displacement Index. While the concept of comparing surface areas is not novel, its use as a measure of aneurysm growth has not, to date, been previously reported.

The algorithm to compute the ASR was developed through analytical examples in `MATLAB`, and applied to the ICA and BT cases. Like the DI, a ASR value is calculated for each point on the t_1 geometry, which allows for the comparison of haemodynamic indices and the ASR at each point.

Figure 2.12 illustrates the basic function of the ASR algorithm. Let us consider a node, $\mathbf{p_i}$ on the surface of the t_1 geometry, which is at some distance from the t_2 geometry. Briefly, the algorithm:

- determines the set of elements, E_i, connected to $\mathbf{p_i}$, and the centrepoint and normal of each element (denoted $\mathbf{c_i}$ and $\mathbf{n_{E_i}}$ respectively) (figure (b));
- connects adjacent centrepoints, and each centrepoint to $\mathbf{p_i}$ to form a set of smaller triangles, $\triangle_{\mathbf{p_i}}$. The sum of the surface areas of the triangles, $\sum A_{\triangle_{\mathbf{p_i}}}$, is the t_1 surface area, SA_{t_1} associated with $\mathbf{p_i}$;

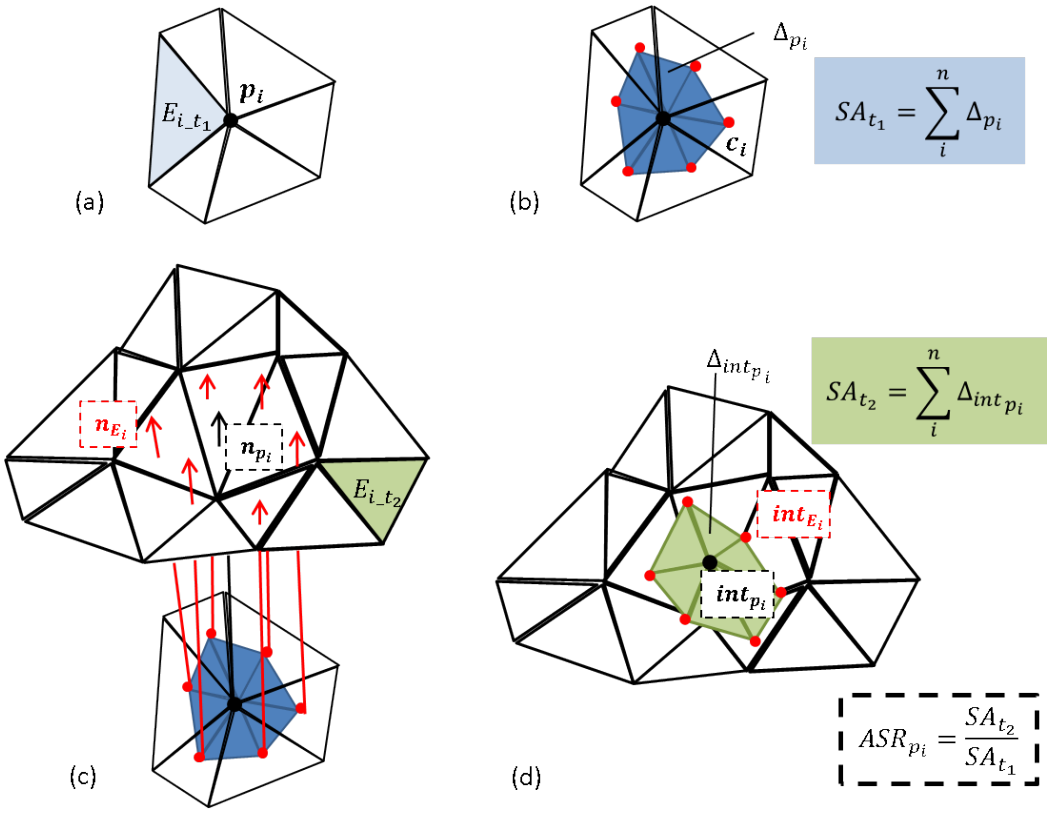


Figure 2.12: (a) for each point, $\mathbf{p_i}$, the surrounding elements, E_i are identified; (b) the element centrepoints are connected to $\mathbf{p_i}$ to form a set of triangles, $A_{\triangle_{\mathbf{p_i}}}$. The surface areas of the triangles are summed, giving SA_{t_1}, the surface area associated with $\mathbf{p_i}$; (c) The intersects of the $\mathbf{p_i}$ and element normals, $\mathbf{n_{p_i}}$ and $\mathbf{n_{E_i}}$, and the t_2 surface are computed and connected to form a set of triangles, $A_{\triangle_{\mathbf{int_{p_i}}}}$. The surface areas of the triangles are summed, giving SA_{t_2}, the surface area associated with $\mathbf{int_{p_i}}$. The ASR at point p_i is then computed as the ratio of SA_{t_2} to SA_{t_1}

- computes a normal at $\mathbf{p_i}$, $\mathbf{n_{p_i}}$, defined as the average of the surrounding element normals;
- determines the intersect of $\mathbf{n_{p_i}}$ and surrounding element normals to the t_2 surface, denoted as $\mathbf{int_{p_i}}$ and $\mathbf{int_{e_i}}$ respectively;
- connects adjacent element intersects, and each intersect to $\mathbf{int_{p_i}}$ to form a set of triangles, $\triangle_{\mathbf{int_{p_i}}}$. The sum of the surface areas of the triangles, $\sum A_{\triangle_{\mathbf{int_{p_i}}}}$ is the t_2 surface area, SA_{t_2}, associated with point $\mathbf{int_{p_i}}$;

- defines the *Area Stretch Ratio* at $\mathbf{p_i}$,

$$ASR_{p_i} = \frac{SA_{t_2}}{SA_{t_1}} = \frac{\sum A_{\triangle_{\mathbf{int_{p_i}}}}}{\sum A_{\triangle_{\mathbf{p_i}}}}$$

It is clear, therefore, that the value of ASR will depend on both the displacement between the t_1 and t_2 surfaces, as well as the curvature of the t_1 surface at each point, the representation of which is in turn affected by the mesh resolution. To investigate the effects of displacement and mesh resolution on the ASR, the simple analytical example of a sphere-within-a-sphere was examined.

2.3.1 The effect of displacement and mesh resolution on the ASR: Analytical example

The four cases defined in §2.2.2 were applied to the sphere-within-sphere example to examine the effect surface displacement and mesh resolution on the ASR. Figure 2.13 compares Case 1 and 3, and shows the effects of mesh resolution on the number (Figure 2.13(a) vs. (b)), and angular dispersion (Figure 2.13(c) vs. (d)) of normals on the *SS* surface. It is obvious that Case 1 will have fewer normals, as it has fewer elements, but it can also be seen that the angles between sets of adjacent normals are greater for Case 1 compared to Case 3.

Figure 2.14 compares the effect of both mesh resolution (Figure 2.14(a) vs. (c) and (b) vs. (d)) and displacement (Figure 2.14(a) vs. (b), and (c) vs. (d)) on the points of intersection of the *SS* normals on *LS* surface, and Figure 2.16 shows the plot of the ASR for the four cases.

It can be seen that in general, a coarser *SS* mesh results in a greater distance between adjacent t_2 intersects (Figure 2.14(a) and (b)) compared to a finer mesh. It can also be seen that for a constant mesh resolution, a smaller displacement (i.e. $r_{SS} = 1.7$) results in a smaller distance between adjacent t_2 intersects compared to a larger displacement ($r_{SS} = 1$).

Figure 2.15, which shows a *SS* of unit radius, with a centre of $(0,0,1)$ inside a *LS* of radius 2, centred about $(0,0,0)$. In this case, the surface of the *SS* is very close to that of the *LS* in the z-axis direction. It can be seen from Figure 2.15(b) that in

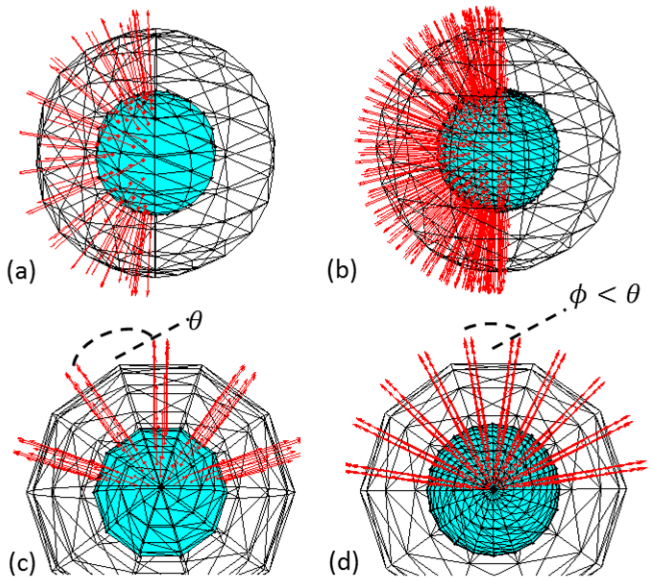


Figure 2.13: Comparison of coarsely ((a) and (c)) vs finely ((b) and (d)) meshed *SS* surfaces (Case 1 vs. Case 3). (a) and (b) The coarsely-meshed *SS* has fewer elements, and therefore fewer outward normals than the finely-meshed *SS*; (c) and (d) The angular displacement between adjacent normals is larger for a coarsely-meshed *SS*

moving from $(0,0,1)$ to $(0,0,0)$, the increasing displacement between the *SS* and *LS* surfaces results in intersects on the *LS* surface that are spaced further apart, giving a large $\sum A_{\triangle_{\mathbf{int}_{\mathbf{p_i}}}}$, and hence, a large ASR.

Figure 2.16 shows the ASR plots corresponding to the four examined cases. Comparison of Figure 2.16(a) and (c) shows that for a large displacement, the difference in mesh resolution results in a less negligible difference in the ASR, compared to the DI. At smaller displacement (Figure 2.16(b) and (d)), the difference in the ASR is smaller for different mesh resolutions. Therefore, the ASR is predominantly affected by surface displacement, with the effect of mesh resolution increasing with an increase in displacement. It can be seen that for a large displacement, the maximum ASR is larger for a finer *SS* mesh. This can be explained by considering the definition of the ASR, i.e.,

$$\text{ASR} = \frac{\sum A_{\triangle_{\mathbf{int}_{\mathbf{p_i}}}}}{\sum A_{\triangle_{\mathbf{p_i}}}}$$

In the case of the coarse *SS* mesh (Figure 2.16(a)), the larger angular displacement between element centrepoints translates into a larger numerator, $\sum A_{\triangle_{\mathbf{int}_{\mathbf{p_i}}}}$, compared to a fine mesh (Figure 2.16(c)). However, the coarse *SS* mesh also has fewer elements, meaning that the centrepoints are located further apart than that of the

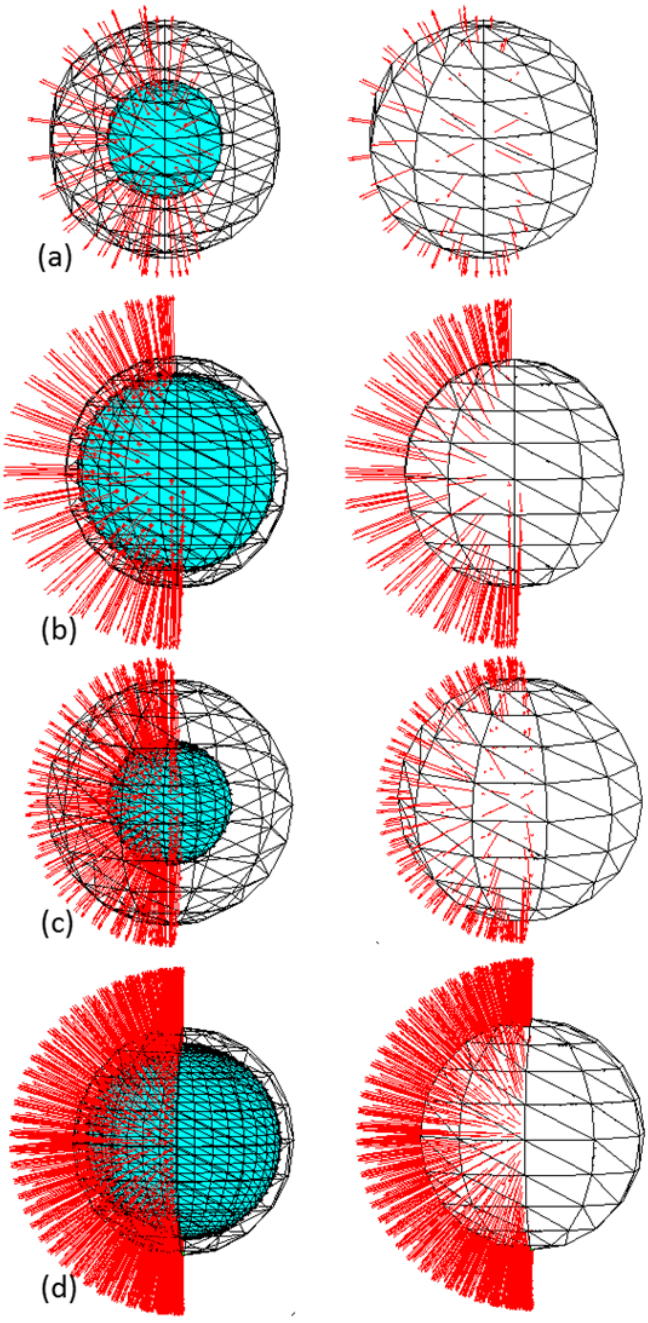


Figure 2.14: The effect of mesh resolution, and displacement between t_1 and t_2 surfaces on location of t_1 normal intersects on the t_2 surface. (a) Case 1: coarse mesh, large displacement; (b) Case 2: coarse mesh, small displacement; (c) Case 3: fine mesh, large displacement; (d) Case 4: fine mesh, small displacement

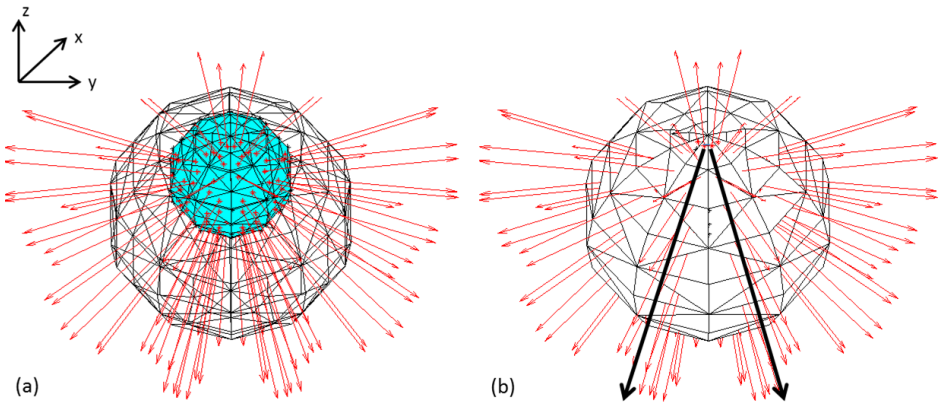


Figure 2.15: Effect of non-uniform displacement between t_1 and t_2 surfaces on t_2 surface intersects. For increasing displacement between the two surfaces, a correspondingly increasing displacement between intersects on the t_2 surfaces is observed

fine *SS* mesh. This results in a larger denominator, $\sum A_{\triangle_{\mathbf{p_i}}}$, which compensates for the larger numerator.

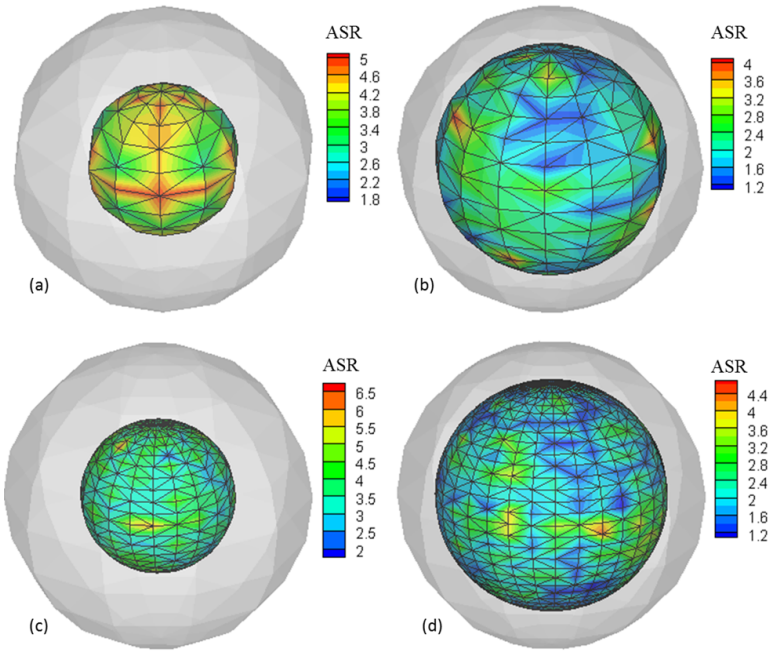


Figure 2.16: Plot of the ASR for different *SS* mesh resolution, E_{SS}, and radius, r_{SS}. (a) $r_{SS} = 1$, $E_{SS} = 180$; (b) $r_{SS} = 1.7$, $E_{SS} = 544$; (c) $r_{SS} = 1$, $E_{SS} = 760$; (d) $r_{SS} = 1.7$, $E_{SS} = 2224$.

Figure 2.17 shows the effect of changing the centrepoint of the *SS* from $(0,0,0)$

to $(0,0,1)$. The ASR is small in the region of the *SS* that is close to the *LS* surface, but becomes very large towards the centre of the *LS*, where the normal displacement between the *SS* and *LS* is at a maximum.

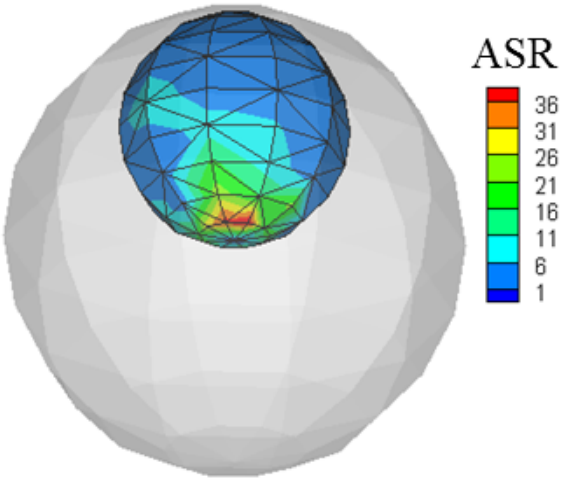


Figure 2.17: Plot of the ASR for the sphere-within-sphere example with *SS* centre-point set to $(0,0,1)$

Unlike the analytical case, the real t_1 geometry has boundary points which represent the neck of the aneurysm. For the purpose of this investigation, coordinates located at geometry boundaries are excluded from computation of the ASR, unless each is connected to 4 triangle elements, which is taken to be the minimum number of elements needed to define the sum of surface areas at any point. Figure 2.18 shows the ASR distributions for the ICA and BT cases.

For the ICA case (Figure 2.18(a)), a large patch of elevated ASR (1.4-2) is observed on the proximal dome. Many smaller patches of elevated ASR are observed throughout the anterior dome, with localised regions of high ASR (2.4-4.4) at the distal anterior dome. The patches are a result of high localisation of nodes on the t_1 surface for which the ASR is positive, i.e. $\sum A_{\triangle_{\mathbf{int}_{\mathbf{p_i}}}} > \sum A_{\triangle_{\mathbf{p_i}}}$. For the BT case (Figure 2.18(b)), several small patches of elevated ASR (1.2-1.8) are observed on the posterior terminus, with a localised patch of high ASR (3-4) at the distal terminus. Like the ICA case, the region of high ASR on the BT case coincides with the region of high DI. In both cases, regions of elevated ASR appear to coincide with regions of high DI, which reflects the dependence of the magnitude of ASR on displacement between the t_1 and

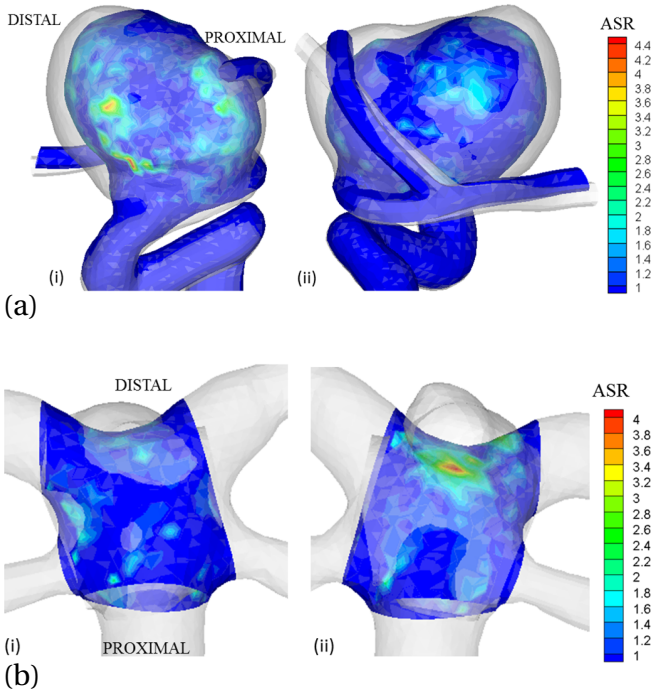


Figure 2.18: The ASR plotted as a surface map on the t_1 geometries of (a) the ICA and (b) the BT

t_2 surfaces.

Unlike the DI, the ASR does not discriminate between "inward" and "outward" growth, and ASR is strictly positive, although the undulation of both surfaces determines whether the ASR is greater than, or less than 1. This is illustrated on the top of the posterior ICA dome (Figure 2.18(a)(ii)) where ASR is between 1.4-2, although the t_1 surface lies outside the t_2 surface in this region. Here, the undulation of the t_2 surface with respect to the t_1 surface is such that $\sum A_{\triangle_{\mathbf{int_{p_i}}}}$ is still greater than $\sum A_{\triangle_{\mathbf{p_i}}}$.

In the next chapter, the ASR and DI distributions are compared to that of five pulsatile-flow haemodynamic indices: WSS, WSSG, OSI, AFI and GON. The following section outlines the CFD methodology, which allows for a quantification of the haemodynamic indices of interest. The quantification of all indices examined is shown in §2.4.2.

2.4 Computational Fluid Dynamics Methods

In this research, modelling of the fluid is accounted for by the ANSYS CFX Solver (ANSYS Inc., Canonsburg, Pensylvania). The conservation of momentum, heat and mass transfer through which equilibrium is attained are described by a set of partial differential equations, the Naviér Stokes Equations, which can be discretised and solved numerically. The equations arise from the governing principles of fluid flow, which require the satisfaction of the conservation of mass (and energy), i.e.

$$\frac{\partial \rho}{\partial t} + \nabla \cdot (\rho v) = 0, \tag{2.6}$$

where ρ is the fluid density, v is the velocity vector; and momentum, which is expressed as below, and constitutes the general form of the Naviér Stokes Equations:

$$\rho \left(\frac{\partial v}{\partial t} + v \cdot \nabla v \right) = -\nabla p + \nabla \sigma + \mathbf{f}, \tag{2.7}$$

where p is the fluid pressure, σ is the deviatoric stress tensor, and f represents the forces acting on the fluid per unit volume.

Equation (2.7) can be solved utilising a number of approaches, with the most common of those being the Finite Volume Method. This method entails the division of a region of interest into smaller "control volumes" (typically referred to as "discretisation of the domain"), with the computational node assigned to the centre, P (Figure 2.19). As such, the average quantity of any variable in the control volume is given by its value at P. The fluid-flow equations are discretised and solved for each control volume.

The spatial discretisation of the t_1 and t_2 geometries was achieved utilising ANSYS **ICEM** (ANSYS Inc., Canonsburg, Pensylvania). The geometries were meshed using the octree method (Mitchell and Vavasis, 1992) with tetrahedral elements. Prism layers were generated near the wall of the artery, which provide a higher grid resolution near the wall, and thereby improve the accuracy and convergence of the solutions (Figure 2.20). The meshing parameters already tested and recommended by the @neurIST project (see Villa-Uriol et al. (2011)) were applied as per Table 4.1. These settings resulted in fine meshes ($\approx 450,000$ elements for the ICA, and $\approx 850,000$ elements for the BT t_1 and t_2 geometries). In an examination on the effect of grid resolution on the spatial distribution and magnitudes of haemodynamic indices, Raberger (2007) showed that a minimum mesh size of $\approx 320,000$

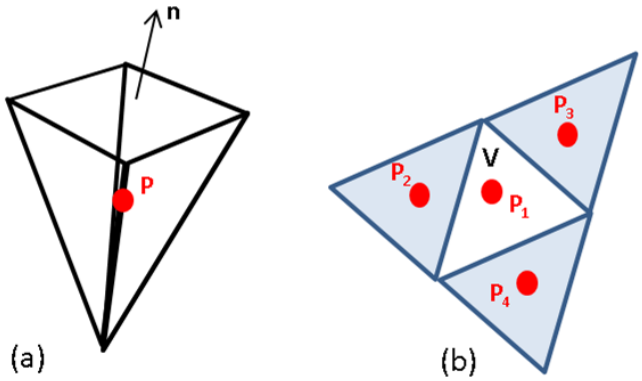


Figure 2.19: (a) Control volume, with cell centre P and cell surface normal, $\mathbf{n}$; (b) Connections between adjacent finite volumes. The averaged quantity of all variables is stored at the centre of each control volume.

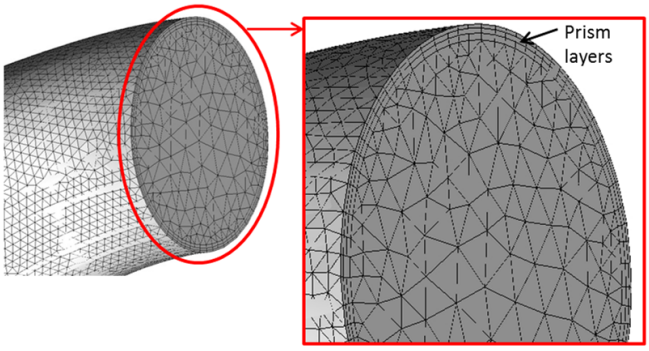


Figure 2.20: A fine mesh, with three prism layers at the vessel boundaries

Table 2.1: Meshing parameters applied to the ICA and BT t_1 and t_2 geometries

Meshing Parameters	Values
Global Parameters	
Element seed size	0.0004
Global Prism Settings	
Number of layers	3
Maximum Prism Angle	170
Parts Parameter List	
Max element size	0.00012
Height ratio	1.3
Number of prism layers	3

elements resulted in adequate spatial resolution of the indices. As sub-, supra- and physiological magnitudes of haemodynamic indices have not yet been clearly defined, this research is concerned primarily with spatial distributions of indices, and relative magnitudes of the indices. The present settings are therefore deemed acceptable for this research.

Volumes (or "bodies" in **ICEM**) were then assigned to each geometry, and the meshes were exported to the ANSYS CFX Solver, where the finite volume formulation is applied to solve the incompressible Naviér-Stokes equations (Patakar (1980); Ferziger and Peric (2001)). The terms of the general transport equation (Equation (2.7)) can be categorised as below:

$$\rho\left(\underbrace{\frac{\partial v}{\partial t}}_{\text{transient}} + \underbrace{v\cdot\nabla v}_{\text{convection}}\right) = \underbrace{-\nabla p + \nabla\sigma}_{\text{diffusion}} + \underbrace{\mathbf{f}}_{\text{sink/source}} \tag{2.8}$$

The equation is integrated over a control volume, and the individual terms are discretised utilising a combination of schemes. The transient term is discretised using a Second-Order Backward Euler scheme, which is robust, fully implicit and does not have a time-step size limitation. For the convection term, a variation of the First-Order Upwind Difference scheme is utilised, where an anti-diffusive, convection correction term is applied to reduce the discretisation errors associated with the first-order upwind scheme. The resulting discretisation is effectively second-order accurate in space, and will better capture steep spatial gradients. However, for both the transient and convection terms, the cost of second-order accuracy is the potential introduction of non-physical oscillations in regions where the solution varies rapidly. For the diffusion and source terms, the finite element approach is utilised, whereby the spatial derivatives of these terms are evaluated using shape functions. To solve for the system as a whole, ANSYS CFX utilises a coupled approach, whereby velocities and pressure are cast and solved as a single system. An algebraic, multigrid accelerated incomplete lower-upper factorisation scheme is used for convergence acceleration (Hutchinson and Raithby, 1986). Due to the highly non-linear nature of the equations, an iterative approach is utilised such that the solution converges towards an approximate solution.

Several assumptions common across CFD studies in the field (Doenitz et al. (2010); Ford et al. (2009); Kulcsár et al. (2011); Mantha et al. (2006); Shimogonya et al. (2009b); Watton et al. (2009a, 2011)) were applied to the model. Firstly, blood

is modelled as a Newtonian fluid (Cebral et al. (2005); Fisher and Rossmann (2009)), with constant density $\rho = 1069\text{kgm}^{-3}$ (Chatziprodromou et al. (2007); Oshima et al. (2001)) and constant viscosity $\mu = 0.0035$ Pas. This is due to the fact that non-Newtonian behaviour of blood is observed in smaller vessels, such as arterioles and capillaries. The average diameter of some of the smallest vessels dealt with in this research (e.g. the opthalmic and posterior communicating arteries) is ≈ 1.5mm, in which the blood can still be considered as a Newtonian fluid.

Furthermore, the vessel walls are considered as rigid, as modelling wall pulsatility would necessitate the continuous re-meshing of the domain as the geometry deforms, at great computational expense. This assumption has been shown to be acceptable: for example, in their cine-mode studies, Boussel et al. (2008) found no observable pulsatility of the aneurysmal wall. Valencia et al. (2008) found that the maximal wall displacement on top of the aneurysm dome at systole was only 10 percent of the parent artery diameter, which results in a negligible change in the WSS distribution. Finally, a no-slip condition is applied for the rigid wall, which is deemed acceptable as the spinning behaviour of blood-cells tends to result in their concentration in the centre of the vessel. This leaves a small layer near the vessel wall of few, or no cells.

Boundary conditions based on realistic physiological values were applied in `@neufuse`, which incorporates a 1D model of the human circulatory system (see Reymond (2011)). In this model, the inlet pulsatile-flow profiles were obtained from contrast magnetic resonance (MR) measurements on real, healthy patients, while the outlet pulsatile pressure profiles were numerically derived. Reymond et al. (2009) validated the derived pressure profiles utilising tonometry measurements on volunteer patients. In `@neufuse`, the velocity and pressure profiles from the 1D model are manually coupled to the 3D geometry in the region of interest (Villa-Uriol et al., 2011). The assumption that conditions corresponding to healthy vasculature can be applied to the vasculature in the vicinity of an aneurysm is generally considered appropriate, as it is assumed that the aneurysm does not significantly affect the flow in the surrounding regions. Figure 2.21 shows the application of boundary conditions in `@neufuse`.

Once segmented, a skeleton is automatically calculated for the geometry (Villa-Uriol et al., 2011). The clipping plane is then moved along the skeleton, which ensures that the plane is perpendicular to the cut boundary. The inlet and outlet

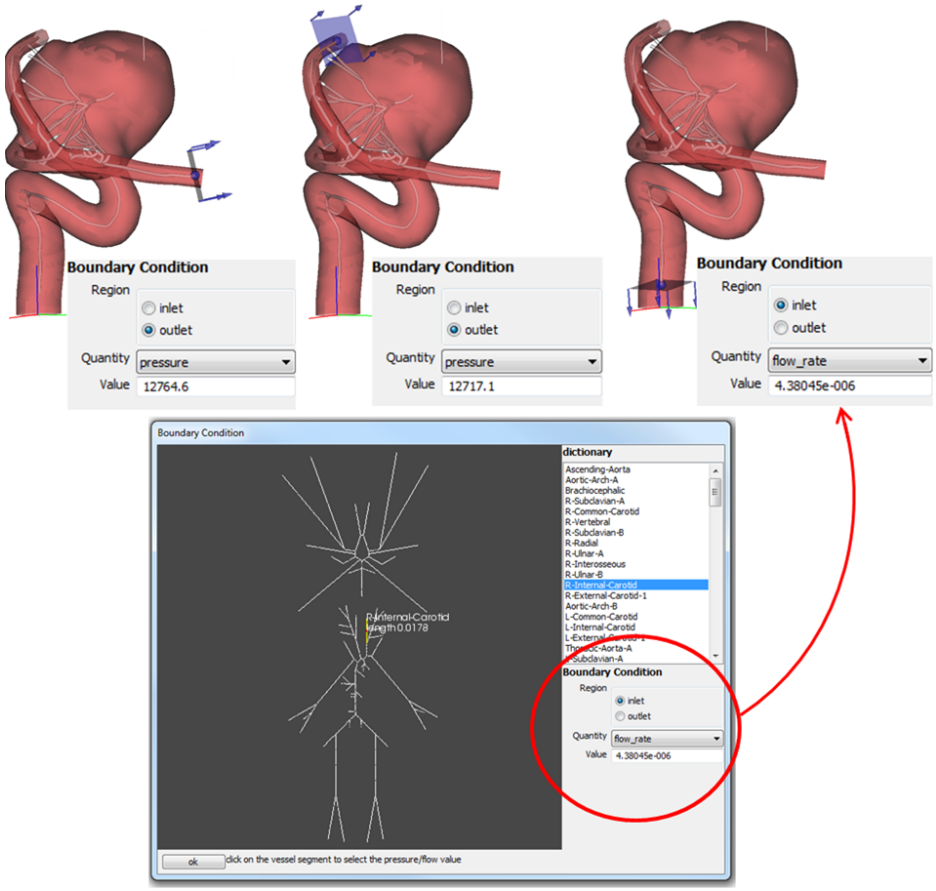


Figure 2.21: Application of inlet velocity and outlet pressure boundary conditions in `@neufuse`. Once the geometry of interest is segmented from the original image, a skeletonisation is automatically calculated for the segmented geometry. Clipping planes are applied perpendicularly to the inlets and outlets of the geometry (top), and manually linked to the nodes of the 1D model of circulation (bottom).

boundaries are then manually linked to the nodes of the 1D model of circulation by the user, who defines the type of boundary (inlet or outlet), and the quantity to be applied (flow-rate or pressure). Figure 2.22 shows the inlet velocity and outlet pressure profiles for the ICA t_1 geometry. With the boundary conditions defined, an *Abstract Problem Definition* file is automatically generated in `@neufuse`, which contains the boundary conditions and blood-flow properties. Together with the mesh, the fluid properties are imported into the ANSYS CFX Pre-Solver module (ANSYS Inc., Canonsburg, Pensylvania), which exports a definition file for the ANSYS CFX Solver. As per the methods of other CFD studies discussed in this and the previous chapter, flow simulations were conducted over three cardiac cycles in order to eliminate artefacts introduced at initialisation. Only the results corresponding to the last

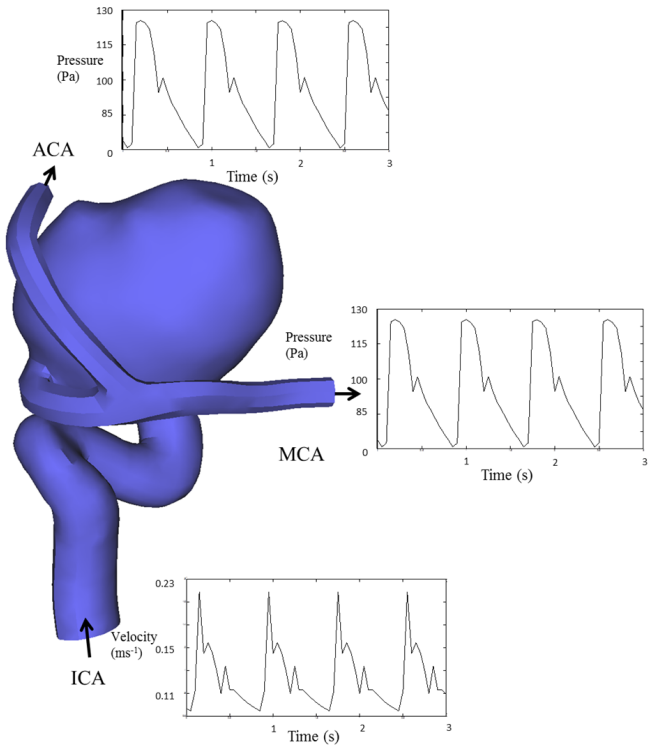


Figure 2.22: Inlet velocity and outlet pressure profiles for the ICA t_1 geometry

cycle were analysed.

For further information, and numerical details of the finite volume method, the interested reader is referred to Chapter 7 of Ferziger and Peric's (2002) excellent text, "Computational Methods for Fluid Dynamics".

2.4.1 Pulsatile-flow haemodynamic indices related to aneurysm formation

The pulsatile-flow indices of interest (WSS, WSSG, OSI, AFI and GON) were introduced in §1.3. Although the oscillatory shear indices (i.e. OSI, AFI and GON) were originally proposed as indicators of aneurysm inception, it is possible that oscillatory shear is also an important factor for aneurysm growth. As such, all five pulsatile-flow indices are investigated in this study. The methods by which each is calculated are outlined in the following section.

2.4.2 Calculation of pulsatile-flow haemodynamic indices

The total fluid stress tensor at any point in the fluid domain can be calculated by:

$$\sigma = -p\mathbf{I} + 2\mu\mathbf{D} = -p\mathbf{I} + \mu[\nabla\mathbf{u} + (\nabla\mathbf{u})^T] \tag{2.9}$$

where p is the fluid pressure, $\mathbf{I}$ is the unit tensor, μ is the blood viscosity, $\mathbf{D}$ is the rate of change of the deformation tensor and $\nabla\mathbf{u}$ is the velocity gradient tensor. At any point on the surface, the inward unit normal vector is denoted as $\mathbf{n}$, and the traction force vector at the same point can then be defined as $\mathbf{t} = \sigma\mathbf{n}$. The WSS vector (the shearing component of the traction vector) can finally be obtained by subtracting out its normal component (Cheng et al., 2002):

$$\mathbf{t_s} = \mathbf{t} - (\mathbf{t}\cdot\mathbf{n})\mathbf{n} \tag{2.10}$$

The magnitude of this shearing component $\mathbf{t_s}$ is defined as the wall shear stress (WSS), and denoted as $\tau(t)$. However, as this study investigates pulsatile-flow indices, the time-averaged value of the wall shear stress is a more appropriate measure, and can be calculated by:

$$\tau_{av} = \frac{1}{T}\int_0^T \tau\, dt \tag{2.11}$$

We also calculate the average WSS vector $\overline{\mathbf{t_s}}$, which is useful for later derivations:

$$\overline{\mathbf{t_s}} = \frac{1}{T}\int_0^T \mathbf{t_s}\, dt \tag{2.12}$$

To obtain the wall shear stress gradient, the tangential component of the WSS gradient vector on the vessel surface is first calculated by:

$$\mathbf{g_s} = \nabla\tau - (\nabla\tau\cdot\mathbf{n})\mathbf{n} \tag{2.13}$$

The WSSG is then defined as the magnitude of $\mathbf{g_s}$, and denoted as γ. As with the WSS, the time-averaged WSSG is the index of interst in this study, and can be obtained by:

$$\gamma_{av} = \frac{1}{T}\int_0^T \gamma\, dt \tag{2.14}$$

The OSI index measures the oscillatory level of the WSS vectors during an entire cardiac cycle, and is obtained from the formula proposed by Ku et al. (1985):

$$OSI = \frac{1}{2}\left\{1 - \frac{\left|\overline{\mathbf{t_s}}\right|}{\tau_{av}}\right\} \tag{2.15}$$

Mantha et al. (2006) defined the AFI as the cosine of the angle between the instantaneous and time-averaged WSS vectors at any time point, given by the following equation:

$$AFI = \frac{\mathbf{t_s}\cdot\overline{\mathbf{t_s}}}{\tau\cdot\left|\overline{\mathbf{t_s}}\right|} \tag{2.16}$$

However, as AFI is an instantaneous quantity, we consider the minimum AFI (hereon referred to as AFI(min)) over the cardiac cycle at each point on the geometry. This allows an explicit interpretation of AFI values. For instance, if AFI(min)=0, then the maximum rotation of the instantaneous WSS vector from the time-averaged WSS vector at that particular point is 90 degrees; AFI(min)=1 corresponds to no deviation (i.e. 0 degrees); AFI(min)=-1 corresponds to a maximum rotation of 180 degrees.

To calculate the GON index, we take the partial derivatives of the three components of the WSS vector (t_{sx}, t_{sy}, t_{sz}) along the x, y, z directions respectively, and denote the new quantity as **G**, **G**=($\frac{\partial t_{sx}}{\partial x}$, $\frac{\partial t_{sy}}{\partial y}$, $\frac{\partial t_{sz}}{\partial z}$). **G** is then projected onto the vessel surface to obtain its tangential component $\mathbf{G_s}$, i.e.

$$\mathbf{G_s} = \mathbf{G} - (\mathbf{G}\cdot\mathbf{n})\mathbf{n} \tag{2.17}$$

The GON is then obtained by the following calculation:

$$GON = 1 - \frac{\left|\int_0^T \mathbf{G_s}\, dt\right|}{\int_0^T |\mathbf{G_s}|\, dt} \tag{2.18}$$

In the next chapter, results of the pulsatile-flow CFD simulations for the ICA and BT geometries are presented, and the distributions of the haemodynamic indices of interest are compared to those of the DI and ASR. Correlations between the haemodynamic and growth indices are determined both by visual and statistical analysis.



CHAPTER 3

HAEMODYNAMICS AND ANEURYSM GROWTH: A CORRELATION?

For both the ICA and BT cases, the haemodynamics indices for the t_1 geometry were obtained from CFX-Post (ANSYS Inc., Canonsburg, Pennsylvania), along with the DI values, and surface maps of the haemodynamics indices of interest were plotted against countour maps of the DI and the ASR. Correlations between haemodynamic and growth indices were assessed both visually (§3.1), and statistically (§3.2).

The aim of the work presented here is

- to determine if correlations between haemodynamic and growth indices deduced utilising the commonly applied method of visual assessment are similar to that deduced utilising a more rigorous, statistical method, and
- to identify if any positive correlations indeed exist, and investigate the effect of linking the relevant haemodynamic indices to G&R hypotheses for the model of cerebral aneurysm evolution (introduced in Chapter 4.

The review on haemodynamics-based hypotheses for aneurysm inception and growth highlighted the lack of clear definitions for supra- and sub-physiological levels of haemodynamic indices. For example, many studies refer to "elevated" or "high" WSS in regions of interest, but do not always explicitly define these terms. As such, for the purpose of visual assessment of correlations between haemodynamic and growth indices, thresholds for each index were required. The thresholds beyond which indices are considered to be elevated (or reduced) were defined as follows:

- **WSS and WSSG**: as discussed in §1.4.3, it appears that the arterial wall adapts to high levels of WSS, but that this ability to adapt is impaired upon introduction of a high WSS gradient. As such, it seems reasonable to consider elevations of WSS to be relevant only in the presence of a high WSS gradient in the same region. In contrast, the literature suggests that low WSS environments contribute to destructive remodelling via more than one mechanism: i.e. aside from being intrinsically linked to flow instability (including high WSSG), low WSS increases the likelihood of inflammatory cell infiltration into the arterial wall. Hence, reductions of WSS are considered independently of WSSG.
  - *high WSS and high WSSG*: In the examined literature, only the study by Sakamoto et al. (2010) was found to report an upper physiological threshold of WSSG. They report a WSSG of greater than 3Pa/mm (3000Pa/m) as high in arterial bifurcations, which are regions of disturbed flow where WSSG is generally higher compared to relatively straight arterial segments. Therefore, in this investigation, WSS values beyond the commonly reported range of 1.5-2Pa are considered elevated only if WSSG in the same region exceeds 3Pa/mm;
  - *low WSS*: In this examination, 1.5Pa is taken as the lower physiological threshold.
- **OSI**: the physiological threshold for OSI is taken to be 0.2, which was suggested in the Glor et al. (2004) study as the value above which EC damage is initiated;
- **AFI(min)**: while there is no strict definition of a physiological threshold of AFI, AFI(min) ≤ 0 (corresponding to an angular deviation of the instantaneous

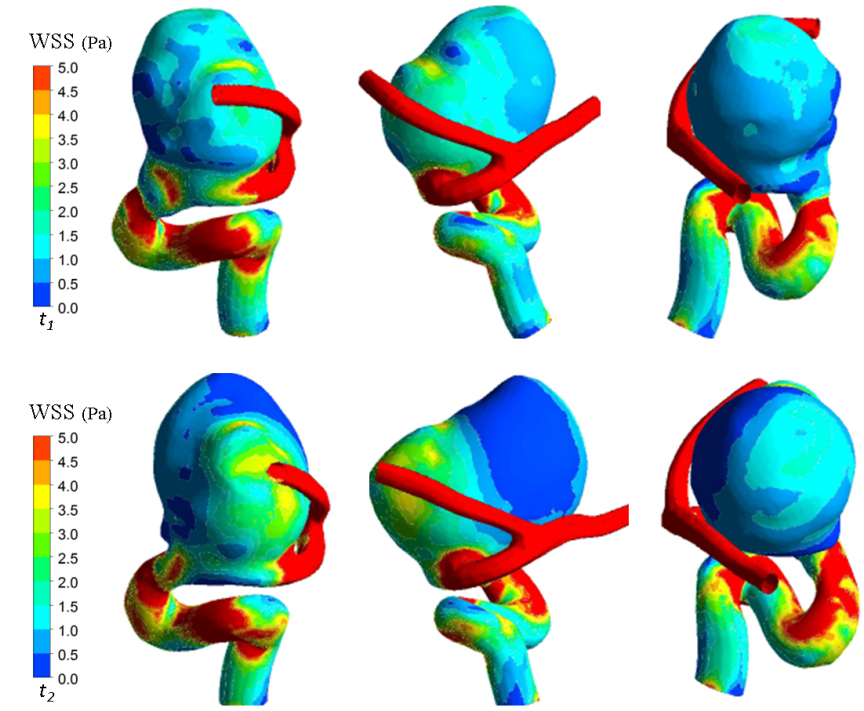
WSS vector from the time-averaged WSS vector of between $90° - 180°$) is considered as a condition for positive correlation in this study;

- **GON**: as with the AFI, no threshold value of GON has been suggested in the literature. It is merely known that GON=0 corresponds to no oscillatory behaviour of the WSSG vector, while GON=1 corresponds to maximal oscillation. As it is unknown to what degree ECs can withstand oscillations of the WSSG vector, the midrange value of GON, i.e. GON=0.5 is considered as the upper threshold for this examination.

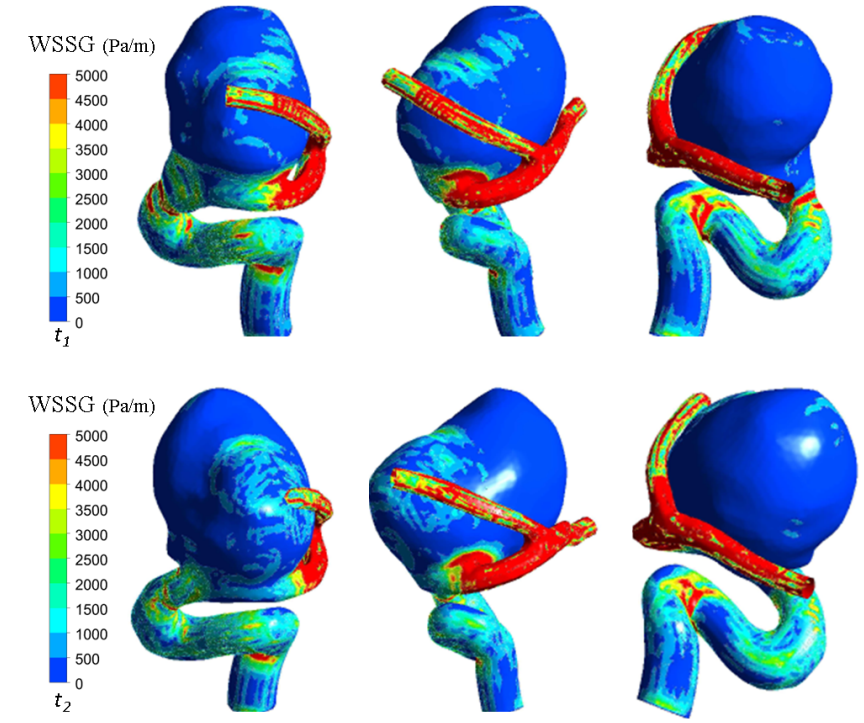
3.1 HAEMODYNAMIC AND GROWTH INDEX DISTRIBUTIONS: CFD RESULTS

The results are presented for the ICA, and then the BT case, as follows. The figures showing distributions of the haemodynamic indices for the ICA and BT cases comprise two rows, with the top three images showing the t_1 geometry, and the bottom three images showing the t_2 geometry, in three orientations, such that distributions of the haemodynamic and growth indices can be examined for the entire ICA dome. The figures incorporating the growth indices comprise three images, where both the haemodynamic indices and the growth indices are examined on the t_1 geometry. It must be noted here that comparison of haemodynamic and growth index distributions is made strictly within the aneurysmal region of both cases, and not at the surrounding vasculature. This is due to the lack of certainty if any growth has indeed occurred in surrounding regions, while it is comparatively clear that growth has occurred in the dome of the ICA geometry, and at the terminus of the BT geometry. As WSS was observed to be generally low throughout the ICA dome, a narrowing of the range of WSS to between 0-5Pa (Figure 3.1(a)) was performed to allow for a better examination of WSS distribution. It appears that following aneurysm growth, the haemodynamics evolve such that there is an enlarging region of very low WSS (0-0.5Pa) at the distal-anterior part of the dome, and an enlarging region of elevated WSS (2-4Pa) at the proximal part of the dome.

Figure 3.1(b) shows the spatial distribution of the average WSS gradient, which, in the case of both the t_1 and t_2 ICA geometries, is generally low across the aneurysm dome (0-500Pa/m), with regions of WSSG of between 500-2000Pa/m at localised regions of the top, proximal and distal parts of the dome. Regions of elevated WSSG



(a)



(b)

Figure 3.1: (a) Average WSS (0-5Pa) and (b) WSSG (0-5000Pa/m) (b) distributions for the t_1 (top) and t_2 (bottom) geometries of the ICA case

occur at both the distal and proximal parts of the neck (up to 4000Pa/m), with the highest WSSG (>5000Pa/m) occurring at the distal neck and throughout the middle and anterior cerebral arteries. As with WSS, the most notable change between the t_1 and t_2 geometries is the shift in the region of elevated WSSG towards the proximal part of the dome, which also appears to coincide with the region where outward growth has occurred.

Figure 3.2 compares the spatial distribution of average WSS, WSSG and the DI in mm. When plotted against the DI, there appears to be no clear correlation be-

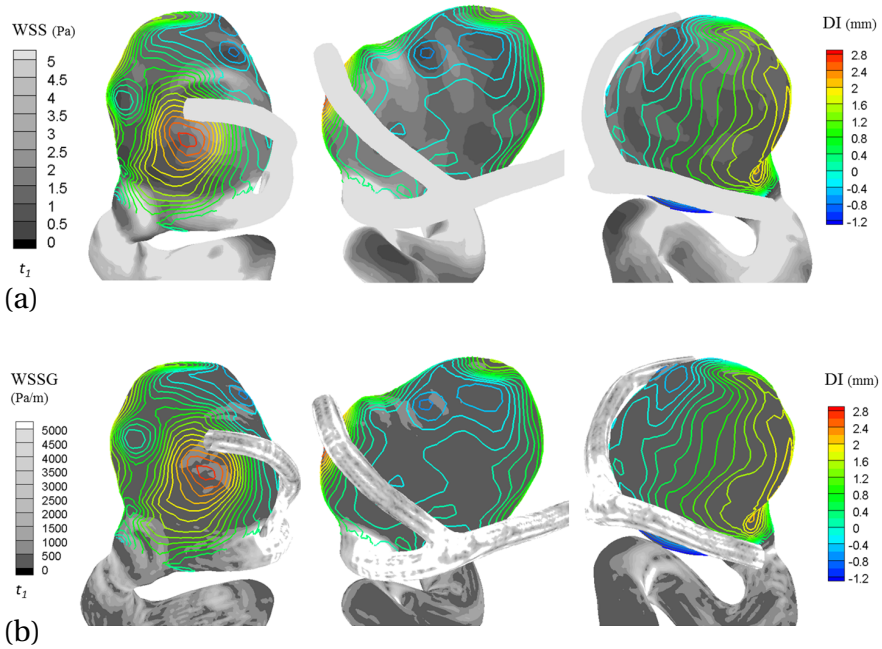


Figure 3.2: Plots of average WSS (a) and average WSSG (b) distributions against DI distributions on the t_1 ICA geometry

tween regions of high growth and regions of low WSS. The distal dome exhibits regions of locally low WSS (<1Pa) and elevated DI (2-2.3mm); in contrast, the region of highest DI (>2.8mm) at the proximal part of the dome appears to correspond to a locally elevated WSS (2-4Pa). However, WSSG is generally low throughout the dome (<3000Pa/m), so by the definition of significant elevation of WSS proposed for this investigation, it appears that correlations do not exist between the DI and high WSS, and DI and WSSG. Figure 3.3 compares the spatial distribution of average WSS, WSSG and the unitless ASR. In contrast to the DI, it appears that regions of high ASR coincide with regions of locally low WSS: the maximum ASR of 4.4 at the

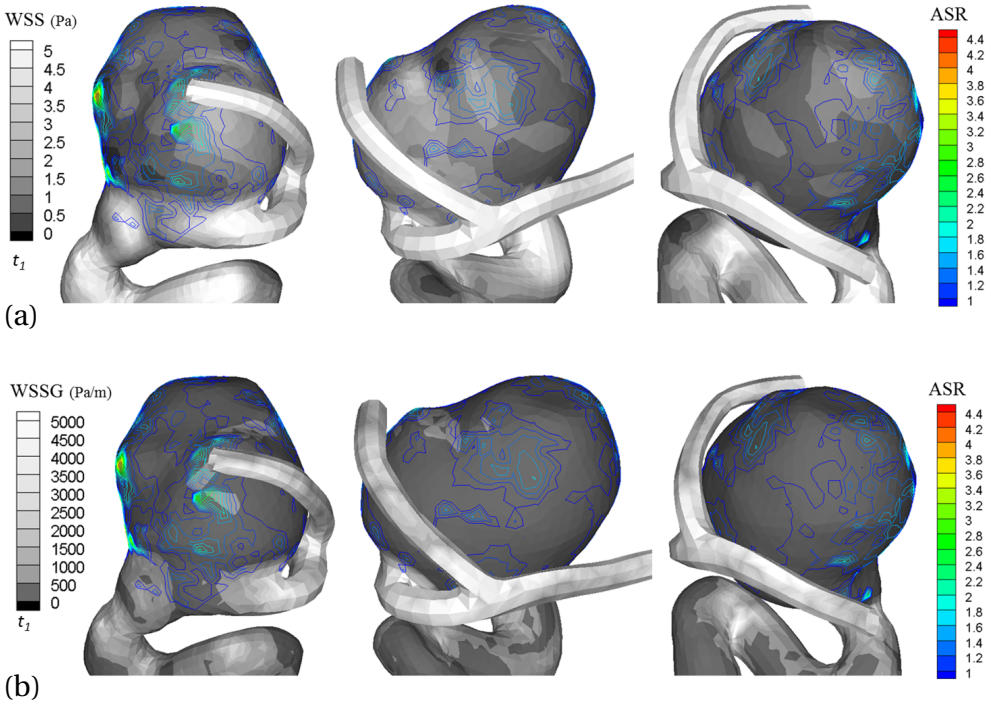


Figure 3.3: Plots of average WSS (a) and average WSSG (b) distributions against ASR distributions on the t_1 ICA geometry

anterior part of the dome coincides with a region where WSS<1Pa. As with the DI, there appears to be no correlation between the ASR and high WSSG.

Figure 3.4(a) shows the average WSS distribution for the t_1 and t_2 geometries of the BT case. It must be noted here that the colour map is extended In line with the study by Doenitz et al. (2010), the results show a locally low WSS (0-4Pa) in both the anterior and posterior regions of the terminus, with elevated patches (6-14Pa) throughout, and a peak WSS ($\geq$ 20Pa) at the apex. In contrast, the t_2 geometry shows that regions where WSS was elevated on the t_1 geometry coincide with regions where local outward remodelling has occurred, which is evident in the bulging of the apex. As such, WSS throughout the t_2 geometry does not exceed 14Pa. The posterior plots show that WSS is low (0-2Pa) in the dome of the aneurysm, and very high (6-14Pa) at the distal aneurysm neck (near the bifurcation apex).

Figure 3.4(b) shows the average WSSG distributions for the BT t_1 and t_2 geometries. It can be seen that WSSG is very high ($\geq$ 5000Pa/m) throughout the LPCA and RPCA, and in patches throughout the basilar artery, LSC and RSC arteries. As with the WSS, a reduced WSSG is observed on the t_2 geometry, although regions of high

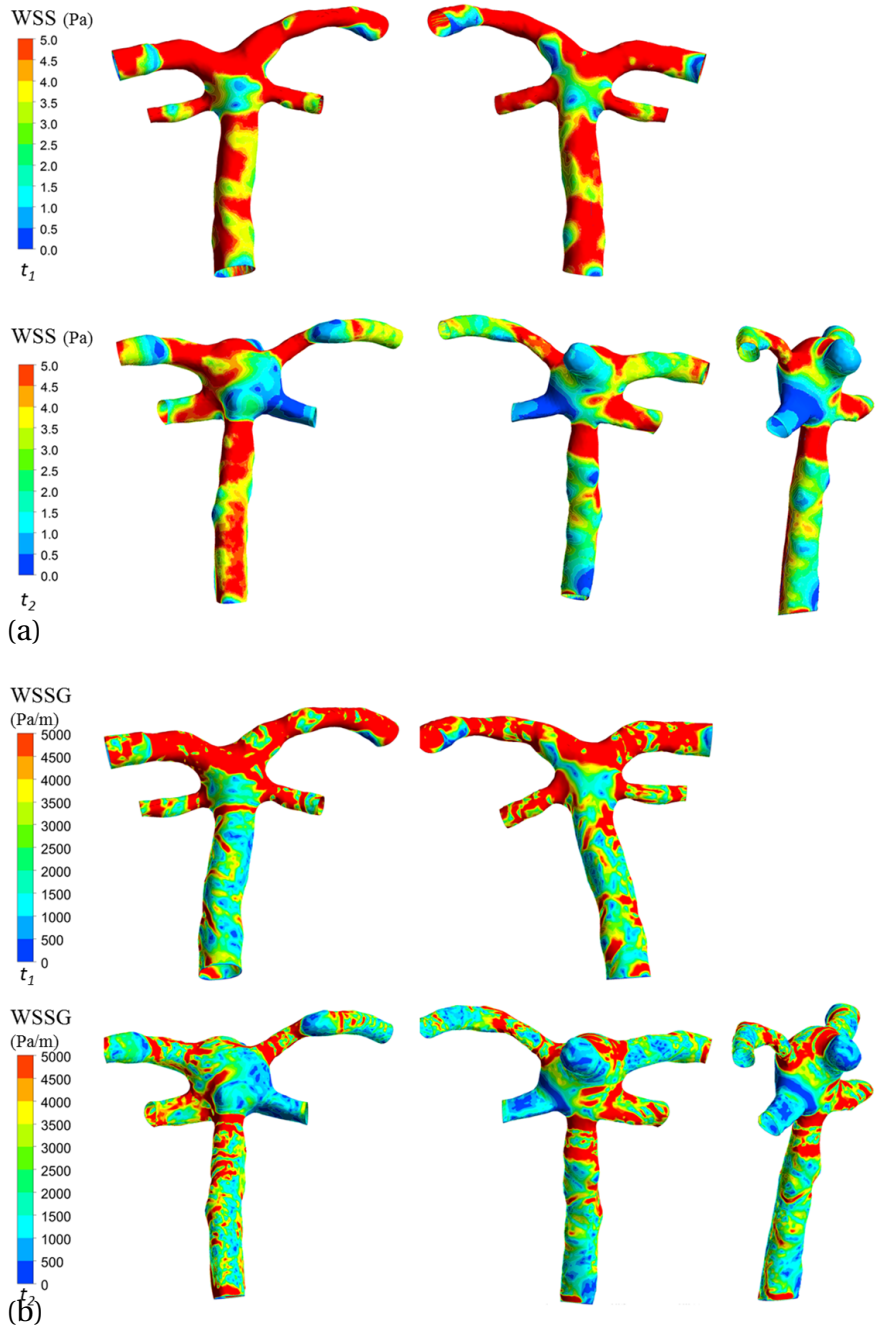


Figure 3.4: (a) Average WSS (0-5Pa) and (b) average WSSG (0-5000Pa/m) (b) distributions for the t_1 (top) and t_2 (bottom) geometries of the BT case

WSSG can be seen in localised patches throughout the geometry, and a large patch at the distal neck of the aneurysm. Figure 3.5 shows the plots of the WSS and WSSG distributions against the DI and ASR distributions respectively. From Figure 3.5(a),

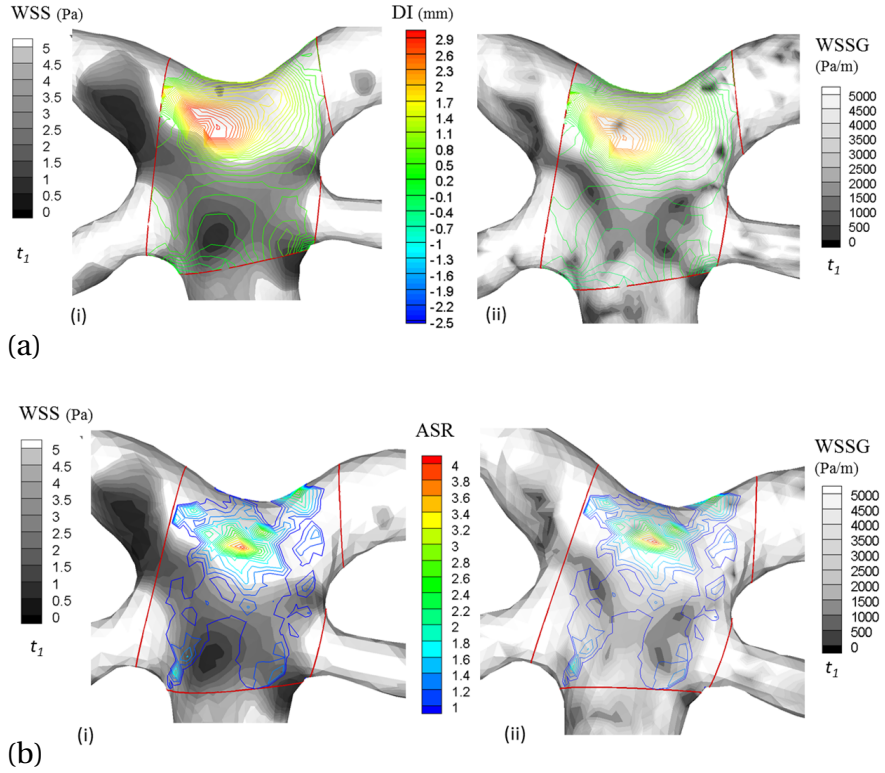


Figure 3.5: Plots of average WSS and average WSSG distributions against (a) the DI and (b) ASR distributions on the t_1 BT geometry

it can be seen that the region of highest DI (>2.8mm) occurs in the region of high WSS (12-16Pa), and that a high WSSG (>4500Pa/m) occurs in the same region. However, a small, localised patch of very low WSSG (<500Pa/m) is observed within the same region. Furthermore, it can be seen that other regions exist where WSS and WSSG are high, but the DI is approximately 0. Hence, although a high DI coincides with regions of high WSS and high WSSG, it is unclear if correlations between the DI and the two haemodynamic indices actually exist.

Figure 3.5(b) compares the WSS and WSSG distributions to the ASR distributions, and the results are nearly identical to the DI comparison: the highest ASR coincides with regions of very high WSS (10-16Pa), where the WSSG is also observed to be high (≥5000Pa/m). However, as with the DI, other regions exist where the WSS

and WSSG are high, but the ASR is low. Therefore, no positive correlations can be visually ascertained between high WSS and high ASR, and high WSSG and high ASR.

Figure 3.6 shows the distribution of the OSI, which is observed to be elevated in several regions of the t_1 ICA dome. Most notably, the proximal part of the dome shows a large region of high OSI (0.35-0.5). A localised region of elevated OSI (≈ 0.35) occurs at the top of the distal part of the dome, while elevated OSI (0.15-0.35) occurs across several large regions of the distal dome. In comparing the two geometries, it appears that following growth, there has been a shift in haemodynamic conditions such that a greater region of the distal dome exhibits elevated OSI (0.15-0.3), with a localised region of high OSI (0.35-0.5) at the posterior part of the distal dome.

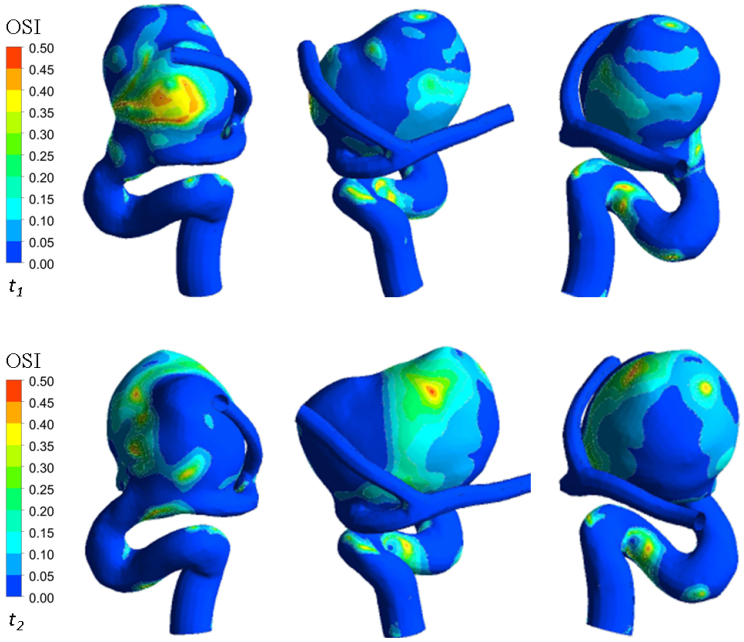


Figure 3.6: OSI distributions for the t_1 (top) and t_2 (bottom) geometries of the ICA case

Comparing the OSI to the DI (Figure 3.7(a)) shows that the region of highest OSI, the proximal-anterior part of the dome, corresponds to the region of largest DI. Similarly, regions of elevated OSI (0.3-0.4) on both the anterior and posterior parts of the dome also appear to correlate well with elevated DI (0.5-1.2mm). However, it can also be seen that there are regions exhibiting elevated OSI where no outward growth has been captured by the growth scalar. This suggests the possibility that growth and remodelling may not be directed strictly outward. From Figure 3.7(b), it

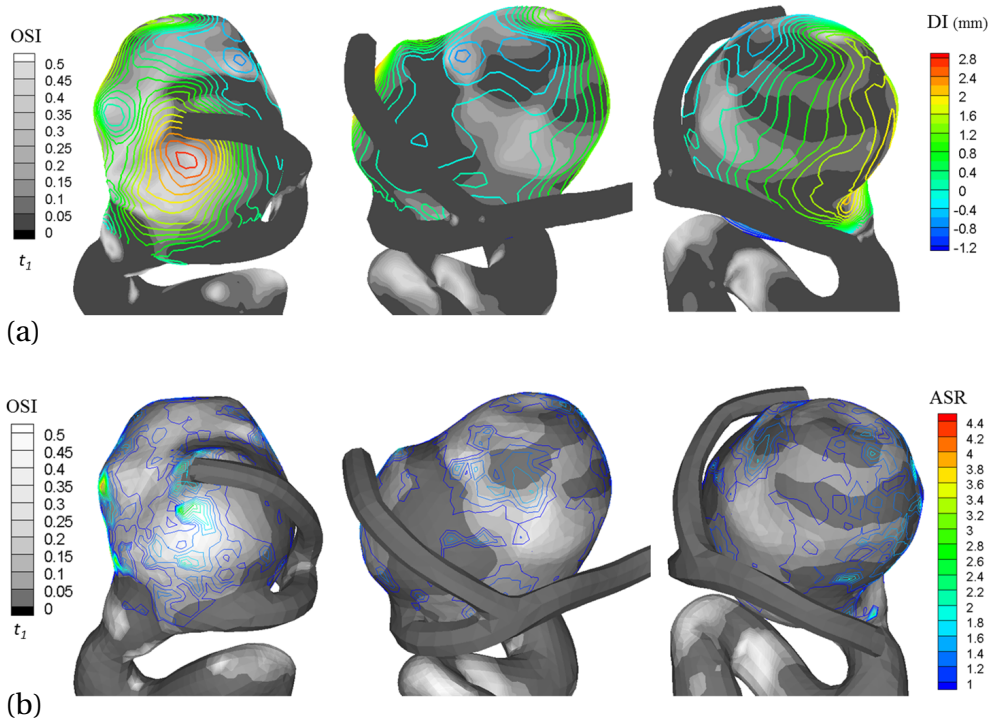


Figure 3.7: Comparison of OSI, and DI (a) and ASR (b) distributions on the t_1 ICA geometry

appears that regions of elevated and high ASR coincide with regions of highest OSI (0.35-0.5). However, other regions are observed on the ICA dome where the OSI is elevated, but the ASR is 1, or very close to 1. Hence, it is unclear if a positive correlation exists between the OSI and ASR.

The plots of the OSI distribution for the BT case (Figure 3.8(a)) show an elevated OSI (0.2-0.3) on the anterior terminus of the t_1 geometry, and at the junctions between the LPC and LSC, and RSC and basilar arteries. The t_2 geometry plots show elevated, and peak OSI (0.3-0.5) at the base of the LSC artery, and also at the distal neck of the aneurysm. Figure 3.8(b) shows that the DI is high in a region where OSI is low ($\leq$0.1), while the DI appears to be close to zero in small patches where OSI is elevated ($\geq$0.2). From the OSI/ASR comparison, it can be seen that the region of peak ASR also coincides with a region of low OSI, suggesting no positive correlation exists between high OSI and the two growth indices.

It can be seen from Figure 3.9 that the AFI exhibits a similar pattern to the OSI. In particular, in comparing the t_1 AFI(min) and OSI plots, it can be seen that the

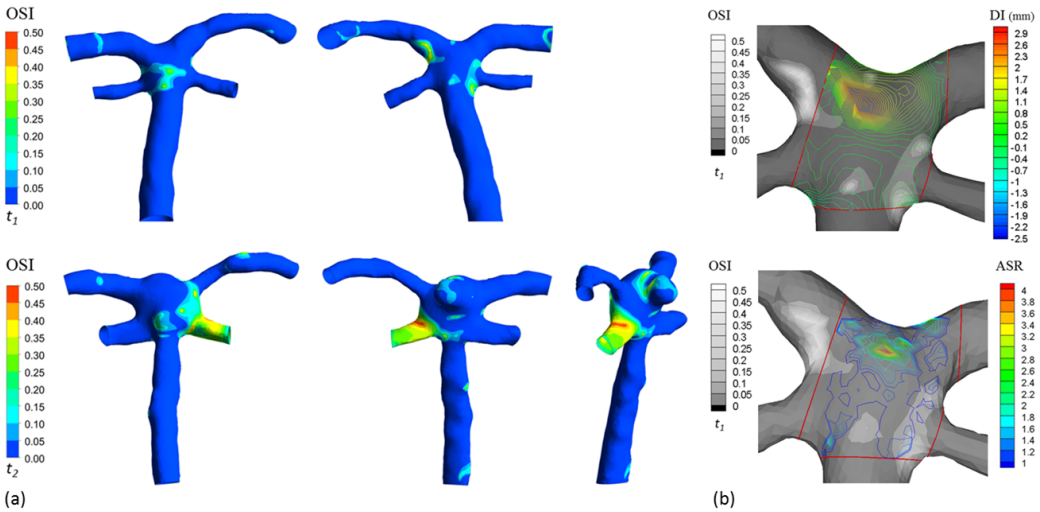


Figure 3.8: OSI distributions for the t_1 (top) and t_2 (bottom) geometries of the BT case

proximal-anterior part of the dome where the reduction in AFI is most pronounced corresponds to the region of maximum OSI. As with the OSI, it appears that the change in haemodynamic conditions between the t_1 and t_2 geometries is such that a greater region exhibiting a reduced AFI evolves across the distal posterior part of the t_2 dome.

Figure 3.9 also shows that the maximum rotation (180 degrees, or AFI(min)=-1) of the instantaneous WSS vector from the time-averaged value occurs across a large portion of the anterior part of the dome, and at localised regions of the posterior dome of the t_1. Following growth, the change in AFI is qualitatively similar to the changes observed for WSS and OSI, in that the region of AFI(min) shifts from the proximal anterior part of the dome, to the distal posterior part of the dome.

When compared to the DI (Figure 3.10(a)), it appears that a positive correlation exists between maximum DI, and AFI(min), particularly in the anterior part of the dome. However, this is less clear at the posterior part of the dome. For instance, as per the OSI and WSS, a small local region of minimum AFI at the top of the dome corresponds to the region where no outward growth is detected (DI<0). However, immediately adjacent to this region is an area of high AFI (AFI(min)>0.9), but no outward growth. This suggests the possibility that growth of the aneurysm may not necessarily always be outward, but rather that the tissue growth and remodelling process may cause some regions of the aneurysm dome to “shrink”, or move in-

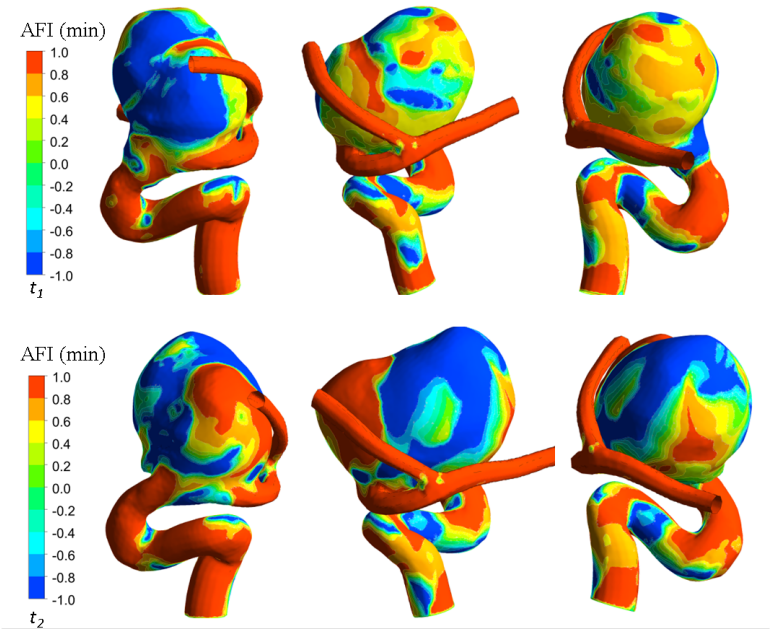


Figure 3.9: (a) AFI(min) distributions for the t_1 (top) and t_2 (bottom) geometries for the ICA case, and (b) comparison of AFI(min) and ASR

wards. Figure 3.10(b) shows that the regions of high ASR fall within the region of lowest AFI, on both the proximal and distal parts of the anterior ICA dome. However, within that same region of low AFI, it can be seen that the ASR is also predominantly 1, or close to 1.

The plots of the AFI(min) distribution for the BT case (Figure 3.11(a)) show a local patch of AFI(min)=0 at the centre of the anterior terminus and the distal parts of the LPC and RPC arteries, and large regions of minimum AFI (i.e. AFI(min)=-1) near the junctions of the RPC and RSC, and LPC and LSC arteries. A region of AFI(min)=-1 is also observed on the proximal part of the posterior terminus. The t_2 geometry shows that the region of AFI(min) at the junction of the RPC and RSC arteries has enlarged, and that regions of AFI(min)=1, AFI(min)=0 and AFI(min)=-1 are observed in the aneurysm dome, and at the distal aneurysm neck. Figure 3.11(b) shows that the region of maximum DI coincides with a region of high AFI (AFI(min)$\geq$ 0.8), while the DI is low near the RPC and RSC artery junction, where AFI(min)=-1. Similarly to the OSI/ASR comparison, the AFI(min)/ASR comparison shows that, by visual inspection, no correlation between the region of peak ASR and low AFI exists (i.e. the region of peak ASR coincides with AFI(min)=1).

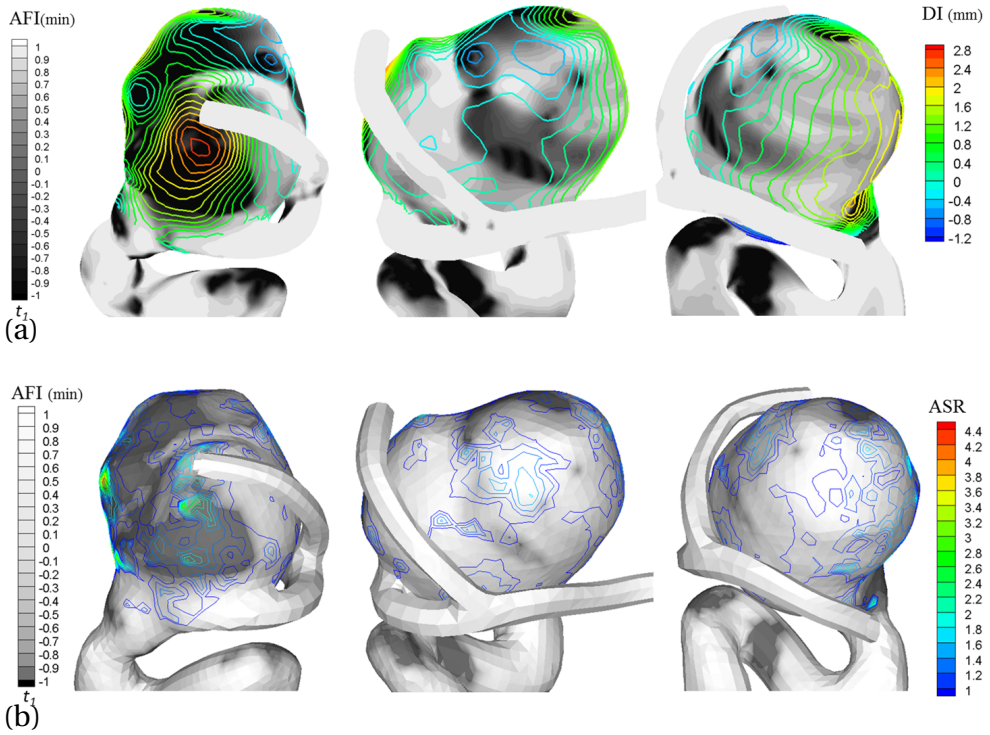


Figure 3.10: Comparison of AFI(min), and DI (a) and ASR (b) distributions on the t_1 ICA geometry

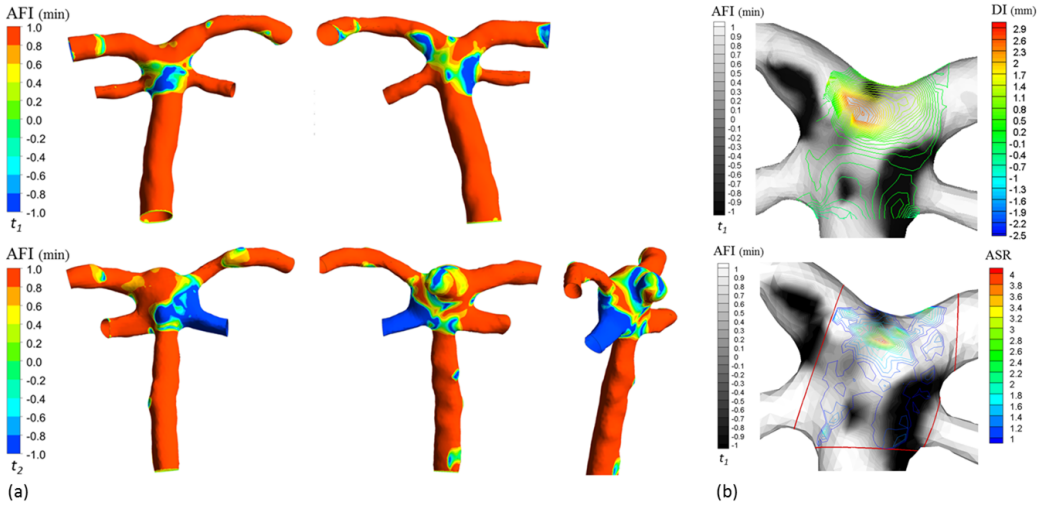


Figure 3.11: AFI(min) distributions for the t_1 (top) and t_2 (bottom) geometries of the BT case

Figure 3.12 shows the distribution of the GON. In their original study on aneurysm inception, (and in a subsequent study performed by Chen et al. (2013)), Shimogonya et al. (2009b) reported results which showed that many regions of the artery exhibit a high GON, and not merely the region of interest. This makes it difficult to determine if a positive correlation really exists between the GON and regions of growth. The same can be said for the results of this study. However, interestingly, the results show a clear local maximum GON at the proximal-anterior part of the dome, which coincides with the region of highest DI (see Figure 3.13(a)).

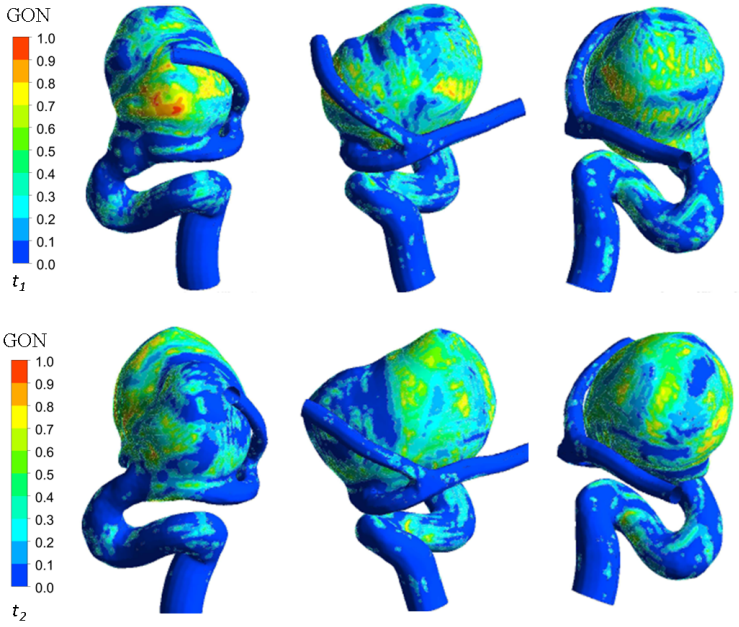


Figure 3.12: GON distributions for the t_1 (top) and t_2 (bottom) geometries of the ICA case

As was the case with the GON/DI comparison, the Figure 3.13(b) shows that GON is elevated (>0.5) in many patches throughout the dome, and it appears that the two small regions where ASR is high in fact coincide with patches where GON is low. Hence, no correlation between high GON and high ASR can be visually ascertained. The plot of the GON distribution for the BT case (Figure 3.14(a)) shows that GON of between 0 and 0.5 occurrs in patches on both the anterior and posterior terminus, with a small local region of high GON (≈ 0.8) on the posterior side of the LPC and LSC artery junction. The t_2 geometry plots show a peak GON (0.8-1) at the base of the RSC artery.

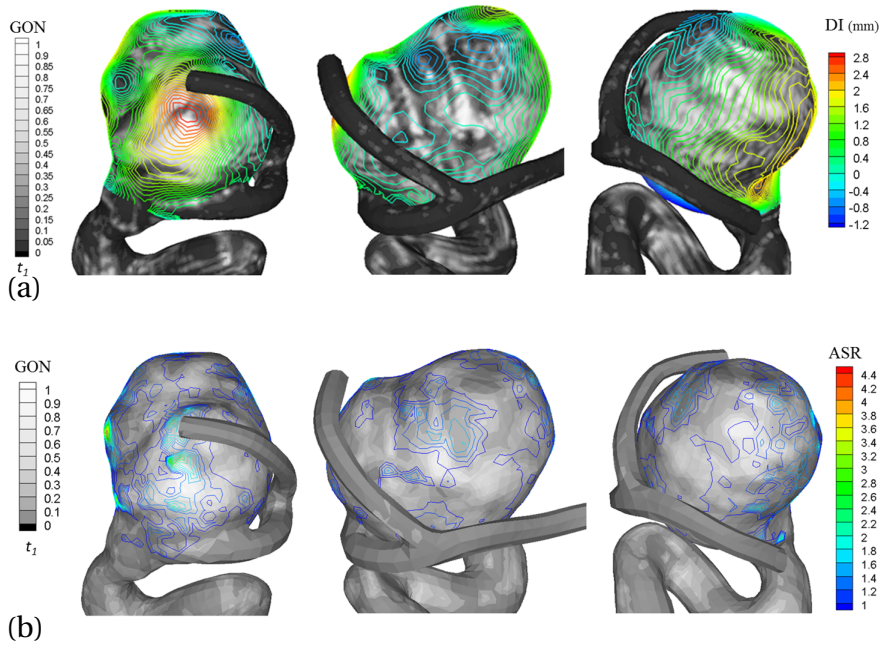


Figure 3.13: Comparison of GON, and DI (a) and ASR (b) distributions on the t_1 ICA geometry

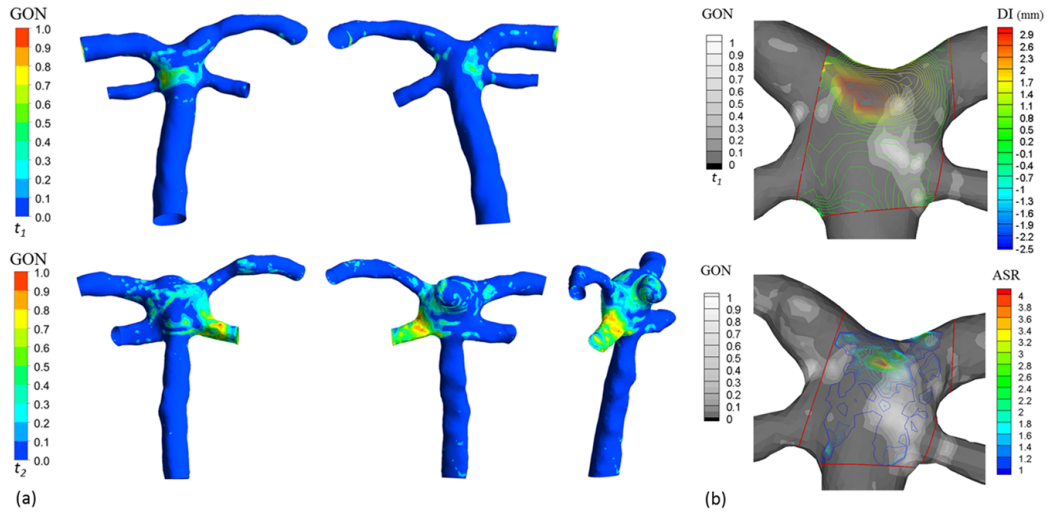


Figure 3.14: GON distributions for the t_1 (top) and t_2 (bottom) geometries of the BT case

Figure 3.14(b) shows that the region of high DI for the BT case coincides with a region of low GON (≤ 0.1), while DI is close to zero in regions where GON is elevated. The same trend is also observed for the GON/ASR comparison, and as such it appears that no correlations exist between a high DI and high GON, and high ASR and high GON.

Table 3.1 summarises the visually-assessed correlations between the two growth indices, and the haemodynamic indices. It can be seen that no existing correlations could be definitively ascertained, many "possible" positive correlations were observed -i.e. in cases where haemodynamic indices are elevated (or reduced) in regions of both high and low growth. As such, a more rigorous analysis is required to determine both the strength and direction of the correlations.

Table 3.1: Summary of visually-assessed correlations between the haemodynamic indices and the DI (a) and ASR (b)

(a)

DI	ICA	BT
WSS	Possible correlation with low WSS	Possible correlation with high WSS
WSSG	No correlation	Possible correlation with high WSSG
OSI	Possible correlation with high OSI	No correlation
minAFI	Possible correlation with low AFI	No correlation
GON	Possible correlation with high GON	No correlation

(b)

ASR	ICA	BT
WSS	Positive correlation with low WSS	Possible correlation with high WSS
WSSG	No correlation	Possible correlation with high WSSG
OSI	Possible correlation with high OSI	No correlation
minAFI	Possible correlation with low AFI	No correlation
GON	No correlation	No correlation

3.2 STATISTICAL ANALYSIS OF CORRELATIONS BETWEEN HAEMODYNAMICS AND GROWTH INDICES

To date, Boussel et al. (2008) appear to be the only group to have statistically examined the relationship between WSS and aneurysm growth. They utilised linear regression analysis, and concluded that a linear trend indeed exists between inverse WSS and growth, shown in Figure 3.15.

In this section, correlations between the haemodynamic and growth index data assessed visually in the previous section are now examined utilising statistical methods so as to quantify the strength and direction of correlations. Correlation and regression analyses are performed on the haemodynamics and growth index data

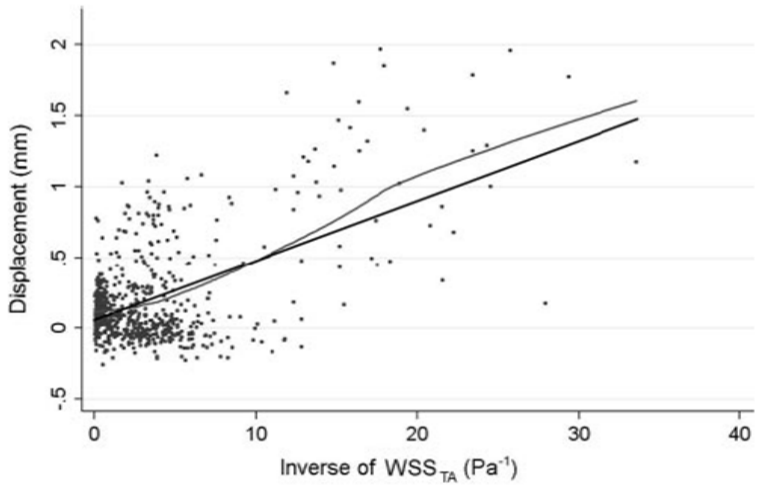


Figure 3.15: Displacement of the aneurysmal wall during growth as a function of WSS^{-1}, with both linear (black) and LOWESS curve (gray) fittings (taken from Bousel et al. (2008))

utilising the statistical software package, SPSS (IBM Corp. Released 2011. IBM SPSS Statistics for Windows, Version 20.0. Armonk, NY: IBM Corp). The two cases considered provide not only a useful comparison between an already established and still-growing aneurysm (the ICA case) and a de-novo aneurysm (the BT case), but they are also representative of the two commonly-occurring types of aneurysms: a saccular side-wall aneurysm (ICA), and a bifurcation aneurysm (BT).

As it is impossible to determine if regions where the t_1 surface lies outside of the t_2 surface represent "inward growth", or are the result of a spatial shift between the geometries, an absolute threshold for *significant* displacement is defined to examine the DI -i.e. only the magnitude, and not the direction of the DI is taken into consideration. Similarly, when examining the ASR, only data corresponding to ASR>1 is assessed.

While specific thresholds for haemodynamic indices were useful for visual assessment of correlations, when applied to statistical examination, the selection of samples based on these thresholds yields significantly reduced sample sizes for assessment. For example, filtering of BT data (where the growth index is the ASR) based on the condition "GON>0.5" yields only a single sample. Obviously, in this case it is impossible to deduce if a positive correlation indeed exists between high GON and high ASR. Therefore, statistical assessment is applied to examine the general trend of data, with selection of samples based only on the magnitudes of the DI

and ASR.

Spearman's Rank correlation and linear regression analyses are first examined on raw data, and the relationship between WSS and the growth indices is specifically examined for comparison with the study by Boussel et al. (2008). The suitability of performing linear regression analaysis on WSS data is verified by checking the closeness of data to a normal distribution. The Kolmogorov-Smirnov test is applied for this purpose, which compares each data set to a normally-distributed set with the same mean and standard deviation. Where data is non-normally distributed, it is transformed (see Table 3.4 for the applied transformations) in an attempt to bring the distribution closer to normal. Statistical significance of correlations is established for $p < 0.05$. In this case, the null hypothesis (that no correlation exists between the examined variables) is rejected.

As per the study by Boussel et al. (2008), the LOWESS curve and simple linear fittings are shown for plots of the inverse WSS against the two growth indices. The LOWESS (Locally Weighted Scatterplot Smoothing) curve is more general than a linear regression in that it merely follows the general trend of the data and fits a smooth curve to it. As the above comprise a set of commonly-applied statistical analyses, the interested reader is referred to Appendix A for further details on each.

3.2.1 Haemodynamics and the DI

In the case of the DI, given that growth was considered to be significant when greater than 0.3mm and 0.5mm by Boussel et al. (2008) and Sforza et al. (2012) respectively, in this analysis, the "happy medium" of |0.4|mm was considered as the minimum threshold for significant growth. Of particular interest in this examination is the relationship between WSS and the DI, which was examined by Boussel et al. (2008) in their study, and hence provides a good example for comparison.

Scatter plots of the raw haemodynamic data (Figure 3.16) are plotted against the DI for the ICA and BT cases. In a case where data are linear, the shape of the data tends to be elliptical about a diagonal. It is clear from visual inspection that, in both cases, the relationship between the DI and each haemodynamic index is complex, and non-linear. As such, a linear regression analysis for this data is inappropriate. In this study, several transformations of both the WSS and DI data are applied in an attempt to improve linearity, and are examined further in this sec-

tion. The Kolmogorov-Smirnov test of normality for the raw DI and haemodynamic

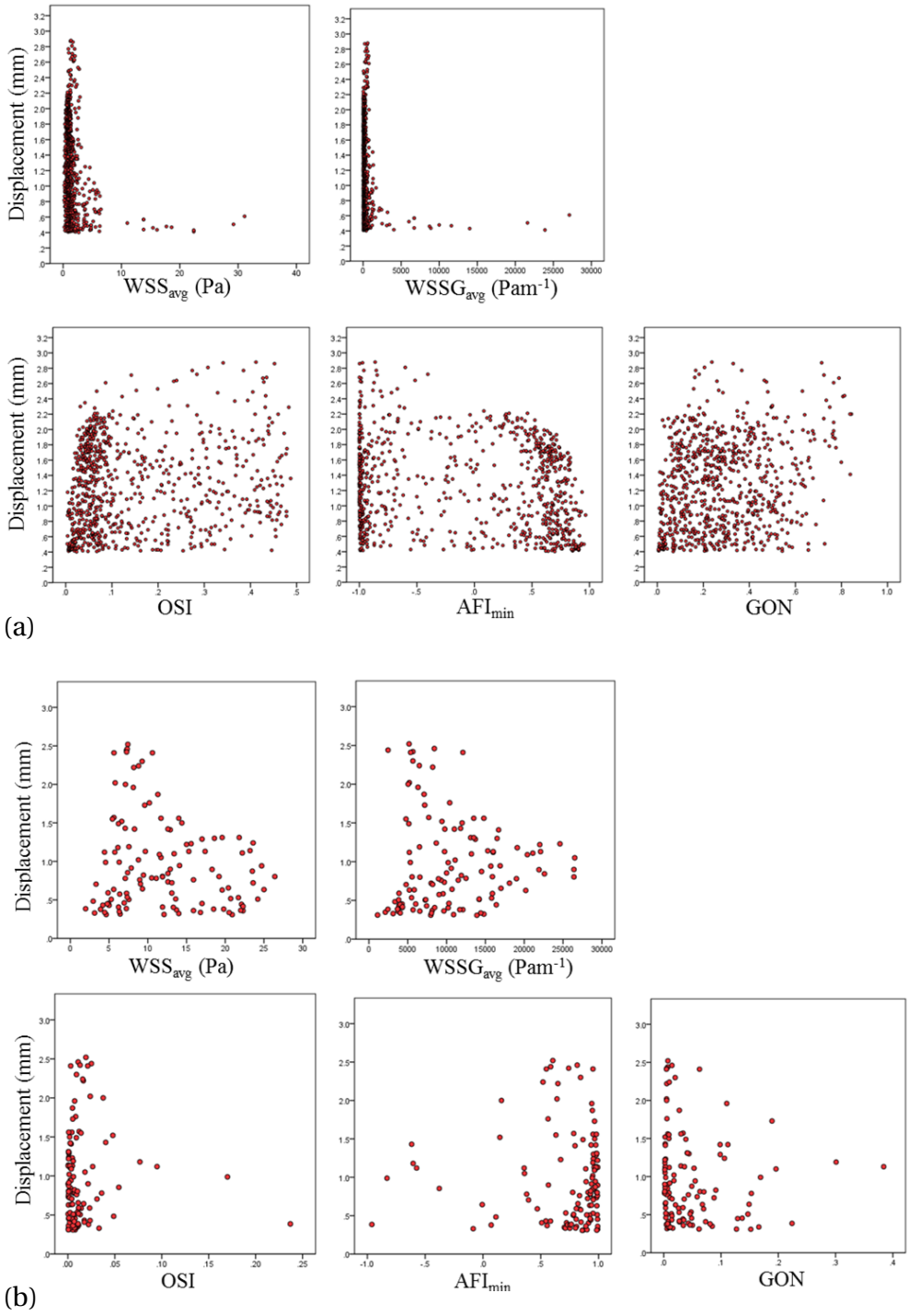


Figure 3.16: Scatterplots of the ICA (a) and BT (b) raw DI and haemodynamic index data

data is shown for both cases in Table 3.2(a). Table 3.2 shows that the significance

Table 3.2: Kolmogorov-Smirnov normality tests for raw (a) and transformed (b) ICA and BT DI and WSS data

Kolmogorov-Smirnov	Significance	
Index	ICA	BT
Displacement	0.000	0.000
WSS (avg)	0.000	0.000
OSI	0.000	0.036
WSSG (avg)	0.000	0.000
minAFI	0.000	0.000
GON	0.000	0.000

(a)

Kolmogorov-Smirnov	Significance	
Index	ICA	BT
log WSS	0.000	0.200
WSS^{-1}	0.000	0.000
$Displacement^{-1}$	0.000	0.036
log(Displacement)	0.000	0.063
$\sqrt{WSS}$	0.000	0.003
$\sqrt{Displacement}$	0.000	0.021

(b)

value for all indices is 0.000 (with exception of the OSI in the BT case, where the significance value is 0.036), and hence confirms that both ICA and BT data are non-normally distributed. Therefore, to examine if a correlation exists between any of the haemodynamic indices and the DI, the Spearman's correlation coefficient, ρ, is more appropriate.

Table 3.3 shows the Spearman's correlation examined across all indices, for the ICA and BT cases. The first column of Table 3.3 (highlighted in red) shows that a statistically weak, positive correlation exists between the DI, and the OSI and GON, while statistically significant, weak *inverse* correlations exist between the DI and WSS_{avg}, $WSSG_{avg}$ and AFI(min). In contrast, for the BT case the only statistically significant correlation is a weak, *inverse* correlation between the DI and GON, Particularly with respect to AFI(min), this is in stark contrast to the conclusion that might be made based on visual inspection: in §3.1, based on observation of the contour maps, it appears that a strong inverse correlation between AFI(min) and the DI exists. For the BT case, the only statistically significant correlation is a weak, inverse correlation between the DI and GON, while no correlation exists between the DI and any other indices.

As discussed at the beginning of §3.2, transformations of raw data are commonly performed when the raw data is deemed inappropriate for analysis. In the previous section, the results showed that all raw data are non-normally distributed, and, when plotted against the DI and the ASR, are non-linear. For this reason, several transformations of data were performed, focusing on the relationship between WSS and the two growth indices so as to allow comparison with the findings of Boussel et al. (2008). As per their study, the inverse of the WSS was performed, and plotted

Table 3.3: Spearman's Rank bivariate correlation for raw ICA and BT DI and haemodynamic index data

Correlations			Displacement ICA	Displacement BT
Spearman's rho	Displacement	Correlation Coefficient	1.000	1.000
		Sig. (2-tailed)	.	.
		N	784	118
	WSSavg	Correlation Coefficient	-.247**	-.045
		Sig. (2-tailed)	.000	.632
		N	784	118
	WSSGavg	Correlation Coefficient	-.229**	.174
		Sig. (2-tailed)	.000	.059
		N	784	118
	OSI	Correlation Coefficient	.184**	.039
		Sig. (2-tailed)	.000	.677
		N	784	118
	AFImin	Correlation Coefficient	-.210**	.060
		Sig. (2-tailed)	.000	.519
		N	784	118
	GON	Correlation Coefficient	.194**	-.195*
		Sig. (2-tailed)	.000	.034
		N	784	118

**. Correlation is significant at the 0.01 level (2-tailed).

*. Correlation is significant at the 0.05 level (2-tailed).

against the growth indices. Additionally, five other common data transformations were performed, detailed in Table 3.4.

Table 3.4: Table of transformations applied to raw growth index and WSS data

Method	Transformation	Regression equation	Predicted value , $\hat{y}$
Standard Linear Regression	None	$y = b_0 + b_1 x$	$\hat{y} = b_0 + b_1 x$
Exponential	$log_{10}(y)$	$log_{10}(y) = b_0 + b_1 x$	$\hat{y} = 10^{b_0 + b_1 x}$
Quadratic	$\sqrt{y}$	$\sqrt{y} = b_0 + b_1 x$	$\hat{y} = (b_0 + b_1 x)^2$
Reciprocal	$1/y$	$1/y = b_0 + b_1 x$	$\hat{y} = 1/b_0 + b_1 x$
Log	$log_{10}(x)$	$y = b_0 + b_1 log_{10}(x)$	$\hat{y} = b_0 + b_1 log_{10}(x)$
Power	$log_{10}(y)$ $log_{10}(x)$	$log_{10}(y) = b_0 + b_1 log_{10}(x)$	$\hat{y} = b_0 + b_1 x$

The K-S normality tests (Table 3.2(b)) on the six chosen data transformations were examined again for both cases. It can be seen from the K-S test that for the ICA case, the applied transformations were unsuccessful in bringing the distribution of data closer to normal. In contrast, for the BT case, it can be seen that the log(DI) and log(WSS) transformations have a K-S significance value greater than 0.05, which suggests that the distribution of the transformed DI and WSS data is now normal.

However, this improvement did not correspond to an improvement in the strength of correlation between the indices ($\rho = -0.045$).

As per the study by Boussel et al. (2008), the LOWESS curve and simple linear fittings are shown for the plot of inverse WSS against the DI for the ICA case (Figure 3.17(a)) and the BT case (Figure 3.18(a)). However, in contrast to the findings of Boussel et al. (2008), the LOWESS curve for both the ICA and BT cases follows a significantly different trajectory to the linear fit, which signifies that a linear fitting is not appropriate. This is further confirmed by the very low R^2 values (0.009 and 0.002 for the ICA and BT cases respectively). Several non-linear models were ap-

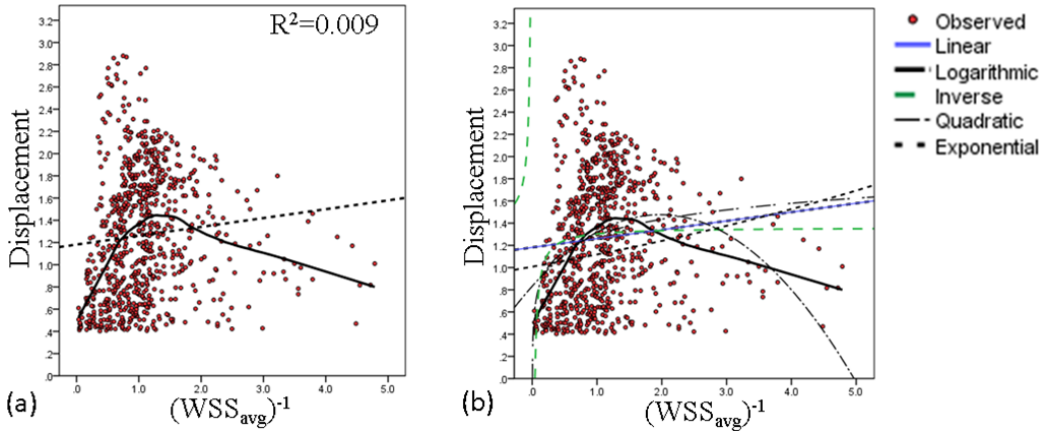


Figure 3.17: Linear, LOWESS (a), and non-linear fittings (b) to the ICA DI vs WSS^{-1} data

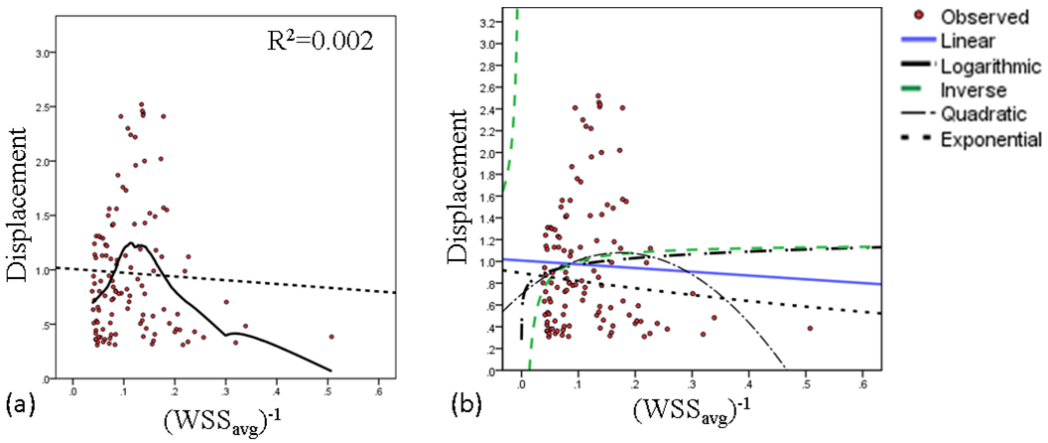


Figure 3.18: Linear, LOWESS (a), and non-linear fittings (b) to the BT DI vs WSS^{-1} data

plied: logarithmic, inverse, quadratic and exponential. These were compared to the

linear fitting (Figure 3.17(b), Figure 3.18(b)). However, in both cases, the R^2 value for all models was much lower than 0.1 (see Table 3.5 and Table 3.6).

Table 3.5: Linear, logarithmic, inverse, quadratic and exponential model summaries for ICA DI vs. WSS^{-1} data

Dependent Variable: Displacement

	Model Summary					Parameter Estimates		
Equation	R Square	F	df1	df2	Sig.	Constant	b1	b2
Linear	.009	7.155	1	782	.008	1.182	.080	
Logarithmic	.063	52.812	1	782	.000	1.293	.207	
Inverse	.064	53.671	1	782	.000	1.362	-.058	
Quadratic	.086	36.597	2	781	.000	.832	.652	-.165
Exponential	.020	16.161	1	782	.000	1.008	.104	

The independent variable is invWSS.

Table 3.6: Linear, logarithmic, inverse, quadratic and exponential model summaries for BT DI vs. WSS^{-1} data

Dependent Variable: Displacement

	Model Summary					Parameter Estimates		
Equation	R Square	F	df1	df2	Sig.	Constant	b1	b2
Linear	.002	.210	1	116	.648	1.008	-.344	
Logarithmic	.007	.802	1	116	.372	1.170	.086	
Inverse	.029	3.492	1	116	.064	1.160	-.016	
Quadratic	.059	3.623	2	115	.030	.698	4.380	-12.587
Exponential	.011	1.246	1	116	.267	.893	-.848	

The independent variable is invWSS.

Even when regression analysis was applied to the successfully transformed BT data (log(DI) and log(WSS), corresponding to a power transformation when compared against each other), simple linear regression yields a R^2 value of only 0.0004. Overall, the results of this study on two patient-specific cases do not support the findings ofBoussel et al. (2008).

3.2.2 The relationship between haemodynamics and the ASR

The same statistical analyses were applied to examine the relationship between haemodynamic indices and the ASR. Figure 3.19 below shows the raw data scatter plots, while Table 3.7 shows the K-S tests for the ICA and BT cases. While the same haemodynamic data was used for both the DI and ASR methods, the number of included cases is different. In the case of the DI, only data corresponding to DI $> +0.4mm$ were considered, while in the ASR case, data corresponding to

ASR>+1 were examined. As such, $N_{\mathrm{ICA_{ASR}}} = 658$, compared with $N_{\mathrm{ICA_{DI}}} = 748$, and $N_{\mathrm{BT_{ASR}}} = 218$, compared with $N_{\mathrm{BT_{DI}}} = 118$. Hence, we can expect that the distributions of the data will be different depending on the growth index.

Table 3.7: Kolmogorov-Smirnov normality tests for raw (a) and transformed (b) ICA and BT ASR and WSS data

Kolmogorov-Smirnov	Significance	
Index	ICA	BT
ASR	0.000	0.000
WSS (avg)	0.000	0.000
WSSG (avg)	0.000	0.000
OSI	0.000	0.000
minAFI	0.000	0.000
GON	0.000	0.000

(a)

Kolmogorov-Smirnov	Significance	
Index	ICA	BT
$\log \mathrm{WSS}$	0.001	0.004
WSS^{-1}	0.000	0.000
ASR^{-1}	0.000	0.000
$\log(\mathrm{ASR})$	0.000	0.000
$\sqrt{\mathrm{WSS}}$	0.000	0.000
$\sqrt{\mathrm{ASR}}$	0.000	0.000

(b)

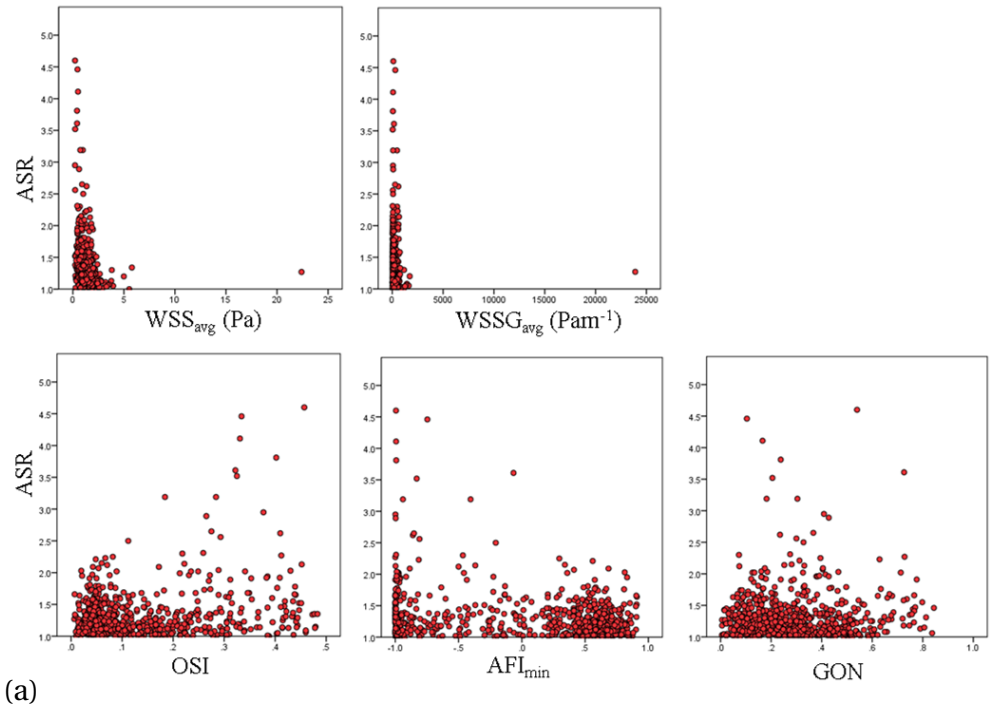
As with the DI, the raw data are non-normally distributed, and the relationships between the haemodynamic indices of interest and the ASR are non-linear. Again, Spearman's Rank Correlation was applied (see Table 3.8). For the ICA case, the correlation table once again shows that of all indices, $\mathrm{WSS_{avg}}$ has the strongest correlation with the ASR, although it is in fact a statistically weak, inverse correlation ($\rho = -0.23$), suggesting that the ASR is high when WSS is low. Of the indices for

Table 3.8: Spearman's Rank bivariate correlation for raw ICA and BT ASR and haemodynamic index data

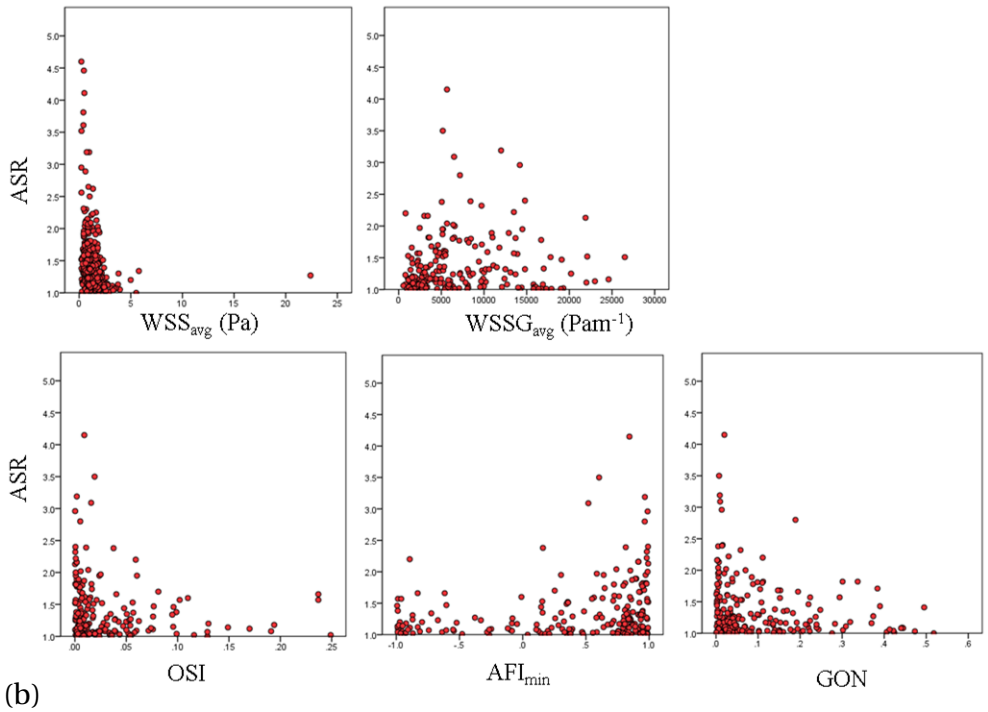
Correlations			ASR	
			ICA	BT
Spearman's rho	ASR	Correlation Coefficient	1.000	1.000
		Sig. (2-tailed)	.	.
		N	658	218
	WSSavg	Correlation Coefficient	-.230**	.229**
		Sig. (2-tailed)	.000	.001
		N	658	218
	WSSGavg	Correlation Coefficient	-.091*	.194**
		Sig. (2-tailed)	.020	.004
		N	658	218
	OSI	Correlation Coefficient	.072	-.130
		Sig. (2-tailed)	.064	.056
		N	658	218
	AFImin	Correlation Coefficient	-.103**	.190**
		Sig. (2-tailed)	.008	.005
		N	658	218
	GON	Correlation Coefficient	-.031	-.192**
		Sig. (2-tailed)	.423	.005
		N	658	218

**. Correlation is significant at the 0.01 level (2-tailed).

*. Correlation is significant at the 0.05 level (2-tailed).



(a)



(b)

Figure 3.19: Scatter plots of the ICA (a) and BT (b) raw ASR and haemodynamic index data

which the correlation is statistically significant, AFI(min) is weakly, inversely correlated ($\rho = -0.103$), while $WSSG_{avg}$ is not correlated with ASR ($\rho = -0.91$). The ρ values for the remaining indices (OSI and GON) are both low and statistically insignificant.

Interestingly, and in contrast to the ICA case, the BT results show that while WSS_{avg} is again the most strongly correlated index, the correlation is positive -i.e. ASR is high when WSS is high. WSSG, AFI(min) and GON all show statistically significant, but weak correlations with the ASR ($\rho = 0.194$, 0.19 and -0.192 respectively). Again, compared with the ICA case, the correlation between AFI(min) and the ASR is positively correlated, while GON is inversely correlated. This indicates that in this case, a high ASR is at least weakly associated with a high AFI, and a low GON. The K-S normality test for the transformed ICA and BT data are shown in Table 3.7(b). In both cases, the transformation of data has not shifted the distributions closer to normal. While there is no improvement in the linearity of the BT data (see Figure 3.20 and Table 3.10), there is a slight improvement in linearity of the *inverse* WSS data for the ICA case, with $R^2 = 0.146$ compared with $R^2 = 0.027$ for the raw WSS data. While the trajectory of the LOWESS curve is still not in line with the linear fitting (see Figure 3.20(a)), the deviation from the linear fitting is less pronounced compared to the WSS^{-1}/DI plot. As with the DI, several models were applied to the WSS^{-1}/ASR plot (Figure 3.20(b)), and it can be seen from the model summary table (Table 3.9) that in fact the best fit is a quadratic model, with $R^2 = 0.155$. This value suggests that 15.5% of variation in the ASR is accounted for by variation of WSS^{-1}, according to the model equation below:

$$\mathrm{ASR} = 1.182 + (\mathrm{WSS}^{-1} + 0.086)(\mathrm{WSS}^{-1} + 0.044)$$

While this value is still small, it is a significant improvement on the models applied to the ICA WSS^{-1}/DI plots, and both the BT WSS^{-1}/DI and WSS^{-1}/ASR plots, where all models applied have an R^2 value of less than 0.1, and in some cases, less than 0.01.

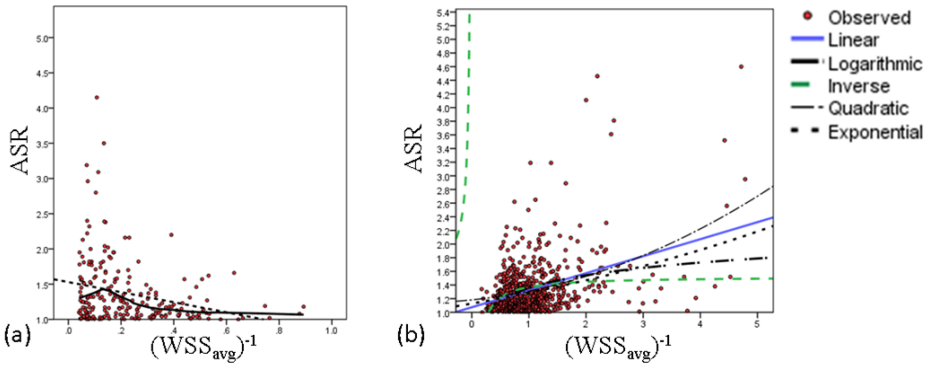


Figure 3.20: Linear, LOWESS (a), and other fittings (b) to the ICA ASR vs WSS^{-1} data

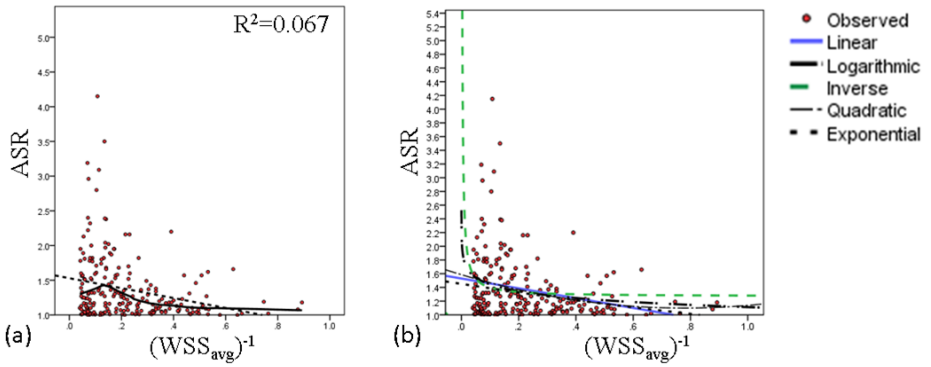


Figure 3.21: Linear, LOWESS (a), and other fittings (b) to the BT ASR vs WSS^{-1} data

Table 3.9: Linear, logarithmic, inverse, quadratic and exponential model summaries for ICA ASR vs. WSS^{-1} data

Model Summary and Parameter Estimates

Dependent Variable: ASR

Equation	Model Summary					Parameter Estimates		
	R Square	F	df1	df2	Sig.	Constant	b1	b2
Linear	.146	112.133	1	655	.000	1.074	.250	
Logarithmic	.105	76.490	1	655	.000	1.356	.269	
Inverse	.056	38.829	1	655	.000	1.523	-.154	
Quadratic	.155	60.030	2	654	.000	1.182	.086	.044
Exponential	.127	95.566	1	655	.000	1.128	.132	

The independent variable is invWSS.

Table 3.10: Linear, logarithmic, inverse, quadratic and exponential model summaries for BT ASR vs. WSS^{-1} data

Model Summary and Parameter Estimates

Dependent Variable: ASR

Equation	Model Summary					Parameter Estimates		
	R Square	F	df1	df2	Sig.	Constant	b1	b2
Linear	.067	15.547	1	216	.000	1.529	-.715	
Logarithmic	.057	13.012	1	216	.000	1.113	-.144	
Inverse	.027	6.020	1	216	.015	1.267	.013	
Quadratic	.072	8.326	2	215	.000	1.585	-1.248	.801
Exponential	.077	17.961	1	216	.000	1.451	-.447	

The independent variable is invWSS.

3.3 Comparison of visually- and statistically-examined correlations: Discussion

In this chapter, correlations between haemodynamic and growth indices were assessed both visually and statistically. Thresholds of haemodyanmic indices were applied for visual assessment; in contrast, selection of data for statistical analysis was based only on the magnitude of the growth indices. As such, the statistical assessment seeks to identify the general trend of data.

From visual assessment, it appears that the haemodynamic indices that correlate best with aneurysm growth (as defined by the DI) for the ICA case are the OSI and AFI(min), both of which aim to capture the change in direction of the instantaneous WSS vector from its time-averaged value. In particular, it appears from the results that the largest growth occurs in the region of maximum deviation (i.e. AFI(min)=-1; OSI=0.5). Where growth is defined by the ASR, the indices that appear most clearly correlated with growth of the ICA are low WSS, the OSI and AFI(min), although this seems to be the case only in the anterior part of the ICA dome. For the BT case, the indices best correlated with the region of highest growth (as defined by both the DI and the ASR) are high WSS and high WSSG, although it can be seen that these indices are also high in regions where growth is low.

Hence, visual assessment of the ICA case suggests that large deviations of the instantaneous WSS vector may be a driver for aneurysm growth. There also appears to be a clear positive correlation (in the case of the ASR), and a possible correlation (in the case of the DI) between regions of low WSS and regions of aneurysm growth.

In the case of the GON, the existence of many localised patches of the aneurysm dome where the GON is high make it difficult to determine if a positive correlation between a high GON and aneurysm growth really exists. Interestingly, a local maximum GON was observed at the region corresponding to the largest DI. This suggests that while the GON alone may not be a reliable indicator of regions of likely growth, it may be a useful indicator in identifying the regions where the largest amount of growth will occur. In fact, in the BT case, this was observed for WSS and WSSG indices for both the DI and ASR -i.e. high DI and ASR was observed to coincide with high WSS and high WSSG, although in other regions where the haemodynamic indices are high, the growth indices were found to be low. Therefore, while it is impossible to say with certainty that high WSS and high WSSG are correlated with regions of aneurysm growth on the BT case, it is noted that these indices are high in the region susceptible to aneurysm formation, and may act together with other factors to fuel destructive remodelling.

The results show a clear distinction between the haemodynamic indices of importance between the ICA and BT cases. While growth of the ICA appears to be correlated with AFI(min) and high OSI (which are often associated with low flow), growth of the BT case appears to be correlated with high WSS and high WSSG. As discussed in §1.4.2, it is likely that features of geometry are the reason for this difference. The basilar terminus, and particularly the region of the apex, is generally exposed to higher WSS and WSSG than the ICA. Figure 3.22 shows the flow patterns of the ICA and BT t_1 geometries. It can be seen that the intra-aneurysmal flow of the ICA is slow and highly complex, with one large vortex. In contrast, the flow at the BT is much faster and near-laminar through the centre of the basilar artery, but more complex at the arterial junctions.

The ICA and BT t_1 geometries represent different stages of aneurysm development: the former represents an already-developed, and still-growing aneurysm, while the latter represents a pre-aneurysmal state. As such, comparison of haemodynamic patterns between the two is in fact a comparison between intra-aneurysmal, and pre-aneurysmal flow conditions, which appear to be in line with observations of haemodynamic patterns discussed in §1.4. In §1.4.4, several CFD studies utilising a series of follow-up images of growing aneurysms (Tateshima et al. (2007); Shojima et al. (2004); Jou et al. (2005); Boussel et al. (2008)) reported the evolution of a low WSS haemodynamic environment following aneurysm growth, while

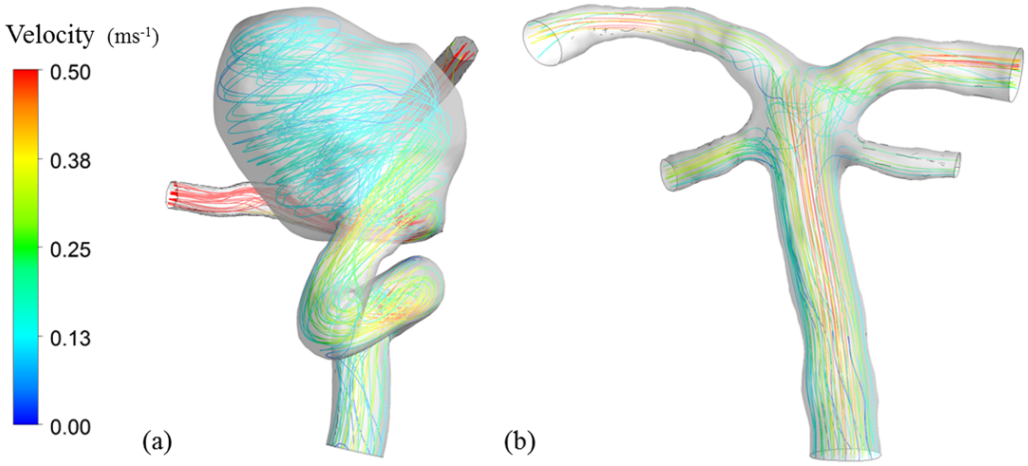


Figure 3.22: Pulsatile-flow blood-flow patterns for the t_1 ICA and BT geometries at an arbitrary time-point during the cardiac cycle

in §1.4.3 the majority of studies described high WSS/high WSSG conditions at pre-aneurysmal bifurcations. The figures showing the distributions of haemodynamic indices for the BT t_2 geometry indeed show a low WSS in the aneurysm dome, and a high WSS and high WSSG at the distal aneurysm neck. As such, from observation of contour maps of haemodynamic indices between the two cases, the results of this study seem to support the notion that a high WSS/high WSSG environment may be an instigator of aneurysm formation, while a low-flow environment, of which low AFI and high OSI are features, may account for subsequent growth.

Comparison of the DI and ASR distributions on the BT case shows that regions of high DI and ASR are similar in size and location, while for the ICA case, regions of high ASR were observed to be smaller and more localised, although roughly in the same location as regions of maximum DI. However, due to the lack of knowledge of the real direction of aneurysm growth, and whether growth occurs predominantly from within the aneurysm neck or dome, it is unclear which of the two indices more accurately capture growth. Finally, while correlations between some haemodynamic indices and growth indices were observed, the real strength and nature of these correlations cannot be accurately deduced by visual inspection. It must also be noted here that visual determination of correlations may be further mired by the lack of clearly defined threshold values beyond and beneath which the various haemodynamic indices can be considered to be elevated and reduced, respectively. For instance, in order to determine if WSSG is above the proposed threshold value

of 3000Pa/m, the colour-maps corresponding to the distribution of WSSG both the ICA and BT cases were clipped to between 0-5000Pa/m. While WSSG is very low throughout the dome of the ICA aneurysm, this reduction in the range of values can be seen to result in a mottled effect on the BT surface. This is because globally, WSSG is in fact higher than 5000Pa/m (the global maximum is approx 30000Pa/m for the t_1 BT geometry). Hence, this calls into question the appropriateness of the proposed upper physiological threshold value.

The statistical analysis of correlations shows that in this study, correlations between the investigated pulsatile-flow indices and the two indices of growth are generally very low. WSS is the most consistently (albeit weakly) correlated index, and in the case of the ICA, the correlations between WSS and DI and WSS and ASR are similar in magnitude, and have the same direction. In contrast, for the BT case the correlation differs between the DI and ASR -i.e. WSS was not at all correlated with the DI, and positively correlated with ASR. Additionally, the comparisons of WSS^{-1} with the growth indices for both cases showed that only the results of the BT WSS^{-1}/ASR comparison show a relationship between WSS^{-1} and the ASR similar to that found by Boussel et al. (2008). However, the growth indices are different (Boussel et al. (2008) utilised normal displacement, like the DI), and hence these results do not directly support their findings. Given that the correlation and regression analyses do not indicate a strong relationship between any haemodynamic indices and the growth indices, it is difficult to judge from the results of this study which of the two -the DI or the ASR -is a better indicator of growth.

In addition to examining the existence of correlations between haemodynamic and growth indices, the correlation tables are useful in examining the relationships between the haemodynamic indices themselves. Although the number of included cases differs between the DI and ASR for each aneurysm, the correlations between haemodynamic indices follow the same trend. It can be seen from Table 3.11(a)(i) and (ii) that for both the ICA and BT cases, the correlation between the average magnitude of WSS and WSSG, OSI and AFI(min) is moderately strong (0.521,-0.510 and 0.435 respectively for the ICA case, and 0.521, -0.601 and 0.514 respectively for the BT case, from table Table 3.11(b)(i) and (ii)). This suggests that a high WSS is correlated with high WSSG, with low OSI and with high AFI. Interestingly, if growth is indeed a continuation of the events that occur at inception, these results could be interpreted as lending support to both high- *and* low-flow theories of growth: i.e.

high WSS is associated with high WSSG, while low WSS is associated with both a high OSI and low AFI. As was discussed in §1.4, both are conditions which have been proposed as instigators of aneurysm formation, and as drivers of growth.

Table 3.11: Correlations between haemodynamic indices for both the ICA and BT cases

ICA: DI

			WSSGavg	OSI	AFImin	GON
Spearman's rho	Displacement	Correlation Coefficient	-.229**	.184**	-.210**	.194**
		Sig. (2-tailed)	.000	.000	.000	.000
		N	784	784	784	784
	WSSavg	Correlation Coefficient	.521**	-.510**	.435**	-.165**
		Sig. (2-tailed)	.000	.000	.000	.000
		N	784	784	784	784

(a)(i)

ICA: ASR

			WSSGavg	OSI	AFImin	GON
Spearman's rho	ASR	Correlation Coefficient	.194**	-.130*	.190**	-.192**
		Sig. (2-tailed)	.004	.056	.005	.005
		N	218	218	218	218
	WSSavg	Correlation Coefficient	.805**	-.716**	.751**	-.302**
		Sig. (2-tailed)	.000	.000	.000	.000
		N	218	218	218	218

(ii)

BT: DI

			WSSGavg	OSI	AFImin	GON
Spearman's rho	Displacement	Correlation Coefficient	.174	.039	.060	-.195*
		Sig. (2-tailed)	.059	.677	.519	.034
		N	118	118	118	118
	WSSavg	Correlation Coefficient	.521**	-.601**	.514**	-.008
		Sig. (2-tailed)	.000	.000	.000	.933
		N	118	118	118	118

(b)(i)

BT: ASR

			WSSGavg	OSI	AFImin	GON
Spearman's rho	ASR	Correlation Coefficient	-.091*	.072	-.103**	-.031
		Sig. (2-tailed)	.020	.064	.008	.423
		N	658	658	658	658
	WSSavg	Correlation Coefficient	.491**	-.313**	.240**	-.011
		Sig. (2-tailed)	.000	.000	.000	.787
		N	658	658	658	658

(ii)

However, it must be noted that the interpretation of the statistical results is affected by the choice of statistical test, assumptions in the definitions of the growth indices, and assumptions relating to performing CFD on geometries obtained from images of vasculature. For example, while the assumption of the existence of a monotonic trend between two sets of data makes the Spearman's correlation less restrictive than Pearson's correlation, it is not always clear whether the data satisfy this assumption. An example of this can be seen in the raw data scatter plots of the ASR against the GON (Figure 3.19), where it is difficult to discern if there is indeed a monotonic trend between the two.

With regard to the definition of the growth indices, both the DI and ASR are affected by the assumption that growth is outwardly directed along the surface normals; in fact, there is currently no knowledge of the trajectory of the aneurysmal surface as it grows. It is also unclear whether growth is driven predominantly from the aneurysmal neck, in which case the DI is the more obvious choice of growth index, or if the dome itself continues to grow, in which case the ASR may be more appropriate. Additionally, and as discussed by Sforza et al. (2012), the regions and direction of growth may be heavily influenced by the presence of surrounding structures, such as bones, which introduces further complexity to the task of determining regions of growth based on a series of images.

Both indices are affected by the assumption that the surface meshes of the geometries adequately represent the real aneurysmal geometries. This, in turn, is affected by both the choice and accuracy of segmentation methods, and any operations on the surfaces, such as smoothing. The original ICA and BT surface meshes (both supplied by Doenitz and colleagues) are coarse (e.g. 5294 and 6082 elements for the t_1 and t_2 ICA geometries respectively), which is likely to affect both the DI and ASR values, as both are dependent on the direction of the normal of each triangle of the mesh.

Furthermore, it must be noted that this method of quantifying growth is reliant on the t_1 geometry having a broadly *convex* shape, with no sharp undulations. For regions of sharp undulation, the sum of surface areas, $\sum A_{\triangle_{\mathbf{int_{p_i}}}}$, may be *smaller* than $\sum A_{\triangle_{\mathbf{p_i}}}$, giving ASR < 1. If the undulation is very high (e.g. a crevice), the projected normals, $\mathbf{n_{E_i}}$, may cross paths and intersect the t_2 geometry at points spaced very far apart, resulting in an unrealistically large sum of surface areas, $\sum A_{\triangle_{\mathbf{int_{p_i}}}}$, and in turn, an unrealistically large ASR. The level of undulation of the t_1 surface in the region of aneurysm growth may be more or less exaggerated by the coarseness of the mesh. For example, a coarse mesh may either flatten sharp bends, or may result in exaggerated ASR and DI values at points where the geometry bends, as each point would be surrounded by fewer triangles with larger angular displacements.

Inherent assumptions of performing CFD on geometries extracted from scanning images may also introduce errors. Firstly, the already coarse, and smoothed geometries are meshed again in ANSYS ICEM CFD (ANSYS Inc, Canonsburg, PA) in preparation for CFD simulations. The coarseness of the original surface meshes may significantly affect the distribution and magnitudes of haemodynamic indices. Furthermore, as Singh et al. (2010) point out, although studies may use very high quality images to reconstruct arteries for CFD simulations, these images are representative of vessel volume filled by contrast agent. Hence, if the filling of the vessel is incomplete, errors in surface prediction may arise. Tateshima et al. (2007) emphasise that "even the small geometric inaccuracy produced by limited image resolution may affect the results of haemodynamic simulations based on clinical images". Considerable inter-individual variability of patient-specific data has also been shown, which results in different haemodynamic profiles (Nixon et al., 2010); hence, the findings of studies where a single, or low number of cases is examined must be treated with particular caution. Lastly, although commonly applied as-

sumptions in CFD models (discussed in §2.4) allow for reasonable computational time, they may skew the results of CFD studies.

In fact, while the studies discussed in the previous sections provide much-needed insight into the effect of haemodynamics on both the *micro-* and *macro-*scale events within the arterial wall during aneurysm development, interpretations of their findings must be pursued with some caution. While animal models provide the best *in-vivo* setting for investigating aneurysm formation and growth, the methods of aneurysm induction are imposed by the investigator -e.g. elastase injections, hypertensive diet, arterial ligation, and surgical manipulation. Furthermore, while the patterns of initiation and growth of anuerysms induced in animal models may be very similar to that observed in humans, differences in scale, anatomic organisation and genetics may significantly influence the results. *In-vitro* experiments are even more controlled, with much of the insight regarding, for example, the behaviour of ECs, gleaned from fluid-chamber experiments on a single monolayer of cells. Such experiments are certainly useful in demonstrating the response of individual groups of cells to flow, but may not capture the response that occurs due to inter-cellular interactions (e.g. interactions between ECs, vSMCs and fibroblasts).

Finally, the results of this study show that visually- and statistically-determined correlations between haemodynamic and growth indices may be vastly different. Firstly, positive correlations are generally difficult to determine definitively. While it appeared that a correlation between both growth indices and a high OSI and low AFI exists from visual inspection of the ICA case, statistical analysis revealed that the correlations do exist, but they are very weak; in fact, the correlation table (Table 3.8) showed that *no* correlation exists between the ASR and OSI for the ICA case. This could be attributed to the fact that there are few nodes on the ICA and BT surfaces at which the growth index was found to be high, which suggests that the growth indices may not be adequately capturing growth. This is certainly possible in the case of the ASR, which is generally high in much more localised regions compared to the DI, and especially so in the ICA case. However, visually comparing regions of high DI and regions that appear to have grown shows that these regions appear to line up well. Hence, it is possible that the DI may be a better means of quantifying growth than the ASR, but since both methods make simple assumptions about the direction of growth (i.e. along a normal to the t_1 surface), and since there is no knowledge of the actual direction of growth, it is difficult to determine if this is indeed the case.

The stark difference between visually- and statistically-determined correlations suggests that great care must be taken when interpreting the results of CFD studies, in which correlations between regions of growth and haemodynamic indices are commonly deduced by visual inspection. Interestingly, even when more rigorous analysis is applied, as in the case of Boussel et al. (2008), it appears that the meaning of statistical findings are somewhat exaggerated. For example, it is interesting that Boussel et al. (2008) so definitively conclude that growth occurs in regions of low WSS, as, across seven examined cases, they report a R^2 range of between only 0.18 and 0.3 for a linear regression analysis of displacement and WSS^{-1}. This means that across the cases, 18-30% of the variation in displacement can be accounted for by their linear regression model, while 70-82% of the variation is unexplained by the model. This suggests that either a linear fitting is not the best descriptor of the relationship between WSS^{-1} and displacement (i.e. up to 82% of the variance of the displacement is explained by an *error* in the fitting), or that up to 82% of variance is explained by one or more other variables, which have not been accounted for in the model, or both. This constitutes a problem in the field of CFD-based research on aneurysm development, as the conclusions drawn from studies such as that of Boussel et al. (2008) are propagated in the research of others: a search on Google Scholar revealed that so far, the paper by Boussel et al. (2008) has been cited 102 times in the literature. Given the conflicting theories on haemodynamic instigators of aneurysm growth that have been reported in CFD studies, it is unsurprising to find editorials, such as that by David Kallmes of the Mayo Institute in the American Journal of Neuroradiology (Kallmes, 2012), which express the view that CFD studies are in effect becoming a means of "Confounding Factor Dissemination".

This, along with the lack of knowledge of the real trajectory of a growing aneurysmal surface, and the assumptions inherent in growth quantification, statistical and CFD methods, suggests that a re-examination of the role of CFD studies in understanding aneurysm development is needed. Assuming negligible effects of CFD assumptions, the distributions of pulsatile-flow haemodynamic indices, as well as intra-aneurysmal flow properties (such as flow trajectory and velocity) can be reliably determined from CFD. For this reason, it seems that in the context of aneurysm research, CFD on static geometries may be more useful as a tool to assist determination of the appropriate intervention methods in the clinic -e.g. flow-diverters, where the best structural arrangement of the struts to achieve flow characteristics that favour clot formation could be assessed. In contrast, the results of this study

and the generally conflicting theories in the literature suggest that CFD performed on static geometries may not be useful in shedding light on the role of haemodynamics in aneurysm growth. Given that growth is a process of tissue change, it seems logical that coupling CFD to a *model* of aneurysm growth may shed more light on the mechanisms of aneurysm growth and the links between haemodynamics and this process.

The approaches to modelling cerebral aneurysms have varied greatly over the course of years and between different research groups. The remaining chapters of this thesis will examine these in detail, as well as the modelling approaches utilised in this research. In particular, the effect of coupling a model of aneurysm development to the real, physiological haemodynamic environment. The following chapter is dedicated to a review of the general principles of modelling the arterial wall, the approaches to creating a *Fluid-Solid-Growth* (FSG) model of aneurysm evolution, and the FSG framework used in this research.



CHAPTER 4

MODELS OF CEREBRAL ANEURYSM EVOLUTION: A REVIEW

A model that not only provides understanding of the aetiology of the disease, but is also useful in the clinical setting as a tool for the prediction of aneurysm behaviour and the assignment of an appropriate treatment requires:

- A model of the healthy artery, which takes into account the contribution to physiological and structural function of the individual constituents of the arterial wall,
- An understanding of mechanobiology, to allow the formation of hypotheses for the growth and remodelling of individual constituents that takes place during aneurysm development, and
- A computational framework, which will
    1. Account accurately for the haemodynamics and the structural mechanics of the artery
    2. Couple fluid and solid mechanics
    3. Capture the growth and remodelling of arterial constituents
    4. Provide a link between haemodynamics and growth and remodelling (G&R) of arterial wall constituents.

This section reviews the work done in the research community towards meeting these requirements. A general computational framework is introduced, which forms the basis for many recent computational models of aneurysm evolution; finally, the section culminates with a review of the modelling technique used in the present research. The model that forms the basis for the remaining chapters of this thesis is the (still evolving) work of Watton and colleagues over the last decade (Watton (2002); Watton et al. (2004); Watton and Ventikos (2009); Watton et al. (2009b,c, 2011, 2013)). This chapter is intended as a summary of the evolution of modelling techniques, which in turn also provides justification for the current modelling approach. It is also intended as an introduction into the key equations of the current model, which are manipulated as part of this research.

4.1 MODELLING THE HEALTHY ARTERY

From the literature, a distinct evolution of models can be seen. These range from 2D models devised to capture the phenomenon of healthy arterial adaptation in response to a sustained change in the loading environment (such as increased flow, pressure and axial stretching), leading up to models that simulate aneurysm development within patient-specific geometries. However, it is clear that major developments in the past decade have a common foundation in the form of the work done by Humphrey, which was published in the 1999 paper on *Remodelling of a Collagenous Tissue at Fixed Lengths*. In this paper, a cell-mediated mechanism of growth and remodelling of collagen fibres in response to mechanical stimuli was proposed. This signified a shift from the purely phenomenological approach to quantification of soft tissue behaviour towards a structurally-motivated approach. In other words, it signified the shift from mathematical modelling of the consequences of G&R to modelling the process by which G&R occurs. Humphrey (1999) used a simple rule of mixtures (incorporating contributions of elastin, and original and newly-formed collagen fibres) and proposed a constitutive relation for the stress in a uniaxial tissue as it is stretched from its original, stress-free configuration to different lengths, at which it is maintained for an extended period of time. It was assumed that collagen fibres are continuously turned-over, and a first-order kinetic model was employed to govern the change in mass fraction. It was also hypothesised that, regardless of the current tissue configuration (i.e. regardless of the current length of the tissue), new collagen fibres are always deposited with the same *attachment* stretch, $\lambda_{AT}^{C} = 1$.

While the model is simplistic in that it is one-dimensional, the results are qualitatively realistic. For example, the results showed that tissue stretched and maintained at a length beyond its original, stress-free length for a time sufficient to allow the turn-over of collagen fibres is more compliant compared to its original state. When the stretched tissue is returned to its original length, the collagen fibres deposited in the extended configuration will now exhibit greater waviness. This means that, from its original configuration, the tissue must be stretched further (increased compliance) before the collagen fibres will straighten and bear load. This is a direct result of the hypothesis that collagen fibres are always deposited in the same state of stretch (λ^{C}_{AT}) regardless of tissue configuration, which has been pivotal in the subsequent work of the group, as well as the work of Holzapfel and colleagues (which will be discussed in this section), which forms the basis for the modelling methodology used in this research.

The work was extended in 2002 by Humphrey and Rajagopal, who proposed a generalised two-dimensional constrained-mixture model for stress in soft tissue. The model is based on the assumption that the major load-bearing constituents deform together (i.e. they form a constrained mixture), but that their respective rates of deposition and degradation may be different, and that each constituent may have a separately evolving natural reference configuration . It has since been specialised to consider the mechanical response of carotid arteries in response to increased flow, pressure and axial loading (Gleason and Humphrey (2004); Gleason et al. (2004); Gleason and Humphrey (2005)) and has later also been used by the group in modelling axisymmetric saccular and fusiform intracranial aneurysms (Baek et al., 2005). However, while the model developed by Gleason and colleagues provides a general framework for modelling the growth and remodelling of collagen fibres, it does not include a constitutive model of the artery.

Almost in parallel with Humphrey and Rajagopal (2002), and with the same aim of addressing the lack of structurally-motivated models, Holzapfel et al. (2000) proposed a new constitutive framework for the mechanics of a healthy arterial wall, in which it is modelled as a thick-walled, two-layered non-linearly elastic cylindrical tube. In this work, the passive mechanical response of the artery is considered to be due to the sum of the individual contributions of the isotropic elastinous, and anisotropic collagenous constituents. Given the highly non-linear stress-strain behaviour of arteries, Holzapfel and colleagues propose a strain energy function

(SEF) from which the stress-strain relationship for arterial tissue can be derived. The proposed SEF is a sum of the isotropic response of the elastinous constituents, and the anisotropic response of collagen fibres (see Figure 1.4 in §1.2). The media and adventitia (the two most relevant structural layers) are represented by two SEFs of the same form, where the distinction between them is captured by the employment of histologically-derived material parameters. It must be noted that, in contrast to Gleason and colleagues, while Holzapfel et al. (2000) developed a constitutive framework for the healthy arterial wall, they did not take into account growth and remodelling of arterial constituents. However, their proposed SEF formulation forms the basis for the aneurysm growth model used in the present research, and will be examined closer in §4.4.1.

4.2 EVOLUTION OF STRUCTURAL MODELS OF CEREBRAL ANEURYSMS

In 2004, Watton, Hill and Heil proposed the first structurally-motivated model for the growth of aortic abdominal aneurysms (AAAs). The artery was modelled as a two-layered cylindrical membrane (i.e. both the medial and adventitial layers were modelled) based on the physiologically realistic constitutive model proposed by Holzapfel et al. (2000). Watton and Ventikos (2009) discuss that at physiological pressures, the ratio of wall thickness to aneurysm diameter will decrease as the aneurysm enlarges, and thus the deformation of the three-dimensional arterial wall of the developing aneurysm is closely related to the deformation of its midplane. Additionally, the residual strain present in the unloaded arterial configuration gives rise to an approximately uniform strain field through the thickness of the arterial wall. Finally, they argue that if the attachment of collagen to the artery is independent of the current configuration of the artery, then the remodelling of collagen fibres may act to naturally maintain a uniform strain field throughout the thickness of the wall. Therefore, and especially given that the measured thickness of the aneurysmal wall has been observed to be in the range of 30-500μm, the use of a membrane approximation to describe the deformation of the arterial wall is considered reasonable, and is often used, as will become evident in this section.

While the model was devised in the context of AAAs, several important features are also pivotal to the cerebral aneurysm (CA) model used in the present research.

These are briefly introduced here, but will be examined more closely in §4.4.1. Firstly, the growth of the aneurysm is based on the concept of collagen growth and remodelling proposed by Humphrey (1999). However, the initiation of growth is modelled in this work in the form of a gradual elastin degradation prescribed to occur in a small circular region of the membrane. The SEF formulation proposed by Holzapfel et al. (2000) is modified in this case to incorporate microstructural variables associated with changes in collagen fibre density, fibre recruitment, and the elastin and collagen concentrations. Of particular distinction is the recruitment stretch variable, which defines the amount by which tissue must be stretched before collagen fibres will straighten and begin to bear load. The recruitment stretch provides a convenient way of capturing collagen remodelling resulting from the deposition and degradation of collagen fibres in altered tissue configurations. The model developed by Watton and colleagues predicted aneurysm dilations and stress distributions that are consistent with in vivo observations and previous studies.

Baek and colleagues (2005) appear to be the first to propose a structurally-motivated model for CA growth. Using the two-dimensional constrained-mixture approach described in the previous section and employing Humphrey's (1999) hypothesis for collagen growth and remodelling (with the attachment stretch $\lambda^{C}_{AT} > 1$), Baek et al. (2005) proposed a membrane model for the growth of an axisymmetric saccular CA and, in a subsequent paper in 2006, a model for the growth of an axisymmetric fusiform CA. In these models, aneurysm growth is considered to be the result of a change in the rate of collagen production by fibroblasts, where production is dependent on the number of fibroblasts and the change in stress from a homeostatic value experienced by these cells. In the latter paper, they also investigate the effect of orientation, or, attachment angle, of newly-deposited collagen fibres. In both cases, the model only takes into account the adventitial layer of the artery, and, in contrast to Watton et al. (2004) who propose gradual degradation of elastin in the media as an initiator for growth, in this work the total loss of the medial elastinous layer is used as a prescribed "insult" to initiate aneurysm growth. The major conclusions from their studies are that stabilisation is affected by the rate of thickening of the arterial wall (i.e. rapid thickening results in minimal enlargement of the aneurysm), but also the orientation of newly-produced collagen fibres.

In 2007, Kroon and Holzapfel also proposed a membrane growth model for an axisymmetric saccular aneurysm, but in contrast to Baek et al. (2005, 2006), colla-

gen production is specified as a function of strain, rather than stress, as the authors argue that the level of collagen production is related to the stretching or deformation of the fibroblasts with respect to their reference configuration. However, in this paper, Kroon and Holzapfel did not incorporate the concept of an evolving reference configuration for fibroblast cells, and, as such, the fibroblast cells continue to stretch as the tissue deforms. This was rectified in subsequent papers (see Kroon and Holzapfel (2008);Kroon and Holzapfel (2009)). Like Baek and colleagues, Kroon and Holzapfel assume a total loss of the medial elastinous layer, and thus the SEF used to capture the response of the artery is purely representative of the adventitia. Furthermore, it omits any elastinous contribution in the adventitia (i.e. load-bearing is done only by collagen fibres). One result of this instantaneous degradation of the elastinous layer is that the shift in load-bearing from the media to the adventitia is not smooth, and yields a maximum stress in the tissue at t = 0, which is unrealistic. However, the model predicted a berry-like shape and size often observed clinically, as well as wall thickness and the steady-state values of wall stress (in particular, a peak stress at the fundus, which is the major site of aneurysm rupture) that correlate well with in vitro mechanical tests. The same two-dimensional, axisymmetric model was extended to incorporate cyclic loading due to blood pressure pulsatility (Kroon and Holzapfel, 2009). Therefore, in this model, the rate of collagen production is governed by the cyclic deformation experienced by fibroblast cells -i.e. the deformation between the diastolic and systolic states. The authors point out that this overcomes the usual problem associated with using a strain measure to govern the growth of biological tissues -i.e. the problem of evaluating strain with respect to a reference configuration, which, in the case of growing biological tissues, is continuously updated. Watton et al. (2004, 2009a,b, 2010) overcome this problem via the assumption that fibroblast cells have the same reference configuration as the collagen fabric which they maintain. Finally, Kroon and Holzapfel (2009) report that, as with the previous model, the adapted model predicted a berry-like aneurysm shape and wall stresses that correlate well with clinical observation and mechanical tests. However, their model predicted much higher stresses, and therefore, failure of the aneurysmal wall at much smaller sizes than has been reported clinically (i.e. failure at 1.2-3.6mm, compared with $\geq 10mm$ reported clinically). The authors themselves point to the likelihood of influence of the shape of the aneurysm on the calculated stresses. The shapes predicted by their conceptual model are highly idealised -i.e. they are perfectly symmetric, smooth, and have a

well-defined neck. While saccular CAs are often described as "berry-like", the shape of the sac can be irregular and asymmetric. Furthermore, the neck of a saccular CA is not always sharply defined, and it is sometimes difficult to define the exact region that separates the healthy arterial wall from the aneurysmal wall. However, the problem of shape and neck definition is not simple, and continues to present a challenge for modelling, even in the present research (see §4.4.1).

With the aim of modelling growth within a realistic setting, Kroon and Holzapfel (2008) also extended the framework to a three-dimensional setting representative of a human middle cerebral artery which is modelled as a two-layered cylindrical structure. However, while the original Holzapfel et al. (2000) SEF for the medial layer of the healthy arterial wall incorporates both an isotropic and anisotropic component, the anisotropy of the media in this case is neglected, and thus the SEF for the media in this work is characteristic of an incompressible neo-Hookean material. As per the previous work (2007), the complete loss of the medial elastinous layer is considered to be instantaneous and an initiator of aneurysm growth, such that the medial layer is only represented in the parent artery, while the aneurysmal wall is considered to be an evolving adventitia. Results of this study showed that its extension to the three-dimensional setting had little effect on the qualitative results of the study. The three-dimensional framework was then used in a subsequent study by Eriksson et al. (2009) to investigate the effect of collagen fibre organisation (i.e. fibre angle) in the medial layer, and axial in-situ stretch on the growth of the saccular CA. As such, the SEF for the medial layer was extended to include the anisotropic contribution characteristic of the presence two families of collagen fibres. Although the degradation of the medial layer in the region of the aneurysm was, as per the previous work, considered to be instantaneous, it was observed that the presence of two families of collagen fibres in the medial layer affected the size, shape, wall thickness and stress distributions at steady state. The inclusion of medial collagen fibres resulted in a reduced aneurysm size and maximum stress at the fundus (due to decreased compliance of the artery), as well as the wall thickness compared to that predicted by the previous three-dimensional model. Medial fibre angle was found to have a negligible effect on aneurysm size and wall thickness, while an increase in the axial in-situ stretch was found to result in an increase in thickness, and a decrease in the definition of the neck region of the aneurysm.

While the models described above certainly represent an important develop-

ment towards a structural approach to modelling growth, none of the models discussed above take into consideration the haemodynamic environment. In particular, none of the models consider the effect of complex arterial geometries on the haemodynamic environment, and in turn, the effect of the complex physiological haemodynamics on the collagen growth and remodelling which governs aneurysm growth in all three models. Conversely, there are studies that consider complex, patient-specific geometries, but do not model aneurysm growth. For example, Raghavan and colleagues ((Raghavan et al., 2006), (Ma et al., 2007),(Zhou et al., 2010)) have focused on improving the interpretability of stress-analyses of patient-specific CAs. They have developed algorithms for determining the stress-free configuration of aneurysm vasculature obtained by image reconstruction, which is commonly, but incorrectly, assumed to be stress-free. However, the focus for this work is primarily on improving our ability to determine the risk of rupture of a detected aneurysm on a patient-specific basis, so growth is not modelled. Therefore, little insight into the mechanisms that govern the development and stabilisation of aneurysms can be gained from such models, and thus, they do not allow the prediction of future behaviour of a detected aneurysm.

Given the current state-of-the-art hypotheses linking haemodynamics to the events characterising aneurysm inception and enlargement, Humphrey (2008a) identified the need for a new class of models, termed *Fluid-Solid-Growth* (FSG) models. It appears that the first such fluid-solid coupling was proposed by Feng et al. (2004) who linked high wall shear stress to the degeneration of endothelial cells, medial elastin and vascular smooth muscle cells. They proposed an initial degradation of the wall, following which subsequent degradation was linked to a local level of WSS exceeding a threshold value. Although they found that their results for WSS distribution were qualitatively similar to that reported in other studies, their model for the arterial wall did not take into account the contributions of individual arterial wall constituents. Furthermore, the mechanical response of the wall was assumed to be linearly elastic and isotropic, and this simplicity limits the interpretation of their results. Shimogonya et al. (2009a) took a step further by proposing an FSG model embedded within a patient-specific geometry. An image of a human internal carotid artery (ICA) featuring an aneurysm was taken, where the original aneurysm was virtually removed, and the artery was virtually reconstructed. The expansion of an aneurysm is linked to elevated levels of a WSS gradient-based index, which was proposed by the same group in 2009. However, like Feng et al., they pro-

pose a simplistic spring-network model for the arterial wall, which does not capture the growth and remodelling of individual arterial wall constituents. Furthermore, they associate aneurysm growth with arterial wall proliferation -i.e. the proliferation, rather than degradation, of vascular smooth muscle cells, which, even by their own admission, is in contrast to most clinical studies that report arterial wall degradation. To interpret "proliferation" as the growth of collagen material is more appropriate.

In summary, the models of CAs discussed in this section represent important improvements in modelling CA evolution. However, it is clear that so far, none of the models meet all requirements described at the beginning of this chapter. While some incorporate physiologically-realistic structural models of the arterial wall, they neglect the effect of complex arterial geometries, and hence, the effect of the haemodynamic environment on aneurysm development. Conversely, others take into consideration a more realistic haemodynamic environment by embedding models within patient-specific geometries. However, they utilise simplistic structural models which do not account for the varying mechanical properties of individual arterial wall constituents. The next section summarises the latest work on modelling CAs by Watton and colleagues (Watton et al. (2004); Watton and Ventikos (2009); Watton et al. (2009b,c, 2011)) which is the first to incorporate a physiologically-realistic constitutive model for the arterial wall, fluid-solid interactions, and a framework linking haemodynamics to growth and remodelling of arterial constituents.

4.3 CAPTURING THE MECHANICAL RESPONSE OF THE ARTERY: A GENERAL COMPUTATIONAL FRAMEWORK

To model the gradual deformation of the arterial wall during aneurysm development, a geometric non-linear membrane theory (e.g., Wempner (1973); Heil (1996)) is adopted. A thin cylinder of radius R, length L_1, and thickness H represents the artery in the unloaded reference configuration, here denoted as Ω_0. The thicknesses of the media and adventitia are denoted H_M and H_A, respectively. In the initially-loaded configuration, Ω_0^t, the artery is subject to a physiological axial prestretch, λ_z, and a constant systolic pressure p = 16kPa, which equates to a circumferential stretch of λ_0. Hence, the artery in this configuration is represented by a cylinder

of length $L = \lambda_z L_1$, radius $r = \lambda_0 R$, and thickness $h = H/(\lambda_z \lambda_0)$ (Figure 4.1). As the thickness ratio decreases during aneurysm enlargement (i.e. $\frac{h}{r} < 0.1$), and the strain field is uniform through the thickness of the wall, the non-linear membrane approximation is considered appropriate (Watton, 2002).

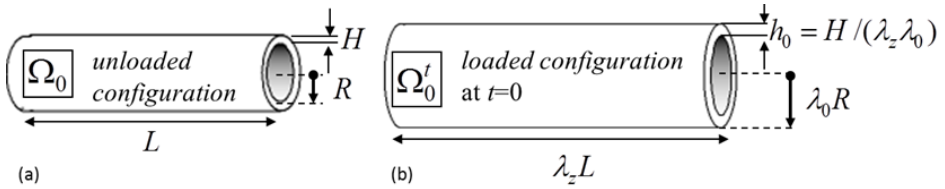


Figure 4.1: Unloaded (a) and initially-loaded (b) configurations of the model artery (adapted from Watton and Ventikos (2009))

The membrane is described by a body-fitted, Lagrangian coordinate system, where coordinates θ_α ($\alpha = 1,2$) lie parallel, and θ_3 lies perpendicular to the mid-plane (see Figure 4.2). The midplane is positioned at $\theta_3 = 0$, and as such, the upper and lower surfaces of the membrane have coordinates $\theta_3 = \pm H/2$. In the following numerical description of the deformation, upper case letters are used to refer to the undeformed configuration, and lower case letters to the deformed configuration; the Einstein summation convention is used throughout.

A material point on the midplane of the membrane is given by the position vector $\mathbf{X}(\theta_1, \theta_2)$. At each point, a set of covariant base vectors is defined as tangents to the coordinate lines θ_α, which are given by

$$\mathbf{A}_\alpha = \mathbf{X}_{,\alpha} = \frac{\partial \mathbf{X}}{\partial \theta_\alpha} \tag{4.1}$$

where the comma denotes partial differentiation with respect to θ_α. The third base vector is defined as the unit normal to the two midplane base vectors, i.e.,

$$\mathbf{A}_3 = \frac{\mathbf{A}_1 \times \mathbf{A}_2}{|\mathbf{A}_1 \times \mathbf{A}_2|} \tag{4.2}$$

Hence, in the undeformed configuration, the covariant midplane metric tensors are $Aij = \mathbf{A}_i \cdot \mathbf{A}_j$. During the deformation, the material point which lies at position $\mathbf{X}(\theta_1, \theta_2)$ in the undeformed configuration, is displaced, and its new position given by i.e.,

$$\mathbf{x}(\theta_1, \theta_2) = \mathbf{X}(\theta_1, \theta_2) + \mathbf{u}(\theta_1, \theta_2) \tag{4.3}$$

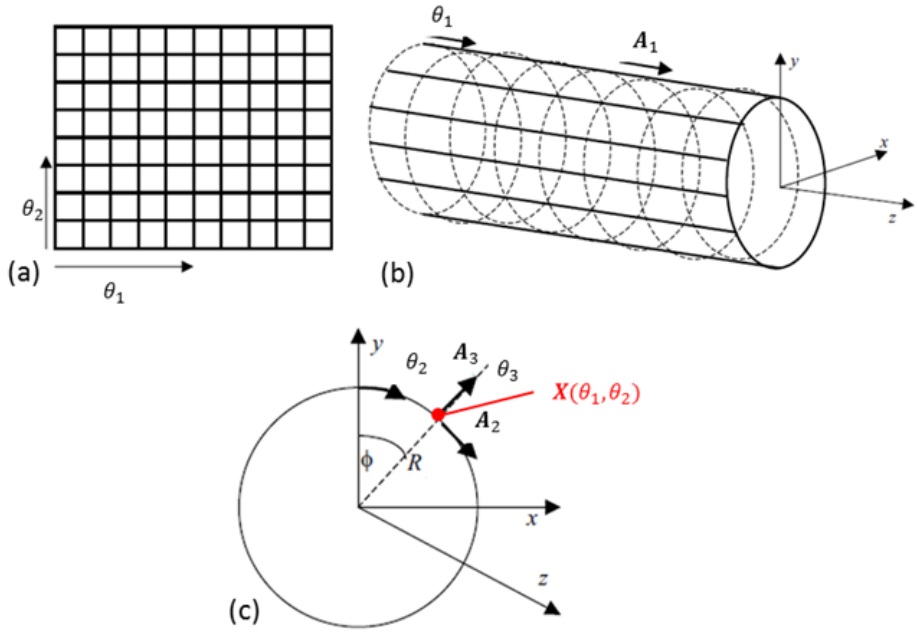


Figure 4.2: A body-fitted Lagrangian coordinate system to describe the arterial membrane (the midplane of the wall is shown here). (a) and (b) Coordinates θ_1 and θ_2 are parallel to the midplane of the arterial wall; (c) θ_3 is perpendicular to the midplane. Any point on the membrane, $\mathbf{X}$ is defined with respect to coordinates θ_1 and θ_2, and at each point, a set of covariant base vectors is defined as tangents to θ_1 and θ_2 (adapted from Watton (2002))

where $u(\theta_1,\theta_2)$ gives the midplane displacement field. The tangent vectors to the deformed midplane can therefore be defined as

$$\mathbf{a}_\alpha = \frac{\partial \mathbf{x}}{\partial \theta_\alpha} = \mathbf{A}_\alpha + \mathbf{u}_{,\alpha} \tag{4.4}$$

The third midplane base vector, $\mathbf{a}_3$, is chosen as the normal to the midplane base vectors. To satisfy the condition of incompressibility on the midplane, the magnitude of $\mathbf{a}_3$ is defined as

$$\mathbf{a}_3 = \frac{(\mathbf{a}_1 \times \mathbf{a}_2)|\mathbf{A}_1 \times \mathbf{A}_2|}{|\mathbf{a}_1 \times \mathbf{a}_2|^2} \tag{4.5}$$

In the deformed configuration, the covariant midplane metric tensors are then $a_{ij} = \mathbf{a}_i \cdot \mathbf{a}_j$, $(i,j = 1,2,3)$. Therefore, assuming that off-midplane and midplane strain fields are equal, the difference between the midplane metrics can then be used to define the components of the Green Lagrange (GL) strain tensor, i.e.,

$$E_{ij} = \frac{1}{2}(a_{ij} - A_{ij}) \tag{4.6}$$

In the case of the specific geometry of the model artery, cylindrical polar Lagrangian coordinates θ_i ($i = 1,2,3$) are used to denote arc lengths in the axial, azimuthal, and radial directions, respectively. Now, the position vector of a material point on the midplane (relative to a Cartesian coordinate system) in the undeformed configuration is given by

$$[\mathbf{X}] = [R\sin(\theta_2/R), R\cos(\theta_2/R), \theta_1] \tag{4.7}$$

for $\theta_1 \in [0, L_1]$ and $\theta_2 \in [0, L_2)$, where $L_2 = 2\pi R$. The position of the point after deformation is then given by

$$[\mathbf{x}] = [(R+u_3)\sin(\theta_2/R)+u_2\cos(\theta_2/R), (R+u_3)\cos(\theta_2/R)-u_2\sin(\theta_2/R), \theta_1+u_1] \tag{4.8}$$

where u_1, u_2, and u_3 denote the displacements in the axial, azimuthal, and radial directions, respectively. Equation (4.1) through to Equation (4.6) gives the strain field for the midplane.

Given the non-linear, anisotropic response of the artery, it is clear that the computational framework for comprehensive modelling of the response must take into account the individual contributions of the major structural constituents that give rise to these properties. As Gasser et al. (2006) explain, continuum-based constitutive relations describe the gross behaviour that results from internal constituents, and are thus useful in describing the mechanical behaviour of soft tissues such as arteries. In the case of aneurysm development, constitutive equations provide a relation between the stresses on the arterial wall and the deformation of the tissue as the aneurysm enlarges, and must be such as to balance laws for linear and angular momentum. Such equations are usually in the form of partial differential equations, which, given the anisotropy and non-linear response of arterial tissue, are computationally complex. As such, the rigorous finite element method (FEM) is usually employed to solve the system. As Bower (2008) states, the basis for FEM modelling in structural mechanics is the principle of virtual work, which states that the work done by all forces acting on the system is zero for any infinitesimal displacement from equilibrium which is consistent with the constraints of the system. This requires that the first variation in the work done must vanish.

The internal work is the stored internal potential energy of the arterial wall, and hence, the principle of virtual work can be equivalently expressed by the principle of stationary potential energy, which states that the first variation of potential energy

of a conservative system in equilibrium must vanish (Bower, 2008), i.e.,

$$\partial\Pi_{\text{int}} - \partial\Pi_{\text{ext}} = 0 \tag{4.9}$$

where $\delta\Pi_{int}$ is the change in internal potential energy stored in the arterial wall, while $\delta\Pi_{ext}$ is the change in the external potential energy caused by normal pressure. Thus, to evaluate the steady deformation of the arterial wall, $\delta\Pi_{int}$ must be computed. The stored internal potential energy can be expressed in the form of a SEF, Ψ, which describes the work done per unit volume to deform a material from a stress-free reference state to a loaded state (Bower, 2008). Hence, the governing equation above can further be expressed as

$$\int_V \partial\Psi \mathrm{d}V - \int_s p(\hat{\mathbf{a}}_3 \cdot \partial\mathbf{x})\mathrm{d}s = 0 \tag{4.10}$$

where $\partial\mathbf{x} = \partial(\mathbf{X}+\mathbf{u}) = \partial u_i \mathbf{A}_i$, $\mathrm{d}s = |\mathbf{a}_1 \times \mathbf{a}_2|\mathrm{d}\theta_1\mathrm{d}\theta_2$, $\hat{\mathbf{a}}_3 = (\mathbf{a}_1 \times \mathbf{a}_2)/|\mathbf{a}_1 \times \mathbf{a}_2|$, and Ψ is the SEF. It is assumed that the midplane and upper/lower surface area elements are equal. Furthermore, the earlier assumption of a uniform strain field through the thickness of the arterial wall implies that the SEFs are independent of θ_3. This enables an immediate integration yielding

$$\int_0^{2\pi R}\int_0^{L_1} \{\partial(H_M\Psi_M + H_A\Psi_A) - p(\mathbf{a}_1 \times \mathbf{a}_2)\cdot\partial u_i\mathbf{A}_i\}\mathrm{d}\theta_1\mathrm{d}\theta_2 = 0 \tag{4.11}$$

For details of the numerical formulation of the solution to Equation (4.11), see Watton et al. (2004).

Lastly, it is important to note that during aneurysm development, the artery evolves through many different configurations. Recall from §4.1 that regardless of tissue configuration, collagen fibres are laid down in the same state of stretch, the attachment stretch, λ_{AC}. Hence, although the tissue may deform further, the collagen fibres will be recruited to bear load only when the stretch reaches a certain level (i.e. the crimped fibres will lengthen out and begin to bear load). Hence, while the stretch of elastinous constituents during deformation is defined relative to the unloaded tissue configuration, Ω_0, the stretch of collagenous fibres must be defined relative to the configuration in which they are recruited to bear load. As such, a *recruitment configuration*, Ω^R, is defined, which provides a means of mapping between different tissue configurations. Figure 4.3 shows the mapping gradients, $\mathbf{F}$, $\mathbf{F}^R$, and $\mathbf{F}^C$, which capture the transition between the unloaded and loaded, unloaded and recruitment, and recruitment and loaded configurations respectively.

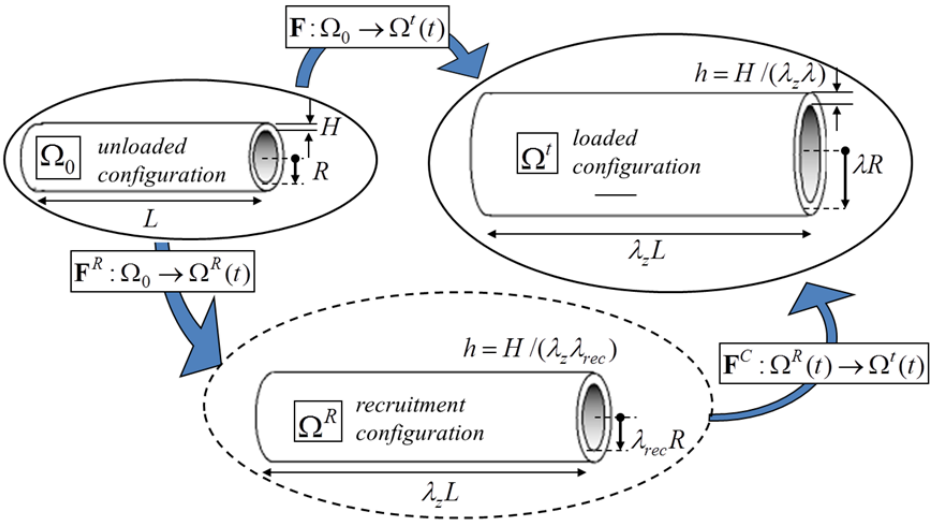


Figure 4.3: Mappings between different cylinder membrane configuration. In the loaded configuration, Ω^t, the cylinder has an axial stretch λ_z and a circumferential stretch λ. The stretch of the elastin is defined relative to the unloaded configuration Ω_0, whereas the stretch of the collagen fibres is defined relative to the configuration in which they are recruited to bear load, Ω^R (adapted from Watton et al. (2009a))

The subsequent sections outline the FSG framework utilised in this research, including the functional forms for the spatially and temporally heterogeneous SEFs for the media, Ψ_M, and the adventitia, Ψ_A, and the equations that describe G&R and its coupling to haemodynamics.

4.4 A FSG MODEL FOR SACCULAR CEREBRAL ANEURYSM EVOLUTION

Following the first mathematical model for AAAs proposed by Watton et al. (2004), a three-dimensional model for the growth, evolution and stabilisation of saccular CAs was developed (Watton and Ventikos (2009); Watton et al. (2009b)). The model incorporates a physiologically realistic constitutive model for the arterial wall based on the work of Holzapfel et al. (2000), and several features from the original AAA model. This model forms the basis for the work discussed over the following chapters.

Let us begin by considering broadly the overall computational framework that couples fluid and solid mechanics, captures the G&R of arterial wall constituents,

and links the haemodynamic environment to G&R, as shown in Figure 4.4 below:

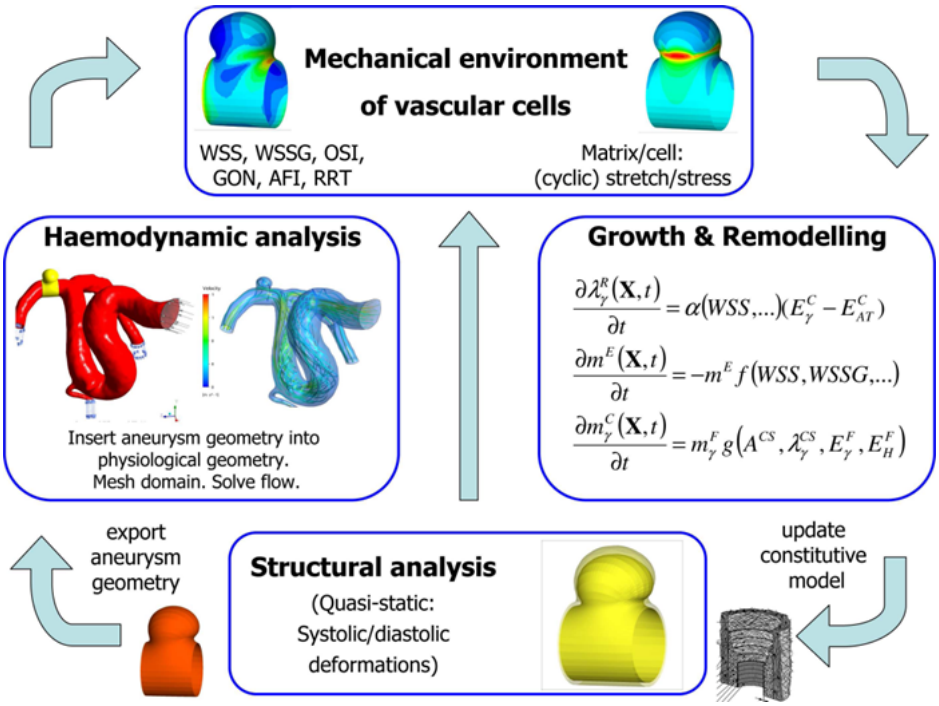


Figure 4.4: Computational framework for fluid-solid modelling of cerebral aneurysm growth (Watton et al., 2013)

The computational cycle begins with a finite element structural analysis of the model aneurysm geometry, whereby an equilibrium deformation field is solved for a given pressure and boundary conditions. Important mechanical quantities such as cyclic stretches and stresses, and cyclic deformation of fibroblast cells are obtained from this analysis. The geometry is meshed using ANSYS ICEM, and flow (steady or pulsatile) is solved, from which haemodynamic quantities of interest (e.g. WSS, WSSG) are obtained. The derived mechanical and haemodynamic quantities are interpolated onto the nodes of the structural mesh. These quantities are fed into G&R equations which simulate cell-mediated adaption of tissue, and the constitutive model is updated. The cycle then begins again with a structural analysis solving a new equilibrium deformation field for the updated tissue, and, as it continues, the CA develops. The key aspects of the computational model are discussed below. We must note that although specific computational tools are used as components and modules of this processing loop, the overall algorithm does not depend on the particular implementation of the individual components. For example, the haemo-

dynamics solver can be replaced by any other such solver capable of providing the same information (pressure, WSS and derivative quantities).

4.4.1 Structural model for an evolving aneurysm

Structurally, the arterial wall is modelled as a two-layered, non-linear cylindrical membrane. The inner layer accounts for the mechanical response of medial elastinous constituents (ground substance, elastin fibres and passive vascular smooth muscle cells), and two sets of collagen fibres helically-wound at an angle of $\pm\gamma$ with respect to the azimuthal axis. The outer layer accounts for the mechanical response of the adventitia, and comprises of two sets of helically-wound collagen fibres and a small elastinous contribution. As per the Holzapfel et al. (2000) approach, two SEFs are used to capture the individual contributions of the elastinous and collagenous constituents respectively. The SEF for the elastinous contribution is a classical neo-Hookean function of the Green-Lagrange (GL) elastin strains E_{11},E_{22} and E_{33} in the axial, azimuthal and radial directions respectively. In this model, the SEF for elastinous constituents is multiplied by a normalised, spatially and temporally-dependent elastin concentration function, $m^E(\theta_1,\theta_2,t)$, where θ_1 and θ_2 represent Lagrangian coordinates, and $m^E(\theta_1,\theta_2,t=0)=1$. This function is employed to prescribe the gradual degradation of elastin in the arterial wall. The SEF representative of the highly non-linear response of the collagenous constituents is an exponential function of the GL collagen strain $E^C_{J_p}$. This SEF is multiplied by a spatially and temporally dependent collagen concentration variable $m^C_{J_p}(\theta_1,\theta_2,t)$. The two concentration variables, m^E and $m^C_{J_p}$ are defined by the ratio of their respective mass densities at time t to their mass densities at t = 0. The overall SEF for the tissue has the form

$$\Psi_J = m^E K^E_J (E_{11}+E_{22}+E_{33}) + \sum_{P=\pm,E^C_{J_p}>0} m^C_{J_p} K^C_J \left\{\exp\left[A^C (E^C_{J_p})^2\right]-1\right\}, J=M,A \quad (4.12)$$

where J denotes the media (M) or adventitia (A); K^E_J and K^C_J are parameters associated with the stiffness of elastinous and collagenous constituents respectively; A^C denotes the exponential constant for the collagenous constituents; subscript 'p' denotes the pitch (positive or negative) of the angle of collagen fibre orientation with respect to the azimuthal axis. The GL collagen strain $E^C_{J_p}$ is a function of the GL strains of elastin resolved in the direction of collagen fibres, and is defined with

respect to the onset of collagen fibre recruitment to load-bearing, i.e.,

$$E^C_{J_p} = \frac{E_{J_p} - E^R_{J_p}}{1 + 2E^R_{J_p}} \tag{4.13}$$

where $E^R_{J_p} = \left(\left(\lambda^R_{J_p}\right)^2 - 1\right)/2$, $\lambda^R_{J_p}(\theta_1, \theta_2, t)$ are the recruitment stretches, and $E_{J_p} = E_{11}\sin^2\gamma_{J_p} + E_{22}\cos^2\gamma_{J_p} + E_{12}\sin\gamma_{J_p}\cos\gamma_{J_p}$. The main material parameters, geometrical and physiological data is summarised in Table 4.1.

Table 4.1: Material, geometry and physiological parameters for modelling the human internal carotid artery (Watton et al., 2011)

Property	**Symbol**	**Value**
Radii		
Reference configuration	R (mm)	1.6
At systole	r_s (mm)	2
Wall thickness		
Total	H (mm)	0.375
Media	H_M	0.25
Adventitia	H_A	0.125
Fibre orientation		
Media	$\gamma_{M_+}, \gamma_{M_-}$ (°)	$+30^\circ, -30^\circ$
Adventitia	$\gamma_{A_+}, \gamma_{A_-}$	$+60^\circ, -60^\circ$
Applied pressure, kinematics		
Systolic pressure	p (kPa)	16
Axial pre-stretch	λ_z	1.3
Ratio of systolic to diastolic circumferential diameters	λ^S_D	1.1
Attachment stretch	λ^C_{AT}	1.07
Recruitment stretches (t=0)		
Media	$\lambda^R_{M+}, \lambda^R_{M-}$	1.18
Adventitia	$\lambda^R_{A+}, \lambda^R_{A-}$	1.20
Material parameters		
Elastin (media)	K^E_M (kPa)	133.8
Collagen (media)	K^C_M (kPa)	1.964
Exponential constant for collagen	A^C	60

In the systolic configuration, the artery has a radius r_S, an axial pre-stretch of 1.3, a circumferential stretch of 1.25 and 80% of the load is assumed to be borne by the elastinous constituents. The magnitude of the collagen attachment stretch λ^C_{AT} is defined to be the stretch in the collagen fabric at systole (t =0). It is assumed that the elastinous response of the adventitia is an order of magnitude weaker than that of

the media, i.e. $K_A^E = \frac{K_M^E}{10}$, where the ratio of the medial and adventitial collagen material parameters is $K_A^C = \frac{K_M^C}{4}$. The three independent material parameters, K_M^E (relating to elastinous constituents), K_M^C and A^C (relating to collagenous constituents) are determined so that the SEFs adequately model the mechanical behaviour of the artery Watton and Hill (2009).

4.4.2 G&R of arterial wall constituents: Elastin

It is useful to note that in this work, growth refers to the change in mass of material constituents, while remodelling refers to the change in the organisation of constituents, with no change in mass. Histologically, a saccular aneurysm is characterised by an abrupt loss of the medial elastinous layer at the aneurysm neck and a thin collagenous tissue within the aneurysmal region. To capture the loss of the elastinous medial layer in the aneurysmal region, a degradation function for elastin degradation is proposed. In the earlier stages of the model (Watton et al., 2009b), elastin degradation was entirely prescribed, but in the most recent work (see Watton et al. (2011)) only an initial degradation was prescribed to simulate aneurysm inception. This initial degradation results in a small outpouching in the arterial wall, which results in a disturbance to the local haemodynamic environment. In turn, this results in a change in the local WSS from normotensive levels, to which subsequent elastin degradation is linked.

Prescribed elastin degradation

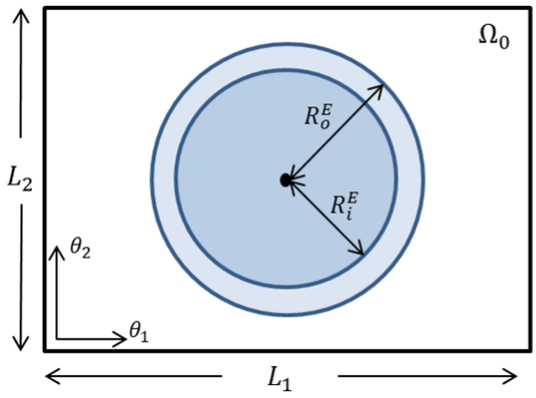
In this work, elastin degradation is prescribed to occur in a small circular patch over a time-scale of T years, which simulates aneurysm inception. The circular patch is divided into two rings with radii R_i^E and R_o^E, such that $R_i^E < R_o^E$ (Figure 4.5). Degradation is prescribed to occur within the inner ring, and is linearly interpolated using radial splines between R_i^E and R_o^E.

Within the circular patch, elastin concentration is defined as below:

$$m^E(\theta_1,\theta_2,t) = 1 - \left(1 - m^E_{\min}(t)\right) \tag{4.14}$$

$$\times \exp\left[-\omega_1\left(\frac{\theta_1 - L_1/2}{L_1/2}\right)^2\right] \tag{4.15}$$

$$\times \exp\left[-\omega_2\left(\frac{\theta_2 - L_2/2}{L_2/2}\right)^2\right], \tag{4.16}$$



L_1	L/λ_z
L_2	$2\pi R$
R_i^E	$0.6L_1$
R_o^E	$0.8L_1$

Figure 4.5: Prescribed degradation of elastinous constituents within a small circular patch in the centre of the domain. Degradation is prescribed to occur within the inner patch of radius R_i^E, and is linearly interpolated using radial splines between R_i^E and R_o^E

where θ_1, θ_2 are Lagrangian coordinates of the computational domain where $\theta_1 \in [0, L_1], \theta_2 \in [0, L_2) : (\theta_1 - L_1/2)^2 + (\theta_2 - L_2/2)^2 \leq (R_i^E)^2$. $m^E_{\min}(t)$ is the minimum elastin concentration at time t, which is located at $(\theta_1, \theta_2) = (L_1/2, L_2/2)$. Parameters ω_1, ω_2 control the degree of localisation of the degradation function. In this work, $\omega_1, \omega_2 = 1$ as per Watton et al. (2011).

It is assumed that the decay of the minimum concentration of elastin is exponential, i.e.

$$m^E_{\min}(t) = (m_T^E)^{(t/T)}, \tag{4.17}$$

where m_T^E is the concentration of elastin at (L_1, L_2), and T is determined with respect to the overall total time of the simulation, and the nature of the simulation -i.e. for structural-only simulations, elastin degradation may be prescribed for the entire time-scale of the simulation; for FSG simulations, T is the time over which aneurysm inception is simulated. In this work, $m_T^E = 0.05$. At $t = 0, m^E_{\min}(t = 0) = 1$. For $\theta_1, \theta 2 : \sqrt{(\theta_1 - L_1/2)^2 + ((\theta_2 - L_2/2)^2} \geq R_o^E$, it is specified that $m^E(\theta_1, \theta_2, t) \equiv 1$.

Elastin degradation linked to local levels of WSS

In FSG simulations, following the prescribed degradation period, subsequent elastin degradation is linked to locally low WSS via a degradation function, such that the evolving elastin concentration can be described as below:

$$\frac{\partial m^E}{\partial t} = -\mathscr{F}_D D_{\max} m^E, \tag{4.18}$$

where $\mathscr{F}_D$ is a spatially-dependent function of WSS (denoted by τ) defined as below:

$$\mathscr{F}_D\left(\tau(\theta_1,\theta_2,t)\right) = \begin{cases} 0, & \tau \geq \tau_{\text{crit}}, \\ \left(\frac{\tau_{\text{crit}}-\tau}{\tau_{\text{crit}}-\tau_X}\right)^2, & \tau_X < \tau < \tau_{\text{crit}}, \\ 1, & \tau \leq \tau_X, \end{cases} \tag{4.19}$$

No elastin degradation occurs for WSS above some critical level τ_{crit} ($\mathscr{F}_D = 0$). A maximum rate, D_{max}, of elastin degradation is assumed to occur for values of WSS below some minimum critical value τ_X ($\mathscr{F}_D = 0$). Finally, for values between τ_X and τ_{crit}, the degradation function is assumed to have a simple quadratic form.

4.4.3 G&R of arterial wall constituents: Collagen

4.4.3.1 Collagen remodelling

The key G&R hypotheses governing the growth of the model aneurysm are that the turnover of collagen fibres is continuous, and that new collagen fibres are always deposited with the same stretch regardless of current tissue configuration, such that a homeostatic level of strain is maintained.

The attachment stretch

Collagen fibres are in a continual state of deposition and degradation (Humphrey, 1999) and they are attached to the artery in a state of stretch. Watton et al. (2004) hypothesised that fibroblasts configure the collagen fibres to achieve a maximum stretch λ^C_{AT} during the cardiac cycle and introduced the terminology *attachment stretch* to denote λ^C_{AT}.

Recruitment stretches

To maintain the GL collagen strain at the equilibrium value, evolution equations are required that represent the developing natural reference configurations of collagen fibres to maintain their GL strain at the equilibrium value E^C_{AT}. Fields of spatially and temporally dependent recruitment stretch variables $\lambda^R_{J_p}(\theta_1,\theta_2,t)$ are defined for this purpose. The recruitment stretch signifies the amount by which the tissue must be stretched before collagen fibres are recruited to bear load, and provides a convenient mapping from the reference configuration of collagen fibres, to some altered configuration. Remodelling of this variable captures the deviation of the collagen strain $E^C_{J_p}$ from its equilibrium value, and is representative of the evolving natural reference configuration of collagen fibres. The proposed evolution equation for the

recruitment stretch variable is

$$\frac{d\lambda^R_{J_p}}{dt} = \alpha \frac{E^C_{J_p}|_{\max} - E^C_{AT}}{E^C_{AT}}, \tag{4.20}$$

where $E^C_{AT} = \left(\left(\lambda^C_{AT}\right)^2 - 1\right)/2$ and $E^C_{J_p}|_{\max} = \max\left(E^C_{J_p}|_{\text{sys}}, E^C_{J_p}|_{\text{dias}}\right)$. $E^C_{J_p}|_{\text{sys}}$ and $E^C_{J_p}|_{\text{dias}}$ are the magnitudes of the collagen strains in systolic and diastolic configurations, respectively. $\alpha > 0$ is a numerically-determined remodelling parameter corresponding to a prescribed half-life of collagen fibres. The exact half-life of collagen fibres in cerebral arteries is unknown, but as Humphrey (1999) suggests, the half-life of collagen ranges between 3 and 90 days, and is known to increase during aneurysm evolution. Through numerical experimentation, Watton (2002) found that physiologically-realistic dilation of the vessel could be achieved for a range of physiologically-realistic remodelling rates, but in subsequent work (e.g. Watton and Ventikos (2009)), the chosen half-life is set to one month. Functions $\mathscr{F}_S$ and $\mathscr{F}_D$ denote the rates of synthesis and degradation of collagen fibres during a cardiac cycle, respectively.

4.4.3.2 Collagen growth and atropy

To capture the growth and atrophy of collagen fibres during aneurysm development, an evolution equation for the change in concentration of collagen $m^C_{J_p}$ is proposed. It is assumed that collagen concentration is dependent on the concentration of fibroblast cells, and the rate of fibroblast-mediated collagen synthesis and degradation.

In turn, the rate of collagen synthesis and degradation by fibroblasts is dependent on the level of cyclic deformation experienced by the fibroblast cells during the cardiac cycle -i.e. collagen production increases in response to an increase in stretch, and decreases in response to a decrease in stretch. Cyclic deformation of the tissue over the cardiac cycle is quantified in the form of the cyclic areal stretch, A^{CS}, which is a function of the systolic and diastolic GL strains. The A^{CS} is evaluated for each element of the computational domain, and a nodal value is determined by taking the average A^{CS} of the four surrounding elements. The A^{CS} is defined as the ratio of the areal stretch at systole to that at diastole, which is equivalent to quantifying the ratio of areas of two parallelograms. The A^{CS} is given by

$$A^{CS} = \sqrt{\frac{(1+2E^S_{11})(1+2E^S_{22}) - 4E^S_{12}}{(1+2E^D_{11})(1+2E^D_{22}) - 4E^D_{12}}} \tag{4.21}$$

For mathematical simplicity, it is assumed that the reference configuration of fibroblast cells is identical to that of the collagen fabric, and that the concentration of fibroblast cells is in direct proportion to that of collagen fibres, i.e., $m^F_{(J_p)} = \zeta_0 m_{(J_p)}{}^C, \zeta_0 > 0$. Thus, the evolution equation for growth and atrophy of collagen fibres has the form

$$\frac{dm^C_{J_p}}{dt} = m^C_{J_p} \mathscr{F}_G \left(E^C_{J_p}|_{\max}, A^{CS} \right), \tag{4.22}$$

where $\mathscr{F}_G = \zeta_0 (\mathscr{F}_S - \mathscr{F}_D)$. The exact functional form of $\mathscr{F}_G$ is unknown; however, the increase and decrease in the stretching of the ECM is known to induce the up- and down-regulation of MMPs and collagenase, respectively. Hence, a simple linear function is proposed for $\mathscr{F}_G$ such that the rate of change in collagen concentration becomes

$$\frac{dm^C_{J_p}}{dt} = m^C_{J_p} \beta(A^{CS}) \left(\frac{E^C_{J_p}|_{\max} - E^C_{AT}}{E^C_{AT}} \right), \tag{4.23}$$

where $\beta(A^{CS})$ represents a phenomenological growth parameter relating to the rate of increase or decrease of the mass of collagen fibres by fibroblasts in response to deviations of cyclic deformation from normotensive levels. In order to constrain unrealistically large cyclic deformations of the tissue during aneurysm evolution, an exponential form was selected as an initial choice, i.e.,

$$\beta\left(A^{CS}\right) = \beta_0 \exp\left[\beta^{CS} \max\left(\frac{A^{CS}}{A^{CS}|_{t=0}} - 1, 0 \right) \right] \tag{4.24}$$

where $A^{CS}|_{(t=0)} = 1.1$ is chosen to reflect the reported physiological level of cyclic stretch of 10% (Ando and Yamamoto, 2011), hereon referred to as the homeostatic cyclic stretch, denoted by A^{CS}_h. β_0 is applied to scale the exponential function, while β^{CS} determines the steepness of the exponential curve.

4.4.4 Model capabilities

Watton and Ventikos (2009) and Watton et al. (2009b) reported that the growth and remodelling equations employed in this model allowed the development of a saccular aneurysm, which stabilised in size despite almost a complete loss of elastinous constituents. During aneurysm enlargement, elastin strains were increased in the aneurysmal region, as expected. Correspondingly, an initial increase in collagen strains was observed, but the G&R of collagen resulted in the return of collagen strains to homeostatic levels.

In the early work (Watton and Ventikos (2009); Watton et al. (2009b)), only the less computationally-demanding steady-flow simulations were performed on the cylindrical geometry. As such, mechanical stimuli arising from pulsatile flow could not be captured. Hence, pulsatile-flow simulations were conducted with the aim of addressing two questions:

1. Are spatial distributions of WSS/WSSG derived from steady (systolic) flow simulations different to the mean WSS/WSSG calculated from the more computationally intensive pulsatile-flow simulations? Thereby, is the steady-flow approach appropriate for investigating the link between WSS/WSSG, and growth and remodelling of the arterial wall during aneurysm development?; and

2. What is the significance of pulsatile haemodynamic indices proposed in the literature to aneurysm development?

The results were published in Watton et al. (2011), in which the authors found that while peak pulsatile-flow WSS and WSSG values were observed to be smaller than their steady-flow counterparts, their respective spatial distributions are nearly identical. These results coincide with the study by Myers et al. (2001) who observed that the time-averaged WSS pattern produced by pulsatile flow through a model of the human right coronary artery was similar to the steady-flow pattern. Myers et al. (2001) concluded that significant features of WSS distribution are related to arterial geometry, and not pulsatility. Similarly, in their investigations on the haemodynamics in a model of the cerebral artery before and after formation of an aneurysm, Mantha et al. (2006) found that pulsatility did not affect the location of maxima and minima of WSS. In their paper, Watton et al. (2011) therefore conclude that the steady-flow approach may be a valid approach for investigating the link between deviations of WSS/WSSG from their normotensive levels, and the growth and remodelling of arterial tissue during aneurysm development.

Watton et al. (2011) also studied the distributions of the Oscillatory Shear Index (OSI) proposed by Ku et al. (1985). However, they conclude that it is unclear how to correlate OSI to aneurysm inception for a computational model comprising an aneurysm developing on a cylindrical arterial section. Hence, implementation of the model within physiologically realistic arterial geometries may reveal different, more significant distributions of the OSI, and other pulsatile-flow indices, which

may more strongly suggest a link between these indices and aneurysm evolution. It will also provide an opportunity to compare the evolution of the model geometry to the real aneurysmal geometry, and determine if the hypothesis for WSS-driven elastin degradation is indeed reasonable. The following chapter discusses and compares two methods for embedding the cylindrical model within patient-specific geometries. The new methods in turn facilitate the investigation of the effect of physiological flow on evolution of the model aneurysm geometry, including an examination of the pulsatile-flow indices described in §2.4.1 at inception.



CHAPTER 5

METHODS FOR PATIENT-SPECIFIC MODELLING UTILISING THE CURRENT FSG FRAMEWORK

The aim of this section is to present methodology to integrate the FSG model (hereon refered to as *the cylinder model* of aneurysm evolution within patient-specific arterial geometries on which aneurysms had developed, so as to enable an investigation of the effects of complex physiological flow on aneurysm evolution. Such patient-specific, CFD studies have, to date, been applied only in the context of static aneurysmal geometries obtained from images of patient vasculature. Coupling a model of aneurysm evolution to patient-specific geometries allows the observation of aneurysm enlargement within a realistic, physiological environment, as well as testing of hypotheses linking specific haemodynamic conditions to growth and remodelling. Given the discrepancies between theories on the influence of haemodynamics on aneurysm evolution (i.e. *high*-flow vs. *low*-flow theories), qualitative comparison of the resulting model aneurysm geometry to the real patient's aneurysm may help to narrow the choice of indices studied, as well as provide clues as to the possible mechanisms by which this influence is exerted.

To embed the cylinder model within patient-specific geometries, initially, a method using **ANSYS ICEM** was developed. Following initial validation, an automated, algorithmic method was later developed (§5.2) to allow the integration of the model within a large number of cases. In both cases, images of patient-specific geometry were obtained and segmented using `@neufuse`, such that the aneurysm section, and two smaller segments immediately adjacent to the aneurysm section were removed (see Figure 5.1(a)). The centreline running through the geometry, as well as the neck-point (the centre-point of the aneurysm neck, Figure 5.1(b)) were also extracted in `@neufuse`.

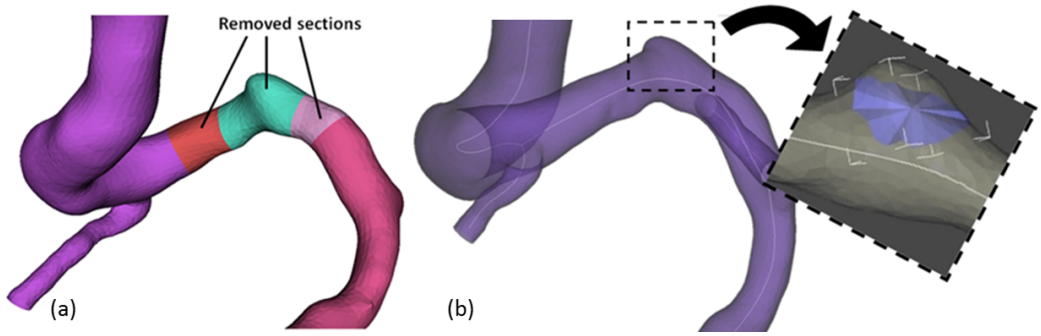


Figure 5.1: Segmentation of geometry and centreline extraction using `@neufuse` software (a) The geometry was segmented into 5 sections. The original, physiological aneurysm, and two segments at a small distance beyond the aneurysm were removed, leaving upstream and downstream segments that were exported to ANSYS ICEM. This allowed adequate space for the placement of the cylinder, and for the creation of smooth connecting surfaces between the up/downstream geometries and the cylinder (b) The centreline running through the length of the geometry, and a point in the centre of the aneurysm neck were extracted, and exported to ANSYS ICEM for the creation of surfaces between the cylinder and physiological geometries

5.1 Integration of the FSG model into patient-specific geometries: ICEM-based methodology

The remaining upstream and downstream geometries, along with the centreline and neck-point were exported to ANSYS ICEM for creation of smooth, connecting

surfaces between the up/downstream segments and the cylinder model, and for mesh generation.

When imported in **ICEM**, the upstream and downstream sections appear at an arbitrary point in space (Figure 5.3(a)). Therefore, the geometry must be translated, so that it sits about the cylinder geometry, which is set such that its left edge is centred about the global axis (the origin of which is located at (0,0,0).

However, the length and radius of the cylinder must first be set, as this partly governs the positioning of the upstream and downstream segments. A minimum length, l_{cylinder}, for the cylinder was set to be equal to the cylinder radius, so as to ensure that elastin degradation can be prescribed in an adequately large circular patch on the cylinder surface. To ensure adequate space between the up/downstream segments and the cylinder (to accommodate the creation of smooth, connecting surfaces between them), and keeping in mind the natural curvature of the physiological geometry, the maximum length of the cylinder was limited to half the straight-line distance, L, between the centres of the up- and downstream inlets. The radius of the cylinder, $r_{cylinder}$, was set to be the average of the radii of the upstream outlet and downstream inlet. The average radius was determined using the general form

$$r = \sqrt{\frac{A_{\text{surface}}}{\pi}}$$

whereby A_{surface} is the average of the sum of the upstream outlet and downstream inlet surface areas, S_1 and S_2, as shown in Figure 5.2.

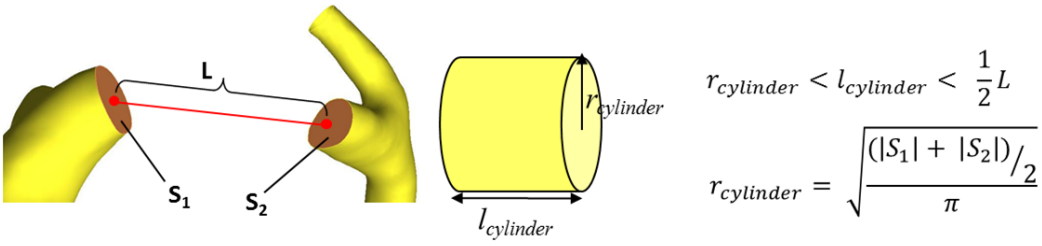


Figure 5.2: Determining cylinder length and radius. To ensure adequate space for the positioning of the cylinder, and the creation of smooth connecting surfaces, the length of the cylinder was set to be half the length of the straight-line distance joining the centres of the upstream outlet and downstream inlet. The radius was given by taking the average of the inlet/outlet radii.

The translation and rotation of the geometry was then performed, as shown in

Figure 5.3.

The centre-point of the physiological aneurysm neck was used to position the geometry such that the model aneurysm would evolve in the same orientation as the physiological aneurysm. To achieve this, a perpendicular line from the neck-point (point D, Figure 5.3(b)) to the centre-line is needed, which serves to set the y-axis of the local coordinate system, from which the geometry must be translated to the global axis. Utilising the **ICEM** 's distance measuring tool, the two closest points to point D, A and B, are identified. A perpendicular is then defined with respect to the segment AB (Figure 5.3(c)). The desired point (point C) along segment AB was found by determining the length of segment AC using the cosine rule (where $AC = AD\cos\theta$, and finding the ratio of segment AC to segment AB. The lengths of segments AB and AC were determined using the distance-measuring tool. With the perpendicular in place, a local coordinate system (shown as ***LCS1*** in Figure 5.3(d)) was created, centred about point C, with the positive z-axis pointing in the direction of flow, the positive y-axis pointing along AD, and the positive x-axis pointing into the frame of view. The geometry was then translated to the global axis, such that the origin of ***LCS1*** coincides with the global origin (Figure 5.3(e)). The cylinder geometry was imported. For the purpose of CFD simulations, the cylinder represents the beginning of the domain of interest, and as such, the entire geometry must be positioned such that the upstream edge of the cylinder is centred about the global origin. Therefore, the geometry is translated a distance equal to half the length of the cylinder in the positive z direction (Figure 5.3(f)).

Once the cylinder was positioned, connecting surfaces between the up/downstream segments and the cylinder were created. The process is depicted in Figure 5.4.

With the cylinder in position (Figure 5.4(a)), four copies of the centreline were created. Two copies were translated a small arbitrary distance (in this case, 0.0003m) in the positive and negative x direction, and the remaining 2 were translated the same distance in the positive and negative y direction (Figure 5.4(b)). Two surface ribbons were created by joining the two centreline copies in the x direction, and the two copies in the y-direction, and creating surfaces over the connected curves (Figure 5.4(c)). The intersections between the two 2D surfaces and the up/downstream and cylindrical geometries were extracted in the form of curves running along the surfaces of the up/downstream and cylinder geometries. The inter-

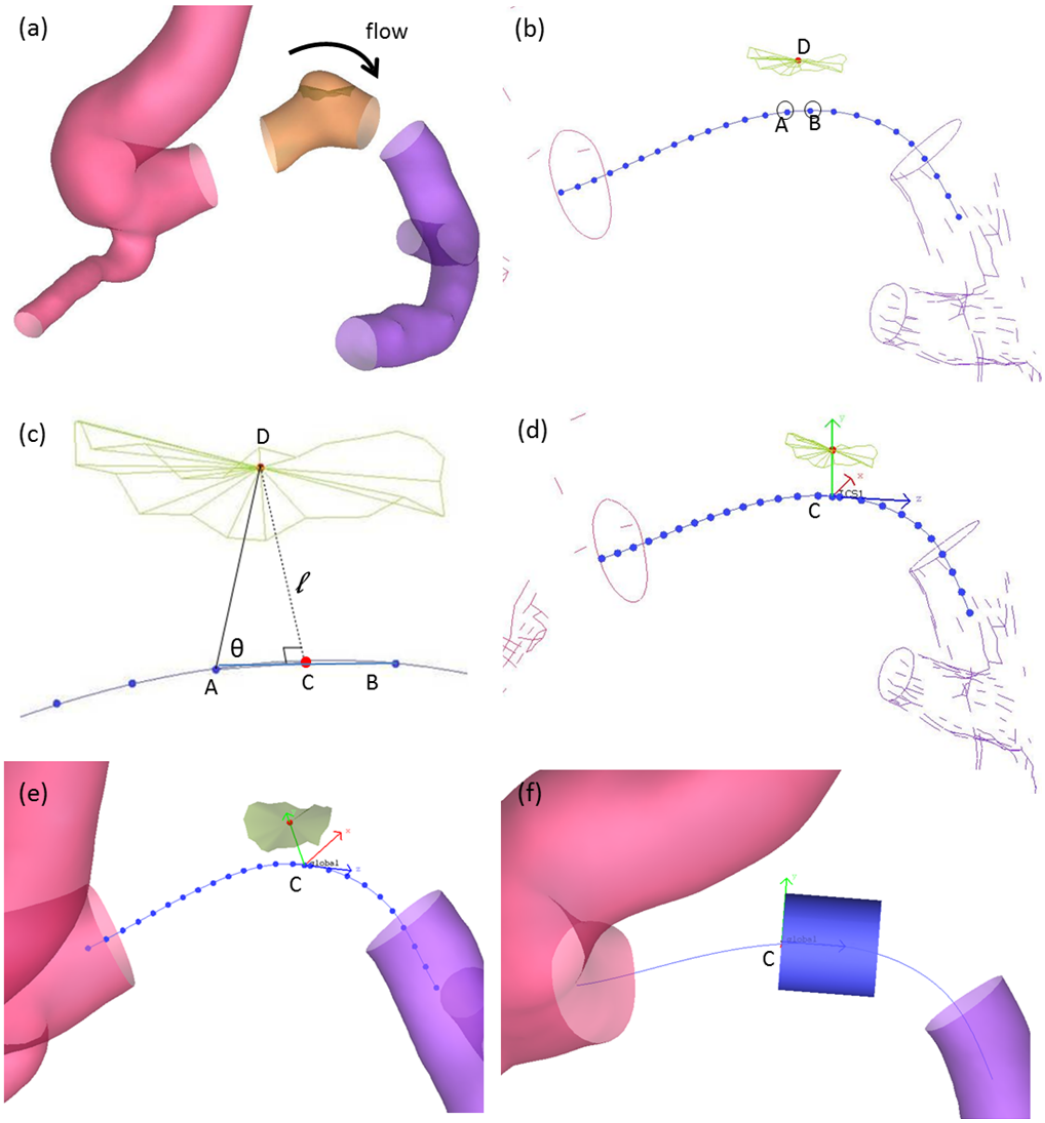


Figure 5.3: Translation of imported geometry to the global axis ((a) - (d)), and positioning of the cylindrical geometry ((e)-(f).) (a) Imported geometry, with the original physiological aneurysm; (b) The geometry in wire-mode, showing the centreline, the aneurysm neck (in green), and the neck centrepoint (in red); (c) - (d) The creation of a local coordinate axis (LCS), from which the upstream and downstream geometry can be translated to the global axis. A perpendicular line from the neckpoint to a short segment on the centreline was found. The intersection of this line to the centreline (point C) represents the point about which the cylinder will be centred. This line was set to coincide with the y-axis of the LCS, while the z-axis was set to point in the direction of flow. (e) The geometry is translated to the global axis. (f) The cylindrical model is imported. As the left edge of the cylinder is centred about the global axis, the upstream and downstream geometry was translated a distance of half the cylinder length such that the cylinder point C lies at the centre of the cylinder.

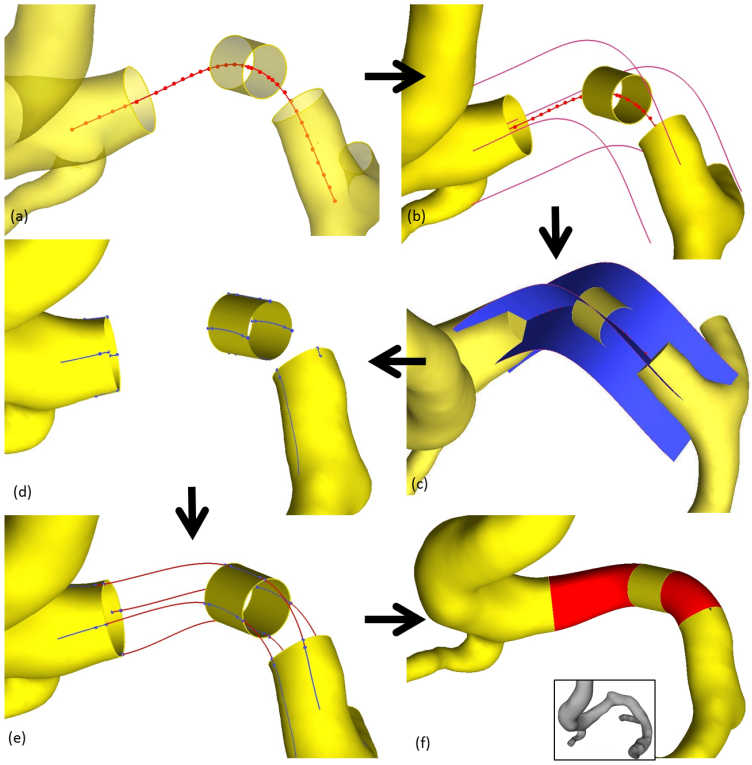


Figure 5.4: Creation of smooth connecting surfaces between the up/downstream geometries and the cylinder in ICEM. (a) and (b) four copies of the centreline are created and positioned a small distance in the positive and negative x and y directions; (c) the ends of curves in the x and y are connected, and surfaces are swept over these to form two, 2D "ribbons'; (d) Extraction of intersections between the created surfaces and the up/downstream surfaces; (e) Connecting curves between cylinder and physiological boundaries; (f) surfaces swept over the connecting curves (inlaid: original geometry)

section between these curves, and the inlet and outlet curves of the up/downstream and cylindrical geometries were marked by points. On each of the curves, a second point was placed a small (arbitrary) distance away from the boundaries (Figure 5.4(d)). Smooth, connecting curves were created linking the corresponding points on the up/downstream and cylinder geometries (Figure 5.4(e)). Using the "Simple Surface" feature in **ICEM**, smooth connecting surfaces were created over the connecting curves (Figure 5.4(f)). The final **ICEM**-based method for smooth surface construction was the result of several revisions. These were performed due to irregular flow profiles observed during simulations, which were attributed to discontinuous gradients at the boundaries between the up/downstream segments and the cylinder.

5.1.1 Demonstration of the ICEM-based surface reconstruction methodology: a study on a physiological geometry

The newly created surfaces were assigned to the up/downstream geometries, and volumes (or "bodies" in **ICEM**) were assigned to the three segments. The cylinder geometry was then removed, and surfaces were placed over all inlets and outlets, including the upstream outlet and downstream inlet where the two segments join to the cylinder. All inlets and outlets were labelled, as per Figure 5.5(a) and (b). The up/downstream geometries were then meshed, utilising the same meshing parameters as per §2.4. A fine mesh (2,585,527 elements, 694962 nodes) was computed. The mesh was exported to **ANSYS CFX** for simulation. Again, boundary conditions were applied utilising `@neufuse` (Figure 5.5(c)).

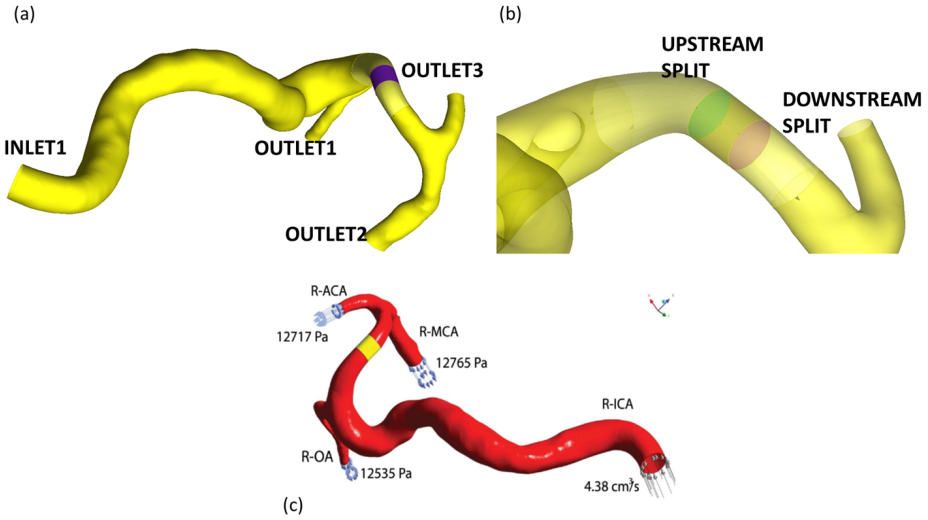


Figure 5.5: Labelling and boundary conditions for the test physiological case. (a) Inlets and outlets; (b) the "splits" between the up/downstream and cylinder segments; (c) Boundary conditions for the haemodynamic domain. R-ACA: right anterior communicating artery; R-MCA: right middle cerebral artery; R-OA: right opthalmic artery; R-ICA: right internal carotid artery

The next step was to validate the **ICEM** methodology for inserting the cylinder into patient-specific geometry, and to determine the potential of gaining further insight into aneurysm development by qualitative comparison of the model aneurysm to the original, physiological aneurysm. Initially, only the less computationally-demanding steady-flow simulations were conducted. As aneurysms generally develop over a number of years (i.e. the average growth-rate

is 0.4cm/year (Humphrey and Rajagopal, 2002), while operation on an aneurysm typically occurs when the diameter is around 5.5cm), a time-period of 12 years was chosen. Computationally, this translates to 600 time-steps (50 time-steps per year, or 0.02 years per time-step), which was found to be an adequate time-discretisation that resulted in time-step independent results (Watton et al., 2004), whilst achieving reasonable computational time.

To determine the threshold value of WSS for elastin degradation (τ_{crit}), and that for maximum elastin degradation (τ_X), the WSS is examined in the circular region at the end of prescribed degradation. In this examination, this time is at $t = 5$ years, and is chosen arbitrarily. The modelling parameters applied are summarised in Table 5.1.

Table 5.1: Summary of modelling parameters applied to the steady-flow simulation on the test physiological case

G&R Parameter	Description	Value
m^E_{min}	Minimum elastin concentration due to prescribed degradation	0.5
t^E_P	Time period over which prescribed elastin degradation occurs	5 years
τ_{crit}	WSS threshold for elastin degradation	15Pa
τ_X	WSS threshold for maximum elastin degradation	0.5Pa
β	Remodelling parameter corresponding to rate at which fibroblasts increase/decrease mass of collagen	0.1
t^β_i, t^β_r	Times at which beta is increased to stabilise aneurysm, and at which beta is restored to original value	11,12 years
b_β	Factor by which β is increased to stabilise aneurysm	100
α	Remodelling parameter corresponding to prescribed half-life of collagen fibres	0.6 $year^{-1}$

The minimum value within the region ($\approx$ 15 Pa in this case) is taken as τ_{crit}, and, as an initial guess, τ_X was set to 0.5Pa to prevent rapid ballooning of the geometry. β is increased by a factor of 100 at $t = 11$ years in order to stabilise the aneurysm.

The most significant observation from steady-flow results is the qualitatively similar evolution of the model aneurysm geometry to the real, physiological aneurysm. The prescribed elastin degradation from $t = 0$ to $t = 5$ years results in a small, initial perturbation to the geometry. In turn, this results in a change in the local levels of wall shear stress, such that the spatial distribution of WSS evolves asymmetrically, with a region of low WSS localised at the proximal part of the dome (Figure 5.6).

As low WSS is linked to elastin degradation, correspondingly, the elastin concentration also evolves asymmetrically, such that it is lowest at the proximal part of the dome. This not only highlights the effect of implementation of the model within a complex, physiological geometry (which results in a more complex blood-flow pattern than that through a cylindrical arterial segment), but also suggests that there may be validity in the hypothesis linking low WSS to elastin degradation.

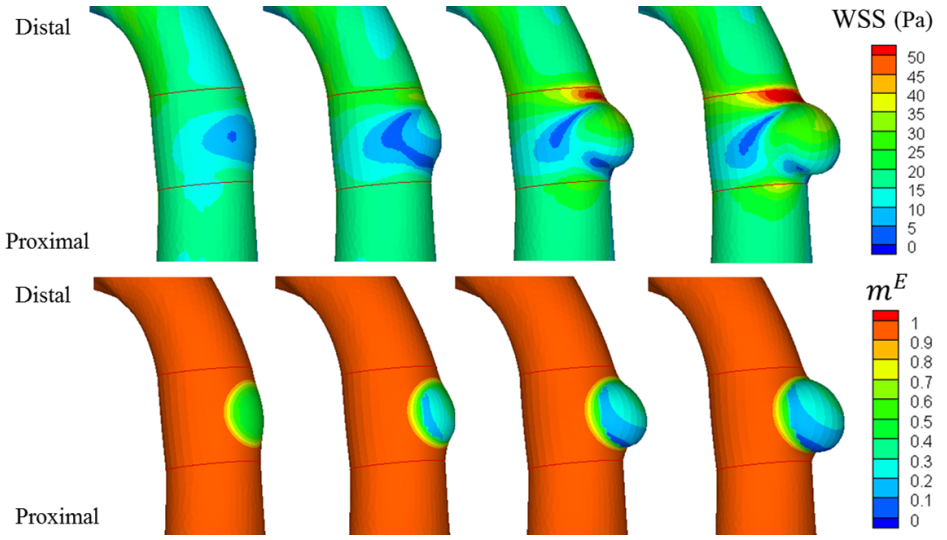


Figure 5.6: Asymmetric evolution of steady-flow WSS (top) following the initial perturbation to the system, and the corresponding asymmetric evolution of the elastin concentration (m^E) (bottom) $t = 5, 8, 10$ and 12 years.

Figure 5.7 shows the evolving non-linear medial elastin strains (defined with respect to the reference configuration) and collagen Green-Lagrange strains (defined with respect to the collagen recruitment configuration). The highest elastin strain is observed to be in the axial direction (i.e. $E_{11}(max) = 18$), which corresponds to a stretch ratio of approximately 6, which is three times higher than the reported failure stretch ratio for elastin Lillie and Gosline (2007). Hence, a fragmentation of elastin fibres is expected, which is not modelled in this work. However, it may bear little influence on the model as elastin degrades over the course of aneurysm evolution -i.e. at $t = 12$ years, the region of highest strain corresponds to an elastin concentration of less than 0.1 (Figure 5.6). and the load-bearing at higher strains The low increase in collagen strain magnitude compared with the elastin strains results from the evolving recruitment configuration of collagen fibres acting to return the strain to the equilibrium (attachment) strain E^C_{AT}.

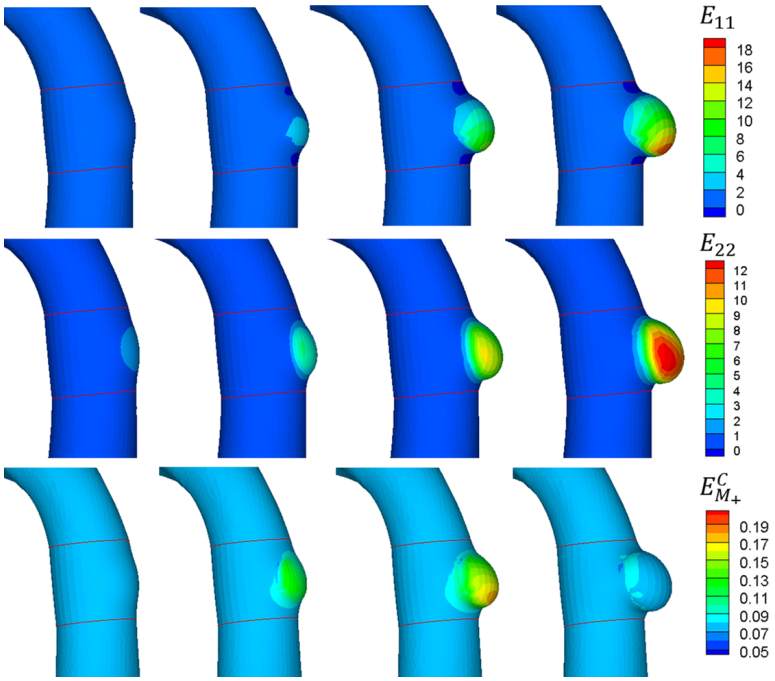


Figure 5.7: Evolution of the medial Green-Lagrange elastin strains E_{11} and E_{22} (top and middle) and the corresponding evolution of the medial collagen Green-Lagrange strain $E^C_{M_+}$ (bottom) at $t = 5, 8, 10$ and 12 years. Elastin strains are observed to steadily increase with increased deformation, while the collagen strain increases only slightly, due to the evolution of the reference recruitment configuration of collagen fibres.

While the **ICEM** method allowed successful implementation of the cylinder model within a patient-specific geometry, it is a method with limitations. While having smooth gradients at the boundaries of the up/downstream and cylinder segments, the created connecting surfaces are themselves smooth, and do not accurately represent the removed segments that they were designed to replace. Figure 5.8 shows the original aneurysm segment and the created connecting surfaces.

Furthermore, while these results are interesting, the single case examined does not provide sufficient grounds for strong conclusions, and as such, implementation of the model into a number of different physiological geometries is necessary. The suspected importance of oscillatory shear in aneurysm development also calls for the investigation of pulsatile-flow haemodynamics in a patient-specific model, and in particular the pulsatile haemodynamic indices discussed in §2.4.1, i.e. OSI, AFI and the GON.

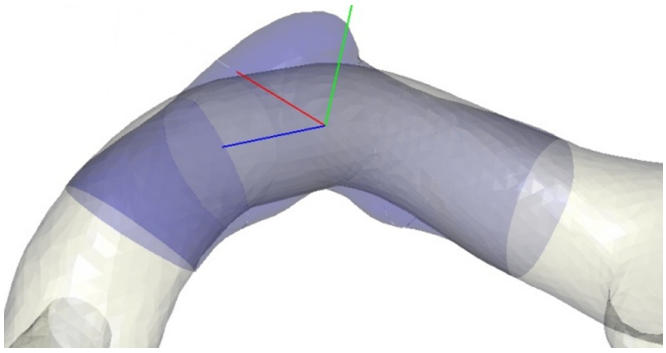


Figure 5.8: Comparison of the original aneurysmal geometry (blue) and the connecting surfaces created in ICEM (transparent yellow overlay)

To this end, our group recently performed a study investigating the correlation of haemodynamic indices proposed in the literature (OSI, AFI, GON, WSS, and WSSG) with the site of aneurysm formation (see Chen et al. (2013)). The study was conducted on 22 clinical cases where the original aneurysm was virtually removed from the vasculature, and a healthy, "pre-aneurysmal" geometry was reconstructed using a novel, algorithmic method developed by Chen et al. (2013). This enabled the investigation of the aforementioned indices prior to aneurysm inception, as well as for a developed aneurysm. It is logical, then, for a study incorporating the cylinder model to be performed on the same 22 cases, as it would enable a cross-comparison of haemodynamic indices at aneurysm inception, during aneurysm growth, and at a later, developed stage. The results of this study will be examined in Chapter 6; here, we are concerned with the development of an automated, algorithmic method for integrating the cylinder model within the patient-specific geometries.

5.2 Integration of the FSG model within patient-specific geometries: a novel, semi-automated algorithmic method

Initially, the algorithmic method for surface reconstruction proposed by Chen et al. (2013) seemed ideally-suited, as the results of their validation study on a healthy arterial segment showed that the geometrical differences between the healthy and reconstructed segments are small, and that the spatial distribution of the haemodynamic indices in the reconstruction region is both quantitatively and qualitatively

similar. Briefly, the core of Chen's methodology is the application of the concept of the torsion of a curve which can be described by a set of basis vectors forming a "moving frame", a frame that moves and rotates along the curve. A section of blood vessel is considered to be formed by the evolution of the boundary plane, i.e. the inlet boundary moves and twists along the centreline, while changing its shape and orientation until it finally matches the outlet boundary. The basis vectors are then used to estimate the shapes of the cross-sections that lie between the inlet and outlet boundaries. By representing the moving boundary by the dynamic basis vectors (including the orientation and the radii of the boundary) at every moment, then the cross sections between the upstream outlet and downstream inlet can be constructed by evaluating the change of basis vectors along the centreline. The new, pre-aneurismal surface is reconstructed by connecting the corresponding points that lie on the cross-sections between the inlet and outlet boundaries (for the interested reader, the methodology is outlined in detail in Chen et al. (2013)). However, the application of the method in the context of connecting the cylinder model to physiological boundaries was limited primarily by the fact that

- the cylinder itself is an unnaturally straight segment that must sit within a naturally curvy physiological geometry, and
- the original physiological aneurysm often occurs very close to a bifurcation, which constrains the length of the surface connecting the cylinder and the physiological boundary close to the bifurcation (see Figure 5.9).

Over a short interpolation interval with high curvature, the cross-sections generated between the inlet and outlet boundaries were observed to overlap. This leads to anomalies in the reconstructed surfaces. Figure 5.10 shows the upstream and downstream segment boundaries of the case shown in Figure 5.9, with different numbers of cross-sections generated between them. Neither limiting nor increasing the number of cross-sections solved the problem. Figure 5.10(d) shows the segments reconstructed using Chen's (2012) method. The connecting segments do not connect smoothly to the cylinder and physiological boundaries, and are observed to intersect the physiological geometry surfaces.

The aforementioned problems necessitated the development of a novel, automated surface reconstruction method, which would avoid the pitfalls of a centreline-based method. One such method used extensively in computer graphics

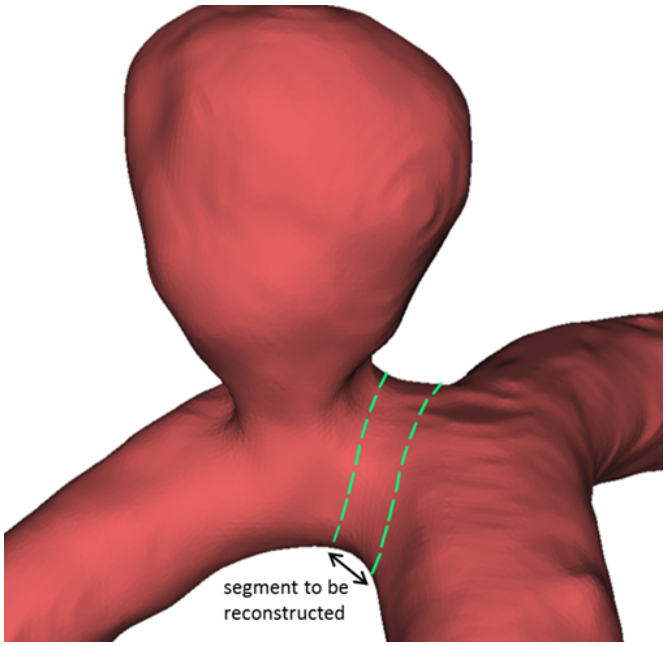


Figure 5.9: Limited length of aneurysmal segment to be removed and reconstructed for an aneurysm developing near a bifurcation

and animation is based on projecting a set of splines across sets of corresponding points on two boundaries to be joined together. The splines can then be connected to form a single continuous surface. The primary advantage of such a method is that it is surface-based, rather than centreline-based. This means that the length of segment to be reconstructed is not an inhibiting factor. In effect, this is an automated version of the **ICEM** surface-reconstruction method.

The primary challenge in developing the method is to find the appropriate spline, which provides a balance between control of the spline trajectory, and user input. While a high level of local control of the spline curvature would be useful in reconstructing surfaces that better resemble the physiological vasculature around them (and is achievable utilising β-splines, for instance) it also increases the amount of user input. For example, in the case of β-splines, visual inspection would be required to determine the weighting of control points, which are used to constrain the trajectory and curvature of the spline. Furthermore, as errors in the geometry are introduced at each stage of image processing and segmentation, what is referred to as the "original, physiological geometry" may not be a strictly accurate representation of the real vasculature. The "lumps and bumps" observed in the segmented physiological geometries may in fact be artefacts arising from the image

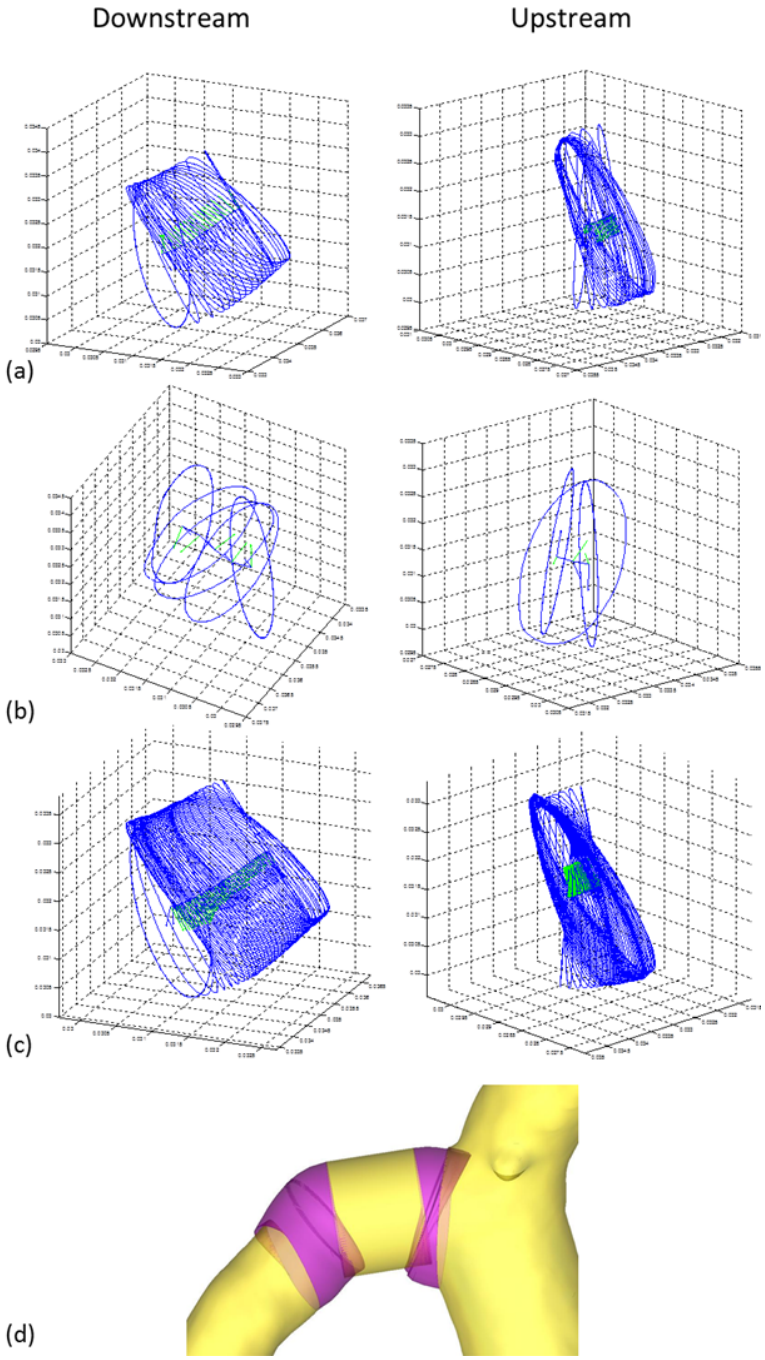


Figure 5.10: Cross-sections generated by Chen's (2012) method, applied to reconstruct surfaces between the cylinder model and the physiological geometry where the original aneurysm developed close to a bifurcation. (a) Cross-sections generated by specifying 5 intervals, with 5 cross-sections/interval; (b) Cross-sections generated by specifying 2 intervals, with 1 cross-section/interval; (c) Cross-sections generated by specifying 5 intervals, with 10 cross-sections/interval; (d) Surfaces (purple) resulting from overlapping cross-sections.

segmentation process. Finally, in this instance we are concerned with implementing a *highly idealised* segment of vasculature within the original physiological geometry. It is logical, therefore, to expect that the surfaces connecting the physiological geometry and the cylindrical segment are unlikely to be realistic representations of their corresponding removed physiological segments, and will likely exhibit differences in spatial location, curvature, and vessel radius.

Given the inherent problems of merging idealised and patient-specific (PS) geometries, the most important condition to be met by an automated surface reconstruction method is the condition of first-order continuity of generated surfaces at the boundaries. Interpolating splines meet this requirement, and require relatively little user input to construct. An investigation into the most appropriate interpolating spline is summarised in §5.2.3.

The sections below describe the complete surface reconstruction algorithm (SRA), which can be divided into a four-stage process of:

1. Geometry clipping and cylinder generation,
2. Physiological boundary re-interpolation,
3. Surface spline generation, and
4. Rotation, translation and export of reconstructed surfaces.

5.2.1 Geometry clipping and cylinder generation

As per the **ICEM** method, the phsyiological geometry is first clipped in `@neufuse` to remove the original aneurysm and a small amount of adjacent vasculature, such that a cylinder can be fitted between. For the cases where the original aneurysm developed near a bifurcation, the maximum length of surrounding vasculature that can be removed is imposed by the proximity of the aneurysm to the bifurcation. For the purpose of comparison, the same physiological case used to develop the **ICEM**-based methodology will be used to demonstrate the SRA here. Figure 5.11 shows how the geometry was segmented to obtain upstream and downstream physiological boundaries. Compared to the **ICEM**-based methodology, this time, a greater portion of the original vasculature surrounding the aneurysmal region is deliberately preserved in order to minimise the length over which the surface splines must

be generated. The reason for this relates to the need for control of the trajectory of interpolating splines, and is discussed further in §5.2.3.

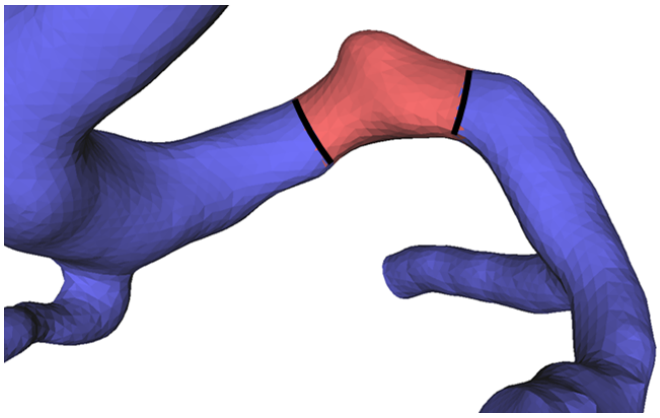


Figure 5.11: Definition of the upstream and downstream segments (blue). Compared to the **ICEM** method, less vasculature around the aneurysmal region (red) is removed

As before, once the vasculature is removed, the up/downstream geometries are exported, along with the aneurysm neckpoint, and the original centreline generated by `@neufuse`. The coordinates of the outlet boundary of the upstream segment and the inlet boundary of the downstream segment are extracted, and, along with the neckpoint and centreline, are imported into `MATLAB`. An algorithm is applied to determine the point on the original centreline which will correspond to the centrepoint of the upstream boundary of the cylinder. The method to determine this point is an automated version of the method employed in the **ICEM**-based methodology (refer to §5.1), and will not be discussed here.

A cylinder with boundaries comprising 120 points is then generated in `MATLAB`, such that it is centred about this point. In this case, the default radius (defined as the average of the physiological outlet and inlet boundary radii), and length (twice the radius value) result in a cylinder with adequate space for generation of connecting surfaces. In cases where the aneurysm developed near a bifurcation, the length of the cylinder needs to be manually adjusted so as to avoid one edge of the cylinder intersecting the physiological geometry surface. In such cases, a length of 1.5 times the radius was adequate.

The cylinder is then exported in Standard Tessellation Language (STL) format, which is a useful format as it is compatible with

- `@neufuse` which is used to segment geometries,
- **Tecplot 360** which is used to extract the coordinates of geometry boundaries, and
- **ICEM**, which is used to mesh the geometry in preparation for CFD simulations

Figure 5.12 shows the cylinder plotted in `MATLAB`, and its STL counterpart between the physiological boundaries of the test ICA case. The points comprising the cylinder boundaries are then extracted, and now, the surface-generation part of the algorithm can be executed.

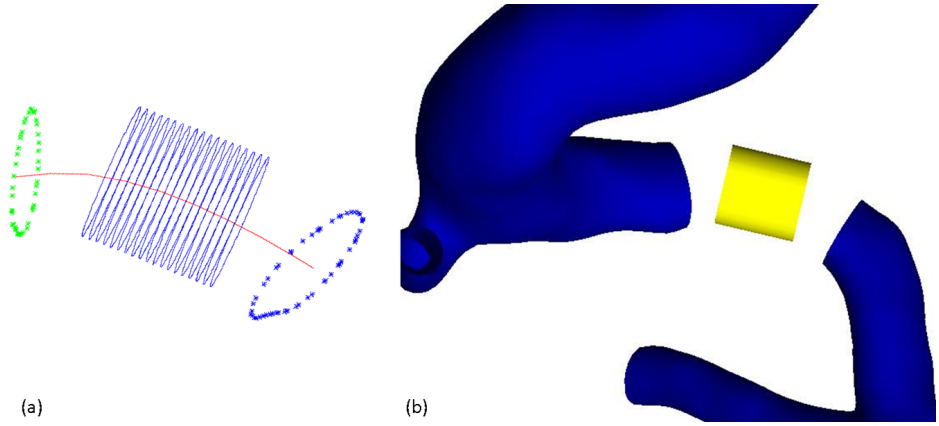


Figure 5.12: Plot of cylinder generated in `MATLAB` (a), and cylinder STL (b) positioned between physiological boundaries

5.2.2 Physiological boundary re-interpolation

In order to create smooth surfaces linking the physiological geometry and the cylinder, the physiological outlet and cylinder inlet (as well as the physiological inlet and cylinder outlet) must have equal numbers of points. It is between these points, referred to as *knots*, that individual splines are created. The physiological inlet and outlet boundaries comprise an arbitrary number of points, in an arbitrary order. Therefore, the physiological boundaries must be re-interpolated so as to have the same number of points and with the same angular displacement as that of the cylinder boundaries. Furthermore, the points must be ordered such that point 1 on the physiological boundary is the point which is closest to point 1 on the cylinder

boundary. This is necessary to avoid the creation of incorrect, or highly twisting surfaces, which arises when correspondingly numbered points on the two boundaries are not at corresponding locations in space.

To achieve this, a radial-spline interpolation is applied to the physiological boundaries (Figure 5.13). Each point on the boundary is defined in terms of R, the radial distance of the point from the centrepoint of the boundary (determined as the mean of all the boundary points), and θ , the included angle counted from the starting point on the boundary. For a set of M points, two adjacent points on the boundary can be defined as $[R(m),\theta(m)]$ and $[R(m+1),\theta(m+1)]$. An intermediate point $[R(i),\theta(i)]$ (where $\theta(m) < \theta(i) < \theta(m+1)$ and i represents 1° increments) can then be determined using

$$R_i = R_m + (R_{m+1} - R_m) \cdot \left(\frac{\theta_i - \theta_m}{\theta_{m+1} - \theta_m} \right) \tag{5.1}$$

Therefore, for each increment of i, two adjacent points with angles $\theta(m)$ and

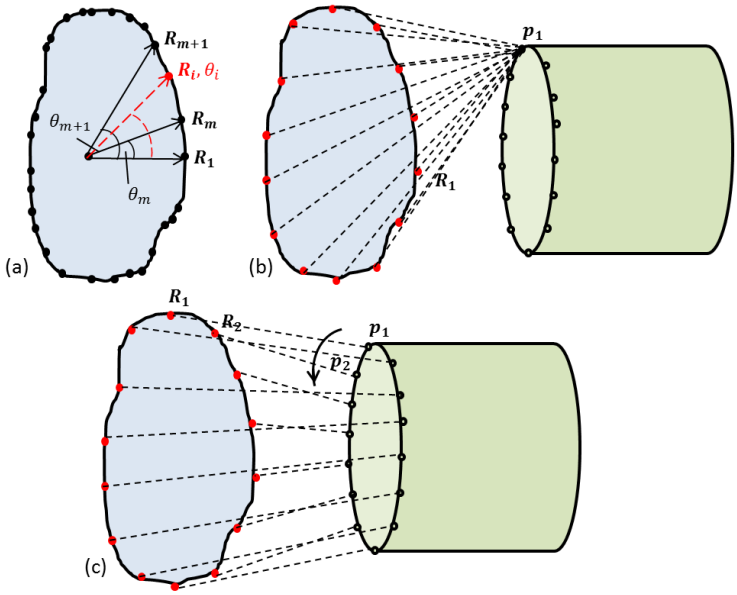


Figure 5.13: Reinterpolation of the physiological geometry boundary (a), so as to achieve an equidistant distribution of points (b). The point on the physiological boundary at position 1 is the point at the shortest absolute distance to point 1 ($\mathbf{p_1}$) on the cylinder.

$\theta(m+1)$ which are closest to the current angle, $\theta(i)$, are determined and used to calculate the interpolated point $R(i)$. This results in a re-interpolated boundary with 360 equidistant points. As the cylinder boundaries each comprise only 120

equidistant points, every third point from the physiological boundary is removed to achieve 120 points. The absolute distance between the first point on the cylinder boundary and each point on the corresponding physiological boundary is evaluated. The point on the physiological boundary which is at the shortest distance from the first point on the cylinder boundary is designated as point '1'. The position of the points increments in an anti-clockwise direction from point 1 on the cylinder. With the physiological boundaries re-interpolated to match the cylinder boundaries, the next task is to generate the splines which form the basis for the reconstructed surfaces.

5.2.3 Surface spline generation

Recall that the splines that form the basis for the reconstructed surfaces must meet the condition of first-order continuity at the knots, and that interpolating splines satisfy this requirement. The simplest interpolating spline is a cubic polynomial, which runs between two corresponding points on the boundaries, and is constructed from a set of parametric curves x, y and z of the form

$$x(t) = a_3 t^3 + a_2 t^2 + a_1 t + a_0$$
$$y(t) = b_3 t^3 + b_2 t^2 + b_1 t + b_0$$
$$z(t) = c_3 t^3 + c_2 t^2 + c_1 t + c_0, t \in [0,1]$$

The coefficients $a_3, \ldots, a_0, b_3, \ldots, b_0, c_3, \ldots, c_0$ are determined from two sets of known initial conditions:

1. The beginning and end-points of the spline, given by each of the 120 corresponding pairs of points on the physiological and cylinder boundaries, and
2. The tangents at these points, which are given by the unit boundary normals.

However, while cubic polynomials are smooth and meet the required continuity conditions, it is difficult to control the degree of spline curvature with only two knots (i.e. the centrepoints of the cylinder and physiological boundaries). In turn, spline curvature is controlled by spline tension. The problem of controlling spline tension is briefly discussed here, as it provides the rationale for the final choice of spline.

Spline tension affects the degree of freedom of twisting of the spline across the interpolating interval. A good illustrative analogy is a piece of string: with each end

of the string held loosely, the string can twist and bend more freely than when the string is pulled taught. Mathematically, this translates to scaling the magnitudes of the tangent vectors at the knots of the spline. The problem lies in selecting the appropriate scaling factors, and a review of the relevant literature reveals that this problem still lacks a definitive answer. Manning (1974), for instance, discovered through experimentation some basic bounds for the magnitude of boundary tangent vectors, with respect to the straight-line distance between two points (Figure 5.14).

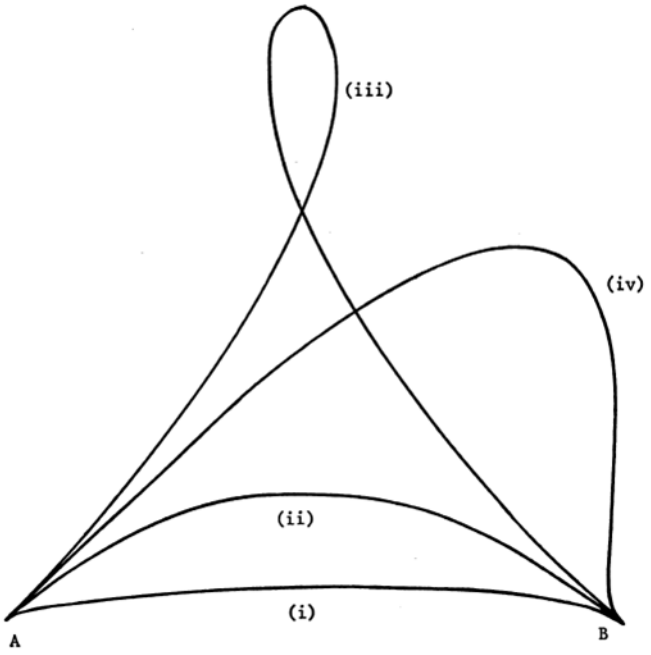


Figure 5.14: Effect on spline curvature of varying cubic spline tangent magnitudes $|T_A|$ and $|T_B|$ at knots A and B (adapted from Manning (1974)

Figure 5.14 shows two points, A and B, with tangent vectors $|\mathbf{T_A}|$ and $|\mathbf{T_B}|$, and W representing the straight-line distance between them, where

- curve (i) represents the spline where $|\mathbf{T_A}|$ and $|\mathbf{T_B}| << W$
- curve (ii) represents the spline where $|\mathbf{T_A}|$ and $|\mathbf{T_B}|$ are comparable to W,
- curve (iii) represents the spline where $|\mathbf{T_A}|$ and $|\mathbf{T_B}| >> W$, and
- curve (iv) represents the spline where $|\mathbf{T_A}| >> W$ while $|\mathbf{T_B}| << W$.

However, Manning emphasises that the determination of the "most acceptable" curves was a subjective judgement. This problem of subjectivity in determining the most acceptable curve is a resonant feature of interpolating splines, even when they are more strictly defined, as per the "Kochanek-Bartels" spline (Kochanek and Bartels, 1984), which is still widely employed in computer animation. Indeed, in their paper on interpolating splines for animation systems, Kochanek and Bartels (1984) introduce tension, continuity and bias as three scaling parameters applied to the tangent vectors in order to control the shape of the spline. However, similarly to Manning, they found that the value of the tension parameter producing the most "natural looking curve" varied between animators. In this instance, an optimal solution is a compromise between a tightly controlled spline (such as the Kochanek-Bartells spline), and one with a greater degree of freedom of curvature (i.e. a basic cubic spline). Specifically, we desire a spline with a trajectory that conforms to the direction of the boundary tangents in the vicinity of the boundaries, and has some, albeit constrained curvature in the region between them.

A novel solution was developed based on a weighted sum of linear segments, utilising a sigmoid weighting function defined over an interval $t \in [-1, 1]$. A sigmoid has the useful property of tending towards two bounds, with a smooth trajectory in between. This makes it ideal for use as a weighting function, which forces the trajectory of the spline to conform to the direction of the two boundary normals. The method for generating the spline between two points is described in the following section. To the knowledge of this author, this method of generating 3D surfaces has not been previously reported in the literature.

5.2.3.1 Sigmoid-weighted spline

Figure 5.15-Figure 5.18 show the process of generating a sigmoid-weighted spline. For simplicity, consider the construction of a single spline that joins the *centre-points*, $\mathbf{c_u}$ and $\mathbf{c_d}$, of two boundaries, one upstream of the other (hereon referred to as u_{bound} and d_{bound}). $\hat{\mathbf{n}}_\mathbf{u}$ and $\hat{\mathbf{n}}_\mathbf{2}$ represent the u_{bound} and d_{bound} normals. Firstly, the straight-line segment, $\mathbf{c}$, between $\mathbf{c_u}$ and $\mathbf{c_d}$ is defined (leftmost panel of Figure 5.15), i.e.

$$\mathbf{c}(t) = \frac{1}{2}t(\mathbf{c_u} + \mathbf{c_d}) + \frac{1}{2}t(\mathbf{c_d} - \mathbf{c_u}). \tag{5.2}$$

We can see that at the beginning and end of the interval, at $t = -1$ and $t = 1$

$$\mathbf{c}(-1) = \mathbf{c_u}, \text{and}$$
$$\bar{c}(1) = \mathbf{c_d}$$

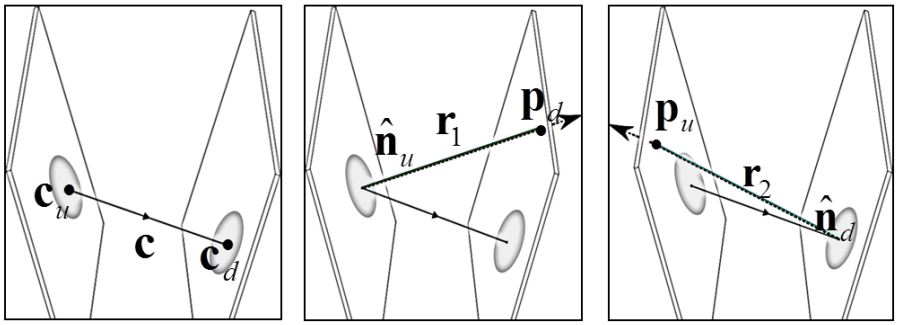


Figure 5.15: Definition of the straight-line segment between boundary centrepoints (panel 1), and segments $\mathbf{r_1}$ and $\mathbf{r_2}$ linking boundary centrepoints and normal-boundary plane intersects $\mathbf{p_u}$ and $\mathbf{p_d}$ (panels 2 & 3)

Two points, $\mathbf{p_d}$ and $\mathbf{p_u}$ -the first representing the intersection between $\hat{\mathbf{n}}_\mathbf{u}$ and the plane of d_{bound}, the second representing the intersection between $\hat{\mathbf{n}}_\mathbf{d}$ and the plane of u_{bound} -are found using the equation for the intersection of a line and a plane (middle and right panels of Figure 5.15). The line segments between $\mathbf{c_u}$ and $\mathbf{p_d}$, and $\mathbf{c_d}$ and $\mathbf{p_u}$ can then be defined as follows:

$$\mathbf{r_1}(t) = \frac{1}{2}t(\mathbf{c_u} + \mathbf{p_d}) + \frac{1}{2}t(\mathbf{p_d} - \mathbf{c_u}) \tag{5.3}$$

and

$$\mathbf{r_2}(t) = \frac{1}{2}t(\mathbf{c_d} + \mathbf{p_u}) + \frac{1}{2}t(\mathbf{p_u} - \mathbf{c_d}) \tag{5.4}$$

Here, we introduce the sigmoid function (Figure 5.16), defined over the interval $t \in [-1, 1]$:

$$f(t) = \frac{1}{1 + e^{-at}} \tag{5.5}$$

At $t = \pm 1$, the function tends towards 0 and 1 respectively. The value of a determines the sharpness of curvature at the inflection point. As we require a smooth curve with a gradually-changing trajectory, the logical choice is a low value of a. Experimentation showed that $a = 2$ consistently produced desirable curves.

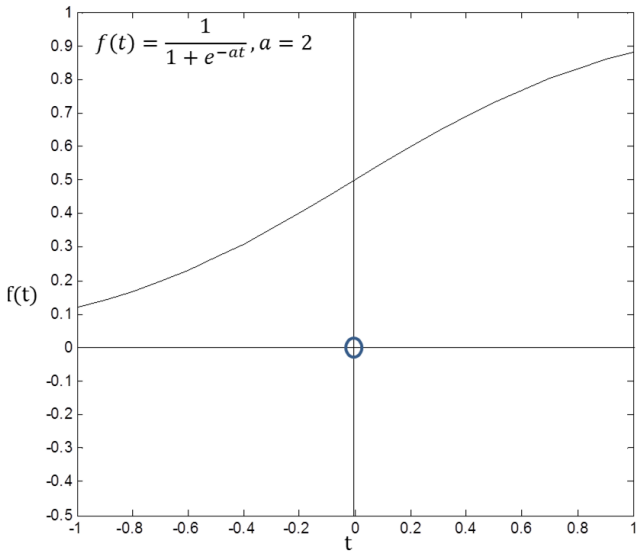


Figure 5.16: Sigmoid function, defined over the interval $t \in [-1, 1]$

We can now define two splines, $\mathbf{r_{c_1}}$ and $\mathbf{r_{c_2}}$ (Figure 5.17), as follows

$$\mathbf{r_{c_1}}(t) = f(t)\mathbf{c}(t) + f(-t)\mathbf{r_1}(t) \tag{5.6}$$

and

$$\mathbf{r_{c_2}}(t) = f(t)\mathbf{r_2}(t) + f(-t)\mathbf{c}(t) \tag{5.7}$$

At the beginning of the interval, where $t = -1$

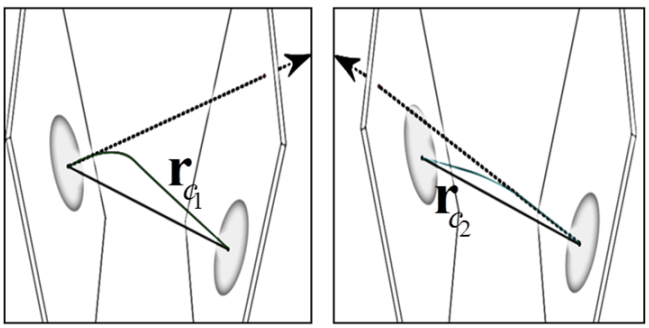


Figure 5.17: Definition of splines $\mathbf{r_{c_1}}$ and $\mathbf{r_{c_2}}$, with tangents continuous at the upstream and downstream boundaries respectively

$$\mathbf{r_{c_1}}(-1) = f(-1)\mathbf{c}(-1) + f(1)\mathbf{r_1}(1) = \mathbf{c_u}$$

Although at $t = \pm 1$, the sigmoid does not evaluate exactly to 0 and 1, the sum $f(-1) + f(1) = 1$. Hence, at the beginning of the interval, we are at the starting point of the spline, $\mathbf{c_u}$. At the mid-point of the interval, where $t = 0$,

$$\begin{aligned}\mathbf{r_{c_1}}(0) &= f(0)\mathbf{c}(0) + f(0)\mathbf{r_1}(0) \\ &= \frac{1}{2}\mathbf{c}(0) + \frac{1}{2}\mathbf{r_1}(0),\end{aligned}$$

which gives a point corresponding to the average value of segments c and r_1 at $t = 0$. Finally, at the end of the interval, where $t = 1$,

$$\mathbf{r_{c_1}}(1) = f(1)\mathbf{c}(1) + f(-1)\mathbf{r_1}(1) \approx \mathbf{c_d}$$

As the sigmoid does not evaluate to 0 and 1 at $t = \pm 1$, the end point of the spline is not exactly $\mathbf{c_d}$. However, this is unimportant, as we are only concerned about the starting point of the spline, which must be such that its trajectory is in line with the upstream boundary normal. Indeed, it can be seen that over the interval $t = -1$ to $t = 1$, the weight of segment $\mathbf{r_1}$ diminishes from 1 to 0, while the weight of segment $\mathbf{c}$ increases from 0 to 1. The resulting spline has a trajectory that is, over the first half of the interval, largely determined by $\mathbf{r_1}$ (the u_{bound} normal). Over the second half of the interval, the trajectory of the spline is predominantly determined by segment $\mathbf{c}$. Evaluation of the second spline, $\mathbf{r_{c_2}}(t)$, over the interval $t \in [-1, 1]$ gives

$$\begin{aligned}&\text{for } t = -1 \\ \mathbf{r_{c_2}}(-1) &= f(-1)\mathbf{r_2}(1) + f(1)\mathbf{r_2}(-1) = \approx \mathbf{c_u}; \\ &\text{for } t = 0 \\ \mathbf{r_{c_2}}(0) &= f(0)\mathbf{r_2}(0) + f(0)\mathbf{c}(0) \\ &= \frac{1}{2}\mathbf{r_2}(0) + \frac{1}{2}\mathbf{c}(0); \\ &\text{for } t = 1 \\ \mathbf{r_{c_2}}(1) &= f(1)\mathbf{r_2}(-1) + f(-1)\mathbf{c}(1) = \mathbf{c_d}\end{aligned}$$

In the case of $\mathbf{r_{c_2}}$, the trajectory of the spline is such that the weight of segment $\mathbf{c}$ diminishes from 1 to 0, while the weight of segment $\mathbf{r_2}$ increases from 0 to 1. In this case, the end-point of the spline is important, and must be such that its trajectory is in line with the downstream boundary normal, $\mathbf{n_d}$. Indeed, it can be seen that

over the first half of the interval, the trajectory of the spline is predominantly determined by **c**, while over the second half of the interval, the trajectory of the spline is predominantly determined by $\mathbf{r_2}$ -i.e. near the cylinder boundary, the direction of $\mathbf{r_{c_2}}$ conforms to that of the cylinder boundary normal.

We now have two splines: $\mathbf{r_{c_1}}$, which meets continuity conditions at u_{bound}, and $\mathbf{r_{c_2}}$, which is continuous at d_{bound}. An average of the two over the interval $t \in [-1,1]$, therefore results in the desired spline (Figure 5.18).

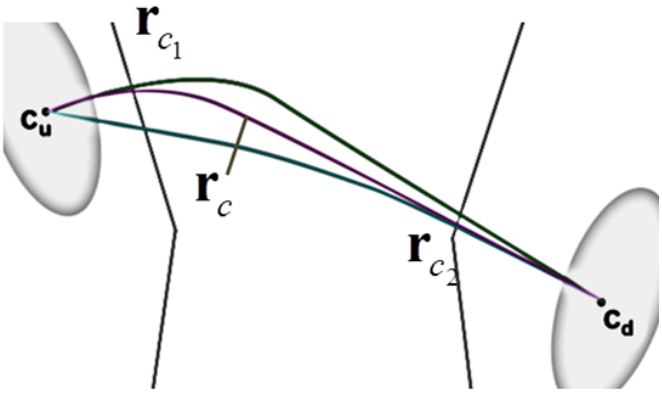


Figure 5.18: Definition of a spline $\mathbf{r_c}$, with tangents continuous at both the upstream and downstream boundaries

We define the final spline, $\mathbf{r_c}$ as follows:

$$\mathbf{r_c}(t) = \frac{1}{2}\left(\bar{r_{c_1}}(t) + \bar{r_{c_2}}(t)\right) + \frac{1}{2}\left(\mathbf{r_{c_2}}(t) - \mathbf{r_{c_1}}(t)\right) \tag{5.8}$$

Evaluation of $\mathbf{r_c}(t)$ over the interval gives

$$\begin{aligned}
&\text{for } t = -1 \\
\mathbf{r_c}(-1) &= \frac{1}{2}\left(\mathbf{r_{c_1}}(-1) + \mathbf{r_{c_2}}(-1)\right) - \frac{1}{2}\left(\mathbf{r_{c_2}}(-1) - \mathbf{r_{c_1}}(-1)\right) \\
&= \mathbf{r_{c_1}}(-1) = \mathbf{c_u}; \\
&\text{for } t = 0 \\
\mathbf{r_c}(0) &= \frac{1}{2}\left(\mathbf{r_{c_1}}(0) + \mathbf{r_{c_2}}(0)\right); \\
&\text{for } t = 1 \\
\mathbf{r_c}(1) &= \frac{1}{2}\left(\mathbf{r_{c_1}}(1) + \mathbf{r_{c_2}}(1)\right) - \frac{1}{2}\left(\mathbf{r_{c_2}}(1) - \mathbf{r_{c_1}}(1)\right) \\
&= \mathbf{r_{c_2}}(1) = \mathbf{c_d},
\end{aligned}$$

which produces a spline that meets continuity conditions at both boundaries, and follows a smooth trajectory (bound strictly by segments $\mathbf{r_1}$ and $\mathbf{r_2}$) from $\mathbf{c_u}$ to $\mathbf{c_d}$. As only two knots are used to generate the spline (spline trajectory is controlled only by the two boundary normals), the interpolating interval is kept deliberately short to constrain the spline trajectory in between the boundaries.

Splines are then generated between the entire set of 120 pairs of points on the physiological and cylinder boundaries. Each spline is sampled 50 times at equidistant intervals, resulting in a total set of $120 \times 51 = 6120$ points, which define the coordinates matrix of each reconstructed surface. The coordinates are arranged in a 6120×3 matrix such that points 1-120 represent the upstream physiological boundary, points 121-240 represent the first sample of each of the 120 splines, end so on. This organisation effectively groups the points of the splines into a set of cross-sections. Figure 5.19(a) shows the upstream and downstream reconstructions for the test ICA case in terms of the points of the sigmoid-weighted splines. As described in §5.2.1, connectivity matrices are specified for the coordinates of both the upstream and downstream sets of splines, which are employed at the end to generate STLs of the newly-constructed connecting surfaces (Figure 5.19(b)).

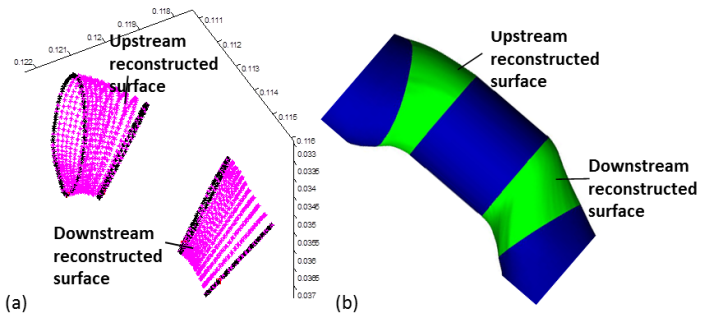


Figure 5.19: Reconstructed surfaces in terms of the points that comprise the sigmoid-weighted splines, plotted in MATLAB (a); (b) the final surfaces

5.2.4 Rotation, translation, and export of reconstructed surface STLs

Recall that the cylinder growth model is set such that the midpoint of the upstream edge of the cylinder coincides with the global origin (i.e. $(0,0,0)$), with the cylinder

axis aligned with the positive z-axis. For the purpose of conducting a haemodynamics simulation with the growth model integrated into the geometry, the entire arterial geometry (the up/downstream, and newly constructed segments) must be rotated and translated, such that the upstream edge of the cylinder sits about the global origin. In the **ICEM**-based methodology, rotation and translation was performed utilising **ICEM**'s geometry tool-suite. Here, rotation and translation is performed algorithmically, in `MATLAB`.

To achieve this, it is useful to consider the arterial geometry in its original location as having some orientation about a local origin, O_l, which is at the centre of a local, right-handed coordinate system B, defined by a set of orthogonal, unit basis vectors **bx**, **by** and **bz**, such that

$$B = \begin{bmatrix} b_{x_1} & b_{x_2} & b_{x_3} \\ b_{y_1} & b_{y_2} & b_{y_3} \\ b_{z_1} & b_{z_2} & b_{z_3} \end{bmatrix}$$

In turn, this *local* coordinate system sits within the global, right-handed coordinate system **A** about a global origin O_g, and defined by a set of orthogonal unit basis vectors **ax**, **ay** and **az**, such that

$$A = \begin{bmatrix} a_{x_1} & a_{x_2} & a_{x_3} \\ a_{y_1} & a_{y_2} & a_{y_3} \\ a_{z_1} & a_{z_2} & a_{z_3} \end{bmatrix}$$

For the purpose of illustration, let us consider the geometry as a cube, which sits about the local coordinate origin such that one corner of the cube coincides with the local origin (Figure 5.20). Translation is simple: since we know the vector $\overrightarrow{O_g O_l}$, and since every point on the cube has a position vector with respect to the global origin (i.e. $\overrightarrow{O_g P_1}, \overrightarrow{O_g P_2}$, etc), then we can simply subtract $\overrightarrow{O_g O_l}$ from the position vector of every point to translate the cube to the global origin.

To complete the task, we require a rotation matrix, ${}^{b}R^{a}$, by which we can multiply all the geometry points, to achieve the desired orientation about the global coordinate axes. A rotation matrix specifies the orientation of our right-handed coordinate system A with respect to B, and its elements $R_{ij(i,j=x,y,z)}$ are given by

$$R_{ij} \equiv \mathbf{a_i} \cdot \mathbf{b_j}$$

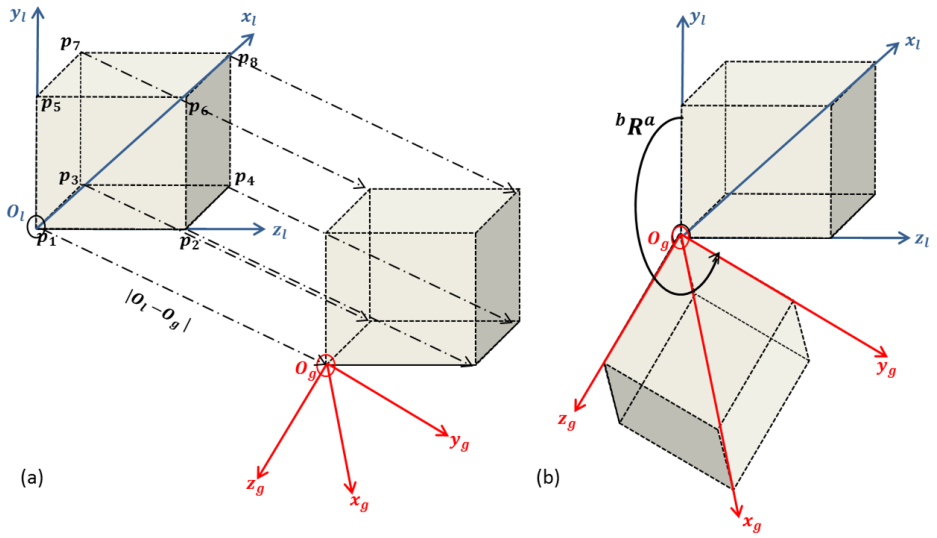


Figure 5.20: Translation and rotation of a geometry between local and global coordinate systems. The distance, $|\mathbf{O_l} - \mathbf{O_g}|$, between the local and global coordinate systems provides the translation distance (a), while the rotation matrix, ${}^{b}R^{a}$, rotates the geometry such that the axes of the local and global coordinate systems align.

To define the rotation matrix ${}^{b}R^{a}$, we can represent the orientation of the local coordinate system B with respect to the global coordinate system, as

$$B = {}^{b}R^{a}.A$$

By rules of matrix algebra,

$$\begin{aligned} B.A^{T} &= {}^{b}R^{a}.A.A^{T} \\ &= {}^{b}R^{a}.I \\ &= {}^{b}R^{a} \end{aligned}$$

Since A represents the global coordinate system, then we can consider the unit basis elements of A as

$$\begin{aligned} a_x &= [100], \\ a_y &= [010], and \\ a_z &= [001], \end{aligned}$$

such that A is in fact a diagonal matrix. Since the transpose of a diagonal matrix is, again, a diagonal matrix, then the equation for the rotation matrix ${}^{b}R^{a}$ simplifies to

$${}^{b}R^{a} = B$$

Thus, to rotate the geometry such that its orientation about the global coordinate system axes is the same as its orientation about the local coordinate system axes, we need only multiply all geometry points by the matrix representative of the local coordinate system.

In the present problem, the orthogonal bases that define the local coordinate system (LCS) B are defined using 3 points:

1. the aneurysm neckpoint, p_{neck},
2. the centrepoint of the cylinder. This point is the local origin, O_l, of LCS B, and
3. a point on the original centreline, p_s that is at the shortest distance from the point about which the cylinder is centred (see Figure 5.3(c) and (d) in §5.1)

The vector joining the local origin to the aneurysm neckpoint defines the local y-axis, while the vector joining the local origin to point p_s defines the local z-axis. By taking the cross-product of their unit vectors, we obtain the local unit x-axis, and hence the unit orthogonal bases of the local coordinate system B. Translation of the coordinates defining the physiological and reconstructed surfaces is performed first. The translation takes into account the additional translation of the geometry of half the cylinder length in the positive z direction, which is required because the upstream edge of the cylinder is centred about the global origin. The coordinates are then multiplied by the rotation matrix to achieve the desired orientation about the global origin.

With the geometry correctly positioned, the connectivity and coordinate matrices corresponding to the upstream physiological (UP) geometry, downstream physiological (DP) geometry and the up/downstream reconstructed geometries are utilised to construct and export new STLs. The new STL files are imported into **ICEM**, and the same meshing procedure described in §5.1.1 is applied. The mesh is then exported to **ANSYS CFX** for the set-up of simulation parameters, and for simulation. The modelling parameters were identical to those applied to the geometry corresponding to the **ICEM** methodology, and are summarised in Table 5.1.

5.2.5 Demonstration of the algorithmic surface reconstruction methodology: a study on a physiological geometry

Figure 5.21 shows the evolving WSS and elastin concentration at $t = 5, 8, 10$ and 12 years. A locally low WSS (and a corresponding reduction in elastin concentration) is observed to arise at both the distal and proximal ends, as well as laterally. As such, a large bulge develops towards the proximal part of the dome, and a smaller one towards the distal end.

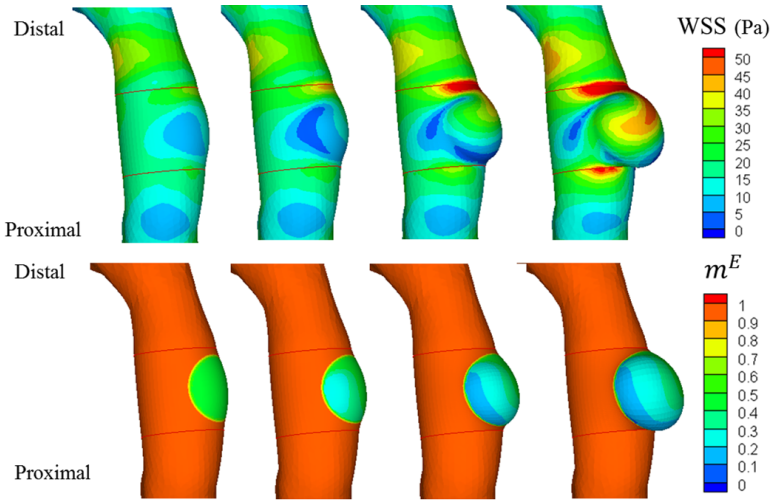


Figure 5.21: Evolution of the WSS (top) and elastin concentration (bottom) for the algorithmically-reconstructed geometry at $t = 5, 8, 10$ and 12 years.

Figure 5.22(a) compares the WSS distribution and size of the final geometries corresponding to the **ICEM**-based vs algorithmic-reconstruction methods (hereon referred to as "the **ICEM** geometry" and "the algorithmic geometry"). Although both geometries evolve asymmetrically towards the proximal part of the vessel, the algorithmic geometry is larger, and the bulging of the dome is more pronounced. A second, smaller bulge is observed at the distal end of the algorithmic geometry. This is the result of the evolving WSS environment, and can be seen by comparing the evolving elastin concentration for the two geometries (Figure 5.22(b)). In the case of the **ICEM** geometry, rapid degradation of elastin is localised to a small patch at the proximal part of the domain, and less so in all other regions, resulting in a pronounced bulge towards the proximal part of the artery. In contrast, in the case of the algorithmic geometry, a rapid degradation of elastin occurs in both the distal and proximal regions of the domain.

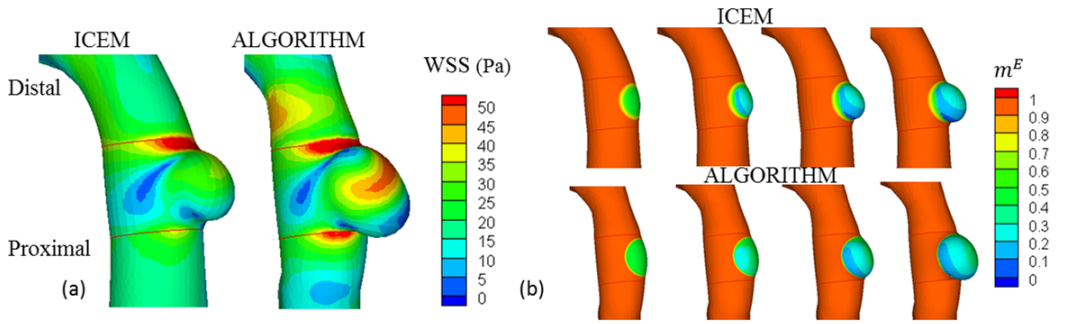


Figure 5.22: Comparison of the final geometries ($t = 12$ years) corresponding to the **ICEM**-based and algorithmic methods. (a) The WSS environment of the final geometries; (b) and the evolving elastin concentration

In turn, the differences in the evolving WSS (and hence, elastin) are accounted for by the differences in arterial geometry immediately adjacent to the cylindrical domain. Of particular consequence is the local haemodynamic environment immediately upstream of the cylindrical domain, from which the haemodynamic patterns *within* the cylindrical domain arise. Figure 5.23 compares the evolving WSS environment for the entire **ICEM** and algorithmic geometries.

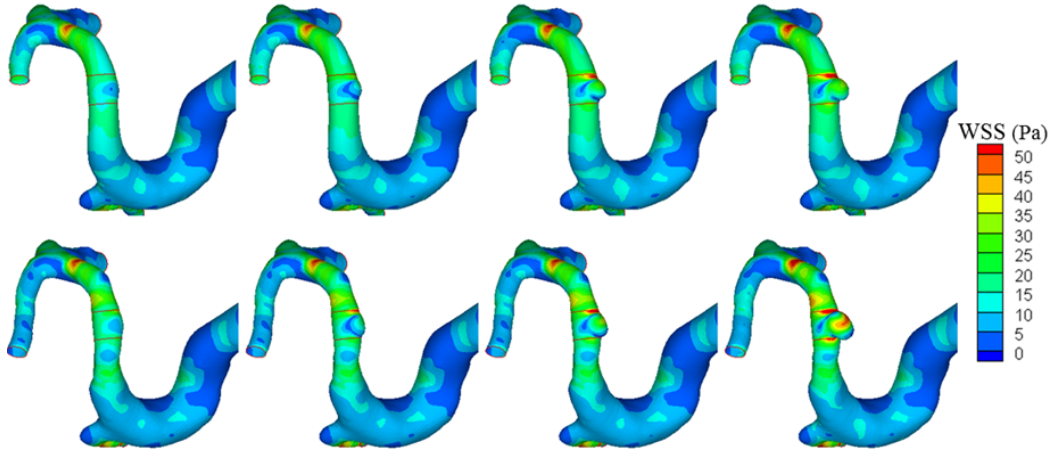


Figure 5.23: The evolving WSS shown for the full **ICEM** and algorithmic geometries from $t = 5$ to $t = 12$ years

For the algorithmic geometry, a greater portion of original vasculature was deliberately preserved. As such, the haemodynamics environment immediately upstream of the cylindrical domain is different, and features a patch of reduced WSS (<10Pa), while WSS is 15-20Pa in the same region of the **ICEM** geometry. Compared to the algorithmic geometry, the surfaces created in **ICEM** are smoother, and the

resulting upstream and downstream reconstructed vessels are narrower than the original vasculature (see Figure 5.8). However, although there are some differences in the WSS environment in the region upstream of the aneurysmal segment, these appear to have a small effect on the region immediately adjacent to the aneurysmal segment. Consequently, the model **ICEM** and algorithmic aneurysm geometries evolve similarly. Compared to Chen's (2013) methodology, the current method has the advantage of being surface-based, rather than centre-line based, which allows the connection of the cylinder model to physiological boundaries over very short, and highly-curved intervals (i.e. in regions where the original aneurysm developed very close to a bifurcation). Like surfaces produced by Chen's (2013) method, the surfaces generated utilising this algorithm are smooth, but in contrast, do not satisfy second-order continuity at the boundaries.

The ease of execution of the algorithmic method makes it ideally suited for application to a large number of cases, which allow a more rigorous examination of the spatial distributions of haemodynamic indices at aneurysm inception. This may shed light on the question of how modelling aneurysm inception, which is prescribed in the current modelling framework (see §4.4.2), may be improved by coupling inception to the local haemodynamic environment. In turn, this may result in an even better approximation of the evolving model aneurysm geometry to the corresponding physiological aneurysm.

As such, the algorithm was employed to embed the cylindrical model within 16 physiological geometries. While "pre-aneurysmal" segments generated by Chen's (2012) surface-reconstruction methodology closely conformed to the general size and location of the original aneurysmal segment, this is not always the case in the present study. Of the 16 geometries, 12 were observed to match very closely with the original geometry both throughout the parent artery and at the aneurysmal region. The age of the patients varies between 56 and 90 years (average 71.25 years), with eight females, and four males. Table 5.2 summarises the information, including the location of the aneurysm, of the patients corresponding to the 12 selected cases. The optimal positioning of the cylinder, and the reconstructed segments connecting the cylinder to the physiological geometry for the remaining 4 cases were such that the original and reconstructed aneurysmal regions did not coincide. As such, these cases were excluded from the investigation. Figure 5.24 shows the cylinder embedded within the 12 included cases.

Table 5.2: Summary of patient information corresponding to the selected 12 cases

Case	Gender	Age	Smoker	Aneurysm location	Aneurysm type
1	Female	N\A	N\A	Posterior communicating artery	Saccular –sidewall
2	Female	65	Yes: quit	Anterior choroidal segment carotid	Saccular –bifurcation
3	Female	56	Yes: quit	Posterior communicating artery	Saccular –bifurcation
4	Male	90	Yes: quit	Anterior communicating artery	Saccular –bifurcation
5	Male	81	No	Anterior communicating artery	Saccular –bifurcation
6	Male	70	No	Posterior communicating artery	Saccular –bifurcation
7	Female	N\A	N\A	Posterior communicating artery	Saccular –bifurcation
8	Male	N\A	N\A	Posterior communicating artery	Saccular -sidewall
9	Female	N\A	No	Opthalmic segment carotid	Saccular –sidewall
10	Female	65	Yes: quit	Posterior communicating artery	Saccular –sidewall
11	Female	71	Yes: quit	Posterior communicating artery	Saccular –sidewall
12	Female	72	Yes: quit	A1 anterior segment	Saccular -sidewall

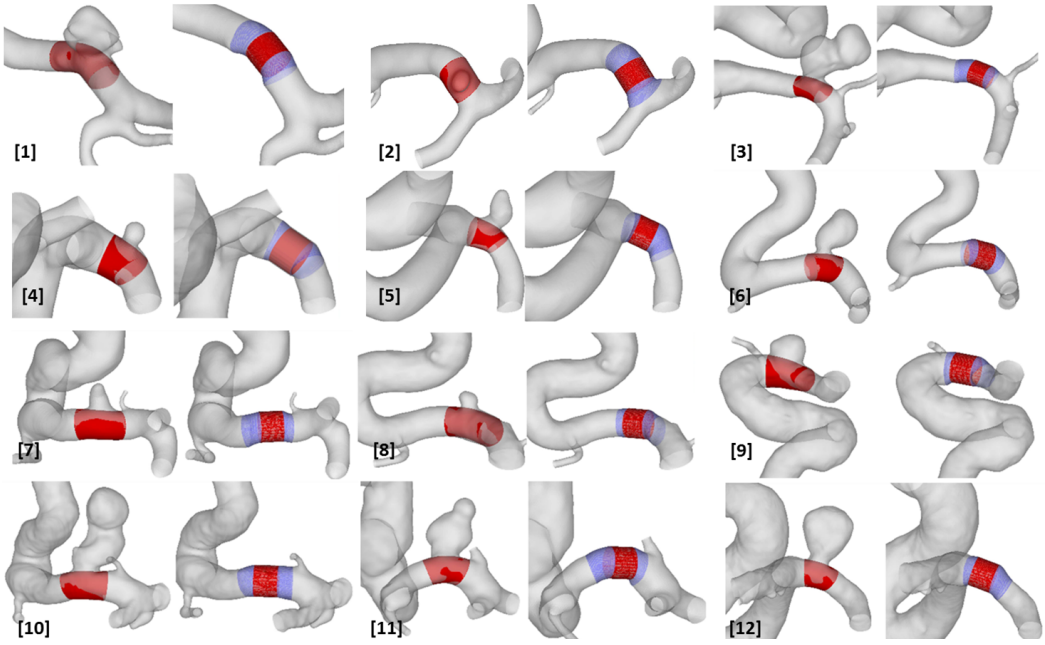


Figure 5.24: The cylindrical model (red) embedded within 16 patient-specific cases, with surface reconstructions highlighted in blue. The original geometry is shown on the left of each case, with Chen et al. (2013) "pre-aneurysmal" reconstructions highlighted in red

Pulsatile-flow simulations were conducted for a period of $t = 5$ years, and the distributions of haemodynamic patterns at inception were examined at this time-point. The main growth and remodelling parameters were set as per Table 5.3.

Table 5.3: Summary of the main growth and remodelling parameters applied to FSG simulations on 12 physiological cases

G&R Parameter	Description	Value
m^E_{min}	Minimum elastin concentration due to prescribed degradation	0.5
t^E_P	Time period over which prescribed elastin degradation occurs	5 years
β	Remodelling parameter corresponding to rate at which fibroblasts increase/decrease mass of collagen	0.01
t^β_i, t^β_r	Times at which beta is increased to stabilise aneurysm, and at which beta is restored to original value	4,16 years
b_β	Factor by which β is increased to stabilise aneurysm	100
α	Remodelling parameter corresponding to prescribed half-life of collagen fibres	0.6 $year^{-1}$

The gross haemodynamic pattern for each case at $t = 5$ years was compared to the results of the study on inception by Chen et al. (2013), which utilised the same 12 cases with the removed physiological aneurysmal segment replaced by a reconstructed, pre-aneurysmal geometry (a selection of cases is shown in Figure 5.25). Overall, the distributions of the pulsatile-flow haemodynamic indices are similar, and thereby the study on inception by Chen et al. (2013) provides a good comparison for the results of this study.

The implementation of the model within physiological geometries also allows the assessment of the impact of arterial geometry on the evolving haemodynamic environment, and consequently, the evolving aneurysmal geometry during enlargement. To simulate aneurysm enlargement, steady-flow simulations were performed on the cases for a period of 16 years (800 time-steps). In the next chapter, the spatial distributions of pulsatile-flow haemodynamic indices are examined for the 12 cases, and correlations between the indices and the site of aneurysm inception are assessed and compared to the findings of Chen et al. (2013). Aneurysm enlargement is assessed on a subset of 6 of the 12 physiological cases, and the effect on the evolving geometry of coupling elastin degradation to locally low WSS, and the rate of change in collagen concentration to cyclic stretch is examined.

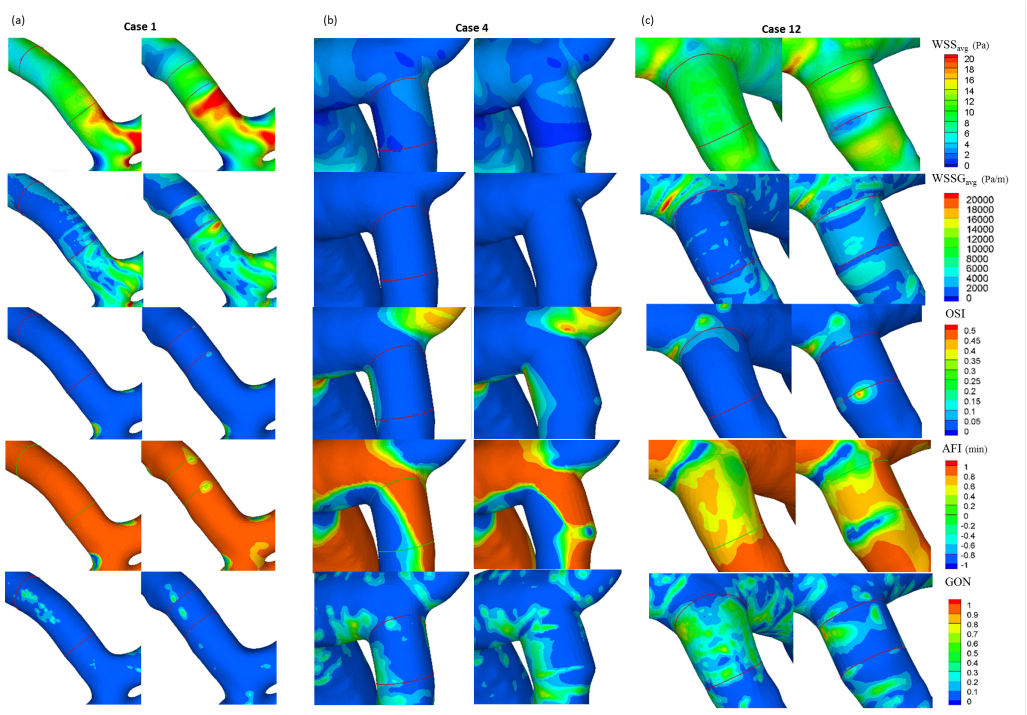


Figure 5.25: Comparison of spatial distributions of haemodynamic indices at inception for case 1 (a), case 4 (b) and case 12 (c). Chen et al. (2013) pre-aneurysmal geometries are shown on the left, while the embedded cylindrical model is on the right. Artefacts can be observed at the cylinder-physiological geometry boundaries (see, for example, the average WSS, and OSI distrubutionis for case 12), which are a result of second-order discontinuity.



CHAPTER 6

PATIENT-SPECIFIC FSG MODELS: A STUDY ON HAEMODYNAMICS AT INCEPTION, GROWTH AND CYCLIC STRETCH

Previous chapters examined the existing hypotheses on the role of haemodynamics in aneurysm evolution. A study on the existence of correlations (Chapter 3) between haemodynamic indices proposed in the literature and regions of aneurysm growth performed on an internal carotid artery and a basilar terminus case revealed that visually- and statistically-determined correlations may differ significantly. Statistical examination showed that correlations, where they exist, are weak, and not always in the same direction as that determined visually. The study also highlighted the myriad of problems in attempting to determine the role of haemodynamics in aneurysm growth (e.g. lack of knowledge of the actual direction of growth and location of growing regions) from assessment of distributions of the indices on non-growing geometries.

The primary aim of this chapter is to re-examine the role of haemodynamics, but this time through the coupling of growth and remodelling (G&R) hypotheses in a model of cerebral aneurysm (CA) evolution to the evolving haemodynamic environment. In the previous chapter, the impact of embedding a cylindrical geometry

on the local haemodynamic environment was assessed by comparing distributions of haemodynamic indices at inception to those observed in the study by Chen et al. (2013), which featured a fully-reconstructed pre-aneurysmal region. As the distributions were observed to be similar, a further comparison to the study by Chen et al. (2013) is made in this chapter of the existing, visually-determined positive correlations between local elevations/reductions of haemodynamic indices and the site of aneurysm formation. The aim is two-fold: first, to determine if embedding the cylinder model influences the observed correlations, and second, to determine which indices may be likely candidates for new G&R hypotheses of aneurysm evolution. Finally, this chapter aims to show the effect of coupling haemodynamic indices to G&R hypotheses on the evolving model aneurysm geometry.

6.1 PULSATILE-FLOW HAEMODYNAMICS AND ANEURYSM INCEPTION: RESULTS

To assess correlations between haemodynamic indices and the region of aneurysm formation, a *region of interest* (ROI)(i.e. the region within which the elevation or reduction of haemodynamic indices is significant) was defined for each case within the cylindrical section. While Chapter 3 made clear the difference between statistical and visual analysis of correlations, it is more difficult to apply statistical methods in this investigation. This is due to the fact that the region within which haemodynamic indices are examined is highly localised, and different for each case. A quantitative method to quickly define the mesh nodes corresponding to the ROI for each case is needed to enable statistical examination of haemodynamics in the ROI. As such, in this study, visual inspection was used to determine if correlations exist between haemodynamics indices and the region *susceptible* to aneurysm formation (hereon referred to as the RSAF). It is important to note that the RSAF is less definitive than "region of aneurysm formation", as it takes into account the fact that haemodynamic indices are often observed to be elevated/reduced in healthy regions of the artery, and may not be the sole instigator of aneurysm formation.

As visual inspection is a subjective process, to further confine the ROI, the original, physiological geometry (with aneurysm) was overlaid on top of the geometry containing the cylinder model, and the region of cylinder encompassed by the aneurysm neck was closely inspected (Figure 6.1).

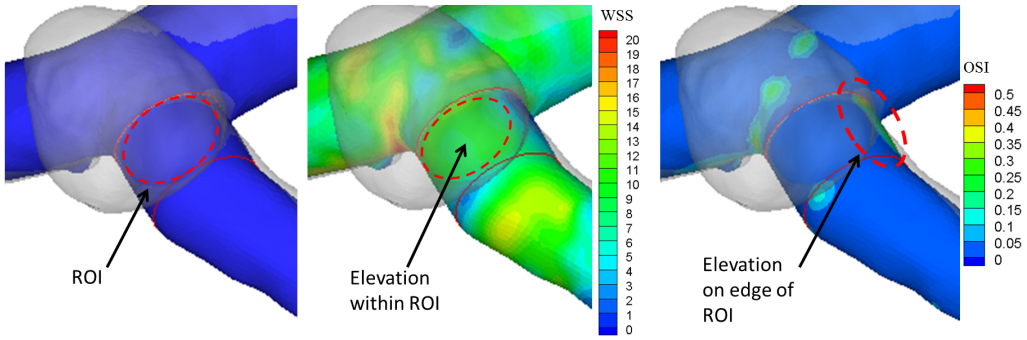


Figure 6.1: Definition of the region of interest, within which correlations are assessed. Elevation within, and on the edge of the region are shown, and counted as positive correlation cases.

A definition for positive correlation was required. In their study, Chen et al. (2013) defined two types of positive correlation, dependent on whether elevation or reduction of an index occurs

1. within the ROI,
2. on the boundary of the ROI, or
3. in the vicinity of the ROI.

In their study, a positive correlation by "Definition I" means that elevation/reduction of an index satisifies any one of the above criteria. By "Definition II", elevation/reduction of an index satisfies either (or both) criterion 1 and 2. In §1.4 of this work, one of the reviewed hypotheses on growth is that it is driven from the *edges* within the aneurysmal domain -i.e. from the aneurysmal neck, or, in the case of daughter blebs, at a point on the dome where there is a clear boundary between WSS magnitudes. With this in mind, a positive correlation in this study was identified for any index observed to be elevated (or reduced) compared to its respective physiological threshold *within*, or *on the edge* of the ROI. This is equivalent to "Definition II" of correlation in the study by Chen et al. (2013). Thresholds for each index beyond which a positive correlation was identified were defined as per §3.1.

The figures below show the distributions of the five haemodynamic indices for each of the 12 cases at $t = 5$ (i.e. at the end of the prescribed degradation period, $t_{\text{inception}}$), and a summary of the results for each index. A summary of correlations is

provided in Table 6.1. The 12 examined cases are compared to the findings of Chen et al. (2013) for the same 12 cases. Only correlations identified *within* or *on the edge* of the ROI were counted from the study by Chen et al. (2013) for comparison with the present results.

Table 6.1: Summary of positive correlations in this study, and compared to that found in the study by Chen et al. (2013) for the same 12 cases

Index	Positive correlations within ROI	Positive correlations on edge of ROI	Total positive correlations	Correlations matching Chen (2012)
High WSS	10	0	11/12	9/11
Low WSS	1	0	1/12	N\A
High WSSG	9	1	10/12	1/10
OSI	2	2	4/12	1/4
AFI (min)	5	1	6/12	2/6
GON	12	-	12/12	10/12

Figure 6.2 shows an elevated WSS (4-14Pa) for cases 1-3,5-10, and 12, and very high WSS ($\geq$ 20Pa) for case 11 within the ROI, giving a positive correlation between elevated WSS and the RSAF for 11/12 cases. WSS $\approx$ 2Pa was observed for case 4. The positively correlated cases matched those identified by Chen et al. (2013) for 9/11 cases.

Figure 6.3 shows that for cases 1-3, 5, 7, and 9-12, patches of WSSG $\geq$ 3000Pa/m are observed within the ROI, and on the edge of the ROI for case 8, giving 10/12 positive correlations. The positively correlated cases matched those identified by Chen et al. (2013) for 1/10 cases.

Figure 6.4 shows that OSI $\geq$ 0.2 within the ROI for cases 4 and 5, and on the edge of the ROI for cases 9 and 12, giving 5/12 positive correlations. The positively correlated cases matched those identified by Chen et al. (2013) for 1/4 cases.

Figure 6.5 shows AFI(min)$\leq$ 0 for cases 4, 5, 8, 9 and 12, and on the edge of the ROI for case 7, giving 6/12 clear positive correlations between AFI(min) and the RSAF. The positively correlated cases matched those identified by Chen et al. (2013) for 2/6 cases.

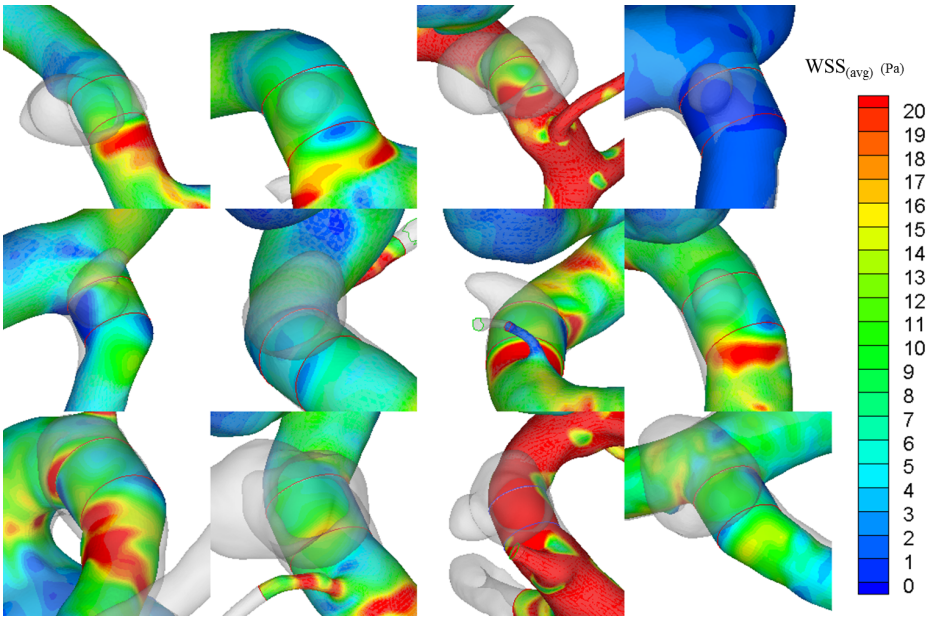


Figure 6.2: WSS distributions for the 12 cases at inception

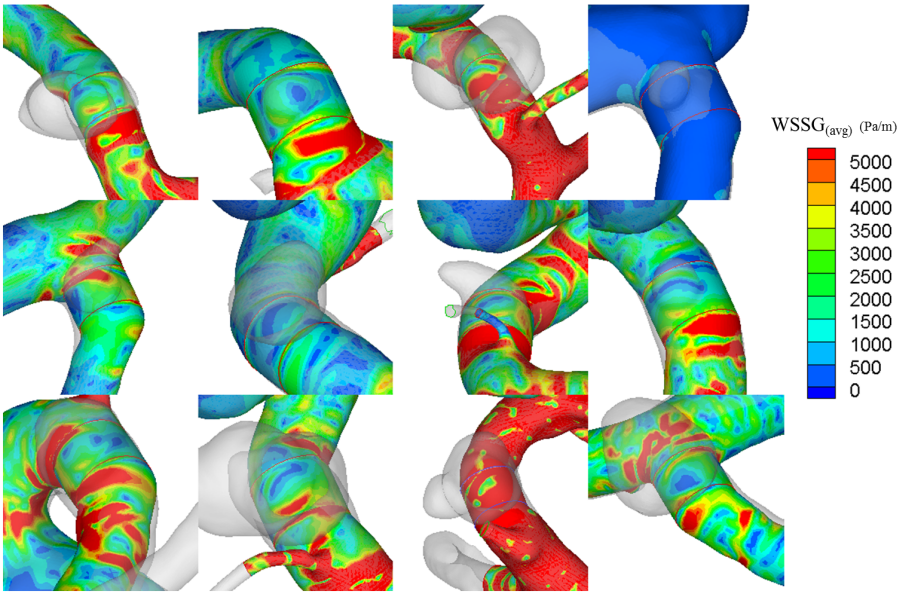


Figure 6.3: WSSG distributions for the 12 cases at inception

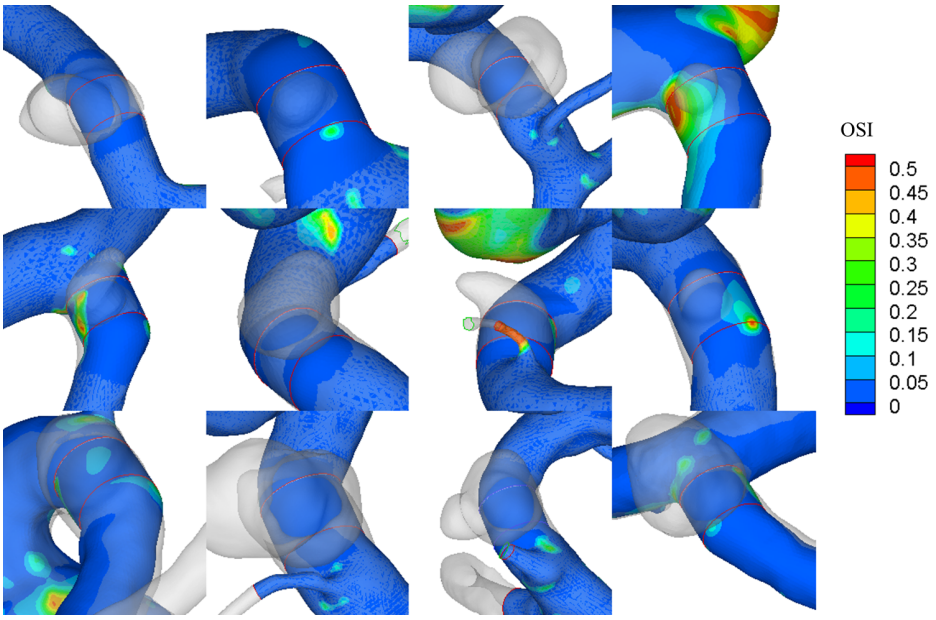


Figure 6.4: OSI distributions for the 12 cases at inception

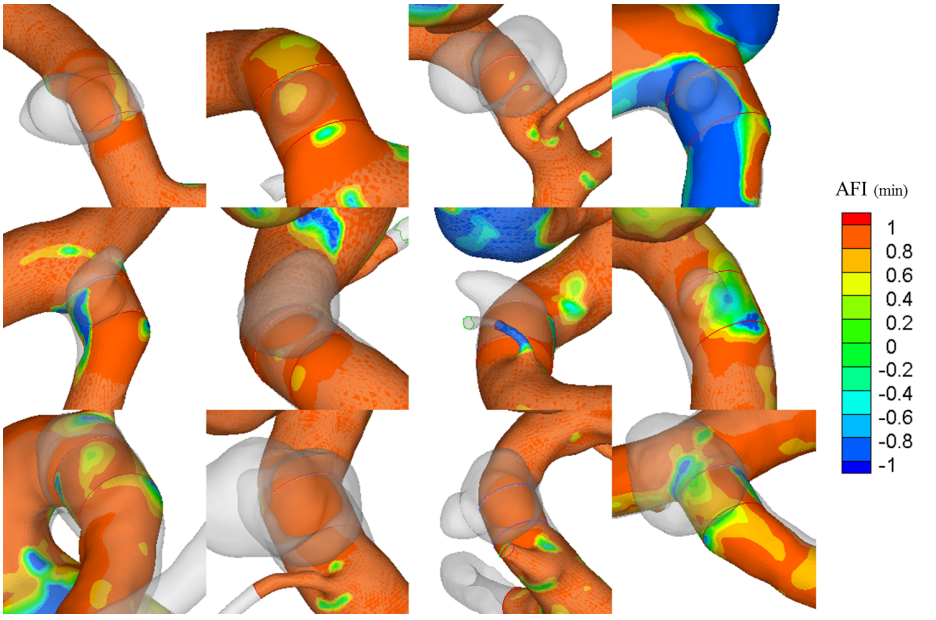


Figure 6.5: AFI(min) distributions for the 12 cases at inception

By the definitions of correlation proposed for this investigation, a positive correlation between GON and the RSAF exists for 5/12 cases. Similar to the findings of Chen et al. (2013), Figure 6.6 shows that GON appears to be elevated in small patches throughout the artery, including the ROI. The positively correlated cases matched those identified by Chen et al. (2013) for 5/5 cases.

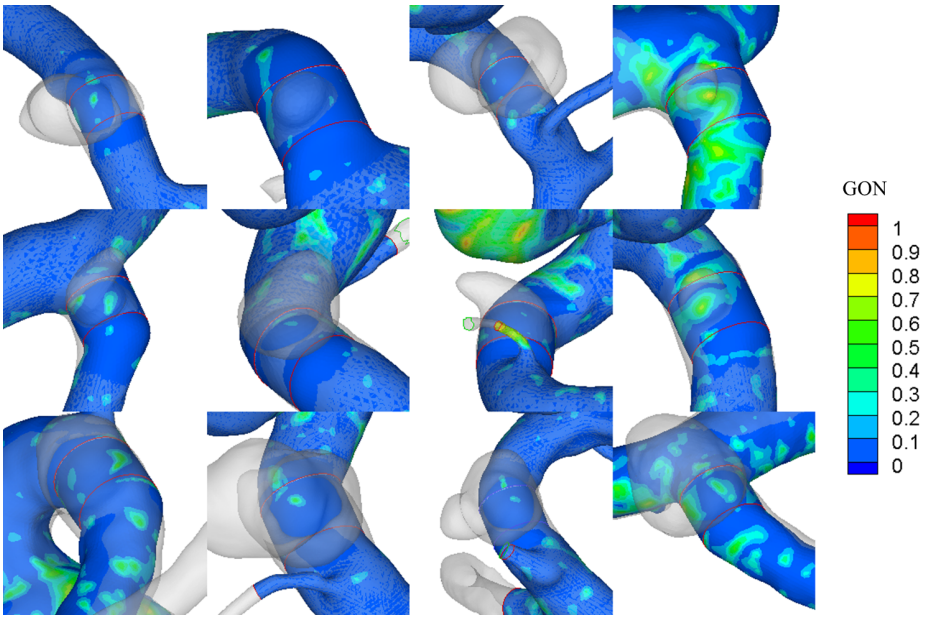


Figure 6.6: GON distributions for the 12 cases at inception

6.1.1 Pulsatile-flow indices and aneurysm inception: Discussion

By the definitions of positive correlation defined for this study, the indices with the highest number of positive correlations are WSS and WSSG (10/12 positive correlations for both). This seems in line with the studies discussed in §1.4.3, which point to the combination of high WSS and high WSSG as the main haemodynamic instigators of aneurysm inception. Both the OSI and AFI(min) were not strongly correlated (4/12 and 6/12 cases respectively), which suggests that oscillatory shear, as captured by these indices, may not be a critical factor for inception. Statistical examination of correlations between the pulsatile-flow haemodynamic indices discussed in §3.3 showed that OSI and AFI(min) are inversely correlated with WSS. Indeed, this correlation can be visually observed from the results of this study. Consider case 4 and 5, where the ROI contains a large region of low WSS. For both cases, the ROI also shows a high OSI and minimum AFI (Figure 6.7).

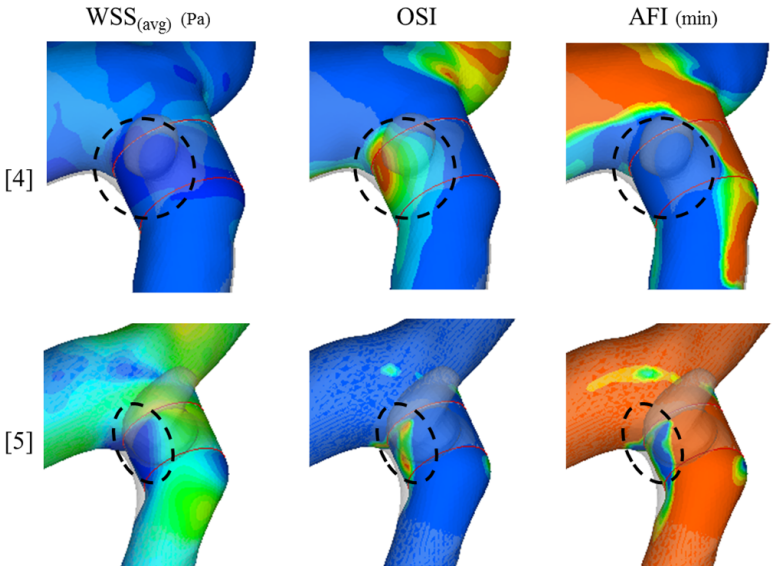


Figure 6.7: Correlation between low WSS, high OSI and minimum AFI, observed from cases 4 and 5

While the GON was observed to be elevated in small patches within the ROI of 5 out of 12 cases, it is also high in patches throughout the artery. This is consistent with the findings of Chen et al. (2013) and Ford et al. (2009), and brings to light the difficulty in deciding if (i) the GON really is correlated with the RSAF, and (ii) if yes, the correct interpretation of this correlation. Furthermore, this problem does not only occur for the GON index. Figure 6.2 shows that for all cases where WSS is considered to be elevated, WSS is also elevated in the nearby, healthy regions. Figure 6.8 shows the WSS distribution across the full geometry of each of the 12 cases. Figure 6.8 shows that, while WSS is indeed elevated in healthy regions of the artery, with exception of case 4 (where WSS is low throughout) and case 12 (where WSS is elevated throughout), the ROI of all other cases appears to be consistently located within a region of locally elevated WSS. Interestingly, some cases (i.e. case 3, 4, 6, 8, 9, 11 and 12) exhibit a clear tapering of the vessel towards the RSAF, which likely accounts for an increase in WSS magnitude in this region. It can also be seen that for almost all cases, the region within which the original aneurysm eventually developed is highly curved, with aneurysms of several cases developing just downstream of a bifurcation, where flow is typically high and complex.

However, it can be seen that for cases 2, 8, 9 and 10 (Figure 6.9), while WSS is generally greater than 2Pa within the ROI, WSS of between 2-7Pa occurs in patches within the ROI, some with WSS>7Pa. Figure 6.10(a) shows cases 3 and 5, which both

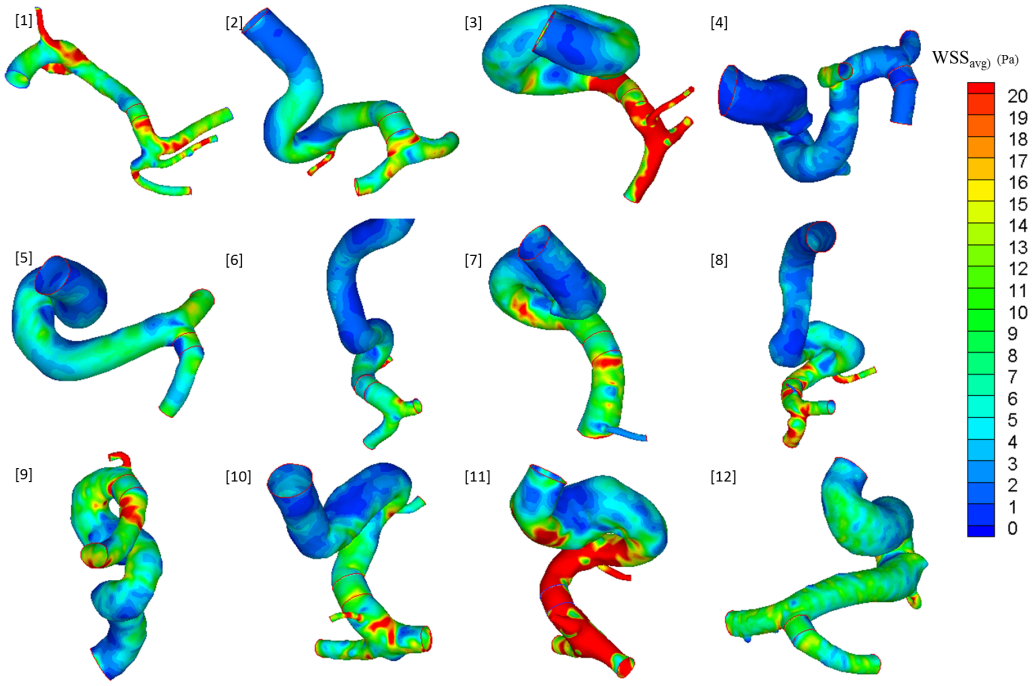


Figure 6.8: WSS distribution across the full geometry for each of the 12 cases

exhibit large reductions in WSS within the ROI compared to the surrounding environment (a region of 8-12Pa compared with >20Pa for case 3, and <2Pa compared with 4-12Pa for case 5). Hence, the interpretation of the results is confounded by the possibility that the ROI in these cases in fact lies within a region of locally *reduced* WSS.

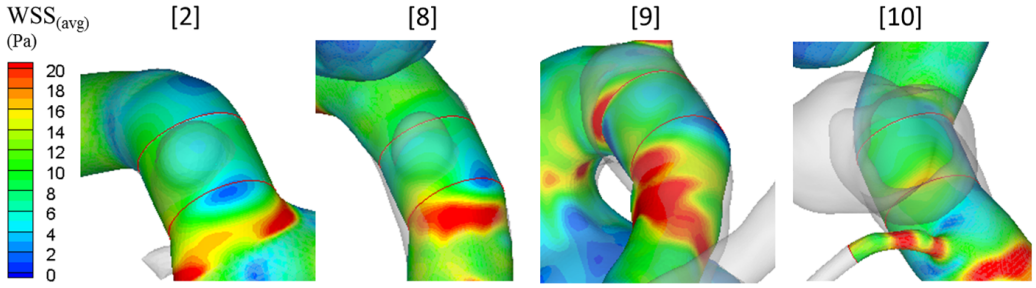


Figure 6.9: Patches of locally elevated *and* reduced WSS within the ROI of cases 2, 8, 9 and 10

Such large differences in WSS between adjacent points translate into a large spatial WSS gradient. The impairment of EC ability to adapt to a high shear stress environment in the presence of shear gradients was discussed in §1.4.3. Indeed,

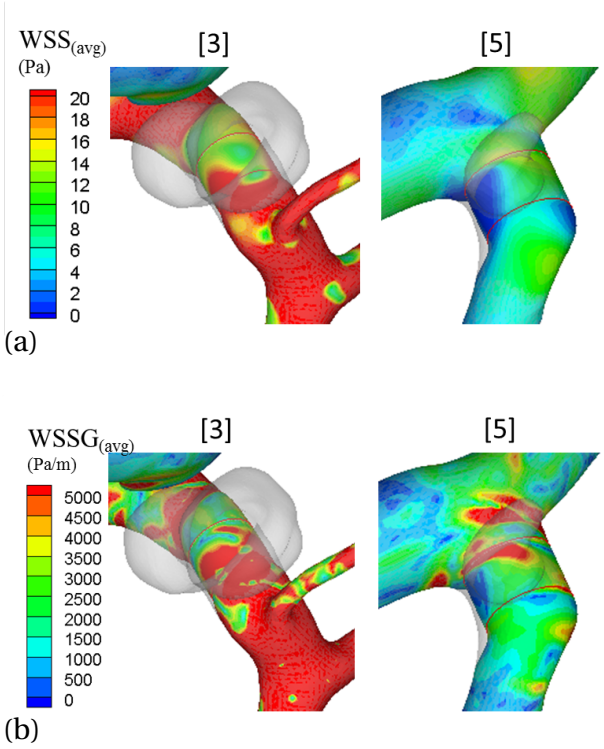


Figure 6.10: Locally low WSS, (a), and high WSSG, (b), within the ROI of cases 3 and 5

Figure 6.10(b) shows that WSSG is elevated (≥3000Pa/m for case 5) and very high (≥5000Pa/m for case 3) at the border of the high and low WSS regions. Hence, the results of this study suggest that aneurysm inception in the modelling framework should be coupled to local levels of WSS and WSSG. A method to achieve this is discussed in Chapter 7.

Interestingly, while the gross haemodynamic patterns are similar between the pre-aneurysmal geometries generated by Chen's (2012) method and those with the cylindrical model embedded, the number of positive correlations identified in the two studies is very different for all indices but the WSS (with 9/11 matching positive correlations). The most striking difference is the number of matching positive correlations for the WSSG index (out of 11 positive correlations identified in this study, only 1 case was also positively correlated in Chen's (2012) study). Firstly, it must be noted that in the study by Chen et al. (2013), a quantitative definition of elevated WSSG is not defined, while in this study, 3000Pa/m is applied as the upper physiological threshold. As such, the definition of "locally elevated" WSSG in Chen's

(2012) study is not clear. The same applies to elevations of other indices. Furthermore, the difference in correlations is likely to be due in great part to the differences in the reconstructed geometries. In general, the reconstructed segments in Chen's (2012) study are smooth, and represent the curvature and diameter of their corresponding original segments well. In contrast, in this study, the cylinder represents a highly ideal, straight segment of constant diameter. Particularly when embedded within highly-curved physiological geometries, the cylinder and the corresponding connecting surfaces may be such that the transition between the physiological and analytically-defined segments is not smooth, due to second-order discontinuity. This may bear some influence on the local haemodynamic environment and account for the differences in the observed positive correlations. Figure 6.11 highlights the effect of second-order discontinuity on the local distributions of WSS (case 2), OSI (case 8) and AFI(min) (case 12).

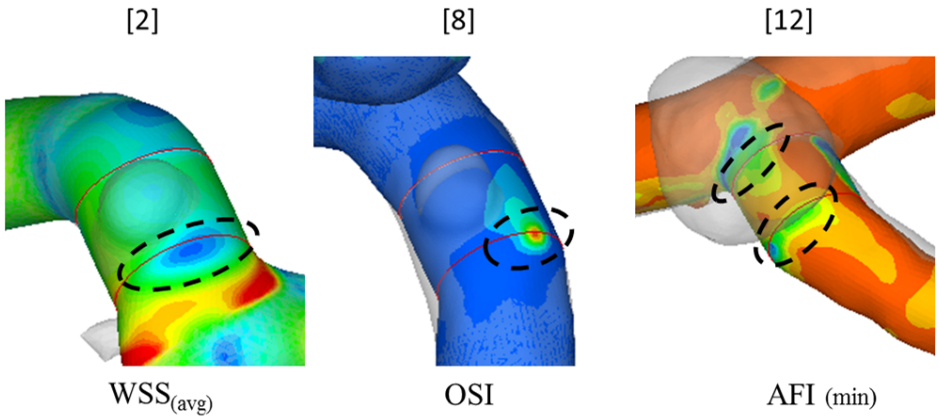


Figure 6.11: Effect of second-order discontinuity of the cylinder-connecting surface boundaries on the distributions of haemodynamic indices. A locally reduced WSS is observed at the downstream cylinder boundary of case 2; A local maximum OSI is observed at the downstream cylinder boundary of case 8; AFI(min) = 0 observed at both the upstream and downstream cylinder boundaries of case 12

Finally, from Chapter 3, it was clear that interpretation of visually-assessed CFD results must be made with great care. Ideally, the bounds of the ROI, as well as a region around the ROI which constitutes "the edge" would be quantified for each case, and the correlations statistically assessed. Furthermore, the lack of a clear definition of physiological, sub-, and supra-physiological levels of haemodynamic indices is yet unsolved. The GON, for example, has no suggested physiological range. However, even in the case of indices for which a physiological range has been re-

ported, the question of its applicability in the context of the particular vessel under investigation remains to be answered. For example, in the case of WSS, it seems unreasonable to assume that the generally reported "physiological band" of WSS (1.5-2Pa) applies to all arteries in the body, as these vary in size and structure, and receive different levels of flow. Hence, a key improvement to CFD studies such as this would be the employment of patient-specific flow data, which would allow for a more rigorous definition of physiological thresholds.

6.2 EVOLUTION OF THE MODEL ANEURYSM GEOMETRY IN RESPONSE TO THE SHEAR STRESS ENVIRONMENT AND CYCLIC STRETCH

A steady-flow investigation of aneurysm growth was performed on a selection of 6 of the original 12 cases, over a time-period equivalent to 16 years (800 time-steps). In order to quantify the cyclic deformation, the aneurysm geometry is determined at systolic and diastolic pressures as it evolves. Recall from §4.4.3 that the evolution equation for the mass of collagen is coupled to cyclic deformation, i.e.

$$\frac{\mathrm{d}m^C_{J_p}}{\mathrm{d}t} = \beta(A^{CS})\, m^C_{J_p} \left(\frac{E^C_{J_p}|_{\max} - E^C_{AT}}{E^C_{AT}} \right), \tag{6.1}$$

where

$$\beta(A^{CS}) = \beta_0 \exp\left[\beta^{CS} \max\left(\frac{A^{CS}}{A^{CS}|_{t=0}} - 1 \right) \right], \tag{6.2}$$

and where A^{CS} is the ratio of cyclic stretch between the diastolic and systolic geometries and is defined in terms of the systolic and diastolic GL strains, as defined in §4.4.3. To assess the effect of coupling G&R to the evolving cyclic area stretch, two sets of simulations were conducted. In the first set (S1), growth is assessed without coupling the evolution equation for the mass of collagen to the evolving cyclic area stretch, A^{CS}, i.e. $\beta^{CS} = 0$, and thereby, $\beta(A^{CS}) = \beta_0$. In the second set of simulations (S2), cyclic area stretch is coupled to the equation for the evolving mass of collagen -i.e. $\beta^{CS} > 0$.

It was anticipated that coupling the collagen concentration to cyclic stretch would result in a rapid deposition of collagen. As such, β_0 was deliberately set to a very low value to allow the initial perturbation to the geometry to form. For both sets of simulations, the main G&R parameters are summarised in Table 6.2.

Table 6.2: Critical WSS thresholds for onset and maximum elastin degradation

G&R Parameter	Description	Value	
		S1	S2
m^E_{min}	Minimum elastin concentration due to prescribed degradation	0.5	0.5
t^E_P	Time period over which prescribed elastin degradation occurs	5 years	5 years
β_0	Remodelling parameter corresponding to rate at which fibroblasts increase/decrease mass of collagen	0.01	0.01
β^{CS}	Exponential parameter controlling the rate of increase of $\beta(A^{CS})$	0	3
t^β_i, t^β_r	Times at which beta is increased to stabilise aneurysm, and at which beta is restored to original value	4,16 years	4,16 years
b_β	Factor by which β is increased to stabilise aneurysm	100	100
α	Remodelling parameter corresponding to prescribed half-life of collagen fibres	0.6 year^{-1}	0.6 year^{-1}

For all cases, inception was prescribed to occur over the first 5 years (250 time-steps) and subsequent degradation is linked to locally low WSS, as per §4.4.2. As the spatial distribution of WSS varies between geometries, the values of τ_{crit} and τ_X need to be specified for each case. Let τ_1 and τ_2 denote the minimum values of WSS within the circular patch for the conceptual healthy artery (i.e. at $t = 0$) and the artery following the prescribed inception ($t = 5$), respectively. It is assumed that the initial perturbation to the geometry leads to a local decrease in WSS, i.e. $\tau_2 < \tau_1$. As such, $\tau_{\text{crit}} = \tau_1$ and $\tau_X = \tau_2$ are specified. The critical thresholds for each case are summarised in Table 6.3. In both cases, the main growth and remodelling parameters were set as per Table 5.3.

Table 6.3: Critical WSS thresholds for onset and maximum elastin degradation

WSS thresholds (Pa)	1	2	3	4	5	6	7	8	9	10	11	12
τ_{crit}	5.9	9.2	13.6	0.45	0.53	7	8.2	6.6	4.7	6.9	25.8	6.4
τ_{X}	3.7	4.59	8.1	0.25	0.08	3.7	8	4.4	3.9	5.6	23.6	4.8

6.2.1 Effect of coupling elastin degradation to locally low WSS

Figure 6.12 shows the WSS distributions of six cases $t = 5$, $t = 8$, $t = 12$ and $t = 16$ years, which illustrate the differences in the local shear stress environment, and the resulting model aneurysm geometries. In some cases the aneurysm geometry grew much more than others (e.g. case 2 and 3). It was also observed that some

aneurysms appear to be growing symmetrically (e.g. case 2 and 4), while others are asymmetric (e.g. case 1, 5 and 6). Like the preliminary results on the example physiological case discussed in Chapter 5, the evolution of the model aneurysm geometry can be explained by the evolving WSS environment. It can be seen that cases 2 and

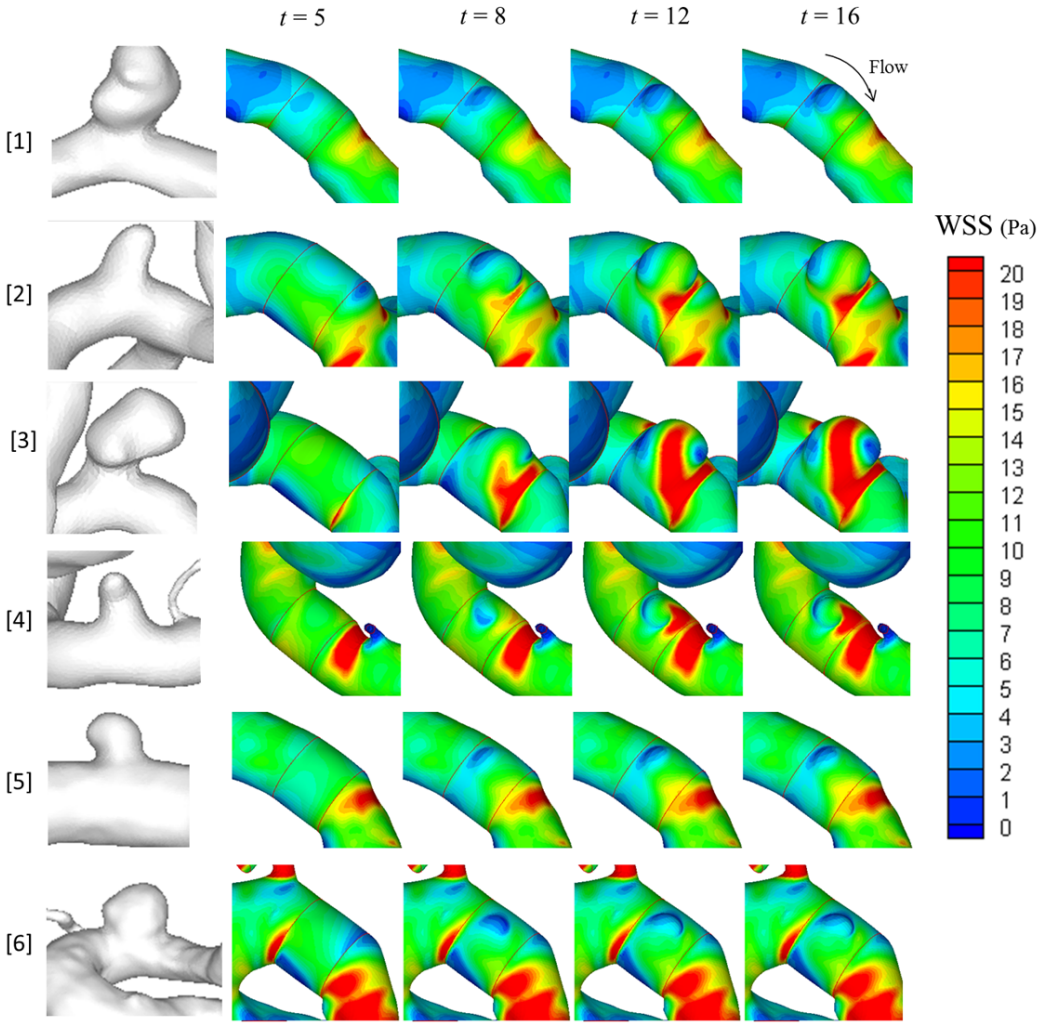


Figure 6.12: The evolving WSS environment of 6 cases at $t = 5$, $t = 8$, $t = 12$ and $t = 16$ years for the 6 cases

3 exhibit evolving patches of low WSS at both the proximal and distal parts of the aneurysm, which drive elastin degradation in these regions, and hence, result in a more symmetric aneurysmal geometry. In contrast, cases 1, 4 and 5 exhibit a patch of low WSS localised to the proximal part of the cylinder, which drives elastin degradation in this region and thereby results in a asymmetric geometry, with the dome growing towards the proximal part of the artery. Similarly, the evolution of a patch

of low WSS on the lateral-distal side of the case 6 cylinder results in the growth of the geometry towards this region.

Interestingly, and like the test physiological case discussed in Chapter 5, the direction of growth of the evolving model aneurysmal domes of cases 3, 5 and 6 appears to mimick the corresponding original aneurysmal geometry (Figure 6.13). While this is less obvious for the remaining three cases, it is possible that low WSS is indeed a driver of elastin degradation. As discussed in §1.4.4.1, low WSS has been linked to EC dysfunction, as well as the infiltration of inflammatory cells, which act to degrade the internal elastic lamina via the release of MMPs.

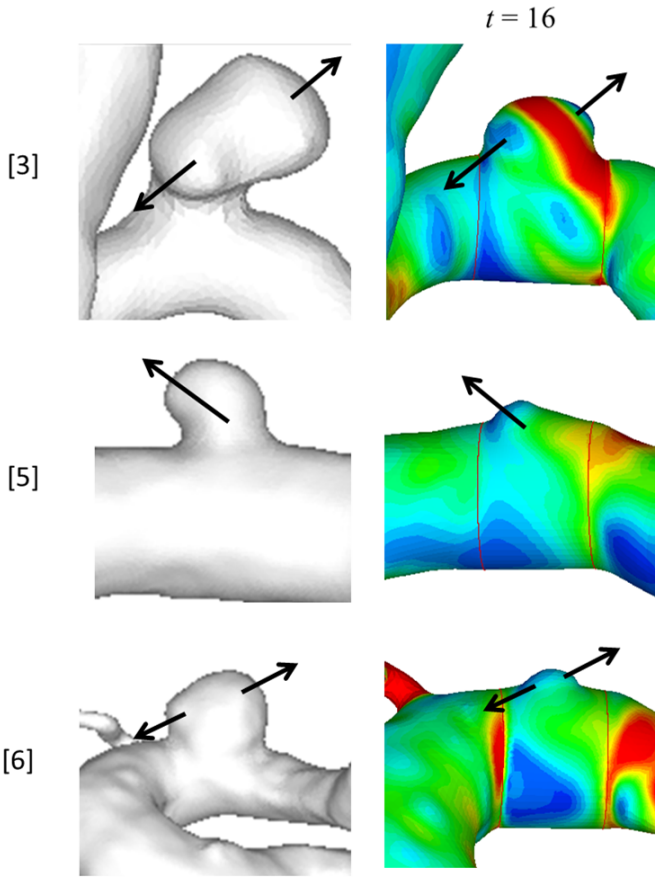


Figure 6.13: Qualitatively similar evolution of model aneurysmal geometries of cases 3, 5 and 6 to the corresponding original aneurysmal segments. The comparison here is shown between the original and model geometry at $t = 16$ years for the 3 cases, and the direction of growth is highlighted by arrows

However, Figure 6.14 suggests that the combination of high WSS/high WSSG cannot be ruled out as a potential instigator of growth. For both case 3 (Fig-

ure 6.14(a)) and case 5 (Figure 6.14(b)), it can be seen that the evolving intra-aneurysmal shear stress environment features adjacent regions of elevated and very low WSS. This gives rise to a large WSSG in this region.

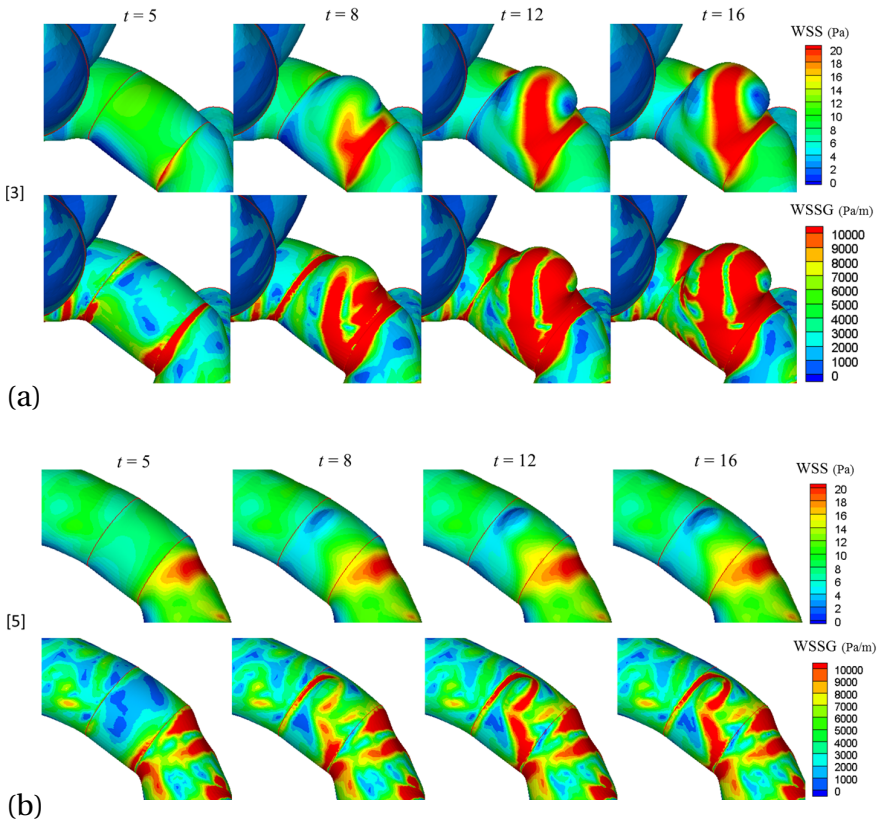


Figure 6.14: Evolving WSS and WSSG distributions on the case 3, (a), and 5, (b), model aneurysmal geometries. In both cases, very high WSSG (>10000Pa/m) is observed in the regions corresponding to large changes in WSS magnitude between adjacent points.

Hence, from the present work, it is unclear whether strictly high or low flow is the main instigator of aneurysm growth. In fact, from the results on inception and growth discussed in this chapter, the studies discussed in §1.4, and the statistically-examined correlations in Chapter 3, a hypothesis on aneurysm inception and growth involving a combination of high and low WSS mechanisms emerges. The inception results presented in the previous section showed that for almost all cases, the original aneurysm developed within a region of locally elevated WSS. Furthermore, these regions typically exhibited high curvature, with several aneurysms developing just downstream of a bifurcation, where WSS and WSSG are high, and flow

is complex. Sustained high WSS may act to cause a sustained release of NO, and in turn, the activation of IEL-destroying MMPs. The destruction of the IEL may be further exacerbated by high WSSG, which causes EC migration, and in turn, a lack of inhibition of MMPs. The subsequent loss of elastin and collagen weakens the wall, resulting in an intial outpouching. Typically in the case of side-wall aneurysms on highly-curved vessels, or near bifurcations, this initial outpouching is a region of reduced WSS, while the distal neck of the evolving aneurysm dome is a point of flow-impingement, and therefore high WSS. The abrupt change in WSS magnitude between the distal neck and the adjacent aneurysmal region creates a high spatial WSSG, and the combination of high WSS and high WSSG in this region may therefore continue to fuel destructive remodelling at the neck. Meanwhile, within the aneurysm dome, adjacent regions of low and high WSS again result in a high spatial WSSG. Like the neck region, high WSSG in the dome may induce EC migration, therby leaving parts of the wall exposed. Low WSS may result in a lack of elongation and alignment of ECs, thereby increasing the junctional gap between adjacent cells. Furthermore, low WSS results in an increase in residence time of inflammatory cells near the wall, which may now more easily migrate into the wall. The release of MMPs by inflammatory cells may therefore speed up the destruction of the key structural components of the wall, leading to further weakening and growth.

To test this, some adaptations to the current framework are needed. Firstly, the current prescribed initial degradation of elastin could be replaced by a function which links initial elastin degradation to locally elevated WSS and WSSG, and later to low WSS/high WSSG to test the low-flow hypotheses on growth. As mentioned in the previous section, a more rigorous definition of “high” and “low” WSS and WSSG is required, which will allow the setting of appropriate threshold magnitudes beyond which the rate of elastin degradation increases or decreases. Furthermore, while the present FSG framework is structurally-motivated, currently only the mechanical response of elastin and collagen is explicitely modelled. It is clear, however, that the degradation of elastin and the G&R of collagen are mediated by a series of chemical cascades that begin with transduction of haemodynamic forces by vascular cells. Hence, the current framework needs to be refined to include an explicit representation of ECs, vSMCs and fibroblasts. A means by which ECs could be incorporated into the current modelling framework is discussed in more detail in the next, and final chapter. An improved understanding of mechanobiological events (e.g. the knock-on effects of EC transduction of WSS on other cells in the wall)

is needed to better inform the coupling of haemodynamics to G&R in the model. Lastly, the reduction of computational time through steady-flow simulations has meant that oscillatory shear indices (i.e. OSI, AFI and GON) could not be examined in this study. While a clear correlation between these indices and aneurysm growth could not be established from pulsatile-flow simulations on static geometries in Chapter 3, more insight may be gained from observing their distributions during the process of growth.

As mentioned in the previous section, the framework will ideally be adapted such that it can be applied to any geometry, which would result in a local haemodynamic environment that is a better representation of the real physiological environment. In the meantime, the surface-reconstruction methods described in Chapter 5 could be refined to satisfy second-order continuity and thereby improve smoothness at the boundaries.

6.2.2 Investigation into the effect of the cyclic stretch on the model geometry evolution

In addition to the improvements mentioned in the previous section, the current G&R hypotheses implemented within the FSG framework must be reviewed and updated in light of new physiological data. For instance, in-vitro experiments (discussed in detail in the following section) have shown that vascular cells are sensitive not only to shear stress, but also to cyclic stretch, with observed responses including changes in cellular alignment, as well as production and degradation of collagen. It is possible that cyclic-stretch mediated collagen production provides a mechanism for aneurysm stabilisation. As such, to reflect the influence of cyclic stretch on collagen production and degradation, a cyclic area function (CAF) was introduced to the model as part of the equation for the evolution of collagen concentration (see §4.4.3.2, Equation (4.24)), the effect of which has not been previously examined in detail. The aim of this section is to investigate if the inclusion of a CAF in the model does indeed provide a mechanism of aneurysm stabilisation, and if so, to determine the most appropriate functional form and implementation of this function in the model. The following section briefly examines the research on the effect of cyclic stretch on ECs, vSMCs and fibroblasts, with the intention to better inform the choice of functional form and implementation of the CAF.

6.2.2.1 The effect of cyclic stretch on vascular cells: A brief review

As Cummins et al. (2007) explain, cyclic stretch experiments on vascular cells are typically performed *in-vitro* (with cells embedded on a deformable membrane), or *ex-vivo*, with whole arterial segments explanted and tested. Cyclic stretch is expressed in terms of the % change in area of cells compared with static cultures, with 0-15% being a commonly applied range (although, like WSS, the "physiological range" seems to be contested in the literature, with some studies suggesting that 6-10% is the physiological range (Ando and Yamamoto, 2011), some that up to 20% is within the physiological range (Howard et al., 1997), some that 15-20% is in the pathological range (Kakisis et al., 2004), and still others that showed homeostatic behaviour of cells at 24% cyclic stretch (Iba and Sumpio, 1991)).

Several studies have investigated the role of cyclic stretch on cell alignment, and it is generally agreed that ECs and fibroblasts are observed to elongate and align perpendicular to the direction of cyclic stretch (Iba and Sumpio (1991); Okada et al. (1998); Wang et al. (2001); Breen (2000)), while vSMCs align in the direction of cyclic stretch (Humphrey, 2008b). Iba and Sumpio (1991) found that at 24% cyclic stretch, ECs were elongated, aligned, and spindle-shaped within 15 minutes, with actin stress fibres oriented perpendicular to the direction of cyclic stretch. Wang et al. (2001) found a similar response to cyclic stretching, but also showed that this behaviour changes in response to the direction of cyclic stretching. They applied three types of cyclic stretch to cells embedded on a 2D membrane: simple elongation, where orthogonal compression was allowed; uniaxial stretch, where the membrane was controlled such that orthogonal compression could not occur; and equi-biaxial stretch, where the membrane was equally stretched in both directions. They found that while simple elongation and uniaxial cyclic stretch induced a similar response from ECs (alignment and orientation perpendicular to the direction of cyclic stretch), equi-biaxial cyclic stretch did not induce EC elongation, and the actin stress fibres were observed to form a "tent-like" pattern, protruding in a direction normal to the cell membrane. As Wang et al. (2001) conclude, the findings of their study support the notion that the formation of actin stress fibres occurs only in the direction of minimal deformation. They also found that the early response of ECs to cyclic stretch was mediated more by the *magnitude* of stretch, while the later response was mediated more by the *rate* of stretch, although the mechanisms for this are not understood.

Several studies have also examined the effect of cyclic stretch on gene expression, and intra- and inter-cellular signalling. Cummins et al. (2007) note that in addition to EC orientation, cyclic stretch has been shown to influence the synthesis of NO (the main vasodilator), endothelin-1 (a potent vasoconstrictor), the expression of growth factors and cytokines (particularly MMPs) which influence celullar proliferation and degradation of ECM constituents respectively, as well as the induction of inflammatory pathways. They suggest that, in regulating NO activity, cyclic stretch in turn affects the expression of MMPs by ECs, which have been shown to be activated in the presence of NO. Therefore, it seems that cyclic stretch may also induce the destruction of the IEL independently of WSS. Cummins et al. (2007) also point to evidence of cyclic stretch mediated EC apoptosis, as well as an increase in EC permeability due to the destruction of cell-cell junction proteins by MMPs. In their studies, Salameh and Dhein (2012) demonstrated that an increase in cyclic stretch caused an upregulation of Cx43, a molecule involved in EC gap junctions, elevations of which have been associated with vascular diseases such as atherosclerosis. Interestingly, however, these studies do not report a magnitude of cyclic stretch beyond which the cellular response becomes pathologic. Thacher et al. (2010), for example, compared porcine ECs exposed to physiological cyclic stretch (4-5% in their study) to ECs exposed to cyclic stretch of less than 1%, and showed that *reduced* compliance downregulates eNOS activation, thereby reducing NO bioavailability. They also found that reduced compliance resulted in an increase in production of reactive oxygen species (ROS), which in turn resulted in increased oxidative stress. Oxidative stress has been shown to diminish NO levels, and cause inflammation and cell death. Interestingly and in contrast to Thacher et al. (2010), Howard et al. (1997) showed that an increase in cyclic stretch (up to 20%) was accompanied by an *increase* in ROS levels, but that this increase was not toxic to ECs. Kakisis et al. (2004) also point to EC and vSMC apoptosis at higher levels of cyclic stretch. Therefore, while it has not been strictly defined, it appears that cyclic stretch magnitude does indeed have a physiological range, outside of which the cellular response to cyclic stretch becomes destructive.

Howard et al. (1997) also point to evidence of cyclic stretch facilitated inflammation, as cyclic stretch has been shown to cause an increase in monocyte adhesion and expression of MCP-1. In an *in-vitro* study on ECs, Okada et al. (1998) applied cyclic stretch of 6.1%, 11.6% and 15.1% and demonstrated that at 15.1% cyclic stretch over 24 hours, EC expression of interleukin-8 and MCP-1 (cytokines involved

in inflammation) was nearly three times higher compared to the static control cells. They also found that the expression of these cytokines was proportional to the amplitude of cyclic stretch. Kakisis et al. (2004) suggest that the inflammatory response is initiated by cyclic-stretch mediated cell-death. Additionally, in their own studies Kakisis et al. (2004) found that EC migration is increased with an increase in cyclic stretch. As previously discussed, it is possible that EC migration may render the arterial wall susceptible to infiltration of inflammatory molecules.

Finally, several studies have shown that in addition to orientation, other differences exist in the response to cyclic stretch by ECs, vSMCs and fibroblasts. For example, while elevated production of ROS was observed for ECs, Howard et al. (1997) did not observe it for vSMCs. Furthermore, they found that collagen synthesis by ECs is reduced under cyclic stretch (the study by (Sumpio et al., 1990) found this to be true for cyclic stretch between 10-24%), while the opposite is true for vSMCs. In the excellent review on the topic of mechanical homeostasis of vascular tissue, Humphrey (2008b) points to early studies by Leung et al. (1976), which showed a 3-5-fold increase in collagen production by vSMCs exposed to 10% cyclic stretch. An increase in collagen production in response to an increase in cyclic stretch has also been observed for fibroblasts Breen (2000). Chiquet et al. (2003) discuss their early *in-vivo* experiments, which showed that externally applied cyclic stretch can lead to induction of specific ECM components in fibroblasts, rather than a generalised production or degradation response. Hence, it is clear that along with, and independently of WSS, cyclic stretch induces characteristic responses from ECs, vSMCs and fibroblasts.

In the following section, the effect of coupling cyclic stretch to the evolution equation for the mass of collagen is first examined in detail on the same test physiological case (TPC) utilised in the previous chapter, and then on the same 6 physiological cases examined in §6.2.1. In the following sections, the way in which cyclic stretch is coupled to the mass of collagen is investigated. The originally-proposed functional expression by which this achieved was presented in Equation (6.1) and Equation (6.2), and is hereon referred to as the "Cyclic Area Function" (CAF).

6.2.3 The effect of the exponential, multiplicative CAF: results on the test physiological case

The CAF was initially tested on the TPC corresponding to the **ICEM** surface reconstruction methodology. For the test case, the CAF was implemented within the evolution equation for the mass of collagen as a multiplicative exponential function, as per Equation (6.1)-2. In the current framework, it is assumed that in the real physiological scenario, new ECs, vSMCs and fibroblasts are deposited in a state of stretch (or rapidly achieve a state of homeostatic stretch). Assuming that $A_c^{CS} = 1$ corresponds to a polygonal shape and non-alignment of ECs, then $A_h^{CS} = 1.1$ is equivalent to 10% cyclic stretch. This seems in line with the findings of studies discussed in §6.2.2.1. The CAF is therefore implemented such that its contribution is included only if the ratio

$$\frac{A_c^{CS}}{A_h^{CS}} > 1, \text{i.e.,}$$
$$A_c^{CS} > 1.1$$

where A_c^{CS} is the current value of the cyclic area stretch. For $A_c^{CS} \leq 1.1$, the CAF is automatically set to 1. Figure 6.15 shows the evolving systolic and diastolic geometries, the A_c^{CS} and medial collagen strain and concentration for the TPC *without* the CAF implemented. As the geometry evolves over time, the deformation at systole is amplified, and the A_c^{CS} continues to increase. However, it can be seen that the mass of collagen increases significantly between $t = 10$ and $t = 12$ years in the proximal part of the dome as the recruitment stretches remodel to return the collagen strain to homeostatic levels. As such, the amount of deformation that occurs in this region between these time-steps is reduced. Furthermore, although the geometry has continued to deform, both the diastolic and systolic geometries are larger. Particularly in the proximal dome, the amplification at systole is countered by a larger diastolic geometry, and the A_c^{CS} is observed to reduce. However, as G&R in this case is applied only with respect to the systolic geometry, a large difference in the size and shape of the systolic and diastolic geometries is observed at $t = 12$ years, particularly towards the distal part of the dome. Consequently, the maximum A_c^{CS} is also very high (3.8, or 380% cyclic stretch). In this case, the rate of change in the mass of collagen is controlled only by β_0 and the deviation of the collagen strain, $E^C_{J_p}|_{\max}$ from the equilibrium value. Although the collagen mass increases over time, the rate of increase is not high enough to constrain the growth of the dome. Corresponding to the increase

in m^C_{M+}, the A^{CS}_c is observed to reduce in the proximal part of the dome. In contrast, it is at a maximum in the distal part of the dome, where the collagen concentration did not increase.

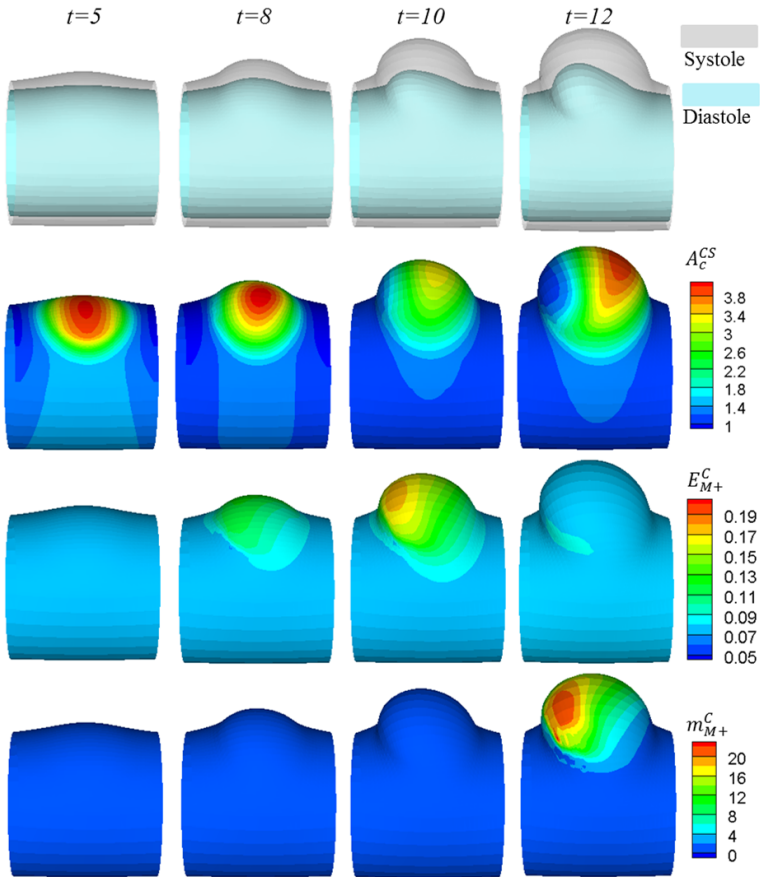


Figure 6.15: Evolving systolic and diastolic geometries, the A^{CS}_c, E^C_{M+} and m^C_{M+} for the test physiological case at $t = 5, 8, 10$ and 12 years, without the CAF. The consequence of performing G&R only with respect to the systolic geometry is an unrealistically-large difference between the systolic and diastolic geometries. As a result, the maximum A^{CS}_c is also unrealistically large.

Figure 6.16 shows the TPC with the CAF implemented. The CAF acts to increase the mass of collagen more rapidly, and the A^{CS}_c is observed to be much smaller compared to the TPC without CAF (1.45 vs 3.8).

It can be seen that the mass of collagen increases in regions where both E^C_{M+} and A^{CS}_c are high, and consequently, the final geometry is smaller. In contrast to the collagen strain, A^{CS}_c is highest at the distal part of the dome, and the increase in collagen mass in this region accounts for a less spherical, and more clearly asym-

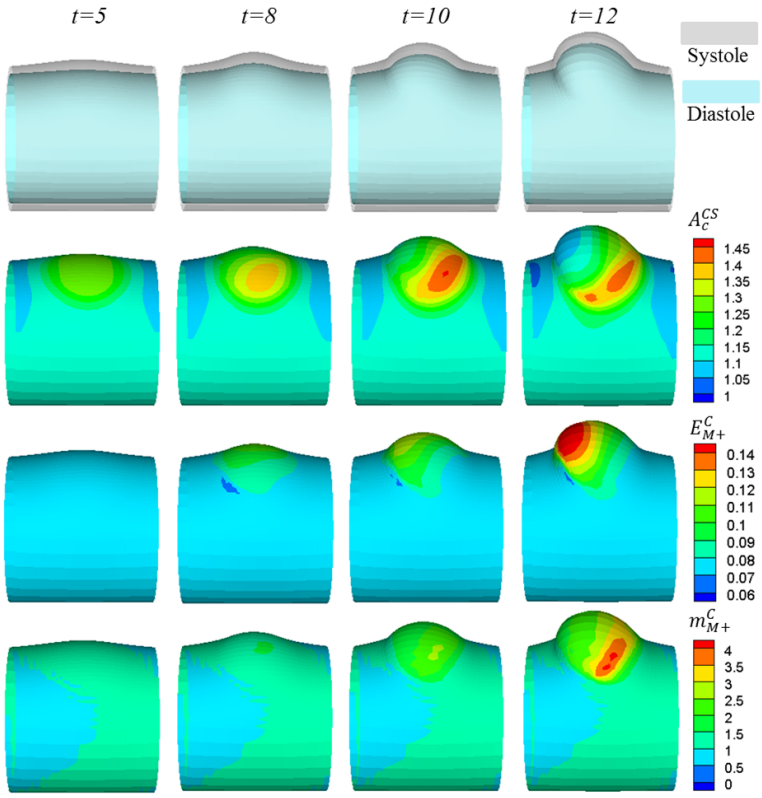


Figure 6.16: Evolving systolic and diastolic geometries, the A_c^{CS}, E_{M+}^{C} and m_{M+}^{C} for the test physiological case at $t = 5, 8, 10$ and 12 years, with the CAF. With collagen mass additionally coupled to cyclic stretch, the mass of collagen increases more rapidly, and the size of the final geometry is smaller.

metrical shape of the model aneurysm, compared to the TPC without the CAF. The difference between the systolic and diastolic geometries is therefore more realistic, and the model aneurysmal geometry with the CAF implemented even more closely resembles the original aneurysmal geometry (see Figure 6.17).

However, while the implementation of the CAF was physiologically-motivated, the choice of functional form, as well as its implementation as a multiplicative function in the evolution equation for the mass of collagen represents an "initial guess". The A_c^{CS} is much smaller with the CAF implemented; however, it continues to increase over time to a maximum of 1.45, or 45% cyclic stretch. This is still nearly double the highest-reported upper physiological value of 24%. Firstly, the maximum cyclic stretches occurring in physiological and pathological conditions are not clearly defined in the literature, so it is unclear if a stretch of 45% is reasonable. Furthermore, if 24% is indeed the upper physiological threshold, then it is likely that

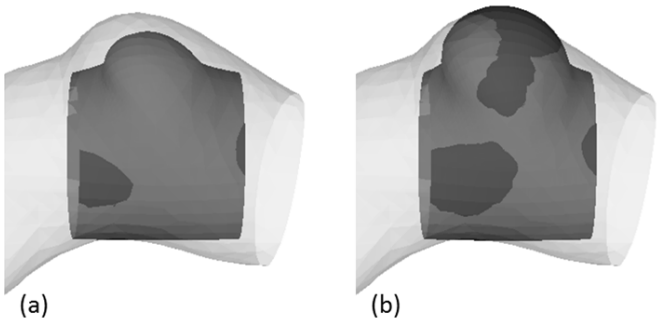


Figure 6.17: Comparison of the final test physiological geometries with (b)without CAF to the original aneurysmal geometry

the normal function of ECs, vSMCs and fibroblasts in degrading and depositing collagen will be disrupted for stretches above this value. This provides motivation to examine alternative functional forms and implementations of the CAF, which will provide a balance of enlargement and stabilisation such that the magnitude of A_c^{CS} is constrained to within a reasonable range. As such, in the following section, the effect of implementing the exponential CAF as an *additive* function is examined for the 6 physiological cases introduced in §6.2.1. In contrast to the multiplicative implementation, the additive CAF is implemented such that

$$\frac{\mathrm{d}m_{J_p}^C}{\mathrm{d}t} = \beta_0 m_{J_p}^C \left(\frac{E_{J_p}^C|_{\max} - E_{AT}^C}{E_{AT}^C} \right) + CAF, \tag{6.3}$$

where

$$CAF = \beta_0 \exp\left[\beta^{CS} \max\left(\frac{A^{CS}}{A^{CS}|_{t=0}} - 1 \right) \right] \tag{6.4}$$

In this case, $\beta_0 = 0.01$, and β^{CS} was reduced to 3, so as to ensure that an initial outpouching of the geometry is not stifled by rapid deposition of collagen. The remaining G&R parameters are set as per Table 6.2.

6.2.3.1 The effect of the exponential, additive CAF: results for 6 physiological cases

To investigate the effect on the evolving aneurysm geometry of linking the exponential additive CAF to the evolving collagen concentration, S1 and S2 results are compared. Figure 6.18 shows growth overlays of the 6 cases with (S1) and without (S2) the CAF at $t = 5$, $t = 8$, $t = 12$ and $t = 16$ years. In all cases, the S1 model aneurysms are observed to be larger than their S2 counterparts, which suggests that the A_c^{CS} is

high in the early stages of evolution, such that the mass of collagen increases rapidly to stabilise the aneurysm.

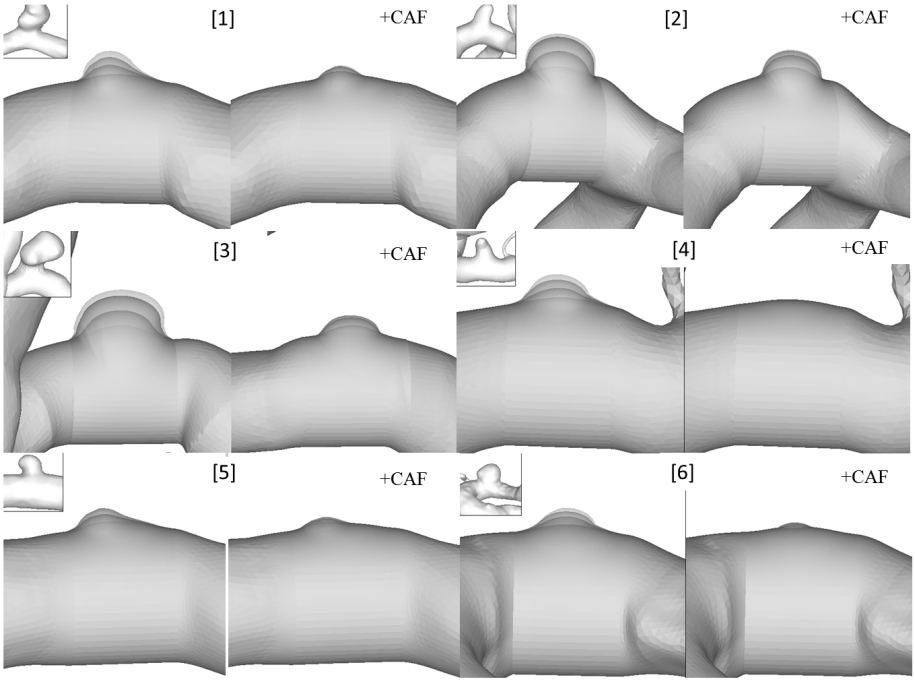


Figure 6.18: Overlays of the evolving aneurysmal geometry at $t = 5$, $t = 8$, $t = 12$ and $t = 16$ years, with (left) and without (right) the CAF, for 6 cases

Interestingly, it can be seen that for some S2 cases (e.g. cases 2 and 3), the aneurysm enlarged despite the introduction of the CAF, while for others (e.g. cases 4 and 6), the aneurysm grew very little. The WSS and elastin concentration plots for the two cases are shown in Figure 6.19.

The evolving WSS distributions for case 2 and 4 are very different: while a patch of low WSS can be seen throughout the evolution of the case 2 aneurysm, such a region does not develop for case 4. Correspondingly, while the elastin concentration is observed to decrease gradually over the course of the case 2 aneurysm evolution, this is not observed for case 4, where the elastin concentration remains between 0.1 and 0.2 within the aneurysm dome. The difference arises due to a combination of the local WSS environment (arising due to the physiological geometry, Figure 6.19(a)) and the CAF.

The critical WSS thresholds for elastin degradation (see §4.4.2) for case 2 were $\tau_{\text{crit}} = 9.2$Pa (at which elastin degradation is initiated), and $\tau_X = 4.6$Pa (at which

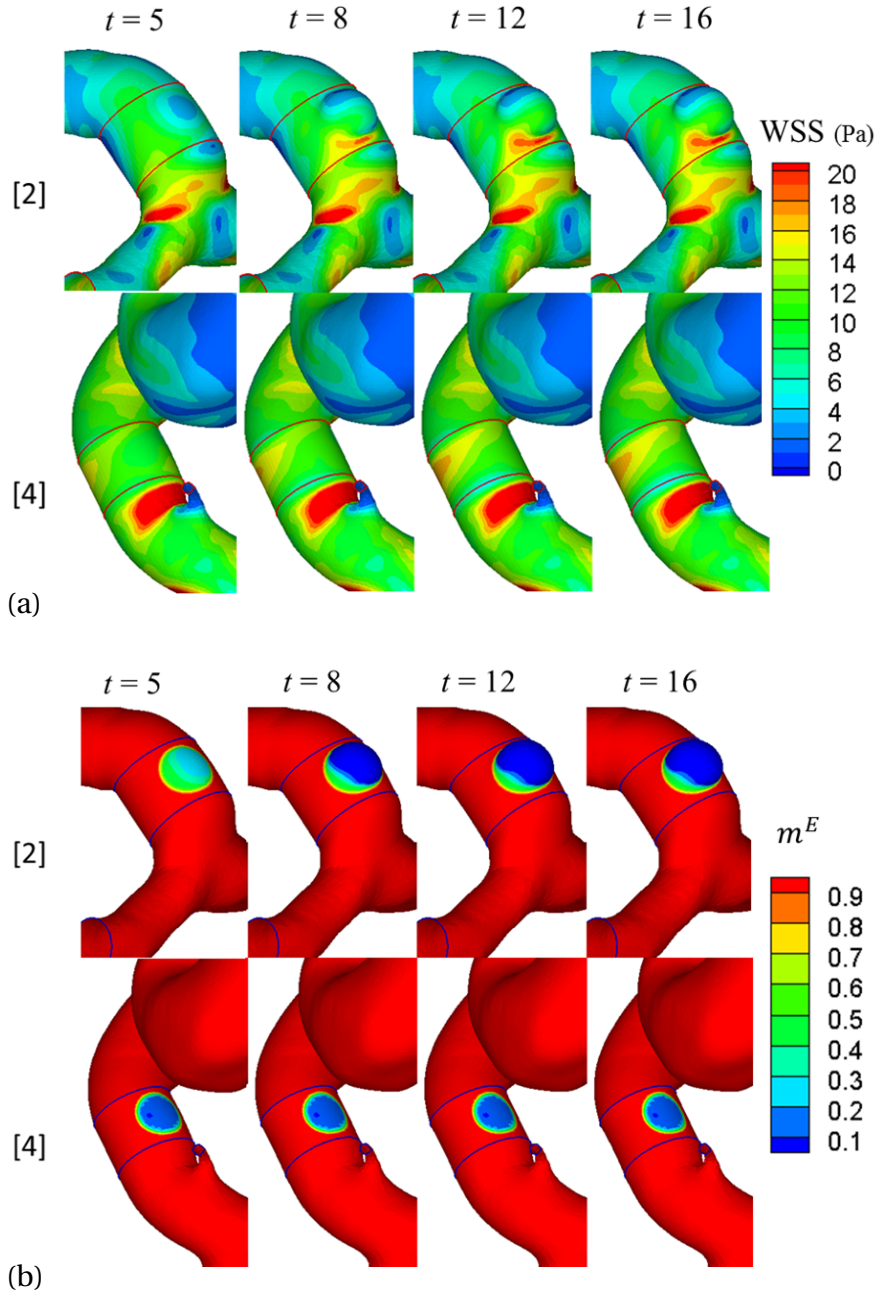


Figure 6.19: Evolving WSS (a) and elastin concentration (b) distributions for cases 2 (top) and 4 (bottom) with CAF, at $t = 5$, $t = 8$, $t = 12$ and $t = 16$ years

the rate of degradation is *maximum*). At $t = 5$ years, 2≤WSS≤8Pa is observed in the upstream region surrounding the circular domain from which the aneurysmal geometry evolves. The curvature of the geometry surrounding the cylinder is such as to result in 2≤WSS≤8Pa within this domain, which results in elastin degradation and growth of the geometry. In this case, elastin degradation occurs faster than the deposition of collagen despite the implementation of the CAF. For case 4, this balance between elastin degradation and collagen growth is tipped the other way. The critical WSS values for elastin degradation for case 4 were $\tau_{\text{crit}} = 8$Pa and $\tau_X = 4.6$Pa. At $t = 5$, WSS in the region upstream of the cylindrical domain for case 4 is observed to be greater than 8Pa, and the curvature of the geometry is such that within the circular domain, the WSS is also greater than this critical value.

However, the case 4 aneurysm grew when the CAF was not implemented (see Figure 6.18). In this case, the lack of growth is accounted for by two interlinked factors:

1. The CAF is implemented from the beginning of the simulation, and as such the deformation of the case 4 geometry due to prescribed elastin degradation is reduced (see Figure 6.21);

2. The lack of deformation of the geometry does not facilitate the creation of a low WSS environment within the domain (in fact, it can be seen from Figure 6.20 that the S2 WSS is elevated within the domain at $t = 5$ years. Hence, the rate of elastin degradation is not high enough to overcome the rate of collagen deposition, and the geometry does not grow further.

Figure 6.22 and Figure 6.23 show the evolving CAF and medial collagen concentration for cases 2 and 4. It can be seen from Figure 6.22 that for case 2, the A_c^{CS} is initially high (≥1.25). For the same time-step, an increase in medial collagen concentration is observed, which continues to increase during the course of aneurysm evolution. As a result, the amount of deformation between subsequent time-steps reduces, and thereby the A_c^{CS} is observed to reduce. Figure 6.23 shows a similar process occurring for case 4, but compared to case 2, the increase in collagen, and hence the reduction of the A_c^{CS} are more rapid.

Hence, it is clear from the results presented in this section that the choice of functional form of the CAF requires more consideratoin, so as to achieve the best

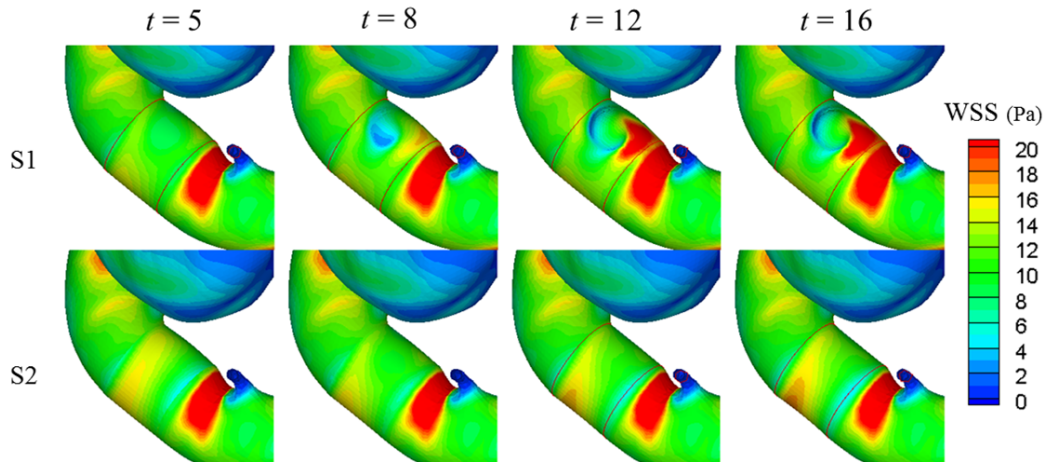


Figure 6.20: Evolution of the WSS distributions for case 4 with (S2) and without (S1) the CAF at $t = 5$, $t = 8$, $t = 12$ and $t = 16$ years

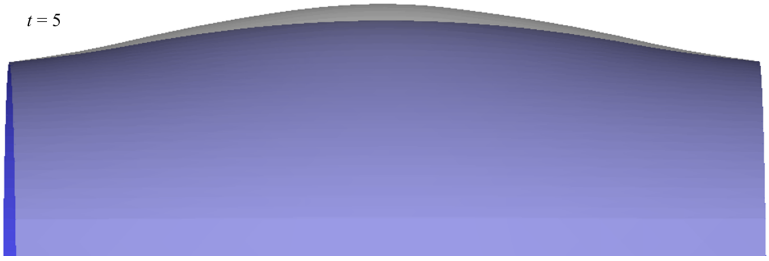


Figure 6.21: Overlay of the case 4 cylindrical geometries with (blue) and without (grey) CAF at $t = 5$ years. In this case, the collagen deposition due to the CAF restricts the deformation of the geometry. In turn, the perturbation to the local haemodynamic environment is not large enough to generate a region of WSS low enough to increase the rate of elastin degradation above that of collagen deposition. Hence, the aneurysmal geometry does not grow.

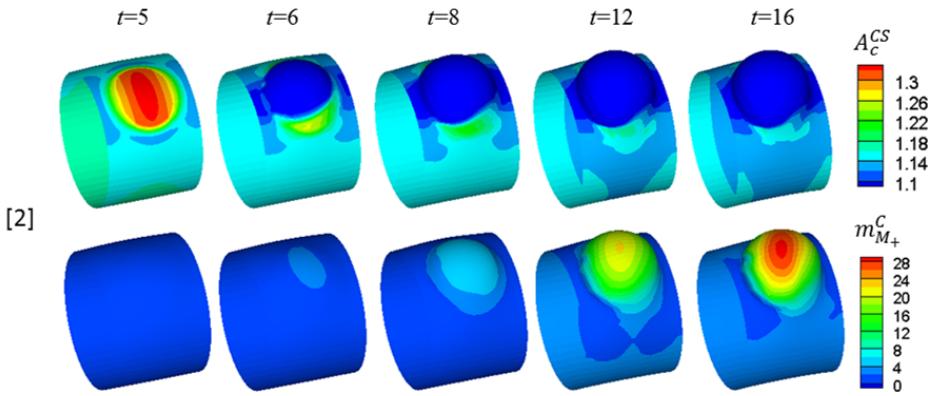
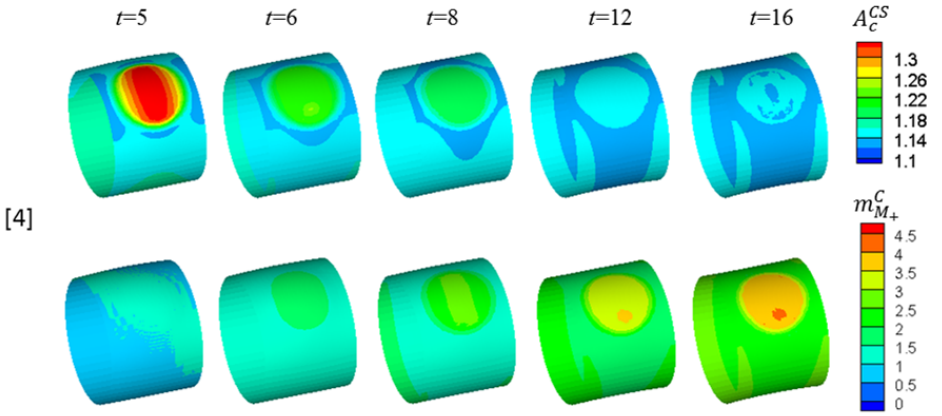


Figure 6.22: Evolving CAF and medial collagen concentration (m^C_{M+}) for case 2, at $t = 5$, $t = 6$, $t = 8$, $t = 12$ and $t = 16$ years



[4]

Figure 6.23: Evolving CAF and medial collagen concentration (m^C_{M+}) for case 4, at $t = 5$, $t = 6$, $t = 8$, $t = 12$ and $t = 16$ years

balance between aneurysm enlargement and stabilisation. In the following sections, the effect on the model aneurysm geometry of several functional forms of the CAF, exponential, quadratic, linear, square-root and sigmoidal, in both multiplicative (CAF_{mult}) and additive (CAF_{add}) implementations is compared on the idealised cylindrical geometry (i.e. solid-only simulations were performed). Subsequently, the best combination of functional form and implementation is chosen and tested on the TPC.

6.2.4 Comparison of different functional forms of the CAF: Experiments on the idealised, cylindrical geometry

Firstly, it is useful to define a general equation for the CAF, i.e.,

$$\text{CAF} = \mathscr{F}(\beta^{CS} x),$$

where $\beta^{CS} = 3$, and

$$x = \left(\frac{A_c^{CS}}{A_h^{CS}} - 1 \right)$$

The evolution equation for the mass of collagen can then be generalised as below:

$$\frac{\mathrm{d}m^C_{J_p}}{\mathrm{d}t} = g(x) m^C \beta \left(\frac{E^C_{J_p} - E^C_{AT}}{E^C_{AT}} \right) + h(x) \tag{6.5}$$

where

$$g(x) = \mathrm{CAF}_{\mathrm{mult}}, \text{and}$$
$$h(x) = \mathrm{CAF}_{\mathrm{add}}$$

Without the CAF,

$$g(x) = 1, \text{and}$$
$$h(x) = 0$$

When the CAF is implemented as a multiplicative,

$$g(x) = \begin{cases} \mathscr{F}(A_c^{CS}) & \text{if } A_c^{CS} > A_h^{CS} \\ 1 & \text{if } A_c^{CS} \leq A_h^{CS} \end{cases} \text{ and}$$
$$h(x) = 0$$

When the CAF is implemented as an additive,

$$g(x) = 1, \text{and}$$
$$h(x) = \begin{cases} \mathscr{F}(A_c^{CS}) & \text{if } A_c^{CS} > A_h^{CS} \\ 0 & \text{if } A_c^{CS} \leq A_h^{CS} \end{cases}$$

In order to enable comparison of various functional forms, a fixed maximum and minimum contribution of the CAF, $\mathrm{CAF}_{\mathrm{max}}$, to the mass of collagen was defined. For this examination, $\mathrm{CAF}_{\mathrm{max}} = 1.35$ was arbitrarily chosen. Utilising the original exponential form of the CAF, a deviation of the cyclic stretch from homeostatic levels of $x = 0.1$ was derived. Hence, scalars $k_{i...5}$ were defined to enable comparison of the five functions over an x interval of 0 to 0.1, with fixed minimum and maximum CAF values of 0 and 1.35 respectively (Figure 6.24). β_0 is set to 0.6.

Figure 6.24 shows that different functional forms of the CAF result in an increase in CAF at different rates. For smaller values of x (i.e. for $0 \leq x \leq 0.05$), the square-root function increases most rapidly, while the exponential function increases at the slowest rate. The converse is true for higher deviations. Solid-only simulations were conducted (up to $t = 10$ years) on the cylindrical geometry to observe the effect on the size of the aneurysmal geometry.

Figure 6.25 shows the comparison of geometries corresponding to no CAF (β_0 only), ($\mathrm{CAF}_{\mathrm{mult}}$) (blue) and $\mathrm{CAF}_{\mathrm{add}}$ (green), at $t = 10$ years. It can be seen that when

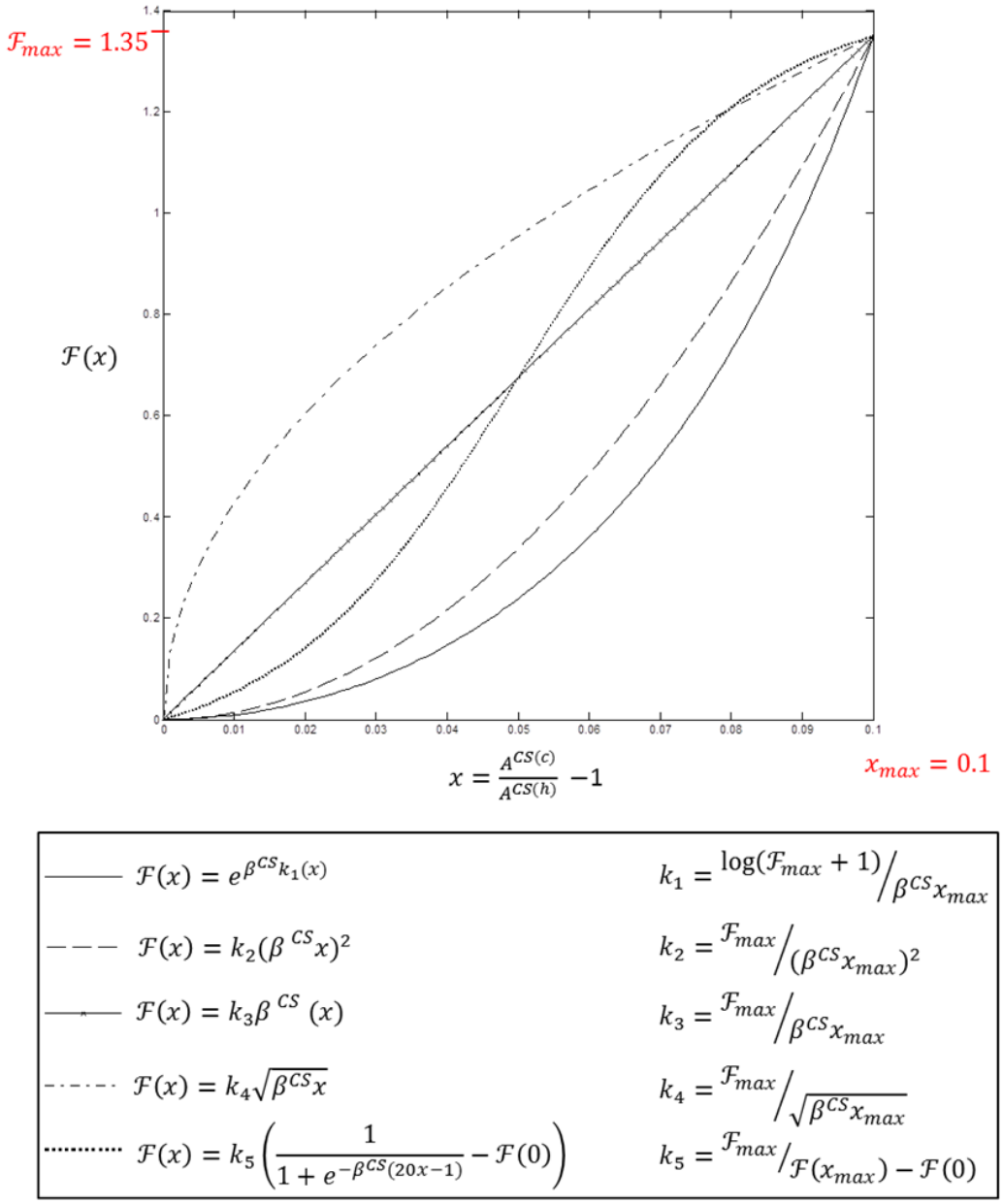


Figure 6.24: Comparison of five functional forms for the CAF, scaled such that the maximum CAF contribution ($\mathcal{F}_{\max}$) is 1.35, while $x = \left(\frac{A_c^{CS}}{A_h^{CS}} - 1 \right) \in [0, 0.1]$

the CAF is implemented as an additive, the geometry at $t = 10$ is smaller than the β_0-only geometry for all functional forms. In contrast, only the exponential and sigmoidal forms of CAF_{mult} result in geometries that are smaller than the β_0-only geometry, while the geometries corresponding to the quadratic, linear and square-root CAF_{mult} are larger. This is due to the fact that the CAF_{mult} is scaled by β_0 (0.6) and the ratio $\left(\frac{E^C - E^C_{AT}}{E^C_{AT}}\right)$, which itself may not always be greater than 1, and which may be negative. In the case of the sigmoid function, the size difference is less significant than for other cases. Although the quadratic CAF_{mult} results in the largest aneurysmal geometry, the quadratic, linear, square-root and sigmoidal forms of the CAF_{mult} result in similarly sized aneurysm geometries at $t = 10$ years.

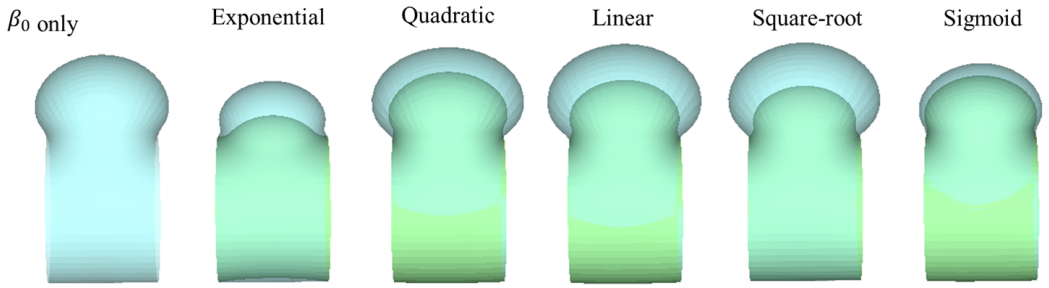


Figure 6.25: Comparison of size of geometries for which the CAF is implemented as a multiplicative (blue) vs. additive (green) function, at $t = 10$ years

In contrast, it can be seen from Figure 6.25 that the geometry corresponding to the exponential CAF is considerably smaller than the others for both implementations. It also exhibits a large difference in size between the multiplicative and additive implementations. Hence, let us consider this case in a closer examination of the CAF. Figure 6.26 shows the difference between the evolving geometries corresponding to the exponential CAF_{mult} and CAF_{add} from $t = 5$ to $t = 10$ years. The difference in size can be explained by comparing the evolving cyclic stretch, and collagen concentration for the two geometries.

At $t = 5$ years, the A_c^{CS} corresponding to CAF_{mult} and CAF_{add} are 1.36 and 1.1 respectively in the aneurysm dome. Recall that the contibution of CAF to the mass of collagen is governed by the magnitude of deviation of A_c^{CS} from A_h^{CS}, such that the CAF is only included in the evolution equation for the mass of collagen if $\frac{A_c^{CS}}{A_h^{CS}} > 1$, i.e. if $A_c^{CS} > 1.1$. Hence, while CAF_{mult} is active at $t = 5$, CAF_{add} is not; at this point, the change in the mass of collagen corresponding to CAF_{add} is purely a function of

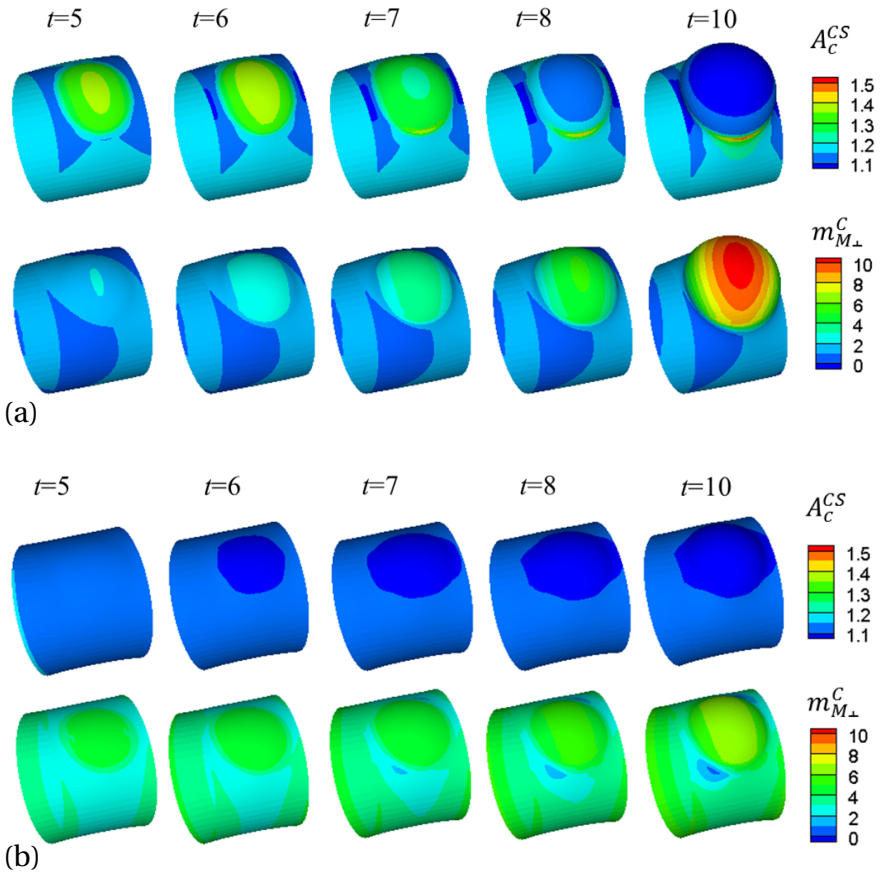


Figure 6.26: Evolution of the areal cyclic stretch (A_c^{CS}) and the medial collagen concentration (m^C_{M+}) for the exponential CAF implemented as a multiplicative (a) vs. additive (b) function, at $t = 5, 6, 7, 8$ and $t = 10$ years

the collagen strain.

Figure 6.27 shows that CAF_{add} acts early in the evolution of the geometry, when the A_c^{CS} is largest. The resulting increase in the mass of collagen limits the deformation of the geometry such that A_c^{CS} rapidly returns to homeostatic levels (at $t = 5$ years). In contrast, the contribution of CAF_{mult} is smaller, and therefore the reduction in A_c^{CS} towards homeostatic levels is slower (occurs at $t = 8$ years). To illustrate the difference in contributions, a sample of the A_c^{CS}, and medial collagen concentration data at a point in the centre of the aneurysm dome was taken for the two geometries at $t = 4$ years (at which the A_c^{CS} corresponding to CAF_{add} is still greater than 1.1 within the aneurysm dome), shown in Table 6.5.

Table 6.5 shows that at $t = 4$ years, m^C_{M+} is higher in the case of the additive. This

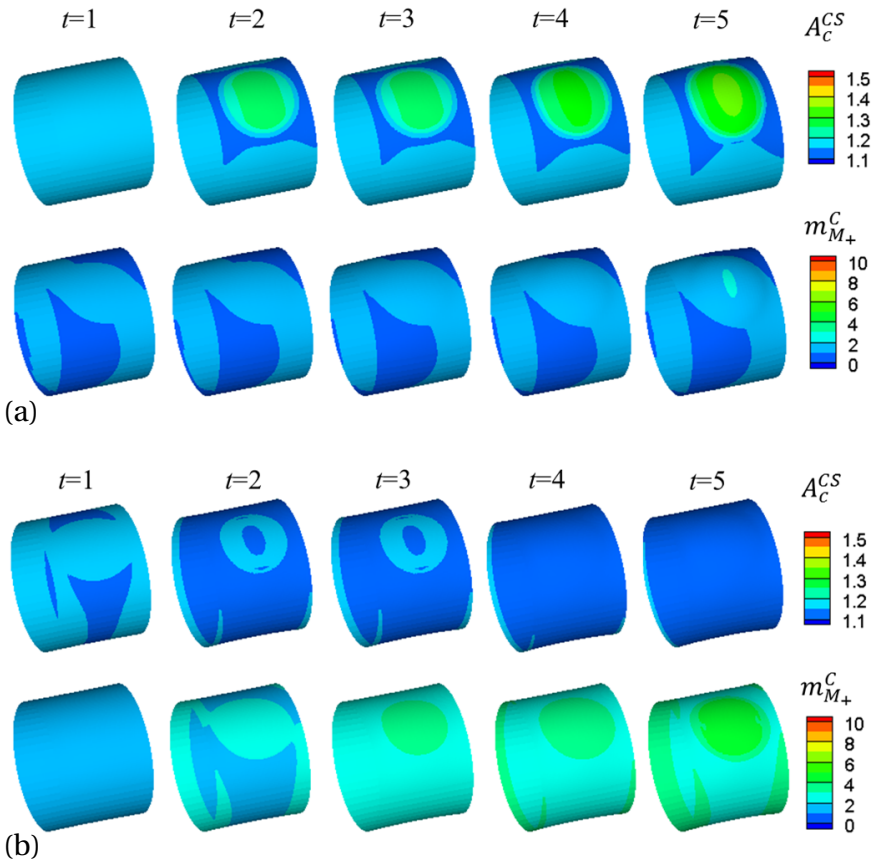


Figure 6.27: Evolution of the areal cyclic stretch (A_c^{CS}) and the medial collagen concentration (m_{M+}^C) for the exponential CAF implemented as a multiplicative (a) vs. additive (b) function, at $t = 1, 2, 3, 4$ and $t = 5$ years

acts to limit the deformation of the geometry, such that the corresponding cyclic stretch and CAF values are smaller compared to their CAF_{mult} counterparts. The medial collagen strain is also smaller for the additive, reflecting the lesser deformation for this case.

Table 6.4: Comparison of medial cyclic stretch (CS_{M+}), CAF, medial collagen concentration m^C_{M+}, and medial collagen strain (E^C_{M+}) data for a point in the centre of the domain of the geometries corresponding to the multiplicative vs additive exponential CAF at $t = 4$ years

Data	Multiplicative	Additive
A^{CS}_c	1.318	1.128
$m^C_{M+(i)}$	1.585	3.661
$E^C_{M+(i)}$	0.082	0.080
Δm^C_{M+}	0.004	0.026
$m^C_{M+(i+1)}$	1.589	3.687

In both cases, the updated collagen concentration, $m^C_{M+(i+1)}$, is given by the sum of the current collagen concentration, $m^C_{M+(i)}$ and the change in collagen concentration, scaled by the time increment, $\Delta t = 0.02$, i.e.

$$m^C_{M+(i+1)} = m^C_{M+(i)} + \frac{dm^C_{M+(i)}}{dt} \times \Delta t,$$

Substituting the values of cyclic stretch, collagen concentration and collagen strain, the change in collagen concentration, $\frac{dm^C_{M+(i)}}{dt}$, and the updated collagen concentration for the next time-step for both the CAF_{mult} and CAF_{add} are obtained. Although both the A^{CS}_c and E^C_{M+} are bigger in the case of the CAF_{mult}, the increment in collagen mass -i.e. $\frac{dm^C}{dt}$ -is larger for the CAF_{add} (0.0236 compared with 0.004). Hence, the additive form of the CAF provides a greater contribution to the mass of collagen compared to the multiplicative form, and, although not high enough to counteract the rate of elastin degradation, this accounts for the lesser growth of the evolving geometry corresponding to CAF_{add}.

This is why, in general, the geometries corresponding to CAF_{mult} are larger for all functional forms than their CAF_{add} counterparts. Furthermore, both the similarities and differences in size (e.g. quadratic vs linear, and linear vs exponential) of the geometries corresponding to CAF_{mult} can be explained by considering the *real* maximum A^{CS}_c that occurred during simulations. Assuming an exponential CAF, the initial guess for a maximum value of the CAF of 1.35 corresponds to a maximum deviation of the A^{CS}_c from A^{CS}_h of 0.1, and scalars $k_{i\ldots5}$ are calculated such that the functions are comparable over this interval. However, Table 6.5 shows that in the case of the multiplicative CAF, the maximum deviation is up to 6 times larger than

0.1. It is therefore useful to visualise the trajectories of the functions over the interval representative of the largest deviation (0.59).

Table 6.5: Comparison of maximum cyclic areal stretch ($A^{CS}_{c_{\max}}$) and the corresponding maximum deviation of the current cyclic stretch from the homeostatic stretch ($x_{\max}$) within the circular domain for the multiplicative (M) and additive (A) implementations of different functional forms of the CAF

Functional form of CAM	$A^{CS}_{c_{max}}$		x_{max}	
	M	A	M	A
Exponential	1.477	1.166	0.34	0.06
Quadratic	1.691	1.221	0.54	0.11
Linear	1.746	1.223	0.59	0.11
Square-root	1.751	1.218	0.59	0.11
Sigmoid	1.555	1.221	0.41	0.11

Figure 6.28 shows that without changing the initial definition of the functions, for $x > 0.1$ the trajectories of the functions change significantly. The quadratic and exponential functions increase more rapidly between 0.1 and 0.59 (with CAF values of ≈ 47 and 154 at $x = 0.59$ respectively). Particularly in the case of the exponential CAF, this accounts for the comparatively smaller final geometry for both the multiplicative and additive implementations of the CAF. While the rate of increase of the linear function remains unaffected, it can be seen that the rate of increase of the square-root function decreases, while the sigmoid plateaus at ≈ 1.421 for $0.1 \leq x \leq 0.59$. Furthermore, while the linear and square-root functions increase more slowly for higher x compared to the quadratic, the converse is true for low x. As such, although the rate of change of the CAF is different depending on the functional form, these differences are balanced by the changing behaviour of the functions over and beyond the initially-defined interval.

Hence, in the final implementation of the CAF, the expected maximum deviation of the A^{CS}_c from A^{CS}_h will be an important consideration in defining the function.

6.2.5 The effect of the CAF when coupled to physiological flow

The experiments on the cylindrical geometry, and the TPC in the previous sections bring to light two important considerations for the implementation of the CAF

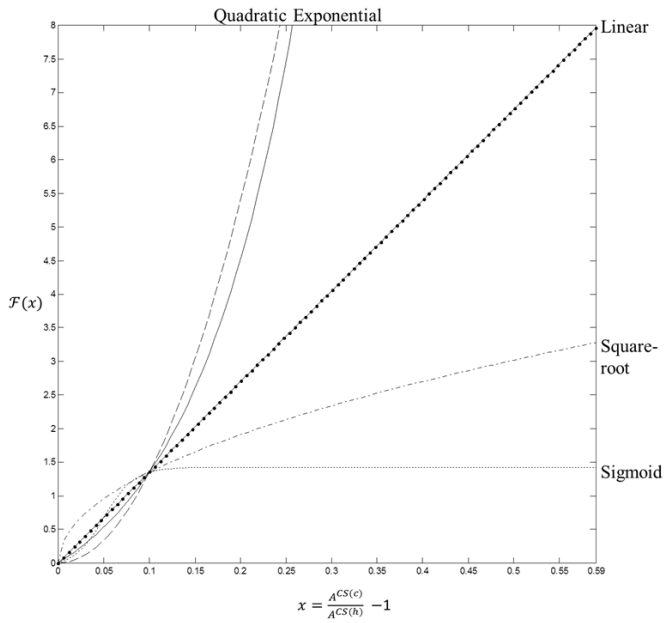


Figure 6.28: Comparison of the five functional forms of the CAF over the extended interval 0-0.59, with the $x_{\max}$ values highlighted in red

within the physiological framework. Firstly, the results so far show that A_c^{CS} evolves differently for symmetrical and asymmetrical geometries. In the case of solid-only simulations, elastin degradation is prescribed to occur symmetrically, and the A_c^{CS} is observed to reduce across the dome. However, the TPC examined in §6.2.3 (Figure 6.16) evolves asymmetrically, and while the A_c^{CS} is observed to reduce in the proximal dome, it continues to increase in the distal dome.

Secondly the maximum A_c^{CS} is very high (up to 1.7 for the idealised cylindrical case) and seems unlikely to occur in the physiological setting, or, if it does, it seems unlikely that the regular function of vSMCs and fibroblasts of secreting collagen would be maintained at this level of stretch.

Therefore, the appropriate implementation of the CAF should be such that the A_c^{CS} does not exceed much beyond some maximum threshold. Given that Iba and Sumpio (1991) found regular function of ECs at up to 24% stretch, a 30% cyclic stretch is proposed here as a maximum physiological cyclic stretch. At 30%, the contribution of the CAF to the mass of collagen should be maximal, and act to rapidly return the A_c^{CS} towards homeostatic levels, even for an asymmetrically-evolving geometry.

In terms of selecting the most appropriate functional form and implementation of the CAF, the final choice will ideally capture a range of different cellular responses to cyclic stretch, which affect collagen concentration. The effect of the function should also reflect what is known about both the structure and physiology of the wall at different stages of aneurysm development. With increasing cyclic stretch, ECs produce more NO and MMPs, which act to degrade elastinous and collagenous constituents, allowing the vessel to dilate. Simultaneously, vSMCs and fibroblasts produce *more* collagen in response to an increase in stretch. However, as the aneurysm grows, the number of medial vSMCs reduces, and hence the contribution to collagen mass by vSMCs reduces. Meanwhile, the cyclic stretch environment changes from uniaxial, to increasingly bi-axial. In this environment, ECs fail to elongate and show no prefered alignment, such that the junctional gaps between them may increase. Furthermore, the locally low WSS within the growing dome increases the residence time, and thereby the likelihood of inflammatory cell infiltration into the wall. Inflammatory cells themselves release MMPs and act to degrade elastin and collagen. Hence, it is possible that during initial deformation, the MMP-mediated degradation of collagen is countered by the production of collagen by vSMCs and fibroblasts. There also appears to be a "tipping point" during aneurysm growth, at which the loss of vSMCs and the degradation of existing collagen by MMPs means that the mass of collagen (now being deposited primarily by fibroblasts) continues to increase, but at a reduced rate. Finally, although some aneurysms grow to large sizes, many stabilise. In these cases, it can be argued that at later stages of growth, although the rate of collagen increase reduces, there is enough collagen to restrict further deformation.

It seems that precisely because of its shape, the sigmoid function is the best suited for implementation within the patient-specific framework. Figure 6.29 shows that in its present form the function acts to significantly increase the collagen concentration in the early stages of deformation: i.e. A_c^{CS} is highest between years 2 and 4. At t = 6 years, A_c^{CS} begins to return towards homeostatic levels, while the collagen concentration continues to increase. This appears to be in line with the hypothesis for physiological events described above. Additionally, Table 6.5 shows that for all functional forms, the ratio $\left(\frac{A_c^{CS}-A_h^{CS}}{A_h^{CS}}\right)$ is greater than the initial guess of 0.1. The plot of the functions over the maximum measured deviation (Figure 6.28) shows that while all other functions continue to increase when the ratio exceeds 0.1, the sigmoidal CAF plateaus at a value very close to the initially-proposed maximum

of 1.35. This means that the maximum contribution of the sigmoidal CAF to the mass of collagen remains fixed above a specified maximum A_c^{CS}. This is in fact a desirable property, and becomes clear when considering fluid-flow simulations.

In fluid-flow simulations where the elastin degradation is linked to the local WSS levels, the early deformation of the geometry is pivotal in creating the initial perturbation to the haemodynamic environment. This allows for the formation of a region of low WSS, which drives subsequent elastin degradation and further deformation. As shown in Figure 6.19, the action of the additive exponential CAF for case 4 resulted in a large increase in the mass of collagen at early stages of deformation, such that a region of low WSS did not evolve, and consequently the aneurysm did not grow. It can be seen from Figure 6.28 that the magnitude of the exponential CAF becomes very large for $\left(\frac{A_c^{CS}-A_h^{CS}}{A_h^{CS}}\right) > 0.1$. In contrast, the magnitude of the sigmoidal CAF is fixed, which prevents it from laying down too much collagen. Additionally, recall that the increment in collagen mass is generally greater for CAF_{add} than for CAF_{mult}. Hence, CAF_{add} will act to constrain deformation more rapidly at early stages, compared to CAF_{mult}, which may prohibit the evolution of a low WSS environment.

For consistency, the sigmoid multiplicative CAF was applied to the TPC presented in §6.2.3. However, as was observed on the TPC case, the multiplicative function alone is not sufficient to return the A_c^{CS} to homeostatic levels, particularly in the case of an asymmetrically-evolving geometry. Figure 6.29 shows that with the sigmoid CAF_{mult} alone, the A_c^{CS} continues to increase, and reaches a maximum of 1.55.

Therefore, the additive CAF is also needed to return the A_c^{CS} towards A_h^{CS}, and to ensure that it does not exceed far beyond the proposed maximum physiological threshold. Given the comparatively rapid action of the exponential CAF compared to other functional forms, this function was chosen and implemented such that it is only active when $A^{CS}c \geq 1.3$, as shown in Figure 6.30. The maximum physiological threshold of $A_c^{CS} = 1.3$ corresponds to $x_{\max} = \left(\frac{A_c^{CS}-A_h^{CS}}{A_h^{CS}}\right) \approx 0.18$. Hence, the sigmoid function was re-defined to fit within this new interval, while its maximum contribution to the mass of collagen was left unchanged at 1.35. This ensures that when the additive is active, the mass of collagen does not increase excessively. For this simulation, the minimum concentration of elastin at the end of the prescribed degradation period (again, $t = 5$ years) was set to 0.1, and β was reduced to 0.01 to

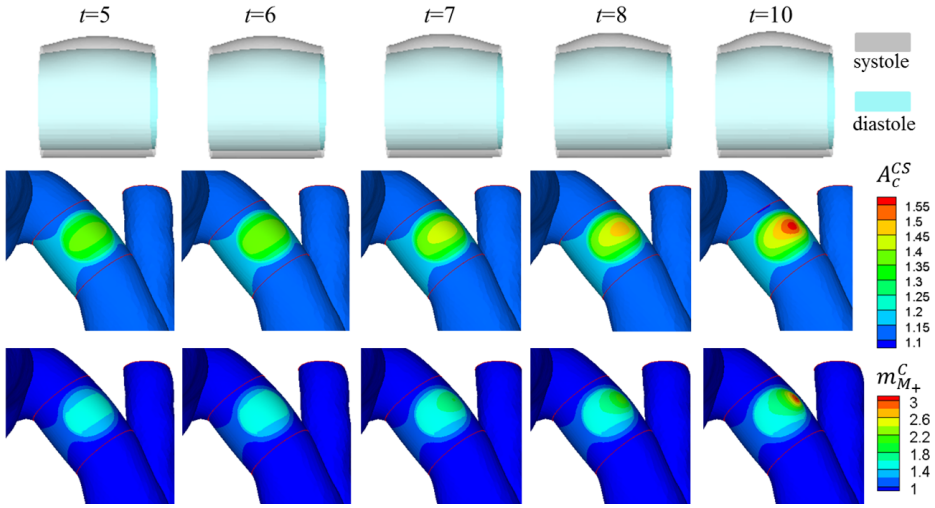


Figure 6.29: The evolving systolic and diastolic geometries (top), and the corresponding systolic areal cyclic stretch (A_c^{CS}) and medial collagen concentration (m^C_{M+}) for the test case with a sigmoid multiplicative CAF, at $t = 5$, $t = 6$, $t = 7$, $t = 8$ and $t = 10$ years

ensure that an initial bulge is created.

Figure 6.31 shows the evolution of the geometry for a combinatory implementation of the sigmoid multiplicative and exponential additive CAF. The maximum A_c^{CS} is 1.35, but the A_c^{CS} is reducing over time. However, while the geometry still evolves asymmetrically, the maximum A_c^{CS} occurs early in the evolution (at $t = 5$), and hence the contribution of the CAF to the mass of collagen is maximal.

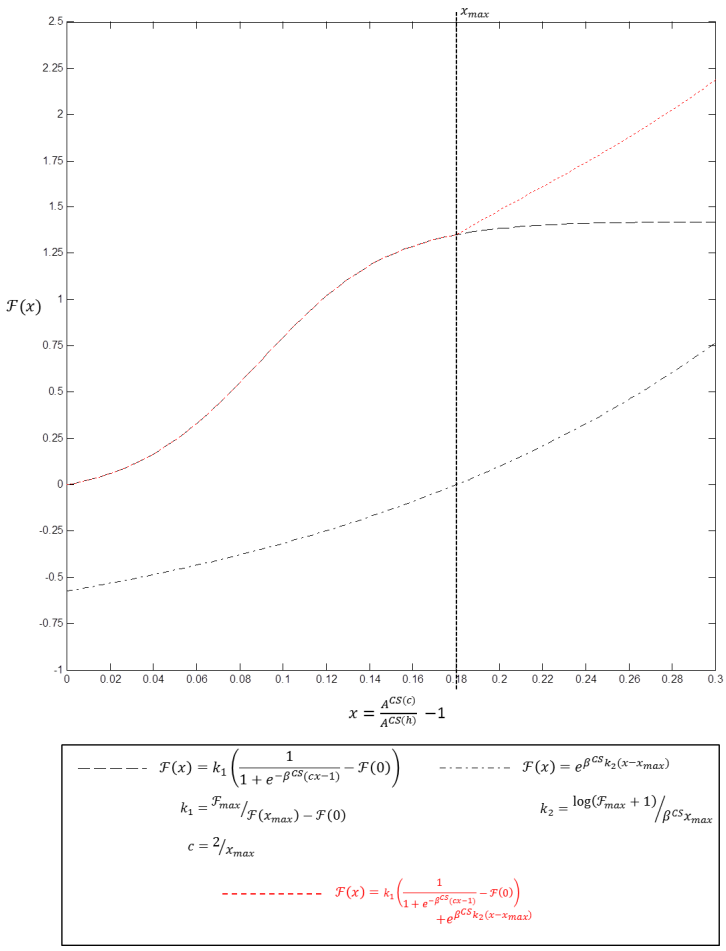


Figure 6.30: The evolution of the CAF when implemented as a combination of a multiplicative sigmoid and additive exponential. Here, $\mathscr{F}(x)$ represents the functional form of the CAF, plotted against the deviation of the current cyclic area stretch, A_c^{CS} from the homeostatic cyclic area stretch, A_h^{CS}

Figure 6.32 shows that although a region of low WSS developed, it is small, thereby facilitating only a small region of continued elastin degradation beyond the prescribed degradation period. This is evident from the plot of the elastin concentration, which shows that only a small patch of $m^E < 0.5$ evolves in the proximal part of the aneurysm dome. Hence, the final geometry is very small.

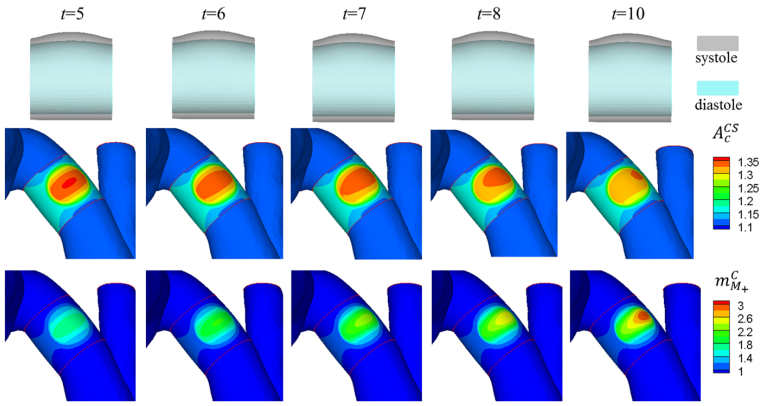


Figure 6.31: The evolving systolic and diastolic geometries (top), and the corresponding areal cyclic stretch (A_c^{CS}) and the medial collagen concentration (m_{M+}^C) for the test case with a sigmoid multiplicative and exponential additive CAF, at $t = 5$, $t = 6$, $t = 7$, $t = 8$ and $t = 10$ years

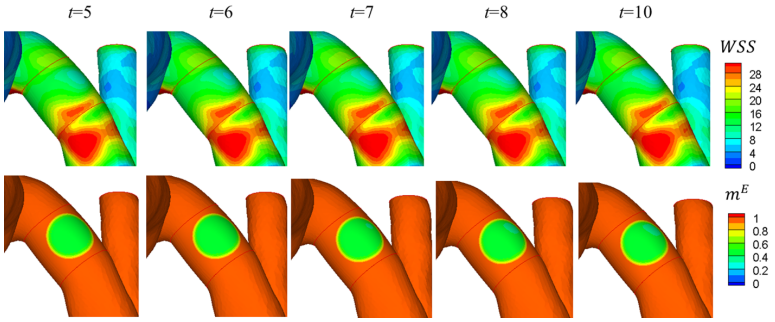


Figure 6.32: The evolving WSS and elastin concentration (m^E) for the test case with a sigmoid multiplicative and exponential additive CAF, at $t = 5$, $t = 6$, $t = 7$, $t = 8$ and $t = 10$ years

6.2.6 Implementation of the CAF within the physiological framework: Discussion

Experimentation with different functional forms and implementations of the CAF allowed for the choice of the best combination of functions for implementation within the physiological framework. The results clearly demonstrated the function of the CAF in rapidly stabilising the model aneurysmal geometry. However, the final example shown in Figure 6.31 and Figure 6.32 in §6.2.5 brings to light a series of questions that must be answered in order to improve the representation of the vascular response to cyclic stretch in the model.

Firstly, it must be noted that many aneurysms grow to very large sizes, but may

remain stable. This suggests that over time a fine balance between collagen deposition and deformation exists for such cases. In the modelling scenario, this equates to a balance between the rate of elastin degradation, and the deposition of collagen due to deviations of collagen strain and areal cyclic stretch from their homeostatic levels. Elastin degradation in the present framework is governed by a combination of prescribed degradation and low levels of WSS. As discussed previously, there is currently no clearly defined *low* and *high* WSS, and indeed these may vary between individuals, and in different vessels. Currently, the thresholds τ_{crit} for initiation of elastin degradation, and τ_X for maximum degradation are the minimum, and half the minimum value in the dome respectively, taken at the end of the prescribed degradation period ($t = 5$ years in this examination). However, this approach is yet to be validated. Ultimately, data that links WSS magnitude to varying rates of elastin degradation is required. Such data might be obtained from *in-vivo* experiments such as those by Meng et al. (2007). Measurements of the relative amounts of IEL within the developing aneurysmal area could be made, which could then be correlated with WSS values obtained from CFD simulations on the geometry to give a better indication of the rate of elastin degradation in response to WSS. Finally, to reduce computational expense, steady-flow conditions were imposed in this examination. In fact, cyclic stretch in the real physiological setting occurs due to the pulsatile nature of blood-flow. Furthermore, while the results discussed in §4.4.4 showed that spatial distributions of WSS and WSSG were similar for steady and pulsatile-flow simulations, the magnitudes were observed to be different. Given that the rate of elastin degradation in this model is coupled to local levels of WSS, and that the effects of oscillatory shear have not yet been examined in the case of a growing model aneurysm, it is clear that a shift towards pulsatile-flow modelling will be an important refinement of this model. This may require adaptation of the structural code to allow parallel processing and reduce computational time.

The implementation of the CAF in the present framework (particularly when an additive function is included) results in rapid stabilisation, and hence, small geometries. Furthermore, *all* positive deviations of the cyclic stretch from homeostatic levels result in an increase in the mass of collagen. In fact, this may not be representative of the real physiological situation. While a stretch of 3.8 (as observed for the TPC without the CAF in §6.2.3) seems unlikely in the physiological scenario, it is possible that stretches higher than 1.3 occur, beyond which cells may be physically "torn" apart, or fail to function normally (i.e. vSMCs and fibroblasts may no longer

secrete collagen). Therefore, it may be more appropriate to set a defined interval of A_c^{CS} (e.g. $1.1 < A_c^{CS} \leq 1.3$) over which the CAF contributes to collagen deposition, but beyond which the CAF is zero, or negative, to indicate the reduction in collagen production due to cell dysfunction or death. Furthermore, both the homeostatic and maximum physiological values of A_c^{CS} proposed in this work (1.1 and 1.3, respectively) need to be validated from experiments on real cells. Vascular cells are not explicitely modelled in the current framework, and the A_h^{CS} may in fact vary greatly between ECs, vSMCs and fibroblasts. In turn, the physiological thresholds of the A_c^{CS} and the contribution to collagen deposition/degradation may also be different for each.

Additionally, the contribution of the CAF to the mass of collagen currently lacks physiological motivation -e.g. the maximum contribution of the sigmoid CAF of 1.35 is arbitrary. A quantification of the mass of collagen produced (or in the case of ECs, indirectly degraded via MMPs) by each cell-type in response to varying levels of stretch is needed to better inform both the functional form of the CAF, as well as the magnitude of its contribution to collagen deposition. This information would also help to guide the selection of parameters such as β^{CS}, which governs the slope of the CAF, and hence may provide the means of modelling the fine balance between elastin degradation and collagen deposition that results in large, but stable aneurysms.

Figure 6.33 shows a comparison in CAF slope and trajectory for β^{CS} values ranging from 0.5 to 10. Over the interval for which only the sigmoid is active ($0 < x \leq 0.18$), a high β^{CS} would result in a sharp transition between the low and high values of CAF. Consequently, the CAF would be low and high for a larger range of A_c^{CS} values. This may be unfavourable, as a larger amount of collagen would continue to be deposited even as the A_c^{CS} reduces. This may mean that the geometry would rapidly stabilise, and the necessary perturbation to the haemodynamic environment would not be generated (i.e. a region of low WSS may not evolve to drive further elastin degradation). Physiological data on the rate of deposition of collagen in response to stretch would better inform the choice of β^{CS}. In fact, it may be more appropriate to define two separate values corresponding to the sigmoid and exponential functions, where β_{sig}^{CS} would reflect the physiological rate of collagen turnover (60-70 days), while β_{exp}^{CS} the pathophysiological rate (17 days).

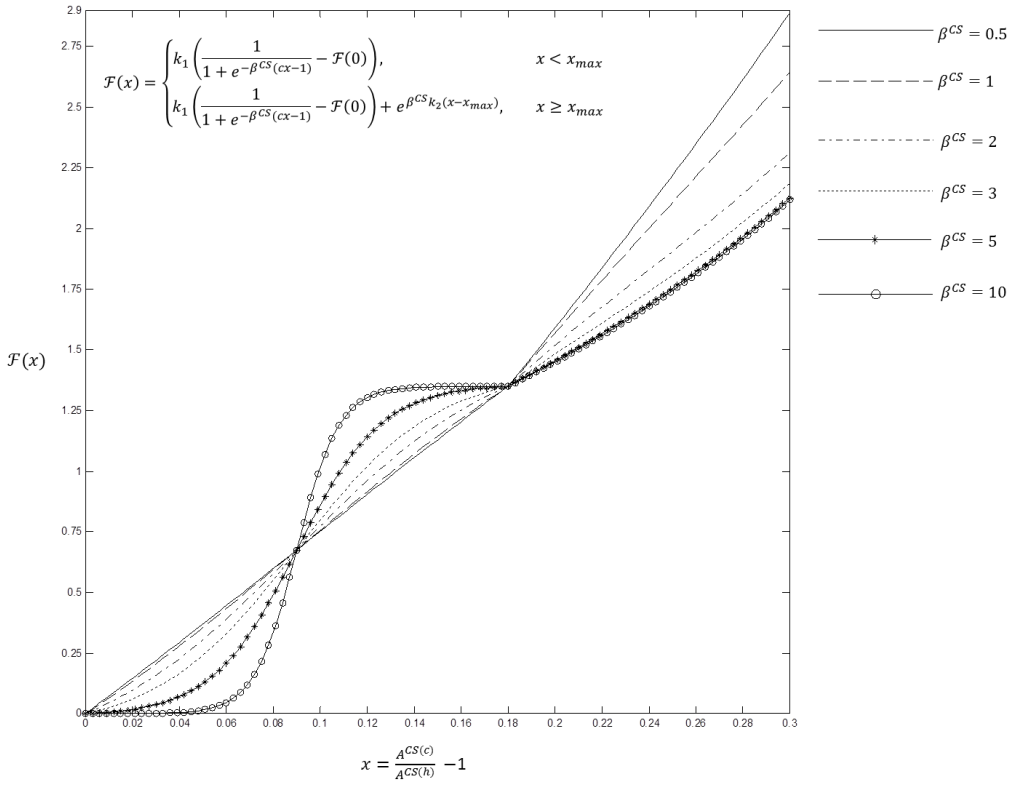


Figure 6.33: Comparison of the trajectory of the CAF as a combination of sigmoid multiplicative and exponential additive functions for varying values of β^{CS}. As β^{CS} increases, the shape of the sigmoid changes from near-linear, towards an "S"-shape with an increasingly steeper transition from low to high CAF for the sigmoid (for $0 < x \leq 0.18$). However, for $x > 0.18$ where both the sigmoid and exponential functions are active, increasing β^{CS} corresponds to a slower increase in the CAF. $x_{\max} = 0.18$.

Lastly, this section again highlights the importance of explicitly modelling vascular cells. In addition to a better representation of events involved in degradation (discussed in §6.1.1), this will also allow better modelling of stabilisation, as each cell-type reponds differently to a combination of shear stress and cyclic stretch to affect elastin and collagen concentrations. Again, physiological data is needed: in this case, an indication of whether a homeostatic level or range of stretches exists for ECs, vSMCs and fibroblasts, as well as upper and lower cyclic stretch thresholds for each cell-type. This will better inform how each cell-type is modelled. As previously discussed, the present framework is highly adaptable, and will allow easy integration of these new models.



CHAPTER 7

SUMMARY AND RECOMMENDATIONS

The focus of this thesis was the investigation of the role of the patient-specific haemodynamic environment in events characteristic of aneurysm evolution, chiefly aneurysm inception, growth and stabilisation. Broadly, the project aimed to shed light on the question of the nature of the relationship between haemodynamic forces (as quantified in the literature) and the growth and remodelling of arterial constituents that occurs during aneurysm development. By embedding a state-of-the-art model of cerebral aneurysm evolution within a range of real, patient-specific arterial geometries (thereby coupling the model of arterial wall growth and remodelling to complex, physiological flow), the project aimed to examine

- the influence of patient-specific haemodynamics on the evolving aneurysmal geometry,
- the existence of patterns in distributions of haemodynamic indices, and
- the effect of implementing new hypotheses for linking haemodynamics to growth and remodelling on aneurysm evolution.

To investigate the existence of correlations between haemodynamic indices proposed in the literature and aneurysm evolution, an investigation was performed utilising commonly-applied methods in the field of CFD-based aneurysm research (i.e. studies on static geometries corresponding to two different time-points in the

course of aneurysm growth), as well as by coupling CFD to a novel FSG framework for cerebral aneurysm evolution. This section summarises the key findings, and makes recommendations for futher development and refinement of the current framework.

Firstly, an extensive review on the role of haemodynamics in aneurysm inception and growth was conducted (§1.4), which revealed that opinion in the field is divided between high- and low- flow theories. The review highlights the adaptability of ECs to a range of shear stress magnitudes, and hence the lack of a clear definition of sub- and supra-physiological thresholds of WSS. However, while evidence exists for the role of both high WSS and low WSS in destructive remodelling, a high WSSG appears to be present in both flow environments, and therefore may in fact be the main haemodynamic instigator of events leading to, and fuelling aneurysm development. The review also highlighted the lack of quantitative methods of capturing growth, that would allow a more rigorous assessment of the relationship between haemodynamic indices and regions of aneurysm enlargement.

In Chapter 2, two methods, one reported in the literature, and one novel, were implemented to quantify the enlargement of aneurysms. The Displacement Index (DI) captures the normal displacement between surfaces, t_1 and t_2, corresponding to two different time-points, while the Area Stretch Ratio (ASR) represents enlargement in terms of the ratio of the areal stretch of the t_1 tissue between two time-points. The distribution of these indices was compared to the spatial distribution of five pulsatile-flow haemodynamic indicies: WSS, WSSG, OSI, AFI and GON for an ICA and a basilar terminus (BT) case. Correlations between the haemodynamic and growth indices were both visually and statistically assessed in Chapter 3 by utilising surface contour maps, and Spearman's Rank and regression analysis respectively. The statistical assessment revealed that visual assessment (which is most commonly applied in the field) can result in a gross exaggeration of the strength, and even direction, of correlations. This indicates that great care must be applied when interpreting plots of surface contour maps of haemodynamic indices. From visual assessment, it appeared that the OSI and AFI, which both quantify the degree of oscillation of the instantaneous WSS vector from the time-averaged vector, were most consistently correlated with regions of high DI and ASR. In fact, the statistical examination revealed that correlations between both growth indices and *all* haemodynamic indices were weak or non-existent, with only the WSS showing a

consistent, albeit weak correlation with both the DI and ASR. Interestingly, the correlation was found to be positive for the BT case, and inverse for the ICA case. The correlation tables also revealed that low WSS is correlated with oscillatory shear indices (a high OSI, low AFI and high GON), while high WSS is correlated with high WSSG. Therefore, as the t_1 geometry corresponding to the BT case represents a "pre-aneurysmal" condition (compared to the ICA t_1 geometry which features an already well-developed aneurysm), these results suggest some support for the hypothesis that high flow may be an instigator of aneurysm inception, while low flow may facilitate further growth.

A regression analysis was also performed in order to determine the trend of the relationship between inverse WSS and the growth indices, as per the study by Boussel et al. (2008). Boussel et al. (2008) also quantified growth as a normal displacement between surfaces, and found a linear relationship between inverse WSS and growth. The results of this study revealed that both the ICA and BT growth and WSS data are highly non-linear, and that even commonly applied non-linear models (e.g. logarithmic, exponential) are poorly fitted to the data. Only the ICA WSS^{-1}-ASR linear and quadratic fittings had R^2 values greater than 0.1 (0.146, and 0.155 respectively). However, as the ASR quantifies growth differently to the DI, a direct comparison to the results of Boussel et al. (2008) could not be made. Furthermore, the low R^2 values suggest that while a relationship between WSS and growth may indeed exist, it is complex and likely to depend on other indices, or other unaccounted-for factors that may be patient-specific.

Given the lack of data on the direction in which growth occurs, it is difficult to say if one index is a "better" indicator of growth than the other. Both are sensitive to errors in image processing and the general shape of the t_1 geometry. Furthermore, both assume that the direction of growth occurs radially outward. The DI does not take into account the possibility that growth may not occur equally in all directions, but may in fact be highly localised, or may be fuelled strictly from the neck region. Hence, and most strikingly, this investigation highlighted the difficulty in elucidating the role of haemodynamics in the process of aneurysm growth through CFD studies on *static* geometries. It highglighted the need for CFD to be coupled to computational models of the structural changes occuring during aneurysm evolution, which allow the observation of growth, as well as the testing of hypotheses on how biological events are coupled to flow.

A review of models of aneurysm evolution, ranging from 1D models of healthy arterial adaption to 3D, patient-specific models of aneurysm evolution, was presented in Chapter 4. It was shown that until recently, none of the proposed models fulfilled all the main requirements for a model of aneurysm evolution, which comprises a model of the healthy artery, G&R hypotheses for individual constituents of the arterial wall, and a framework to couple G&R to fluid flow and cyclic deformation. While some models incorporate a sophisticated structural framework for the arterial wall, they do not model G&R; conversely, while others capture aneurysm growth, and the influence of haemodynamic forces on G&R, they do so using overly simplistic models of the arterial wall that do not account for complex mechanical properties arising from individual arterial wall constituents. However, the review highlights the important early work by Humphrey (1999), in which the concept of an "attachment stretch" of collagen fibres was introduced, whereby new collagen fibres are deposited in the same state of stretch regardless of the current stretch of tissue. This is a pivotal concept utilised in the fluid-solid-growth (FSG) model discussed in this work. The key elements of the model include:

- a sophisticated constitutive model for the healthy artery based on the strain-energy formulation proposed by Holzapfel et al. (2000). The original model was adapted to incorporate concentration and stretch variables such that the adaptation of the arterial microstructure during aneurysm development could be modelled;
- G&R hypotheses that link the degradation of elastin to the local shear stress environment, and the growth and remodelling of collagen fibres to cyclic stretch;
- a collagen recruitment stretch variable, the evolution of which simulates the evolving natural reference configuration of collagen fibres, which are assumed to remodel to achieve an equilibrium level of stretch during the cardiac cycle; and
- a highly adaptable computational framework, which couples the structural deformation of the tissue to the evolving haemodynamic environment, and allows the easy implementation of new G&R hypotheses.

Initially, the model aneurysm developed on a highly-idealised cylindrical geometry. Elastin degradation is prescribed in order to generate a small perturbation to the haemodynamic environment, following which any subsequent degradation is linked to local levels of WSS. While the symmetric, nearly-spherical growth of the model aneurysm reflects the idealised haemodynamic environment, it was adequate to assess the differences in spatial distribution of WSS and WSSG arising from steady- vs. pulsatile-flow conditions. In line with other studies, the results showed that while magnitudes of the indices are different, the spatial distributions are similar and merit the use of the less computationally-expensive steady-flow conditions in examinations of these indices. Pulsatile-flow simulations allowed for an examination of the OSI distribution. However, it was difficult to elucidate the role of this index in aneurysm evolution from distributions on an idealised geometry. This highlighted the need for implementing the model within real, patient-specific geometries, such that evolution of the aneurysm geometry, as well as the various indices discussed in Chapter 2 could be observed within a real, physiological setting.

As such, Chapter 5 was dedicated to the task of implementing the cylindrical model within patient-specific geometries. Two methods were developed, one manual, the other automated, although the key processes are the same for both, comprising

1. segmentation of the patient-specific geometry to virtually remove the original aneurysmal segment and some surrounding vasculature to facilitate placement of the cylindrical geometry, which represents a hypothetically healthy arterial segment;
2. positioning of the cylinder between the physiological upstream and downstream geometries;
3. construction of smooth connecting surfaces between the physiological and cylinder boundaries; and
4. rotation and translation of the final geometry such that it sits about the global origin, with respect to which the computational domain is defined.

The manual method utilises tools provided in ANSYS ICEM (although the process can be repeated utilising similar CAD-like software) to achieve the above tasks, and implement a cylinder within a test physiological case, featuring a side-wall

aneurysm on an ICA. Physiological and cylinder geometries were connected by surfaces swept over a series of splines linking the physiological and cylinder boundaries. Steady-flow simulations demonstrated an asymmetric evolution of the WSS environment following initial perturbation, which in turn resulted in an asymmetric evolution of the model aneurysm geometry. Interestingly, the shape of the model geometry was observed to be qualitatively similar to the original, removed aneurysm, which suggests some support for the hypothesis that low WSS is linked to aneurysm growth.

However, the method did not facilitate easy processing of a large number of cases. As such, a algorithmic method was developed in `MATLAB`, which performs tasks 2-4 automatically for a set of geometry-specific inputs (i.e. physiological boundary coordinates, connectivity matrices, and arterial segment centrelines). The key part of the automated process is the surface reconstruction algorithm, which generates a series of splines between corresponding points on the physiological and cylinder boundaries, for which a connectivity matrix is specified such as to generate triangulated surfaces. Experimentation showed that, in addition to meeting continuity requirements at the boundaries, averaged sigmoid splines provide the best compromise between control of spline trajectory while allowing for a realistic degree of curvature, minimal subjectivity, and ease of implementation. The method was implemented on the same test case, and the results of steady-flow simulations were compared. It was observed that the model aneurysm evolved asymmetrically, but that the shear stress environment within the computational domain, and in the region immediately upstream differed, as more of the original vasculature was preserved in the case of the algorithmic reconstruction.

The algorithmic method was then employed to embed the physiological model within 12 patient-specific cases, which facilitated an investigation (Chapter 6) into the existence of correlations between pulsatile-flow indices and the site of aneurysm inception. A region of interest (ROI) was defined for each case utilising an overlay of the original geometry as a guide. Although the findings of Chapter 3 highlighted the problems inherent in visual assessment of correlations from surface countour maps, a statistical method requires a rigorously-defined ROI, which is difficult to quantify. As such, visual assessment was employed for this investigation, where a positive correlation was ascertained only if

- an index was elevated/reduced within, or on the edge of the ROI, and

- the elevation/reduction was beyond/beneath a specified threshold for the index

Where available, thresholds found in the literature were applied.

The results were examined for 12 cases, and compared to a previous study performed by Chen et al. (2013) whereby the aneurysmal segment was entirely reconstructed for the same set of cases. Although in this investigation, a highly-idealised cylindrical segment is incorporated within the physiological geometry, the gross haemodynamic patterns were observed to be similar. In line with the study by Chen et al. (2013), high WSS was found to be the most consistently correlated index, with 10/12 positive correlations. In contrast to the findings of Chen et al. (2013) and due to the differences in the shape of reconstructed segments imposed by the cylinder, WSSG was also found to be highly correlated in this study, with 9/12 positive correlations. This suggests further support for the hypothesis that high flow may be an important condition for aneurysm inception, and as such, the functions governing the degradation of elastin could be updated to reflect this. Particularly, the framework could be adapted to replace prescribed degradation with a function that couples the initial degradation to WSS levels. However, the lack of data on the pre-aneurysmal state of the original artery and clear definitions of high and low WSS, as well as the idealised cylindrical domain impose a limitation on the interpretation of these results. The transition between cylindrical and physiological boundaries, while meeting continuity conditions, was often observed to be sharp, resulting in an artificial elevation or reduction of indices. Ideally, the framework would be adapted such that the model aneurysm can evolve on any geometry, which would allow better integration within the real artery. In the meantime, a deeper investigation into the choice of spline could be performed to refine the current surface-reconstruction methodology. Finally, physiological data on the rate of elastin degradation in response to varying levels of WSS is needed to inform a new elastin degradation function.

In Chapter 6, evolution of the aneurysm geometry during growth, and the effect of coupling growth of collagen fibres to the evolving cyclic area stretch was also examined for a subset of 6 cases. Similarly to the test ICA case, 4/6 of the examined geometries were observed to evolve such that the final model geometry resembled the original, removed aneurysm. This suggests further support for the hypothesis of low WSS-driven growth.

However, a brief review on the effect of cyclic stretch on vascular cells revealed that the alignment and funcitonality of endothelial cells (ECs), smooth muscle cells (vSMCs) and fibroblasts is not only sensitive to WSS, but also to cyclic stretch. Importantly, cyclic stretch has been observed to stimulate EC production of matrix metallo-proteinases (MMPs) which act to degrade elastin and collagen fibres. In contrast, cyclic stretch has been shown to stimulate collagen production by vSMCs and fibroblasts, indicating a delicate balance between deposition and degradation. In this investigation, the evolving cyclic stretch was coupled to the evolving concentration of collagen via a cyclic metric function (CAF). The CAF is a function of the current cyclic areal stretch, A_c^{CS}, which itself is the ratio of cyclic area stretch at systole to that at diastole. Initially, it was implemented as a multiplicative exponential function in the evolution equation for the mass of collagen, such that for values of A_c^{CS} greater than the homeostatic value, A_h^{CS}, the action of the CAF is to increase the mass of collagen and return the A_c^{CS} towards homeostasis. Initial experimentation on a test physiological case showed that this implementation resulted in an improved approximation of the model aneurysm geometry to the corresponding physiological aneurysm. However, the peak magnitudes of A^{CS} were observed to be unrealistically high.

As such, the effect of implementing the CAF as an additive exponential was examined on 6 physiological cases. The evolving model geometries *without* the CAF coupled to collagen concentration were generally observed to be larger than their CAF-coupled counterparts. It was observed that the CAF resulted in an early and rapid increase in the mass of collagen, which reduces the size of the initial, prescribed perturbation. Comparing cases where growth did and did not occur when the CAF was implemented revealed that the curvature of the surrounding geometry ultimately governs whether growth will occur, as it affects the WSS environment to which subsequent elastin degradation is linked.

While the coupling of the CAF to collagen concentration was physiologically motivated, the initial implementation was, in effect, a “first guess”. The remainder of Chapter 6 explored the effect of different functional forms of the CAF, as well as different implementations (as a multiplicative, versus an additive funciton) on the cylindrical geometries. An arbitrary maximum contribution of the CAF, and a corresponding maximum deviation of the A_c^{CS} from the homeostatic value of 1.1 (or 10% stretch) were defined, such that five functional forms of the CAF (exponential,

quadratic, linear, square-root and sigmoid) could be compared over the same interval. Solid-only simulations were conducted on the cylindrical geometry, yielding symmetrically-evolving, spherical aneurysmal geometries.

It was observed that in general, all functional forms of the CAF resulted in larger geometries when implemented as multiplicatives versus additives. For a multiplicative implementation, the difference in size between quadratic, linear and square-root functions was negligible, while the exponential and sigmoid functions yielded noticeably smaller geometries. For an additive implementation, the exponential function yielded the smallest geometry, and the quadratic the largest. In all cases, the evolving A_c^{CS} was observed to reduce towards the homeostatic value over the course of aneurysm evolution, with the rate of this reduction reflecting the rate of change of each individual functional form of the CAF. However, a high maximum A_c^{CS} was observed in all cases (as high as 2.1) which is unlikely to occur in a physiological setting, or, if it does, is likely to disrupt the normal functioning of ECs, vSMCs and fibroblasts. Furthermore, while the A_c^{CS} was observed to reduce over the course of aneurysm evolution for symmetrically-evolving aneurysms, this was not the case for asymmetrically-evolving aneurysms. The test ICA case used to develop the surface-reconstruction algorithm was used to demonstrate that in the case of an asymmetrically-evolving aneurysm, the A_c^{CS} continues to increase throughout aneurysm evolution in the region coinciding with the region of growth of the aneurysm dome.

Hence, the choice of the most appropriate function and implementation within the physiological framework was informed by the need

- to represent real physiological events -i.e. the balance of deposition and degradation of collagen fibres by vSMCs, fibroblasts, and ECs, and the change in this balance at different stages of aneurysm development,
- to constrain the A_c^{CS} to a "reasonable" range of values, beyond which the contribution of the CAF is such as to rapidly increase the mass of collagen and return the A_c^{CS} to homeostatic levels, and
- to ensure that the initial perturbation resulting from prescribed elastin degradation is not excessively constrained, so as to facilitate the formation of a low WSS environment, which in turn fuels further elastin degradation and growth of the model geometry.

With these considerations in mind, a combination of the sigmoid multiplicative, and exponential additive functions was selected as the most appropriate implementation of the CAF. The shape of the sigmoid makes it well suited for representing the initial balance between collagen deposition and degradation over the physiological range of stretches, while the rapid increase of the exponential function makes it suitable as a means of constraining the deformation when stretches exceed the upper physiological threshold. As homeostatic behaviour of ECs was observed in the literature for stretches of up to 24%, the maximum threshold of the physiological range of stretch in this investigation was set to 1.3 (or 30% stretch). The exponential additive was implemented so as to be active only for values of stretch exceeding 30%.

The results of implementation of this combinatory form of the CAF within the test ICA geometry showed that, while the A_c^{CS} was indeed effectively constrained by the additive exponential function, the final geometry did not grow very much. While this illustrates that CAF is an effective mechanism of rapid stabilisation, it does not reflect observations of large aneurysms that are never-the-less stable. In terms of modelling, the action of the CAF is controlled by a series of parameters, which in turn control the rate of change of the sigmoid and exponential functions, as well as the magnitude of the contribution of each to the mass of collagen. Again, there is a need for physiological data on the real rates of collagen deposition and degradation in response to varying levels of cyclic stretch to inform the choice of these parameters. The adaptability of the framework makes the implementation of this data simple, and in the interim, comparison of the evolving model geometries to their original counterparts provides a qualitative means of assessing the effect of parameters.

However, it must be noted that the extension of the model to a patient-specific framework will remain only qualitatively useful until further sophistication of the FSG model is achieved. In addition to implementation of more physiological data (which is difficult to obtain in vivo), the refinement of FSG models calls for the implementation of data that is currently available, but has previously been omitted for the purposes of reducing model complexity. In particular, there is a need for a more explicit representation of vascular cells in the arterial wall, i.e. ECs, vSMCs and fibroblasts. As the primary component in direct contact with blood-flow, ECs are the main sensors of the haemodynamic environment, and act to translate haemody-

namic forces into a host of both intra- and inter-cellular responses. As such, the implementatino of a model of ECs may be a good starting point for the refinement of the model. The sections below describe a potential means by which this refinement could be achieved.

7.1 A POTENTIAL METHOD FOR MORE EXPLICIT REPRESENTATION OF ECS

As discussed in the previous chapters, vascular ECs are aligned with the direction of flow under the influence of strongly-directed WSS. WSS has been found to affect EC shape, with ECs adopting an ellipsoidal shape under the influence of high WSS, and a more rounded shape under influence of low WSS, and, as discussed in §1.4, under the influence of high WSSG.

Furthermore, the experiments of Chien (2008) showed that the up- and down-regulation of proatherogenic signalling pathways depends on the WSS-sensitive orientation of ECs, where a strongly-directed WSS characteristic of laminar flow (and resulting in aligned ECs) results in activation of atheroprotective signalling pathways, while the converse is true for a randomly-directed WSS characteristic of disturbed flow (and resulting in non-aligned ECs). Given that there appears to be some overlap between the pathological processes that underlie atherosclerosis and aneurysm development (for example, the release of pro-inflammatory molecules and shear-stress mediated oxidative stress that leads to ECM remodelling (Golledge and Norman, 2010)), it is possible that EC alignment plays a similar role in aneurysm development. One proatherogenic pathway upregulated by disturbed flow is the MCP-1 pathway, which leads to an increase in monocyte attraction to the wall, to which a non well-aligned EC layer is more permeable. Furthermore, matrix metalloproteinase (MMP) 9, which can potentially degrade the cellular membrane of ECs via proteolysis (thus potentially affecting EC vitality) and is a likely instigator of degradation of the internal elastic lamina, is produced in response to high flow. Aside from being produced by ECs, MMP-9 is also produced by inflammatory cells (i.e. monocytes and macrophages).

As such, a step towards the refinement of the Watton et al. FSG model could be the implementation of a more explicit representation of EC orientation, permeability and release of MMPs, which entails several steps, as detailed below. Figure 7.1 is

useful in visualising the various components discussed in the following sections.

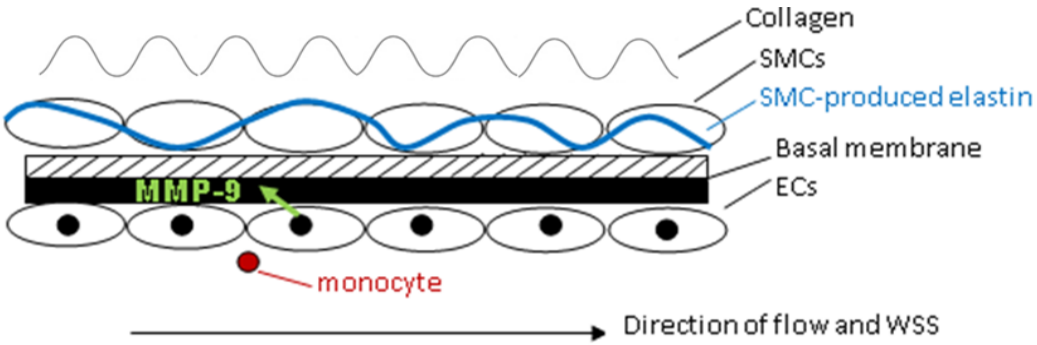


Figure 7.1: Layers of the artery, showing ECs,the internal elastic lamina, vSMCs and vSMC-produced elastin, and collagen. The permeability of the EC layer will determine the uptake of monocytes into the arterial wall, while oscillatory shear affects the production of MMP-9 by ECs and inflammatory cells such as monocytes

7.1.1 Definition of an endothelial cell orientation vector, $\mathbf{n}^{\mathbf{EC}}$

Let $\mathbf{n}^{\mathbf{EC}}$ be a vector to represent the spatial distribution of EC orientations. The directions of $\mathbf{n}^{\mathbf{EC}}$ are governed by local mechanical stimuli. For example, ECs align in the direction of the mean WSS vector and perpendicular to the direction of (uniaxial) cyclic stretching (see Figure 7.2). For the healthy artery, these two mechanisms act synergistically, however as the flow becomes more complex (particularly with an increase in WSSG) and the tissue experiences equibiaxial stretch it is unclear how the EC will orientate itself. The general form of $\mathbf{n}^{\mathbf{EC}}$ can be expressed as

$$\mathbf{n}^{\mathbf{EC}} = \mathbf{n}^{\mathbf{EC}}(\tilde{\mathbf{WSS}}, \tilde{\mathbf{WSSG}}, \lambda_1^{EC-CS}, \lambda_2^{EC-CS}), \tag{7.1}$$

where λ_1^{EC-CS}, and λ_2^{EC-CS} represent the cyclic stretches of the endothelial cells in the axial and azimuthal directions, respectively. The next task is to devise an appropriate functional form for n^{EC}, which incorporates the above variables.

7.1.2 Definition of an EC-permeability function, $\mathbf{p}^{\mathbf{EC}}$

In §1.4, an increase in transendothelial permeability was discussed as a possible mechanism for destruction of the IEL, by facilitating the migration of inflammatory cells into the arterial wall, which secrete MMPs. In turn, transendothelial permeability may be directly linked to the structural arrangement of ECs, particularly EC

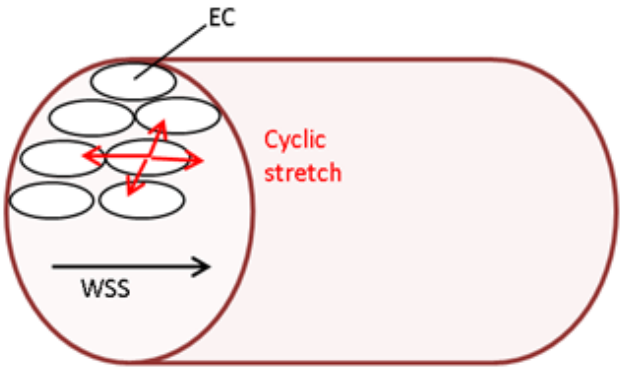


Figure 7.2: The preferentially axial alignment of ECs, influenced by WSS and cyclic stretching

shape, and consequently, alignment. Several studies discussed in §1.4 (Chien (2007, 2008); Meng et al. (2007)) discuss the fact that, particularly in high WSSG environments, ECs exhibit a polygonal shape, resulting in a widening of junctional gaps. Hence, it is hypothesised that non well-aligned ECs result in increased permeability of the EC layer. A reasonable assumption then is that minimum permeability occurs for parallel alignment of all ECs. A maximum permeability must also exist, which corresponds to the maximum level of deviation from parallel alignment of a group of ECs at any point in the tissue. To quantify this dispersion, an appropriate mathematical operation, e.g. $(\nabla \cdot n^{EC})$, must be defined, which will quantify the deviation of the field of EC orientation vectors from parallel alignment in the form of a parameter. The permeability at any point in the tissue can then be defined as a function of this parameter, i.e.

$$p^{EC}(\mathbf{X}, t) = \mathscr{F}(\nabla \cdot \mathbf{n}^{\mathbf{EC}}) \tag{7.2}$$

The task, then, will be to define and investigate an appropriate functional form for $\mathbf{p}^{\mathbf{EC}}$.

7.1.3 Definition of a function to capture the change in MMP concentration

For the purpose of simplicity, consider a general elastase MMP, which is produced during the course of aneurysm development, and which acts to degrade elastin. Thus, during the course of aneurysm development, it is hypothesised that the concentration of MMP increases. Given that it has been found to increase in response

to an increase in oscillatory shear, then it seems appropriate for the increase to be a function of the magnitude of WSS, and a quantification of OS, such as the OSI (though other haemodynamic indices mentioned in §1.4.3.2, such as the AFI, or GON may be more appropriate). Given that MMP is also produced by inflammatory cells (e.g. monocytes), which accumulate in the artery wall during aneurysm development, then the increase in concentration of MMP must also be a function of EC permeability. However, the increase in MMP is balanced by a natural degradation of MMP, as well as a loss occurring through the interaction with elastin (i.e. in acting to degrade elastin, MMP is chemically converted to another molecule). Thus, the overall, general form for the rate of change of MMP can be expressed as

$$\frac{dm^{\mathrm{MMP}}}{dt} = \mathscr{F}(|\mathbf{WSS}|, OSI, \mathbf{p}^{\mathbf{EC}}) - A_1 m^{\mathrm{MMP}} - A_2 m^E m^{\mathrm{MMP}}, \tag{7.3}$$

where A_1 and A_2 are parameters quantifying the percent natural loss of MMP, and the loss of elastin and MMP through chemical interaction respectively. Bounds for these parameters will be determined based on values found in the literature, and numerical analysis. Hence, the first task will be to define an appropriate functional form for the increase in MMP (i.e. define $\mathscr{F}(|\mathbf{WSS}|, OSI, \mathbf{p}^{\mathbf{EC}})$, followed by tuning of parameters A_1 and A_2. In future, a further sophistication could be to consider specific forms of MMP (such as MMP-2 and MMP-9).

7.1.4 Integration of EC permeability and the change in MMP concentration as determinants of the rate of elastin degradation

Once $\frac{dm^{\mathrm{MMP}}}{dt}$ is defined, the current MMP concentration value can then be incorporated to sophisticate the function governing the change in elastin concentration, i.e.

$$\frac{\partial m^E}{\partial t} = -A m^E m^{\mathrm{MMP}},$$

where a higher concentration of MMP results in an increase in the rate of elastin degradation, and A is a parameter obtained via the |**WSS**|-dependent elastin degradation function, $\mathscr{F}_D$, as defined in §4.4.2.

Furthermore, in the present FSG formulation the SEF representative of the elastinous constituents considers single material, and single concentration parameters k^E and m^E, which take into account the contributions of the internal elastic

lamina (IEL) and the passive response of the vSMCs themselves. Therefore, when elastin degradation is modelled, this implies that the rate of degradation of the IEL and medial elastin is the same. However, given the difference in the position of the IEL with respect to medial elastin and vSMCs in the arterial wall (see Figure 7.1), then the degradation/apoptosis of the different constituents should be modelled individually. In fact, disruption of the IEL may allow more elastin degrading enzymes to permeate into the media and lead to increased degradation of elastin.

The new developments should first be explored and tested on a conceptual cylindrical model of aneurysm evolution. This will enable the numerical investigation of a range of functions and parameters for minimum computational time. Subsequently, the new developments could be incorporated into the present FSG framework.

7.2 CONCLUDING COMMENTS

In this work, a novel FSG model was presented, along with the methodology to embed the model within patient-specific arterial geometries. It was shown that coupling the local haemodynamic environment to growth and remodelling hypotheses profoundly affects the shape and size of the model aneurysm geometry, in some cases resulting in qualitative similarities between the model and physiological aneurysm geometries. This suggests some tentative support for the hypotheses which link specific haemodynamic conditions to aneurysm enlargement, and motivates the need for models such as the one presented here: multi-scaled models, which couple the physiological function and structure of the arterial wall to the mechanical forces exerted on it. It also provides motivation for gaining an improved understanding of how the complex micro-structure of the arterial wall adapts in physiological conditions. In turn, this will not only facilitate improvement of the modelling framework, but will also provide a means of validating the model against physiological data. Animal models will likely play a pivotal role towards this goal. For instance, this research group is currently in collaboration with Associate Professor Anne Robertson of the Swanson school of Engineering at the University of Pittsburgh, whose team has been gathering histological and biomechanics data corresponding to rabbit cerebral aneurysms (Zeng et al., 2011). It is therefore planned to embed the present FSG model within an image of the rabbit artery, and to employ

specific material parameters gathered through the work of Prof. Robertson's group in the model. It is hoped that the qualitative comparison between the model and original aneurysm geometries will provide some validation for the present model, as well as allow the testing of the influence of changing hypotheses for the coupling of fluid dynamics to growth and remodelling.

While the current framework was devised with respect to modelling saccular cerebral aneurysms, the adaptability of the framework makes it well suited to modelling other vascular diseases. It has already been applied to model abdominal aortic aneurysms (Watton et al. (2004, 2009a, 2013)); there is also great scope for incorporation of related models into the present framework, such as models of thrombosis (clot formation) and stent deployment, which are a research focus of this group. Such refinements may lead to predictive models of vascular disease, which could be applied in the clinic to assist decisions on the most appropriate treatment methods on a patient-specific basis. Additionally, methods developed through this research, and in particular, automatic generation of surfaces from splines, may be useful in other geometric problems, e.g. computer graphics problems where it may be of interest to generate surfaces with minimal user subjectivity. Also, the existing 12 patient-specific models provide a useful dataset for comparison with studies that employ future, updated versions of the FSG model. For instance, when the model is updated so as to evolve over any geometry, Chen's (2013) surface reconstruction methodology could be employed on the 12 cases, and the evolution of the model aneurysm observed to occur from within a realistic representation of the pre-aneurysmal region. Equally, it would be interesting to observe the differences in the shape and size of model aneurysm geometries (against the original aneurysm, as well as between individual updates of the model) when an explicit model of vascular cells is incorporated into the model. The existing cases could therefore be used to iteratively 'tune' and improve the model. Naturally, FSG modelling generally presents a complex and challenging task, as it necessitates the coming together of multiple research fields. As such, collaboration between medical engineers, clinicians and biologists is pivotal to the successful application of these models.

REFERENCES

ALBERTS, B., JOHNSON, A., LEWIS, J., RAFF, M., ROBERTS, K., AND WALTER, P. *Molecular Biology of the Cell, 4th edition*. New York: Garland Science, 4th edition, 2002.

ANDO, J. AND YAMAMOTO, K. Effects of shear stress and stretch on endothelial function. *Antioxidants & redox signaling*, 15(5):1389–403, September 2011. ISSN 1557-7716.

AOKI, T. AND NISHIMURA, M. Molecular mechanism of cerebral aneurysm formation focusing on NF-κB as a key mediator of inflammation. *Journal of Biorheology*, 24(1):16–21, September 2010. ISSN 1867-0466.

BAEK, S., RAJAGOPAL, K. R., AND HUMPHREY, J. D. Competition Between Radial Expansion and Thickening in the Enlargement of an Intracranial Saccular Aneurysm. *Journal of Elasticity*, 80(1-3):13–31, November 2005. ISSN 0374-3535.

BLANCO, P. J., LARRABIDE, I., URQUIZA, S. A., AND FEIJOO, R. A. Sensitivity of Blood Flow Patterns to the Constitutive Law of the Fluid. *III European Conference on Computational Mechanics*, (June):5–8, 2006.

BOUSSEL, L., RAYZ, V., MCCULLOCH, C., MARTIN, A., ACEVEDO-BOLTON, G., LAWTON, M., HIGASHIDA, R., SMITH, W. S., YOUNG, W. L., AND SALONER, D. Aneurysm growth occurs at region of low wall shear stress: patient-specific correlation of hemodynamics and growth in a longitudinal study. *Stroke; a journal of cerebral circulation*, 39(11):2997–3002, November 2008. ISSN 1524-4628.

BOWER, A. F. Applied Mechanics of Solids, 2008.

BREEN, E. C. Mechanical strain increases type I collagen expression in pulmonary fibroblasts in vitro. *Journal of applied physiology (Bethesda, Md. : 1985)*, 88(1):203–9, January 2000. ISSN 8750-7587.

BRISMAN, J. L., SONG, J. K., AND NEWELL, D. W. Cerebral aneurysms. *The New England journal of medicine*, 355(9):928–39, August 2006. ISSN 1533-4406.

BUCHANAN, J., KLEINSTREUER, C., HYUN, S., AND TRUSKEY, G. Hemodynamics simulation and identification of susceptible sites of atherosclerotic lesion formation in a model abdominal aorta. *Journal of Biomechanics*, 36(8):1185–1196, August 2003. ISSN 00219290.

CEBRAL, J. R. AND MENG, H. Counterpoint: realizing the clinical utility of computational fluid dynamics–closing the gap. *AJNR. American journal of neuroradiology*, 33(3):396–8, March 2012. ISSN 1936-959X.

CEBRAL, J. R., CASTRO, M. A., BURGESS, J. E., PERGOLIZZI, R. S., SHERIDAN, M. J., AND PUTMAN, C. M. Characterization of cerebral aneurysms for assessing risk of rupture by using patient-specific computational hemodynamics models. *AJNR. American journal of neuroradiology*, 26(10):2550–9, 2005. ISSN 0195-6108.

CHATZIPRODROMOU, I., POULIKAKOS, D., AND VENTIKOS, Y. On the influence of variation in haemodynamic conditions on the generation and growth of cerebral aneurysms and atherogenesis: a computational model. *Journal of biomechanics*, 40(16):3626–40, January 2007. ISSN 0021-9290.

CHEN, H., SELIMOVIC, A., THOMPSON, H., CHIARINI, A., PENROSE, J., VENTIKOS, Y., AND WATTON, P. N. Investigating the Influence of Haemodynamic Stimuli on Intracranial Aneurysm Inception. *Annals of biomedical engineering*, April 2013. ISSN 1521-6047.

CHENG, C. P., PARKER, D., AND TAYLOR, C. A. Quantification of Wall Shear Stress in Large Blood Vessels Using Lagrangian Interpolation Functions with

Cine Phase-Contrast Magnetic Resonance Imaging. *Annals of Biomedical Engineering*, 30(8):1020–1032, September 2002. ISSN 0090-6964.

CHIEN, S. Mechanotransduction and endothelial cell homeostasis: the wisdom of the cell. *American journal of physiology. Heart and circulatory physiology*, 292(3):H1209–24, March 2007. ISSN 0363-6135.

CHIEN, S. Effects of disturbed flow on endothelial cells. *Annals of biomedical engineering*, 36(4):554–62, April 2008. ISSN 1521-6047.

CHIQUET, M., RENEDO, A. S., HUBER, F., AND FLÜCK, M. How do fibroblasts translate mechanical signals into changes in extracellular matrix production? *Matrix biology : journal of the International Society for Matrix Biology*, 22(1):73–80, March 2003. ISSN 0945-053X.

CUMMINS, P. M., VON OFFENBERG SWEENEY, N., KILLEEN, M. T., BIRNEY, Y. A., REDMOND, E. M., AND CAHILL, P. A. Cyclic strain-mediated matrix metalloproteinase regulation within the vascular endothelium: a force to be reckoned with. *American journal of physiology. Heart and circulatory physiology*, 292(1):H28–42, January 2007. ISSN 0363-6135.

DEPAOLA, N., GIMBRONE, M. A., DAVIES, P. F., AND DEWEY, C. F. Vascular endothelium responds to fluid shear stress gradients. *Arteriosclerosis and thrombosis : a journal of vascular biology / American Heart Association*, 12(11):1254–7, November 1992. ISSN 1049-8834.

DOENITZ, C., SCHEBESCH, K.-M., ZOEPHEL, R., AND BRAWANSKI, A. A mechanism for the rapid development of intracranial aneurysms: a case study. *Neurosurgery*, 67(5):1213–21; discussion 1221, November 2010. ISSN 1524-4040.

ERIKSSON, T., KROON, M., AND HOLZAPFEL, G. A. Influence of medial collagen organization and axial in situ stretch on saccular cerebral aneurysm growth. *Journal of biomechanical engineering*, 131 (10):101010, October 2009. ISSN 1528-8951.

ESTEBAN, X. M., LARRABIDE, I., HERNANDEZ, M., AND FRANGI, A. Flux driven medial curve extraction. *The Insight Journal*, pages 1–9, 2007.

FENG, Y., WADA, S., TSUBOTA, K., AND YAMAGUCHI, T. Growth of intracranial aneurysms arising from curved vessels under the influence of elevated wall shear stress -a computer simulation study. *Japan Soc Mech Eng (JSME) Int J Series*, C 47:1035–1042, 2004.

FERZIGER, J. AND PERIC, M. *Computational Methods for Fluid Dynamics*. Springer, 3rd edition, 2001.

FIELD, A. *Discovering Statistics Using SPSS (and sex, drugs and rock 'n' roll)*. SAGE Publications Ltd, London, 2nd edition, 2005.

FISHER, C. AND ROSSMANN, J. S. Effect of non-newtonian behavior on hemodynamics of cerebral aneurysms. *Journal of biomechanical engineering*, 131(9):091004, September 2009. ISSN 1528-8951.

FORD, M. D., HOI, Y., PICCINELLI, M., ANTIGA, L., AND STEINMAN, D. A. An objective approach to digital removal of saccular aneurysms: technique and applications. *The British journal of radiology*, 82 Spec No:S55–61, January 2009. ISSN 1748-880X.

FRÖSEN, J., TULAMO, R., PAETAU, A., LAAKSAMO, E., KORJA, M., LAAKSO, A., NIEMELÄ, M., AND HERNESNIEMI, J. Saccular intracranial aneurysm: pathology and mechanisms. *Acta neuropathologica*, January 2012. ISSN 1432-0533.

GAO, L., HOI, Y., SWARTZ, D. D., KOLEGA, J., SIDDIQUI, A., AND MENG, H. Nascent aneurysm formation at the basilar terminus induced by hemodynamics. *Stroke; a journal of cerebral circulation*, 39(7):2085–90, July 2008. ISSN 1524-4628.

GASSER, T. C., OGDEN, R. W., AND HOLZAPFEL, G. A. Hyperelastic modelling of arterial layers with distributed collagen fibre orientations. *Journal of the Royal Society, Interface / the Royal Society*, 3(6):15–35, February 2006. ISSN 1742-5689.

GIDDENS, D. P., ZARINS, C. K., AND GLAGOV, S. The role of fluid mechanics in the localization and detection of atherosclerosis. *Journal of biomechanical engineering*, 115(4B):588–94, November 1993. ISSN 0148-0731.

GLEASON, R. L. AND HUMPHREY, J. D. A mixture model of arterial growth and remodeling in hypertension: altered muscle tone and tissue turnover. *Journal of vascular research*, 41(4):352–63, 2004. ISSN 1018-1172.

GLEASON, R. L., TABER, L. A., AND HUMPHREY, J. D. A 2-D Model of Flow-Induced Alterations in the Geometry, Structure, and Properties of Carotid Arteries. *Journal of Biomechanical Engineering*, 126(3): 371, 2004. ISSN 01480731.

GLEASON, R. L. AND HUMPHREY, J. D. A 2D constrained mixture model for arterial adaptations to large changes in flow, pressure and axial stretch. *Mathematical medicine and biology : a journal of the IMA*, 22(4):347–69, December 2005. ISSN 1477-8599.

GLOR, F. P., ARIFF, B., HUGHES, A. D., CROWE, L. A., VERDONCK, P. R., BARRATT, D. C., THOM, S. A. M., FIRMIN, D. N., AND XU, X. Y. Image-based carotid flow reconstruction: a comparison between MRI and ultrasound. *Physiological Measurement*, 25(6): 1495–1509, December 2004. ISSN 0967-3334.

GOLLEDGE, J. AND NORMAN, P. E. Atherosclerosis and abdominal aortic aneurysm: cause, response, or common risk factors? *Arteriosclerosis, thrombosis, and vascular biology*, 30(6):1075–7, June 2010. ISSN 1524-4636.

HAHN, C. AND SCHWARTZ, M. A. The role of cellular adaptation to mechanical forces in atherosclerosis. *Arteriosclerosis, thrombosis, and vascular biology*, 28(12):2101–7, December 2008. ISSN 1524-4636.

HASHIMOTO, T., MENG, H., AND YOUNG, W. L. Intracranial aneurysms: links among inflammation, hemodynamics and vascular remodeling. *Neurological research*, 28(4):372–80, June 2006. ISSN 0161-6412.

HEIL, M. THE STABILITY OF CYLINDRICAL SHELLS CONVEYING VISCOUS FLOW. *Journal of Fluids and Structures*, 10(2):173–196, February 1996. ISSN 08899746.

HOI, Y., MENG, H., WOODWARD, S. H., BENDOK, B. R., HANEL, R. A., GUTERMAN, L. R., AND HOPKINS, L. N. Effects of arterial geometry on aneurysm growth: three-dimensional computational fluid dynamics study. *Journal of neurosurgery*, 101(4):676–81, October 2004. ISSN 0022-3085.

HOLZAPFEL, G. A., GASSER, T. C., AND OGDEN, R. A. Y. W. A New Constitutive Framework for Arterial Wall Mechanics and a Comparative Study of Material Models. *Journal of Elasticity*, (61):1–48, 2000.

HOWARD, A. B., ALEXANDER, R. W., NEREM, R. M., GRIENDLING, K. K., AND TAYLOR, W. R. Cyclic strain induces an oxidative stress in endothelial cells. *The American journal of physiology*, 272(2 Pt 1):C421–7, February 1997. ISSN 0002-9513.

HUMPHREY, J. D. Remodeling of a collagenous tissue at fixed lengths. *Journal of biomechanical engineering*, 121(6):591–7, December 1999. ISSN 0148-0731.

HUMPHREY, J. D. Review Paper: Continuum biomechanics of soft biological tissues. *Proceedings of the Royal Society A: Mathematical, Physical and Engineering Sciences*, 459(2029):3–46, January 2003. ISSN 1364-5021.

HUMPHREY, J. D. Vascular adaptation and mechanical homeostasis at tissue, cellular, and sub-cellular levels. *Cell biochemistry and biophysics*, 50(2):53–78, January 2008a. ISSN 1085-9195.

HUMPHREY, J. D. AND CANHAM, P. B. Structure , Mechanical Properties , and Mechanics of Intracranial Saccular Aneurysms. *Journal of Elasticity*, 61:49–81, 2000.

HUMPHREY, J. D. Mechanisms of arterial remodeling in hypertension: coupled roles of wall shear and intramural stress. *Hypertension*, 52(2):195–200, August 2008b. ISSN 1524-4563.

HUMPHREY, J. AND RAJAGOPAL, K. R. A Constrained Mixture Model For Growth and Remodelling of Soft Tissues. *Mathematical Models and Methods in Applied Sciences*, 12(03):407–430, March 2002. ISSN 0218-2025.

HUTCHINSON, B. R. AND RAITHBY, G. D. A MULTIGRID METHOD BASED ON THE ADDITIVE CORRECTION STRATEGY. *Numerical Heat Transfer*, 9 (5):511–537, May 1986. ISSN 0149-5720.

IBA, T. AND SUMPIO, B. E. Morphological response of human endothelial cells subjected to cyclic strain in vitro. *Microvascular Research*, 42(3):245–254, November 1991. ISSN 00262862.

INGALL, T., ASPLUND, K., MAHONEN, M., AND BONITA, R. A Multinational Comparison of Subarachnoid Hemorrhage Epidemiology in the WHO MONICA Stroke Study. *Stroke*, 31(5):1054–1061, May 2000. ISSN 0039-2499.

JOU, L.-D., WONG, G., DISPENSA, B., LAWTON, M. T., HIGASHIDA, R. T., YOUNG, W. L., AND SALONER, D. Correlation between lumenal geometry changes and hemodynamics in fusiform intracranial aneurysms. *AJNR. American journal of neuroradiology*, 26(9):2357–63, October 2005. ISSN 0195-6108.

JUVELA, S. Treatment options of unruptured intracranial aneurysms. *Stroke; a journal of cerebral circulation*, 35(2):372–4, February 2004. ISSN 1524-4628.

KAKISIS, J. D., LIAPIS, C. D., AND SUMPIO, B. E. Effects of cyclic strain on vascular cells. *Endothelium : journal of endothelial cell research*, 11(1):17–28, 2004. ISSN 1062-3329.

KALLMES, D. F. Point: CFD–Computational Fluid Dynamics or Confounding Factor Dissemination. *AJNR. American journal of neuroradiology*, 33(3): 395–6, March 2012. ISSN 1936-959X.

KANEMATSU, Y., KANEMATSU, M., KURIHARA, C., TADA, Y., TSOU, T.-L., VAN ROOIJEN, N., LAWTON, M. T., YOUNG, W. L., LIANG, E. I., NUKI, Y., AND HASHIMOTO, T. Critical roles of macrophages in the formation of intracranial aneurysm. *Stroke; a journal of cerebral circulation*, 42(1):173–8, January 2011. ISSN 1524-4628.

KOCHANEK, D. H. U. AND BARTELS, R. H. Computer Graphics Volume 18, Number 3 July 1984 Interpolating Splines with Local Tension, Continuity, and. *Computer Graphics*, 18(3):33–41, 1984.

KOLAHI, K. S. AND MOFRAD, M. R. K. Mechanotransduction: a major regulator of homeostasis and development. *Wiley interdisciplinary reviews. Systems biology and medicine*, 2(6):625–39, 2010. ISSN 1939-005X.

KOLEGA, J., GAO, L., MANDELBAUM, M., MOCCO, J., SIDDIQUI, A. H., NATARAJAN, S. K., AND MENG, H. Cellular and molecular responses of the basilar terminus to hemodynamics during intracranial aneurysm initiation in a rabbit model. *Journal of vascular research*, 48(5):429–42, January 2011. ISSN 1423-0135.

KROON, M. AND HOLZAPFEL, G. A. Modeling of saccular aneurysm growth in a human middle cerebral artery. *Journal of biomechanical engineering*, 130 (5):051012, October 2008. ISSN 0148-0731.

KROON, M. AND HOLZAPFEL, G. A. A theoretical model for fibroblast-controlled growth of saccular cerebral aneurysms. *Journal of theoretical biology*, 257 (1):73–83, March 2009. ISSN 1095-8541.

KU, D. N., GIDDENS, D. P., ZARINS, C. K., AND GLAGOV, S. Pulsatile flow and atherosclerosis in the human carotid bifurcation. Positive correlation between plaque location and low oscillating shear stress. *Arteriosclerosis (Dallas, Tex.)*, 5(3):293–302, 1985. ISSN 0276-5047.

KULCSÁR, Z., UGRON, A., MAROSFOI, M., BERENTEI, Z., PAÁL, G., AND SZIKORA, I. Hemodynamics of cerebral aneurysm initiation: the role of wall shear stress and spatial wall shear stress gradient. *AJNR. American journal of neuroradiology*, 32(3):587–94, March 2011. ISSN 1936-959X.

LAMACK, J. A. AND FRIEDMAN, M. H. Individual and combined effects of shear stress magnitude and spatial gradient on endothelial cell gene expression. *American journal of physiology. Heart and circulatory physiology*, 293(5):H2853–9, November 2007. ISSN 0363-6135.

LAMACK, J. A., HIMBURG, H. A., LI, X.-M., AND FRIEDMAN, M. H. Interaction of Wall Shear Stress Magnitude and Gradient in the Prediction of Arterial Macromolecular Permeability. *Annals of Biomedical Engineering*, 33(4):457–464, April 2005. ISSN 0090-6964.

LASHERAS, J. C. The Biomechanics of Arterial Aneurysms. *Annual Review of Fluid Mechanics*, 39 (1):293–319, January 2007. ISSN 0066-4189.

LEE, R. M. Morphology of cerebral arteries. *Pharmacology & Therapeutics*, 66(1):149–173, January 1995. ISSN 01637258.

LEUNG, D. Y., GLAGOV, S., AND MATHEWS, M. B. Cyclic stretching stimulates synthesis of matrix components by arterial smooth muscle cells in vitro. *Science (New York, N.Y.)*, 191(4226):475–7, February 1976. ISSN 0036-8075.

LILLIE, M. A. AND GOSLINE, J. M. Mechanical properties of elastin along the thoracic aorta in the pig. *Journal of biomechanics*, 40(10):2214–21, January 2007. ISSN 0021-9290.

MA, B., LU, J., HARBAUGH, R. E., AND RAGHAVAN, M. L. Nonlinear anisotropic stress analysis of anatomically realistic cerebral aneurysms. *Journal of biomechanical engineering*, 129(1):88–96, February 2007. ISSN 0148-0731.

MANNING, J. R. Continuity conditions for spline curves. *The Computer Journal*, 17(2):181–186, February 1974. ISSN 0010-4620.

MANTHA, A., KARMONIK, C., BENNDORF, G., STROTHER, C., AND METCALFE, A. Hemodynamics in a Cerebral Artery before and after the Formation of an Aneurysm. *Ajnr. American Journal Of Neuroradiology*, 27:1113–18, 2006.

MARILL, K. A. Advanced Statistics : Linear Regression , Part II : Multiple Linear Regression. *Academic Emergency Medicine*, pages 94–102, 2004.

MENG, H., METAXA, E., GAO, L., LIAW, N., NATARAJAN, S. K., SWARTZ, D. D., SIDDIQUI, A. H., KOLEGA, J., AND MOCCO, J. Progressive aneurysm development following hemodynamic insult. *Journal of neurosurgery*, 114(4):1095–103, April 2011. ISSN 1933-0693.

MENG, H., WANG, Z., HOI, Y., GAO, L., METAXA, E., SWARTZ, D. D., AND KOLEGA, J. Complex hemodynamics at the apex of an arterial bifurcation induces vascular remodeling resembling cerebral aneurysm initiation. *Stroke; a journal of cerebral circulation*, 38(6):1924–31, June 2007. ISSN 1524-4628.

METAXA, E., MENG, H., KALUVALA, S. R., SZYMANSKI, M. P., PALUCH, R. A., AND KOLEGA, J. Nitric oxide-dependent stimulation of endothelial cell proliferation by sustained high flow. *American journal of physiology. Heart and circulatory physiology*, 295 (2):H736–42, August 2008. ISSN 0363-6135.

MITCHELL, S. A. AND VAVASIS, S. A. Quality mesh generation in three dimensions. In *Proceedings of the eighth annual symposium on Computational geometry - SCG '92*, pages 212–221, New York, New York, USA, 1992. ACM Press. ISBN 0897915178.

MOFTAKHAR, R., AAGAARD-KIENITZ, B., JOHNSON, K., TURSKI, P. A., TURK, A. S., NIEMANN, D. B., CONSIGNY, D., GRINDE, J., WIEBEN, O., AND MISTRETTA, C. A. Noninvasive measurement of intra-aneurysmal pressure and flow pattern using phase contrast with vastly undersampled isotropic projection imaging. *AJNR. American journal of neuroradiology*, 28(9):1710–4, October 2007. ISSN 0195-6108.

MÖLLER, T. AND TRUMBORE, B. Fast , Minimum Storage Ray-Triangle Intersection Fast , Minimum Storage Ray-Triangle Intersection. (May):37–41, 1997.

MYERS, J. G., MOORE, J. A., OJHA, M., JOHNSTON, K. W., AND ETHIER, C. R. Factors Influencing Blood Flow Patterns in the Human Right Coronary Artery. *Annals of Biomedical Engineering*, 29(2):109–120, February 2001. ISSN 0090-6964.

NISSEN, R., CARDINALE, G. J., AND UDENFRIEND, S. Increased turnover of arterial collagen in hypertensive rats. *Proceedings of the National Academy of Sciences of the United States of America*, 75(1):451–3, January 1978. ISSN 0027-8424.

NIXON, A. M., GUNEL, M., AND SUMPIO, B. E. The critical role of hemodynamics in the development of cerebral vascular disease. *Journal of neurosurgery*, 112(6):1240–53, June 2010. ISSN 1933-0693.

OGUNRINADE, O., KAMEYA, G. T., AND TRUSKEY, G. A. Effect of Fluid Shear Stress on the Permeability of the Arterial Endothelium. *Annals of Biomedical Engineering*, 30(4):430–446, April 2002. ISSN 0090-6964.

OHASHI, T. AND SATO, M. Remodeling of vascular endothelial cells exposed to fluid shear stress: experimental and numerical approach. *Fluid Dynamics Research*, 37(1-2):40–59, July 2005. ISSN 0169-5983.

OKADA, M., MATSUMORI, A., ONO, K., FURUKAWA, Y., SHIOI, T., IWASAKI, A., MATSUSHIMA, K., AND SASAYAMA, S. Cyclic Stretch Upregulates Production of Interleukin-8 and Monocyte Chemotactic and Activating Factor/Monocyte Chemoattractant Protein-1 in Human Endothelial Cells. *Arteriosclerosis, Thrombosis, and Vascular Biology*, 18(6):894–901, June 1998. ISSN 1079-5642.

OSHIMA, M., TORII, R., KOBAYASHI, T., TANIGUCHI, N., AND TAKAGI, K. Finite element simulation of blood flow in the cerebral artery. *Computer Methods in Applied Mechanics and Engineering*, 191(6-7):661–671, December 2001. ISSN 00457825.

PATAKAR, H. *Numerical Heat Transfer and Fluid Flow (Hemisphere Series on Computational Methods in Mechanics and Thermal Science)*. Taylor & Francis, 1980. ISBN 0070487405.

PENN, D. L., KOMOTAR, R. J., AND SANDER CONNOLLY, E. Hemodynamic mechanisms underlying cerebral aneurysm pathogenesis. *Journal of clinical neuroscience : official journal of the Neurosurgical Society of Australasia*, 18(11):1435–8, November 2011. ISSN 1532-2653.

PETERS, D. G., KASSAM, A. B., FEINGOLD, E., HEIDRICH-O'HARE, E., YONAS, H., FERRELL, R. E., AND BRUFSKY, A. Molecular Anatomy of an Intracranial Aneurysm : Coordinated Expression of Genes Involved in Wound Healing and Tissue Remodeling. *Stroke*, 32(4):1036–1042, April 2001. ISSN 0039-2499.

PLATT, M. O., ANKENY, R. F., SHI, G.-P., WEISS, D., VEGA, J. D., TAYLOR, W. R., AND JO, H. Expression of cathepsin K is regulated by shear stress in cultured endothelial cells and is increased in endothelium in human atherosclerosis. *American journal of physiology. Heart and circulatory physiology*, 292 (3):H1479–86, March 2007. ISSN 0363-6135.

RABERGER, N. B. *Modelling the Influence of Haemodynamic Factors on the Growth of Cerebral Aneurysms*. PhD thesis, 2007.

RAGHAVAN, M. L., MA, B., AND FILLINGER, M. F. Non-invasive determination of zero-pressure geometry of arterial aneurysms. *Annals of biomedical engineering*, 34(9):1414–9, September 2006. ISSN 0090-6964.

RESNICK, N., YAHAV, H., SHAY-SALIT, A., SHUSHY, M., SCHUBERT, S., ZILBERMAN, L. C. M., AND WOFOVITZ, E. Fluid shear stress and the vascular endothelium: for better and for worse. *Progress in biophysics and molecular biology*, 81(3):177–99, April 2003. ISSN 0079-6107.

REYMOND, P. *Pressure and Flow Wave Propagation in Patient-Specific Models of the Arterial Tree PAR*. PhD thesis, 2011.

REYMOND, P., MERENDA, F., PERREN, F., RÜFENACHT, D., AND STERGIOPULOS, N. Validation of a one-dimensional model of the systemic arterial tree. *American journal of physiology. Heart and circulatory physiology*, 297(1):H208–22, July 2009. ISSN 1522-1539.

SAKAMOTO, N., SAITO, N., HAN, X., OHASHI, T., AND SATO, M. Effect of spatial gradient in fluid shear stress on morphological changes in endothelial cells in response to flow. *Biochemical and biophysical research communications*, 395(2):264–9, April 2010. ISSN 1090-2104.

SALAMEH, A. AND DHEIN, S. Effects of mechanical forces and stretch on intercellular gap junction coupling. *Biochimica et biophysica acta*, January 2012. ISSN 0006-3002.

SFORZA, D. M., PUTMAN, C. M., TATESHIMA, S., VIÑUELA, F., AND CEBRAL, J. R. Effects of Perianeurysmal Environment during the Growth of Cerebral Aneurysms: A Case Study. *AJNR. American journal of neuroradiology*, pages 1–6, March 2012. ISSN 1936-959X.

SFORZA, D. M., PUTMAN, C. M., AND CEBRAL, J. R. Hemodynamics of Cerebral Aneurysms. *Annual review of fluid mechanics*, 41:91–107, January 2009. ISSN 1545-4479.

SHADWICK, R. E. Mechanical design in arteries. *The Journal of experimental biology*, 202(Pt 23):3305–13, December 1999. ISSN 0022-0949.

SHIMOGONYA, Y., ISHIKAWA, T., IMAI, Y., MATSUKI, N., AND YAMAGUCHI, T. A realistic simulation of saccular cerebral aneurysm formation: focussing on a novel haemodynamic index, the gradient oscillatory number. *International Journal of Computational Fluid Dynamics*, 23(8):583–593, September 2009a. ISSN 1061-8562.

SHIMOGONYA, Y., ISHIKAWA, T., IMAI, Y., MATSUKI, N., AND YAMAGUCHI, T. Can temporal fluctuation in spatial wall shear stress gradient initiate a cerebral aneurysm? A proposed novel hemodynamic index, the gradient oscillatory number (GON). *Journal of biomechanics*, 42(4):550–4, March 2009b. ISSN 1873-2380.

SHOJIMA, M., OSHIMA, M., TAKAGI, K., TORII, R., HAYAKAWA, M., KATADA, K., MORITA, A., AND KIRINO, T. Magnitude and role of wall shear stress on cerebral aneurysm: computational fluid dynamic study of 20 middle cerebral artery aneurysms. *Stroke; a journal of cerebral circulation*, 35(11):2500–5, November 2004. ISSN 1524-4628.

SHYU, K.-G. Mechanosensitivity and Mechanotransduction. *Stress: The International Journal on the Biology of Stress*, pages 193–217, 2011.

SINGH, P. K., MARZO, A., HOWARD, B., RUFENACHT, D. A., BIJLENGA, P., FRANGI, A. F., LAWFORD, P. V., COLEY, S. C., HOSE, D. R., AND PATEL, U. J. Effects of smoking and hypertension on wall shear stress and oscillatory shear index at the site of intracranial aneurysm formation. *Clinical neurology and neurosurgery*, 112(4):306–13, May 2010. ISSN 1872-6968.

STEINMAN, D. A., VORP, D. A., AND ETHIER, C. R. Computational modeling of arterial biomechanics: insights into pathogenesis and treatment of vascular disease. *Journal of vascular surgery : official publication, the Society for Vascular Surgery [and] International Society for Cardiovascular Surgery, North American Chapter*, 37(5):1118–28, May 2003. ISSN 0741-5214.

SUGIYAMA, S.-I., MENG, H., FUNAMOTO, K., INOUE, T., FUJIMURA, M., NAKAYAMA, T., OMODAKA, S., SHIMIZU, H., TAKAHASHI, A., AND TOMINAGA, T. Hemodynamic Analysis of Growing Intracranial Aneurysms Arising from a Posterior Inferior Cerebellar Artery. *World neurosurgery*, 4(Figure 2):1–7, November 2011. ISSN 1878-8750.

SUMPIO, B. E., BANES, A. J., LINK, G. W., AND IBA, T. Modulation of endothelial cell phenotype by cyclic stretch: inhibition of collagen production.

The Journal of surgical research, 48(5):415–20, May 1990. ISSN 0022-4804.

TAKAO, H., MURAYAMA, Y., OTSUKA, S., QIAN, Y., MOHAMED, A., MASUDA, S., YAMAMOTO, M., AND ABE, T. Hemodynamic Differences Between Unruptured and Ruptured Intracranial Aneurysms During Observation. *Stroke; a journal of cerebral circulation*, February 2012. ISSN 1524-4628.

TANOUE, T., TATESHIMA, S., VILLABLANCA, J. P., VIÑUELA, F., AND TANISHITA, K. Wall shear stress distribution inside growing cerebral aneurysm. *AJNR. American journal of neuroradiology*, 32(9): 1732–7, October 2011. ISSN 1936-959X.

TATESHIMA, S., TANISHITA, K., OMURA, H., VILLABLANCA, J. P., AND VINUELA, F. Intra-aneurysmal hemodynamics during the growth of an unruptured aneurysm: in vitro study using longitudinal CT angiogram database. *AJNR. American journal of neuroradiology*, 28(4):622–7, April 2007. ISSN 0195-6108.

TATESHIMA, S., CHIEN, A., SAYRE, J., CEBRAL, J., AND VIÑUELA, F. The effect of aneurysm geometry on the intra-aneurysmal flow condition. *Neuroradiology*, 52(12):1135–41, December 2010. ISSN 1432-1920.

THACHER, T., GAMBILLARA, V., DA SILVA, R. F., SILACCI, P., AND STERGIOPULOS, N. Reduced cyclic stretch, endothelial dysfunction, and oxidative stress: an ex vivo model. *Cardiovascular pathology : the official journal of the Society for Cardiovascular Pathology*, 19(4):e91–8, 2010. ISSN 1879-1336.

TOZER, E. C. AND CAREW, T. E. Residence Time of Low-Density Lipoprotein in the Normal and Atherosclerotic Rabbit Aorta. *Circulation Research*, 80(2):208–218, February 1997. ISSN 0009-7330.

TREMMEL, M., DHAR, S., LEVY, E. I., MOCCO, J., AND MENG, H. Influence of intracranial aneurysm-to-parent vessel size ratio on hemodynamics and implication for rupture: results from a virtual experimental study. *Neurosurgery*, 64(4):622–30; discussion 630–1, April 2009. ISSN 1524-4040.

VALENCIA, A., MORALES, H., RIVERA, R., BRAVO, E., AND GALVEZ, M. Blood flow dynamics in patient-specific cerebral aneurysm models: the relationship between wall shear stress and aneurysm area index. *Medical engineering & physics*, 30(3):329–40, April 2008. ISSN 1350-4533.

VENTIKOS, Y., BOWKER, T. J., WATTON, P. N., KAKALIS, N. M., AND BYRNE, J. V. Risk evaluation and interventional planning for cerebral aneurysms: computational models for growth, coiling and thrombosis. *International Journal of Computational Fluid Dynamics*, 23(8):595–607, September 2009. ISSN 1061-8562.

VILLA-URIOL, M. C., BERTI, G., HOSE, D. R., MARZO, A., CHIARINI, A., PENROSE, J., POZO, J., SCHMIDT, J. G., SINGH, P., LYCETT, R., LARRABIDE, I., AND FRANGI, A. F. @neurIST complex information processing toolchain for the integrated management of cerebral aneurysms. *Interface focus*, 1(3):308–19, June 2011. ISSN 2042-8901.

WANG, J. H., GOLDSCHMIDT-CLERMONT, P., WILLE, J., AND YIN, F. C. Specificity of endothelial cell reorientation in response to cyclic mechanical stretching. *Journal of biomechanics*, 34(12):1563–72, December 2001. ISSN 0021-9290.

WANG, J. H.-C. AND THAMPATTY, B. P. An introductory review of cell mechanobiology. *Biomechanics and modeling in mechanobiology*, 5(1):1–16, March 2006. ISSN 1617-7959.

WATTON, P. AND VENTIKOS, Y. Modelling evolution of saccular cerebral aneurysms. *The Journal of Strain Analysis for Engineering Design*, 44(5):375–389, July 2009. ISSN 0309-3247.

WATTON, P. N. *Mathematical modelling of the abdominal aortic aneurysm*. PhD thesis, University of Leeds, 2002.

WATTON, P. N. AND HILL, N. A. Evolving mechanical properties of a model of abdominal aortic aneurysm. *Biomechanics and modeling in mechanobiology*, 8(1):25–42, February 2009. ISSN 1617-7940.

WATTON, P. N., HILL, N. A., AND HEIL, M. A mathematical model for the growth of the abdominal aortic aneurysm. *Biomechanics and modeling in mechanobiology*, 3(2):98–113, November 2004. ISSN 1617-7959.

WATTON, P. N., SELIMOVIC, A., RABERGER, N. B., HUANG, P., HOLZAPFEL, G. A., AND VENTIKOS, Y. Modelling evolution and the evolving mechanical environment of saccular cerebral aneurysms. *Biomechanics and modeling in mechanobiology*, 10 (1):109–32, February 2011. ISSN 1617-7940.

WATTON, P. N., HUANG, H., AND VENTIKOS, Y. Multi-Scale Modelling of Vascular Disease: Abdominal

Aortic Aneurysm Evolution. In *Computational Modeling in Tissue Engineering*, volume 10, pages 309–339. Springer Berlin Heidelberg, 2013.

WATTON, P. N., RABERGER, N. B., HOLZAPFEL, G. A., AND VENTIKOS, Y. Coupling the hemodynamic environment to the evolution of cerebral aneurysms: computational framework and numerical examples. *Journal of biomechanical engineering*, 131 (10):101003, October 2009a. ISSN 1528-8951.

WATTON, P. N., VENTIKOS, Y., AND HOLZAPFEL, G. A. Modelling the growth and stabilization of cerebral aneurysms. *Mathematical medicine and biology : a journal of the IMA*, 26(2):133–64, June 2009b. ISSN 1477-8602.

WATTON, P. N., VENTIKOS, Y., AND HOLZAPFEL, G. A. Modelling the mechanical response of elastin for arterial tissue. *Journal of biomechanics*, 42(9):1320–5, June 2009c. ISSN 1873-2380.

WEMPNER, G. *Mechanics of Solids*. McGraw-Hill, New York, 1973.

ZENG, Z., KALLMES, D. F., DURKA, M. J., DING, Y., LEWIS, D., KADIRVEL, R., AND ROBERTSON, A. M. Hemodynamics and anatomy of elastase-induced rabbit aneurysm models: similarity to human cerebral aneurysms? *AJNR. American journal of neuroradiology*, 32(3):595–601, March 2011. ISSN 1936-959X.

ZHOU, X., RAGHAVAN, M. L., HARBAUGH, R. E., AND LU, J. Patient-specific wall stress analysis in cerebral aneurysms using inverse shell model. *Annals of biomedical engineering*, 38(2):478–89, February 2010. ISSN 1521-6047.



APPENDIX A

STATISTICAL METHODS FOR ASSESSING CORRELATIONS

This section briefly examines the statistical methods applied in Chapter 3. For further details on the numerical methods associated with each, the interested reader is referred to the Marill (2004) paper on advanced linear regression, and Andy Field's excellent text on statistics and SPSS, *Discovering Statistics Using SPSS* (Field, 2005).

A.1 CORRELATION VS. REGRESSION

Firstly, it is useful to appreciate the difference between correlation and regression. The former gives an indication of the *strength* of an association between variables (in the form of the *correlation coefficient*), while the latter gives an indication of how well a variable can be *predicted* from the values of one or more other variables. Hence, a regression can be thought of as a model for prediction, and is therefore often reported as an equation that captures how one or more independent variables predict the dependent variable. While the possibility of a causative relationship between the variables cannot be ruled out, it is important to note that neither analysis indicates causality. Simple linear regression is often used in medical statistics, and assumes that a single dependent variable is predicted from a single independent variable. In simple linear regression, the relationship between these variables is de-

scribed by the equation of a line, i.e.

$$y = bx + c,$$

where y is the dependent, and x the independent variable, c is the y-axis intercept, and b gives the slope of the relationship where the higher the slope, the larger the change in the dependent variable in response to small changes in the independent variable. The strength of the association is commonly expressed in the form of a R^2 value, which represents the amount of variation in the dependent variable that can be explained by the regression model. The closer the R^2 value is to 1, the stronger the association.

A.2 CHOOSING THE CORRECT CORRELATION TEST

Properties of the data, such as linearity and distribution, help to narrow down the choice of correlation test. The most commonly used test is the Pearson's Product-Moment Coefficient, r, which is in fact the square root of R^2 introduced above. Correlation between two variables for N samples is, in general, a measure of their covariance -i.e. it is a means of determining if changes in one variable lead to similar changes in the other. The values of r range from -1 to 1, where $r = 1$ indicates a perfect linear, positive correlation (i.e. an increase in one variable is associated with a linear increase in the other), while $r = -1$ indicates a perfect linear, *inverse* correlation (i.e. an increase in one variable is associated with a linear decrease in the other). However, Pearson's test of correlation assumes that data are parametric -i.e. that the two variables exhibit a linear relationship, and that each is normally distributed.

For non-normally distributed data, the most common test of correlation is the Spearman's Rank Coefficient, ρ, which is effectively the Pearson's Correlation Coefficient, but applied to *ranked*, rather than raw data -i.e. each data point is considered in terms of its rank, which is in turn determined by its magnitude. However, unlike Pearson's coefficient, Spearman's coefficient assess whether a monotonic relationship exists between the examined variables -i.e. whether the variables increase or decrease together -but it does not require that the increase or decrease is linear. It is therefore less sensitive to non-normal distributions of the examined variables. As with Pearson's coefficient, the values of the Spearman correlation coefficient range between -1 and +1. The r values can be further categorised within regions of different correlation strength, i.e.

- 0.8 – 1 indicates a strong correlation;
- 0.5 – 0.8 indicates a moderately strong correlation;
- 0.2 – 0.5 indicates a weak correlation;
- 0 – 0.2 indicates no correlation;

To determine the appropriate correlation test, frequency distributions of data are examined, and a Kolmogorov-Smirnov (K-S) test is often used to determine the degree of deviation of the distribution from normal. In this research, the K-S test is used to examine the distance between the distribution of each variable, and the normal distribution. For a distance value with a significance level greater than 0.05, the data is considered to be normally distributed. Where data are found to be non-normally distributed, a transformation of the data (the dependent, independent, or both variables) may be applied in an attempt to bring the data closer to a normal distribution. While it may be difficult to elucidate the nature of a relationship between two sets of raw data, this may become clearer when the data are transformed (e.g. a growth index may be more clearly associated with the *log*, *inverse*, or *square-root* of WSS data, compared to raw WSS data). Indeed, Boussel et al. (2008) found that a linear regression analysis was only appropriate when the displacement was plotted against *inverse* WSS.

A.3 STATISTICAL SIGNIFICANCE OF CORRELATIONS

Finally, it is not only the measure of strength of the correlation that is important, but the level of *significance*, α, of the correlation coefficient, where statistical significance indicates that the association between variables is unlikely to have occurred by chance. Commonly used levels of significance are 95% ($\alpha = 0.05$) and 99% ($\alpha = 0.001$), which are often used to define "confidence intervals". A *test of significance* is commonly expressed in the form of a p value, which, if less than the chosen value of α, can be interpreted as significant within a certain confidence value -e.g. for $r = 0.65$, $p < 0.001$ is interpreted as a moderately strong correlation, significant within the 99% confidence interval. In this study, for values of $p < 0.05$, the null hypothesis (i.e. that no correlation exists between the examined variables) is rejected.